IBRACON
Instituto Brasileiro do Concreto

REVISTA IBRACON DE ESTRUTURAS E MATERIAIS
IBRACON STRUCTURES AND MATERIALS JOURNAL

Volume 8, Number 4
August, 2015
ISSN 1983-4195

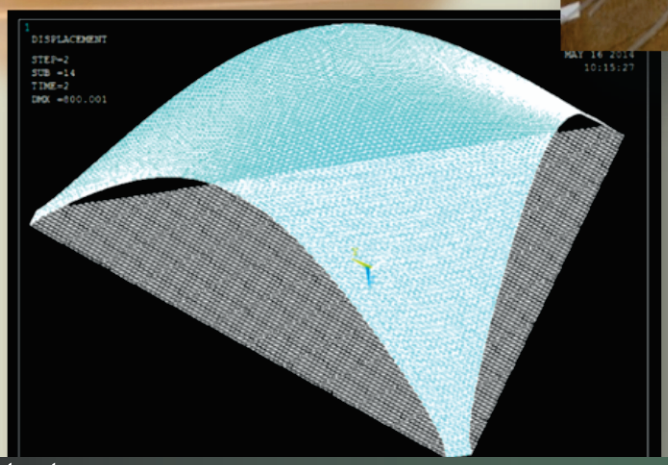

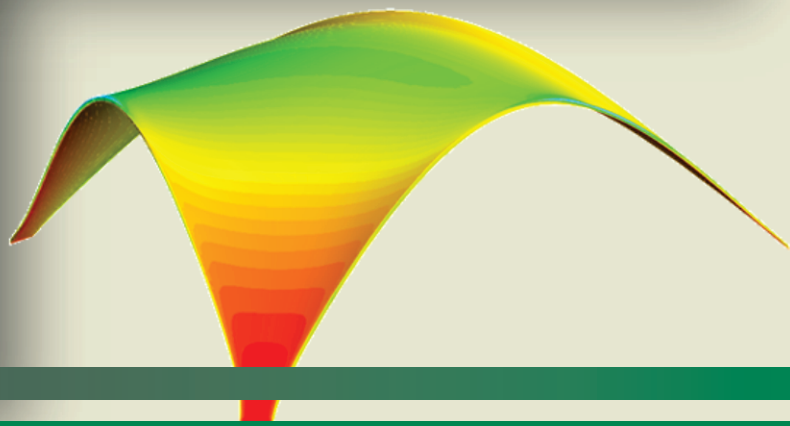

Contents

Editorial

http://dx.doi.org/10.1590/S1983-41952015000400001

We are publishing the fourth issue of the eighth volume of the IBRACON Structures and Materials Journal. In this issue, the first of eight articles presents interaction curves for concrete-encased composite columns subjected to combined compression and bending, based on the deformation domains of reinforced concrete structures defined by ABNT NBR 6118. The second article describes a numerical and experimental analysis of the behavior of structural elements composed of double lattice panels filled with cast-in-place concrete. A probabilistic failure scenarios analysis is described in the third article for the assessment of the influence of reinforcement corrosion on statically indeterminate reinforced concrete beams. In the next article the B-WIM technique is applied for weighing in motion and characterization of the railroad traffic. Finite element analysis of composite concrete-timber beams is the subject of the fifth article. The use of electrochemical impedance spectroscopy for monitoring the corrosion of reinforced concrete is approached in the sixth article. The impacts of the 2014 Revision of the Brazilian Standard ABNT NBR 6118 in the structural design are discussed in the seventh article. The issue closes with an article on the behavior of granular rubber waste tire reinforced soil for application in geosynthetic reinforced soil wall.

We congratulate the authors for the quality of their contributions. All the articles are original and were reviewed by specialists selected among the IBRACON members and other invited reviewers, whose contribution is acknowledged.

Américo Campos Filho, José Luiz Antunes de Oliveira e Sousa, Rafael Giuliano Pileggi, Roberto Caldas de Andrade Pinto and Romilde Almeida de Oliveira, Editors

Estamos publicando o quarto número do oitavo volume da Revista IBRACON de Estruturas e Materiais. Neste número, o primeiro de oito artigos apresenta curvas de interação para pilares mistos de concreto totalmente revestidos, submetidos a flexo-compressão, com base nos domínios de deformação de estruturas de concreto armado definidos pela ABNT NBR 6118. O segundo artigo descreve uma análise numérica e experimental do comportamento de elementos estruturais constituídos por painéis duplos treliçados preenchidos com concreto moldado no local. Uma análise probabilística dos cenários de falha para a avaliação da influência da corrosão das armaduras em vigas hiperestáticas de concreto armado é descrito no terceiro artigo. No artigo seguinte a técnica B-WIM é utilizada para a pesagem em movimento e a caracterização do tráfego ferroviário. Análise de elementos finitos de vigas mistas de concreto e madeira é o tema do quinto artigo. A utilização de espectroscopia de impedância eletroquímica para o monitoramento da corrosão em concreto armado é abordada no sexto artigo. Os impactos da versão 2014 da norma ABNT NBR 6118 no projeto estrutural são discutidos no sétimo artigo. O número se encerra com um estudo sobre os efeitos da aplicação dos resíduos granulares de pneus nas propriedades físicas de solos argilosos.

Parabenizamos os autores pela qualidade de suas contribuições. Todos os artigos são originais e foram revisados por especialistas selecionados dentre os membros do IBRACON e outros revisores convidados, cuja contribuição é apreciada.

Américo Campos Filho, José Luiz Antunes de Oliveira e Sousa, Rafael Giuliano Pileggi, Roberto Caldas de Andrade Pinto e Romilde Almeida de Oliveira, Editores

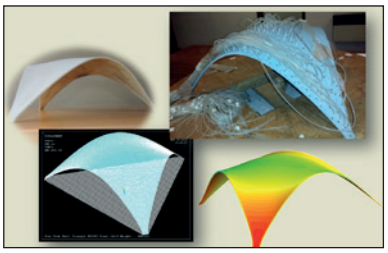

Cover: ULTRA-THIN FREE FORM CONCRETE SHELL

Courtesy: I. VIZOTTO – UNICAMP, CAMPINAS & E. N. B. S. JÚLIO – IST, LISBOA

IBRACON

Ibracon Structures and Materials Journal
is published bimonthly (February, April, June, August, October and December) by IBRACON.

IBRACON
Instituto Brasileiro do Concreto
Founded in 1972

R. Julieta do Espirito Santo Pinheiro, 68
Jardim Olímpia, São Paulo – SP
Brasil – 05542-120
Phone: +55 11 3735-0202
Fax: +55 11 3733-2190
E-mail: arlene@ibracon.org.br
Website: http://www.ibracon.org.br

Cover design & Layout:
Ellementto-Arte
www.ellementto-arte.com

Volume 8, Number 4
August 2015
ISSN: 1983-4195

REVISTA IBRACON DE ESTRUTURAS E MATERIAIS

IBRACON STRUCTURES AND MATERIALS JOURNAL

Contents

Aims and Scope

Aims and Scope

The IBRACON Structures and Materials Journal is a technical and scientifical divulgation vehicle of IBRACON (Brazilian Concrete Institute). Each issue of the periodical has 5 to 8 papers and, possibly, a technical note and/or a technical discussion regarding a previously published paper. All contributions are reviewed and approved by reviewers with recognized scientific competence in the area.

Objectives

The IBRACON Structures and Materials Journal´s main objectives are:

- Present current developments and advances in the area of concrete structures and materials;
- Make possible the better understanding of structural concrete behavior, supplying subsidies for a continuous interaction among researchers, producers and users;
- Stimulate the development of scientific and technological research in the areas of concrete structures and materials, through papers peer-reviewed by a qualified Editorial Board;
- Promote the interaction among researchers, constructors and users of concrete structures and materials and the development of Civil Construction;
- Provide a vehicle of communication of high technical level for researchers and designers in the areas of concrete structures and materials.

Submission Procedure

The procedure to submit and revise the contributions, as well as the formats, are detailed on IBRACON's WebSite (www.ibracon.org.br). The papers and the technical notes are revised by at least three reviewers indicated by the editors. The discussions and replies are accepted for publication after a revision by the editors and at least one member of the Editorial Board. In case of disagreement between the reviewer and the authors, the contribution will be sent to a specialist in the area, not necessarily linked to the Editorial Board.

Contribution Types

The periodical will publish original papers, short technical notes and paper discussions. Announcements of conferences and meetings, information about book reviews, events and contributions related to the area will also be available in the periodical's WebSite. All contributions will be revised and only published after the Editorial and Reviewers Boards approve the paper. Restrictions of content and space (size) are imposed to the papers. The contributions will be accepted for review in Portuguese, Spanish or English. The abstracts are presented in Portuguese or Spanish, and in English, independently of the language in which the paper is written. After the review process, papers originally written in Portuguese or Spanish should be translated into English, which is the official language of the IBRACON Structures and Materials Journal. Optionally, papers are also published in Portuguese or Spanish.

Original papers will be accepted as long as they are in accordance with the objectives of the periodical and present quality of information and presentation. The instructions to submit a paper are detailed in the template (available on IBRACON's WebSite).

The length of the papers must not exceed 20 pages.

A technical note is a brief manuscript. It may present a new feature of research, development or technological application in the areas of Concrete Structures and Materials, and Civil Construction. This is an opportunity to be used by industries, companies, universities, institutions of research, researchers and professionals willing to promote their works and products under development. The instructions to submit a technical note are detailed on IBRACON's WebSite.

A discussion is received no later than 3 months after the publication of the paper or technical note. The instructions to submit a discussion are detailed on IBRACON's WebSite. The discussion must be limited to the topic addressed in the published paper and must not be offensive. The right of reply is guaranteed to the Authors. The discussions and the replies are published in the subsequent issues of the periodical.

Internet Access

IBRACON Structural Journal Page in http://www.ibracon.org.br

Subscription rate

All IBRACON members have free access to the periodical contents through the Internet. Non-members have limited access to the published material, but are able to purchase isolated issues through the Internet. The financial resources for the periodical´s support are provided by IBRACON and by research funding agencies. The periodical will not receive any type of private advertisement that can jeopardize the credibility of the publication.

Photocopying

Photocopying in Brazil. Brazilian Copyright Law is applicable to users in Brazil. IBRACON holds the copyright of contributions in the journal unless stated otherwise at the bottom of the first page of any contribution. Where IBRACON holds the copyright, authorization to photocopy items for internal or personal use, or the internal or personal use of specific clients, is granted for libraries and other users registered at IBRACON.

Copyright

IBRACON

Rua Julieta do Espírito Santo Pinheiro, nº 68 ,Jardim Olímpia,
São Paulo, SP – Brasil CEP: 05542-120
Phone: +55 11 3735-0202 Fax: +55 11 3733-2190
E-mail: arlene@ibracon.org.br.

Disclaimer

Papers and other contributions and the statements made or opinions expressed therein are published on the understanding that the authors of the contribution are the only responsible for the opinions expressed in them and that their publication does not necessarily reflect the support of IBRACON or the journal.

Objetivos e Escopo

A Revista IBRACON de Estruturas e Materiais é um veículo de divulgação técnica e científica do IBRACON (Instituto Brasileiro do Concreto). Cada número do periódico tem 5 a 8 artigos e, possivelmente, uma nota técnica e/ou uma discussão técnica sobre um artigo publicado anteriormente. Todas as contribuições são revistas e aprovadas por revisores com competência científica reconhecida na área.

Objetivos

Os objetivos principais da Revista IBRACON de Estruturas e Materiais são:

- Apresentar desenvolvimentos e avanços atuais na área de estruturas e materiais de concreto;
- Possibilitar o melhor entendimento do comportamento do concreto estrutural, fornecendo subsídios para uma interação contribua entre pesquisadores, produtores e usuários;
- Estimular o desenvolvimento de pesquisa científica e tecnológica nas áreas de estruturas de concreto e materiais, através de artigos revisados por um corpo de revisores qualificado;
- Promover a interação entre pesquisadores, construtores e usuários de estruturas e materiais de concreto, e o desenvolvimento da Construção Civil;
- Prover um veículo de comunicação de alto nível técnico para pesquisadores e projetistas nas áreas de estruturas de concreto e materiais.

Submissão de Contribuições

O procedimento para submeter e revisar as contribuições, assim como os formatos, estão detalhados na página Internet do IBRACON (www.ibracon.org.br). Os artigos e as notas técnicas são revisadas por, no mínimo, três revisores indicados pelos editores. As discussões e réplicas são aceitas para publicação após uma revisão pelo editores e no mínimo um membro do Corpo Editorial. No caso de desacordo entre revisor e autores, a contribuição será enviada a um especialista na área, não necessariamente do Corpo Editorial.

Tipos de Contribuição

O periódico publicará artigos originais, notas técnicas curtas e discussões sobre artigos. Anúncios de congressos e reuniões, informação sobre revisão de livros e contribuições relacionadas à área serão também disponibilizadas na página Internet da revista. Todas as contribuições serão revisadas e publicadas apenas após a aprovação dos revisores e do Corpo Editorial. Restrições de conteúdo e espaço (tamanho) são impostas aos artigos. As contribuições serão aceitas para revisão em português, espanhol ou inglês. Os resumos serão apresentados em português ou espanhol, e em inglês, independentemente do idioma em que o artigo for escrito. Após o processo de revisão, artigos originalmente escritos em português ou espanhol deverão ser traduzidos para inglês, que é o idioma oficial da Revista IBRACON de Estruturas e Materiais. Opcionalmente, os artigos são também publicados em português ou espanhol.

Artigos originais serão aceitos desde que estejam de acordo com os objetivos da revista e apresentam qualidade de informação e apresentação. As instruções para submeter um artigo estão detalhadas em um gabarito (disponível no sítio do IBRACON).

A extensão dos artigos não deve exceder 20 páginas.

Um nota técnica é um manuscrito curto. Deve apresentar uma nova linha de pesquisa, desenvolvimento ou aplicação tecnológica nas áreas de Estruturas de Concreto e Materiais, e Construção Civil. Esta é uma oportunidade a ser utilizada por indústrias, empresas, universidades, instituições de pesquisa, pesquisadores e profissionais que desejem promover seus trabalhos e produtos em desenvolvimento. As instruções para submissão estão detalhadas na página de Internet do IBRACON.

Uma discussão é recebida não mais de 3 meses após a publicação do artigo ou nota técnica. As instruções para submeter uma discussão estão detalhadas na página de Internet do IBRACON. A discussão deve se limitar ao tópico abordado no artigo publicado e não pode ser ofensivo. O direito de resposta é garantido aos autores. As discussões e réplicas são publicadas nos números subseqüentes da revista.

Acesso via Internet

Página da Revista IBRACON de Estruturas e Materiais em http://www.ibracon.org.br

Assinatura

Todos os associados do IBRACON têm livre acesso ao conteúdo do periódico através da Internet. Não associados têm acesso limitado ao material publicado, mas podem adquirir números isolados pela Internet. O financiamento para suporte à revista é provido pelo IBRACON e por agências de financiamento à pesquisa. A revista não receberá qualquer tipo de anúncio privado que possa prejudicar a credibilidade da publicação.

Fotocópias

Fotocópias no Brasil, A Lei Brasileira de Direitos Autorais é aplicada a usuários no Brasil. O IBRACON detém os direitos autorais das contribuições na revista a menos que haja informação em contrário no rodapé da primeira página da contribuição. Onde o IBRACON detém os direitos autorais, autorização para fotocopiar itens para uso interno ou pessoal, ou uso interno ou pessoal de clientes específicos, é concedida para bibliotecas e outros usuários registrados no IBRACON.

Direitos autorais

IBRACON

Rua Julieta do Espírito Santo Pinheiro, nº 68 , Jardim Olímpia,
São Paulo, SP –Brasil CEP: 05542-120
Fone: +55 11 3735-0202 Fax: +55 11 3733-2190

E-mail: arlene@ibracon.org.br.

Aviso Legal

Artigos e outras contribuições e declarações feitas ou opiniões expressas aqui são publicadas com o entendimento que os autores da contribuição são os únicos responsáveis pelas opiniões expressas neles e que sua publicação não necessariamente reflete o apoio do IBRACON ou da revista.

Diretoria

Diretoria
Biênio 2013/2015

Diretor Presidente
Túlio Nogueira Bittencourt

Assessores da Presidência
Augusto Carlos de Vasconcelos
José Tadeu Balbo
Selmo Chapira Kuperman

Diretor 1º Vice-Presidente
Julio Timerman

Diretor 2º Vice-Presidente
Nelson Covas

Diretor 1º Secretário
Antonio Domingues de Figueiredo

Diretor 2º Secretário
Arcindo Vaqueiro Y Mayor

Diretor 1º Tesoureiro
Claudio Sbrighi Neto

Diretor 2º Tesoureiro
Carlos José Massucato

Diretor de Marketing
Hugo da Costa Rodrigues Filho

Diretor de Eventos
Luiz Prado Vieira Júnior

Assessor de Eventos
Maurice Antoine Traboulsi

Diretor Técnico
Inês Laranjeira da Silva Battagin

Diretor de Relações Institucionais
Ricardo Lessa

Diretor de Publicações e Divulgação Técnica
Paulo Helene

Diretor de Pesquisa e Desenvolvimento
Ana Elisabete Paganelli Guimarães A. Jacintho

Diretor de Cursos
Iria Lícia Oliva Doniak

Diretor de Certificação de Mão-de-obra
Roseni Cezimbra

Conselho Diretor
Biênio 2013/2015

Sócios Titulares Individuais

Inês Laranjeira da Silva Battagin
Cláudio Sbrighi Neto
Ana Elisabete Paganelli Guimarães A. Jacintho
Augusto Carlos de Vasconcelos
Nélson Covas
Vladimir Paulon
Antonio Laranjeiras
Enio Pazini Figueiredo
Júlio Timermam
Luis Prado Vieira Júnior

Sócios Titulares Mantenedores e Coletivos

ABCP – Associação Brasileira de Cimento Portland
POLI-USP – Escola Politécnica da Universidade de São Paulo
IPT – Instituto de Pesquisas Tecnológicas de São Paulo
L. A. FALCÃO BAUER
FURNAS
ABCIC – Associação Brasileira da Construção Industrializada em Concreto
GERDAU
ABESC – Associação Brasileira das Empresas de Serviços de Concretagem
CNO – Companhia Norberto Odebrecht
OTTO BAUMGART

Conselheiros Permanentes

Eduardo Antonio Serrano
Paulo Helene
Ronaldo Tartuce
Rubens Machado Bittencourt
Selmo Chapira Kuperman
Simão Priszkulnik

Volume 8, Number 4 (August 2015) p. 447-466 • ISSN 1983-4195
http://dx.doi.org/10.1590/S1983-41952015000400002

REVISTA IBRACON DE ESTRUTURAS E MATERIAIS
IBRACON STRUCTURES AND MATERIALS JOURNAL

Construction of the interaction curve of concrete–encased composite columns based on the deformation domains of reinforced concrete sections

Construção da curva de interação para pilares mistos de aço e concreto totalmente revestidos com base nos domínios de deformação de seções de concreto armado

P. A. S. ROCHA [a]
paulorocha@em.ufop.br

K. I. DA SILVA [a]
katia@em.ufop.br

Abstract

This paper proposes a methodology for obtaining the interaction curve for composite steel–concrete sections subject to combined compression and bending based on the deformation domains of reinforced concrete structures defined by ABNT NBR 6118 [1]. For this, were developed expressions for the axial force, the moment and the strains of concrete, longitudinal reinforcement and the elements comprising the metal profile in each deformation domain. Based on these expressions a computer program called MDCOMP (2014) was created. In this study the same limit values of longitudinal reinforcement strain defined by ABNT NBR 6118 [1] were used for the steel profile strains. To verify the numerical implementations performed, the interaction curves and the plastic resistance of the section obtained by MDCOMP program were compared with those determined from the recommendations of Eurocode 4 [2], of ABNT NBR 8800 [3] or literature responses.

Keywords: composite steel–concrete columns, deformation domains, interaction curve, reinforced concrete.

Resumo

Neste trabalho se propõe uma metodologia para a obtenção da curva de interação para seções mistas de aço e concreto, sujeitas à flexão composta normal, com base nos domínios de deformação de estruturas de concreto armado definidos pela ABNT NBR 6118 [1]. Para isso, foram desenvolvidas expressões para o esforço normal, o momento fletor e para as deformações do concreto, das armaduras e dos elementos que compõem o perfil metálico em cada domínio de deformação. Com base nessas expressões criou–se um programa computacional denominado MDCOMP (2014). Neste trabalho utilizaram–se como valores limites das deformações do perfil metálico nos trechos comprimidos e tracionados, os mesmos estabelecidos pela ABNT NBR 6118 [1] para as deformações das armaduras de aço. Para verificar as implementações numéricas realizadas, as curvas de interação e os esforços máximos de plastificação da seção obtidos com o programa MDCOMP (2014) foram comparados com os determinados a partir das recomendações do EUROCODE 4 [2], da ABNT NBR 8800 [3] ou com respostas da literatura.

Palavras-chave: pilares mistos de aço e concreto, domínios de deformação, curva de interação, concreto armado.

[a] *Universidade Federal de Ouro Preto, Departamento de Engenharia Civil, Escola de Minas, Campus Morro do Cruzeiro.*

Received: 18 Nov 2014 • Accepted: 13 Apr 2015 • Available Online: 7 Aug 2015

1. Introduction

A composite steel–concrete system is every system in which a rolled, folded or welded steel profile works with reinforced concrete. Among the various systems, we can mention composite columns, beams, slabs and connections.

Composite structures appeared in the United States in the late nineteenth century, more precisely in 1894, with the initial purpose of protecting metals against corrosion and fire. Researches by Faber [4] and Jones and Rizk [5] allowed assessing the contribution of concrete to the structural performance of composite structural systems subject to axial loads (composite columns).

Some of the advantages of composite systems are, for instance, a considerable reduction of the structural steel consumption, the possibility of not needing forms and propping, a reduction of the own weight and volume of the structure and an increase in the dimensional accuracy of the construction. Moreover, when composite structures are compared with concrete and steel structures, there is an increase of the section's stiffness and strength, the elimination or reduction of local buckling in metal profiles, the protection against the profile's corrosion, and finally, an increased fire resistance especially in completely concrete encased columns.

Figure 1 shows two usual cross–sections of composite columns, one of which is partially encased with concrete and the other fully encased with concrete.

The mixing of concrete and steel in composite columns subject to simple compression or to the simultaneous action of axial compressive force and bending moments is also a way to leverage the advantages of both materials in order to find the best structural solution.

The first studies on composite steel–concrete columns date from the 60s. Jones and Rizk [5] studied the behavior of fully concrete encased columns taking into account variables such as column length, dimensions of the cross–section and volume of the piece reinforcement and, based on this study, they concluded that the concrete encased steel profile greatly contributed to increasing its load capacity, compared with a steel column.

In [6] the results of tests made with 22 composite columns fully encased with concrete, subject to bending around the lower inertia axis, with load applied by considering different eccentricities. The two failure modes observed after a certain applied load level were the concrete crushing on one side close to the top of the steel profile, and the concrete crushing on one side and the yielding of steel under compression, together with cracks in concrete on the opposite side.

Naka *et al.* [7] show the results of the experimental analysis of four composite columns with supported ends and subject to bending in relation to the greatest inertia axis. The results indicated that the failure mode of the columns was divided into two categories: concrete crushing and local buckling of the metal profile flange in the compressed side; concrete crushing, buckling of the steel reinforcements under compression and yielding of the reinforcements on the tensioned side.

Yamada *et al.* [8] analyzed composite columns subject to the combination of axial forces and transverse loads applied to the extremities of the column, considering bending of the structural system in relation to the greatest inertia axis. In most models studied, there was a reduction in the maximum load capacity of the column when the concrete started cracking and the reinforcement bars started yielding in the tensioned region.

Ricles and Paboojian [9] show the experimental results of eight composite columns fully encased with concrete, with cross–section dimensions equal to 406mmx406mm and shear connectors. Columns were subject to bending in relation to the greatest inertia axis and tested under monotonic axial load and cyclic lateral load. It was verified that the maximum load caused the yielding of the metal profile flange and of the reinforcing bars, and that shear connectors were not effective in improving the flexural strength.

Mirza *et al.* [10] studied the behavior of sixteen 4m long columns, fully encased with concrete, subject to bending in relation to the greatest inertia axis, taking into account the second order effects in the analysis. The tests carried out showed that the concrete strain in the most compressed fiber ranged from 0.0025 to 0.004 before the models collapsed. The presence of shear connectors had little influence on the ultimate capacity of the composite column.

Figure 1 – Composite sections partially and fully encased with concrete

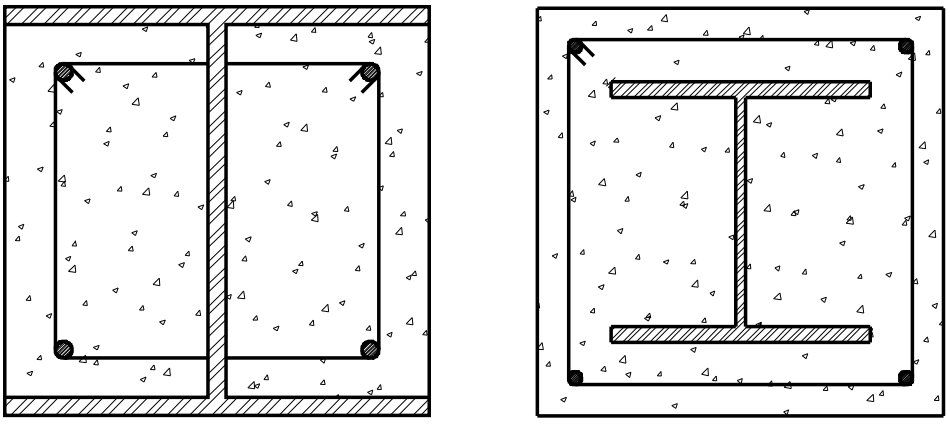

Yokoo *et al.* [11] performed experimental analysis on nineteen short composite columns fully encased with concrete with $f_{ck} = 30\,MPa$. In this experimental program, large cracks were identified on the lower side of the models and the failure occurred due to concrete crushing. The conclusion was that short columns show a failure mechanism characterized by the yielding of steel and concrete crushing and thus are not influenced by second order effects.

Slender columns, in turn, are subject to geometric imperfections capable of amplifying acting forces, resulting in buckling and characterizing the so-called stability criterion. They behave inelastically and fail due to the partial inelasticity of steel, concrete crushing in the compressed region and cracking of concrete in the tensioned region.

Other important effects in those structures such as ductility and energy dissipation capacity of composite columns fully encased with concrete have been investigated and are being explored in Japan and North America. Among some important works, we can mention the researches carried out by Wakabayashi *et al.* [12, 13].

Liew *et al.* [14] demonstrated, from studies on composite columns partially and fully encased with concrete, that the results of the design of composite columns defined by Eurocode 4 [2], British code BS 5400 [15] and AISC/LRFD [16] were not necessarily the same. Such differences have been attributed to different values of load and resistance factors and to the design considerations regarding creep concrete and load eccentricity.

Saw and Liew [17] presented the evaluation of the design of composite columns with I sections partially and fully encased with concrete and with tubular sections filled with concrete, based on criteria established by Part 1.1 of Eurocode 4 [2], by part 5 of British code BS 5400 [15] and by the American code AISC/LRFD [16]. In this research, design parameters were studied and comparisons were made between the nominal strength predicted by the three codes and the predicted strengths with the experimental tests results. In some cases, the results obtained from normative codes varied considerably due to different project considerations regarding each code. However, design procedures in general showed more conservative responses when compared with the results of experimental tests. In turn, EUROCODE 4 [2] presents important favorable factors in terms of its scope and broad range of application.

For columns subject to pure compression, concrete strain limit is of 0.2%. Thus, in order to prevent the premature collapse of the concrete in the element, the steel strain of the profile and reinforcements shall also be limited to this value [18].

Weng and Yen [19] investigated the differences between the approaches of code ACI 318 [20] and AISC/LRFD [16] for the design of composite steel–concrete columns fully encased with concrete and evaluated how their results were close to the responses of a real column. This was confirmed by a series of statistical comparisons. Studies were conducted in order to compare estimated relevant issues using the codes ACI 318 [20] and AISC/LRFD [16]. These approaches were compared with results of composite columns fully encased with concrete obtained in previous researches. Among such researches, we may mentioned the physical tests conducted by Stevens [6], Naka et al. [7], Yamada et al. [8], Ricles and Paboojian [9], Mirza et al. [10], Yokoo et al. [11] and Wakabayashi et al. [12].

Figure 2 – Deformation domains for reinforced concrete sections

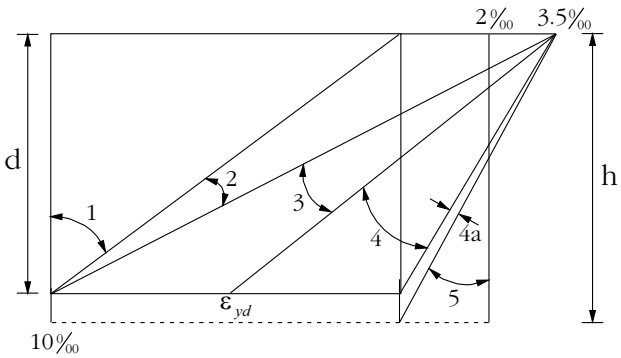

Among the numerical modeling of composite steel–concrete columns, Fong [21] points out that many codes tend to recommend the use of a second order analysis and design method to efficiently obtain more accurate results. Some recent studies were developed to obtain numerical formulations for advanced analysis of composite steel–concrete structures, based on the refined plastic hinge method.

An effective numerical procedure for the construction of the interaction curve of composite steel–concrete columns is the fiber method consisting in the subdivision of the cross–section area in smaller single material regions, distributed along the length of the column [22].

In this paper, we propose a calculation procedure based on the deformation domains of reinforced concrete sections, as shown in Figure 2, to obtain the interaction curve of composite columns fully encased with concrete in a computational manner. This approach was adopted due to the similarities found between the interaction curves of reinforced concrete sections and composite steel–concrete sections. The computational package developed is called MDCOMP (2014) and was implemented in FORTRAN language. Results obtained using MDCOMP (2014) are compared with the responses defined by Part 1.1 of Eurocode 4 [2], which is one of the most important codes used to design this type of structural element, and also with the answers presented in the works of Saw and Liew [17], Weng and Yen [19] and Naka et al. [7].

2. Interaction curve of composite column cross section

The interaction curve is the geometric locus of M–N pairs that define the limits of strength of the cross–section of a structural member under combined compression and bending.

Figure 3 shows the curve adopted by Part 1.1 of Eurocode 4 [2], as well as the simplified polygonal diagram adopted by NBR 8800 [3], which is represented by the dotted curve in Figure 3. In this case, we shall consider that there is a total plastic stress distribution between points A, which corresponds to the maximum axial force, and D, which is the maximum bending moment.

At point A, the interaction curve has only the contribution of the

Figure 3 – Interaction curve according to EUROCODE 4 (2)

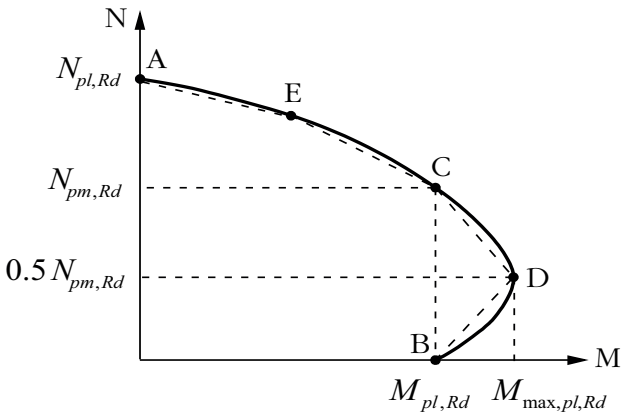

axial force on the piece, thus concrete, metal profile and steel reinforcements are subject to compressive normal force, with

$$N_A = N_{pl,Rd} \quad \text{and} \quad M_A = 0 \tag{1a}$$

At point B, column is subject only to pure bending, where

$$N_B = 0 \quad \text{and} \quad M_B = M_{pl,Rd} \tag{1b}$$

At point C, we find the combination of axial load and bending, i.e.,

$$N_C = N_{pm,Rd} = \frac{0.85\,A_c\,f_{ck}}{\gamma_c} \quad \text{e} \quad M_C = M_{pl,Rd} \tag{1c}$$

and at point D, we see

$$N_D = 0.5\,N_{pm,Rd} = 0.5\,\frac{(0.85A_c\,f_{ck})}{\gamma_c} \quad \text{and} \quad M_D = M_{\max,pl,Rd} \tag{1d}$$

$$M_{pl} = \frac{Z_{Pa}\,f_y}{\gamma_a} + \frac{Z_{Ps}\,f_s}{\gamma_s} + \frac{1}{2}\,\frac{Z_{Pc}(0.85\,f_{ck})}{\gamma_c} \tag{1e}$$

Point E is located on the average point of the curve between points A and C.

In the above equations, $N_{pl,Rd}$ is the design value of the plastic resistance of the composite section to compressive normal force, $N_{pm,Rd}$ is the design value of the resistance of the concrete to compressive normal force, $M_{pl,Rd}$ is the design value of the plastic resistance moment of the composite section and Z_{Pa}, Z_{Ps}, Z_{Pc} are, respectively, the plastic resistance modulus of steel profile, reinforcement bars and concrete.

3. Definition of balance and deformation equations

Figure 4 schematically shows the strain diagram of the composite section fully encased with concrete, as well as the resulting forces acting on the section.

Figure 4 – Composite section and strain diagram with scheme of resultant forces

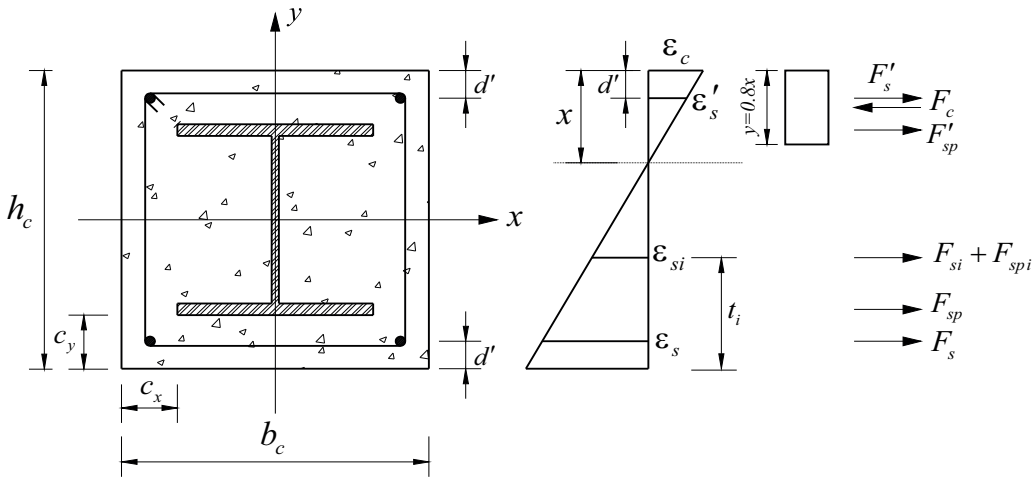

In this figure, F'_s, F'_{sp}, F_{si}, F_{spi}, F_{sp} and F_s are, respectively, the resulting forces on the upper reinforcements of the composite section, on the top flange of the metal profile, on the generic reinforcements located between the profile flanges, on the web of the metal profile, on the bottom flange of the metal profile and on the bottom reinforcements of the composite section.
Considering the equilibrium of normal force and bending moment in the section, we find:

$$N_{Rd} = -F_c + \sum_{i=1}^{n} F_i \quad (2)$$

$$M_{Rd} = N_d \frac{h}{2} + F_c (h - 0.4\,x) - \sum_{i=1}^{n} F_i t_i \quad (3)$$

The sums of the equations above correspond to the contributions of forces and bending moments of concrete, reinforcements and metal profile.
The position of the neutral axis of the composite section (x) is defined based on the relation

$$x = \frac{\varepsilon_c}{\varepsilon_c + \varepsilon_s} \quad (4)$$

where ε_c is the concrete strain, ε_s is the lower reinforcement's steel strain and d' is the distance from the centroid of steel reinforcements and the edge of the composite steel–concrete section, which results from:

$$d' = c + \phi_t + 0.5\phi_l \quad (5)$$

In Eq. 5, c is the thickness of concrete cover, ϕ_t is the diameter of the transverse reinforcement (stirrups) and ϕ_l is the diameter of the longitudinal reinforcement.
Equations that relate the strain of steel reinforcements and of the elements making up the metal profile with concrete strain are:

$$\varepsilon'_s = \frac{\varepsilon_c (x - d')}{x} \quad (6a)$$

$$\varepsilon_s = -\frac{\varepsilon_c (d - x)}{x} \quad (6b)$$

$$\varepsilon'_{sp} = \frac{\varepsilon_c (x - c_y - 0.5\,t_f)}{x} \quad (6c)$$

$$\varepsilon_{sp} = -\frac{\varepsilon_c (h_c - x - c_y - 0.5\,t_f)}{x} \quad (6d)$$

$$\varepsilon_{spi} = -\frac{\varepsilon_c (d - x + d' - 0.5\,h_c)}{x} \quad (6e)$$

In the above equations, ε'_s and ε_s are, respectively, the strains of upper and lower steel reinforcements, ε'_{sp} and ε_{sp} are the strains of the upper and lower flange of the metal profile, respectively, ε_{spi} is the strain of the metal profile web, d is the distance between the steel reinforcement in tension to the extreme fiber of the composite section on the compressed side (effective height of the composite section), c_y is the thickness of concrete cover and h_c is the depth of the concrete encasement to a steel section (see Fig. 4).
In this study, the strain of steel reinforcements and metal profile were limited to 1% in traction and 0.35% in compression, as determined by ABNT NBR 6118 [1], since concrete does not show strains beyond these limits.
As in domain 5, the neutral axis is outside the reinforced concrete section, i.e., $h_c < x < +\infty$, ensuring the equilibrium of forces and moments in the section, not taking into account the strength portion corresponding to reinforcements, and setting the moment equation equal to zero, the limit amount of the neutral axis position in this domain is reached and equal to $x = 1.25h$.
The limit value x for the composite steel–concrete section was obtained in a manner similar to that described above for the reinforced concrete section, but considering the portion of strength related to concrete and metal profile. Thus, the equilibrium of forces and moment on section provides:

$$N_{Rd} = -F_c + A_a f_{yd} \quad (7)$$

and

$$M_{Rd} = N_{Rd} \frac{h}{2} + F_c (h - 0.4\,x) \quad (8)$$

Figure 5 – Interaction curve of the cross-section of a reinforced concrete column

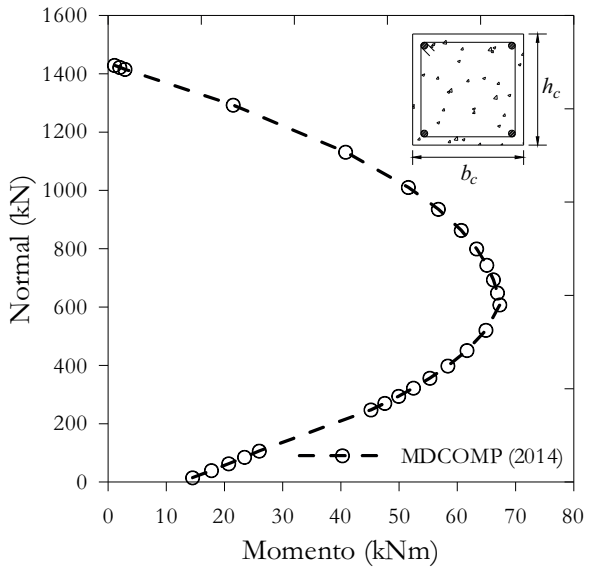

By substituting (7) by (8) and doing $M_{Rd} = 0$, taking into account that Fc = 0.85 fcd b x, we reach the following second degree equation:

$$0 = 0.85 f_{cd}\, b\, 0.8 x\, (0.5 h - 0.4 x) + A_a\, f_y\, 0.5 h \qquad (9)$$

The largest root of equation (9), x = 2.305h, corresponds to a null value for the bending moment and to the maximum value for the axial force in the section and is, therefore, the limit value for the position of the neutral axis of the composite steel–concrete section.

4. Examples

This section presents the interaction curves of cross–sections of a reinforced concrete column and various cross–sections of composite steel–concrete columns obtained numerically from the computer program MDCOMP (2014). Comparisons are made, where possible, with the curves obtained according to current codes and/or with the answers provided by other researchers.

Table 1 – Sizes of concrete cross-section

Composite section	h_c (mm)	b_c (mm)	c_y (cm)	$\rho_s = \frac{A_a}{A_c}$ %
SM1	333	334	4.0	8.33
SM2	403	454	7.5	5.10
SM3	553	654	15.0	2.56

4.1 Interaction curve of the cross–section of a reinforced concrete column

In this example, we analyze the cross–section of a reinforced concrete column with section $33.3\,cm \times 33.4\,cm$. The concrete has $f_{ck} = 20MPa$ and longitudinal reinforcement consists of four CA50 steel bars with a $\phi_l = 10\,mm$ diameter, as to know $d' = 3.5\,cm$. Figure 5 shows the interaction curve moment x normal for the section obtained from the variation of the concrete and steel strains within the six deformation domains (see Figure 2). The portion of the curve corresponding to combined tension and moment, which includes domain 1 and a portion of domain 2, was deleted, i.e., only portions referring to the section behavior under compression and bending are presented.

4.2 Interaction curve of the cross–section of a composite steel–concrete column

In this example, we find the analysis of the cross–section of a composite steel–concrete column formed by a Gerdau rolled metal profile $W250 \times 73\,kg/m$ and considering three different values for the depth and width of the concrete encasement to the steel section, i.e., h_c and b_c, as shown in Table 1.
In Table 1, ρ_s is the ratio of the area of the steel profile cross–section (A_a) and the area of the concrete cross–section (A_c).
The concrete used has $f_{ck} = 20MPa$, four CA50 steel bars with a $\phi_l = 10\,mm$ diameter for the longitudinal reinforcement and $d' = 3.5\,cm$.

Figure 6 – Interaction curve of cross-sections of composite steel-concrete column

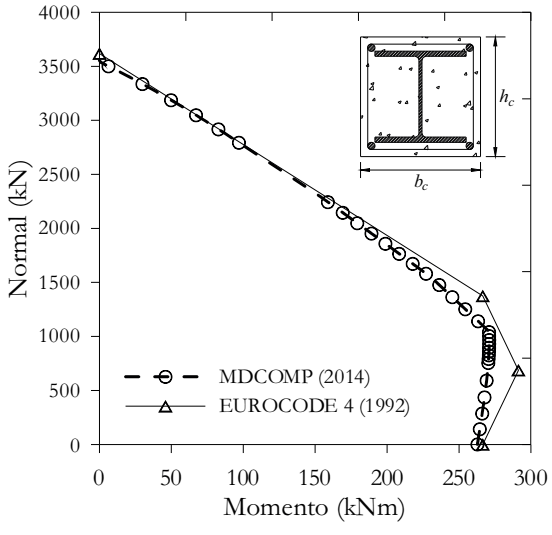

Figure 6b – Interaction curve of cross-sections of composite steel-concrete column

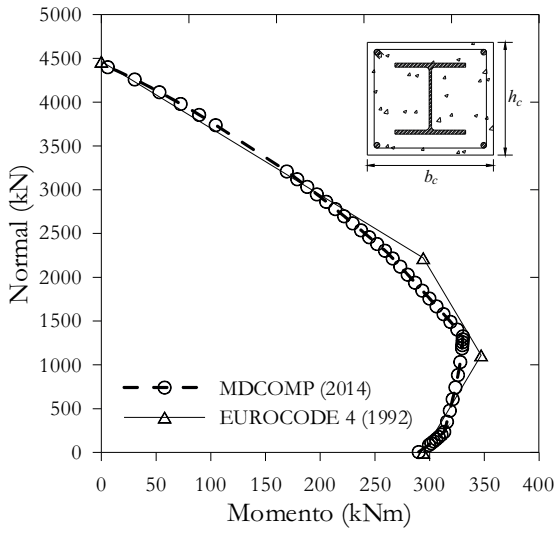

B Section SM2

Figure 6c – Interaction curve of cross-sections of composite steel-concrete column

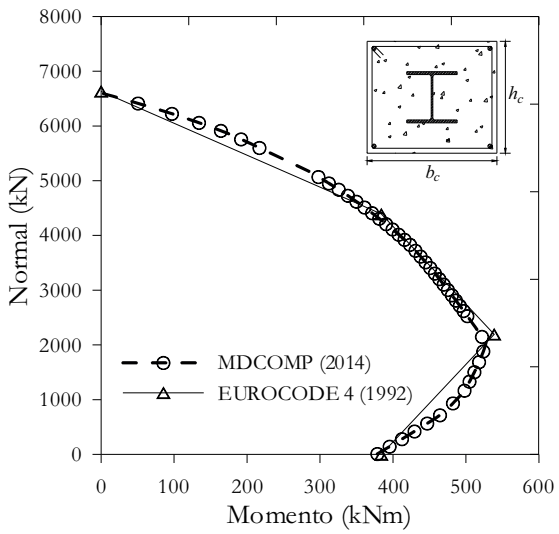

C Section SM3

In the graphs shown in Figure 6, we see the interaction curves moment x normal obtained with the MDCOM computational package (2014) for the three composite steel–concrete sections, being compared to the curves obtained based on the EUROCODE 4 [2] considerations.

Tables 2 and 3 show, respectively, the numerical results of design value of the resistance to moment and normal force to the composite steel–concrete section and comparisons with responses obtained based on the recommendations of Eurocode 4 [2].

4.3 Comparison with results found in books

In this section, we make a comparison between the results of the MDCOMP computer program (2014) and the responses obtained by other researchers or from current codes.

The first interaction curves shown refer to the cross–section of a composite steel–concrete column previously analyzed by Saw and Liew [17] in accordance with the recommendations of Eurocode 4 [2]. The section is formed by a $UC\,254\times254\times107\,kg/m$ steel profile with $f_y = 355MPa$, four steel bars with $f_{yk} = 460MPa$ and longitudinal reinforcement with $\phi_l = 12.5\,mm$, concrete with $f_{ck} = 20MPa$ and $b_c = h_c = 400\,mm$ dimensions.

The interaction curves obtained in this analysis are presented in Figure 7.

Table 4 presents the comparisons between the resistant capabilities obtained with the MDCOMP program (2014) and the ones obtained by Saw and Liew [17].

The second comparison was made with an interaction curve obtained from the recommendations of the American code ACI 318 [20]. For this analysis, we used a section with $b_c = h_c = 240mm$ ($f_{ck} = 25.6\,MPa$), which fully covers a metal profile $H96\times100\times5.1\times8.6\,mm$ ($f_y = 311.2\,MPa$ and four steel bars

Table 2 – Maximum design value of the plastic resistance moment ($M_{max,pl,Rd}$) and design value of the plastic resistance moment ($M_{pl,Rd}$)

Composite section	$M_{max,pl,Rd}$ (kNm)			$M_{pl,Rd}$ (kNm)		
	EC4	MDCOMP	$\frac{M_{MDCOMP}}{M_{EC4}}$	EC4	MDCOMP	$\frac{M_{MDCOMP}}{M_{EC4}}$
SM1	291.28	270.44	0.93	291.28	270.44	0.99
SM2	346.98	330.31	0.95	346.98	330.31	0.99
SM3	538.63	527.49	0.98	538.63	527.49	0.99

Table 3 – Design value of the plastic resistance to compressive normal force ($N_{pl,Rd}$)

Composite section	$N_{pl,Rd}$ (kN)		
	EC4	MDCOMP	N_{MDCOMP}/N_{EC4}
SM1	3618.22	3553.66	0.98
SM2	4465.09	4430.69	0.99
SM3	6635.02	6602.54	0.99

with $f_{yk} = 634\,MPa$ and $\phi_l = 10\,mm$ for longitudinal reinforcements. We found $\rho_s = 3.7\%$ and $\rho_r = 0.5\%$, where ρ_r is the steel rate of the longitudinal reinforcement ($\rho_r = A_s/A_c$). Results are shown in Figure 8.

Table 5 shows comparisons between the resistant capabilities obtained with the MDCOMP program (2014) and the ones defined by the American code ACI 318 [20].

In the last analysis, another comparison of MDCOMP program (2014) results was made with those obtained from the recommendations of the American code ACI 318 [20] and with the experimental results presented by Naka *et al.* [7].

The analyzed cross–section is formed by a steel profile $H\,180\times120\times4.5\times12\,mm$ ($f_y = 344.8\,MPa$) encased with concrete with $f_{ck} = 25.5\,MPa$, and $b_c = 240\,mm$ and $h_c = 300\,mm$ dimensions. Four steel bars $f_{yk} = 461.3\,MPa$ and $\phi_l = 10\,mm$ were used for longitudinal reinforcement. We found $\rho_s = 4.6\%$ and $\rho_r = 3.2\%$. Graphs in Figure 9 show the interaction curves obtained in this analysis.

Table 4 – Parameterized maximum design value of the plastic resistance moment ($M_{max,pl,Rd}$), design value of the plastic resistance moment ($M_{pl,Rd}$) and design value of the plastic resistance to compressive normal force ($N_{pl,Rd}$)

Force	EC4	MDCOMP	MDCOMP/EC4
$M_{max,pl,Rd}/M_u$	0.97	0.92	0.95
$M_{pl,Rd}/M_u$	0.90	0.89	0.99
$N_{pl,Rd}/N_u$	0.92	0.96	1.04

5. Conclusions

In this paper, we presented a methodology that allows the construction of the interaction curve for composite steel–concrete sections subject to combined compression and bending, based on the deformation domains of reinforced concrete structures defined by ABNT NBR 6118 [1]. To this end, relationships were described for the strains of reinforcements and elements comprising the metal profile, according to the strains of concrete, as well as equations for the normal force and bending moment in each deformation domain. From these expressions, the M–N pairs were determined in the ultimate limit state, needed to build the interaction curve.

Tables 2 to 5 show that the design value of the plastic resistance to compressive normal force ($N_{pl,Rd}$), the design value of the plastic resistance moment ($M_{pl,Rd}$) and the maximum design value of the plastic resistance moment ($M_{max,pl,Rd}$) of the composite section

Figure 7 – Interaction Curves – MDCOMP (2014) x Saw and Liew (2000)

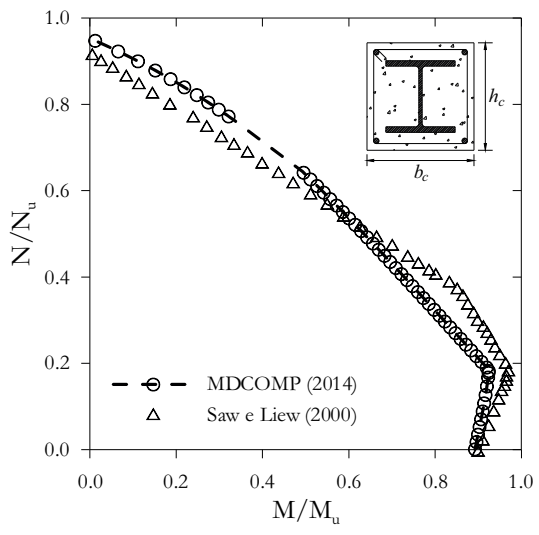

Figure 8 – Interaction Curves – MDCOMP (2014) x ACI 318 (1999)

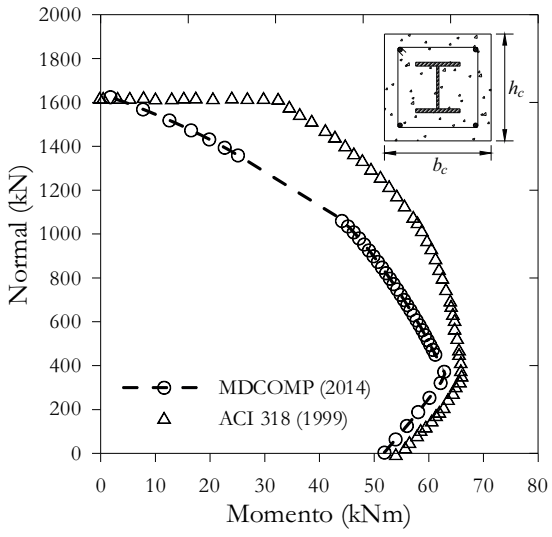

Table 5 – Maximum design value of the plastic resistance moment ($M_{max,pl,Rd}$), design value of the plastic resistance moment ($M_{pl,Rd}$) and design value of the plastic resistance to compressive normal force ($N_{pl,Rd}$)

Force	ACI 318	MDCOMP	MDCOMP / ACI318
$M_{max,pl,Rd}$ (kNm)	66.00	62.91	0.95
$M_{pl,Rd}$ (kNm)	53.95	51.88	0.96
$N_{pl,Rd}$ (kN)	1622.19	1644.11	1.01

obtained from MDCOMP computer program (2014), which is based on relationships defined by NBR 6118 [1], are very close to those set by both the EUROCODE 4 [2] and ACI 318 [20]. From the graph in Figure 9, we can find that in the comparison between the experimental results of Naka *et al.* [7], the approach of ACI 318 [20] provides more precisely than the procedure based on deformation domains recommended by NBR 6118 [1], although the results corresponding to maximum resistances ($N_{pl,Rd}$ and $M_{pl,Rd}$) are very similar in the two processes.

With regard to the variation rate of the steel in the metal profile in the composite section (ρ_s), we may verify that the smaller the value, the more the curve approaches the theoretical graphic for composite steel–concrete columns defined by EUROCODE 4 [2] (see Figure 6 and Tables 2 and 3). This is evidenced by comparing curve in Figure 6c with curve in Figure 3.

Finally, it is clear from the examples analyzed that the numerical results obtained via MDCOMP (2014) showed a good correlation with the interaction curves defined by Eurocode 4 [2], but there were some discrepancies with the answers defined by ACI 318 [20] (see Figures 8 and 9). This is due to the different values of partial safety factors for strength and loads, as well as to design considerations regarding creep concrete and load eccentricity adopted by each code.

Figure 9 – Comparison of interaction curves

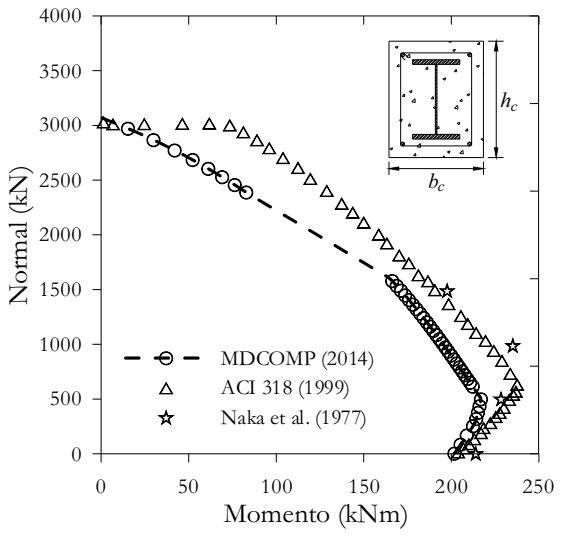

6. References

[1] ASSOCIAÇÃO BRASILEIRA DE NORMAS TÉCNICAS (2003), NBR 6118:2003. Projeto de estruturas de concreto armado. Rio de Janeiro, RJ.

[2] EUROPEAN COMMITTEE FOR STANDARDIZATION (1992), EUROCODE 4, Design of composite steel and concrete structures – Part 1.1: General rules and rules for buildings, CEN, Bruxelas, Belgium.

[3] ASSOCIAÇÃO BRASILEIRA DE NORMAS TÉCNICAS (2008), NBR 8800:2008. Projeto e execução de estruturas de aço e de estruturas mistas aço–concreto de edifícios: Projeto de revisão. Rio de Janeiro.

[4] Faber, O. (1956), Savings to be affected by the more rational design of encased stanchions as a result of recent full size tests, The Structural Engineer, vol. 34, pp. 88–109.

[5] Jones, R. and Rizk, A.A. (1963), An investigation on the behaviour of encased steel columns under load, The Structural Engineer, Vol. 41, N° 1, pp. 21–33.

[6] Stevens, R.F. (1965), Encased stanchions, The Structural Engineer, 43(2), pp. 59–66.

[7] Naka, T., Morita, K. and Tachibana, M. (1977), Strength and hysteretic characteristics of steel–reinforced concrete columns (in Japanese), Transaction of AIJ; 250, pp. 47–58.

[8] Yamada, M., Kawamura, H., and Zhang, F. (1991), Research on the elasto–plastic deformation and fracture behaviors of wide flange steel encased reinforced concrete columns subjected to bending and shear (in Japanese), Journal of Structural Construction Engineering, AIJ Architectural Institute of Japan); 420, pp. 63–74.

[9] Ricles, J.M. and Paboojian, S.D. (1994), Seismic performance of steel–encased composite columns, Journal of Structural Engineering, ASCE; 120(8), pp. 2474–2494.

[10] Mirza, S.A., Hyttinen, V. and Hyttinen, E. (1996), Physical tests and analyses of composite steel–concrete beam–columns, Journal of Structural Engineering, ASCE; 122(11), pp. 1317–1326.

[11] Yokoo, Y., Wakabayashi, M. and Suenaga Y. (1967), Experimental studies on steel concrete members with H–shape steel (in Japanese). Transaction of AIJ; 136, pp. 1–7.

[12] Wakabayashi, M., Shibata, M., Matsui, C. and Minami, K. (1974), A study on the behaviour of steel–reinforced concrete columns and frames. In: IABSE Symposium, pp. 53–60.

[13] Wakabayashi, M. (1987), A historical study of research on composite construction in Japan. In: Composite construction in steel and concrete. Proc. of eng. foundation conf. Henniker, New Hampshire: ASCE, pp. 400–427.

[14] Liew, J.Y.R., Saw, H.S. and Yu, C.H. (1998), Composite column design in buildings – Assessment of current methods and interim guidance. Research Report n. CE 026/98, National University of Singapore, May.

[15] BS 5400 (1979), Steel, concrete and composite bridges,

Part 5, Code of practice for design of composite bridges. London: British Standards Institution.

[16] AISC/LRFD (1993), Load and Resistance Factor Design Specification for Structural Steel Buildings, 1st edn., American Institute of Steel Construction, AISC, Chicago, IL.

[17] Saw, H.S. and Liew, J.Y.R. (2000). Assesment of Current Methods for the Design of Composite Columns in Buildings. Journal of Constructional Steel Research, v. 53, p. 121–147.

[18] Queiroz, G., Pimenta, R.J. and Da Mata, L.A.C. (2001), Elementos das Estruturas Mistas Aço–Concreto, Belo Horizonte, 1ª edição, Editora O Lutador.

[19] Weng, C.C. and Yen, S.I. (2002). Comparisons of Concrete–encased Composite Column Strength Provisions of ACI Code and AISC Specification, v. 24, p. 59–72.

[20] Buildings code requirements for Structural Concrete (ACI 318–99) (1999). Detroit (MI): American Institute (ACI).

[21] Fong, M. (2012). Second–order analysis of imperfect light–weight and composite structures. Doctoral thesis, Department of civil and structural engineering, The Hong Kong Polytechnic University, Hong Kong, China.

[22] Sfakianakis, M.G. (2002). Biaxial bending with axial force of reinforced, composite and repaired concrete sections of arbitrary shape by fiber model and computer graphics. Advances in engineering software, v. 33, p. 227–242.

Volume 8, Number 4 (August 2015) p. 447-466 • ISSN 1983-4195
http://dx.doi.org/10.1590/S1983-41952015000400002

REVISTA IBRACON DE ESTRUTURAS E MATERIAIS
IBRACON STRUCTURES AND MATERIALS JOURNAL

Construction of the interaction curve of concrete–encased composite columns based on the deformation domains of reinforced concrete sections

Construção da curva de interação para pilares mistos de aço e concreto totalmente revestidos com base nos domínios de deformação de seções de concreto armado

P. A. S. ROCHA [a]
paulorocha@em.ufop.br

K. I. DA SILVA [a]
katia@em.ufop.br

Abstract

This paper proposes a methodology for obtaining the interaction curve for composite steel–concrete sections subject to combined compression and bending based on the deformation domains of reinforced concrete structures defined by ABNT NBR 6118 [1]. For this, were developed expressions for the axial force, the moment and the strains of concrete, longitudinal reinforcement and the elements comprising the metal profile in each deformation domain. Based on these expressions a computer program called MDCOMP (2014) was created. In this study the same limit values of longitudinal reinforcement strain defined by ABNT NBR 6118 [1] were used for the steel profile strains. To verify the numerical implementations performed, the interaction curves and the plastic resistance of the section obtained by MDCOMP program were compared with those determined from the recommendations of Eurocode 4 [2], of ABNT NBR 8800 [3] or literature responses.

Keywords: composite steel–concrete columns, deformation domains, interaction curve, reinforced concrete.

Resumo

Neste trabalho se propõe uma metodologia para a obtenção da curva de interação para seções mistas de aço e concreto, sujeitas à flexão composta normal, com base nos domínios de deformação de estruturas de concreto armado definidos pela ABNT NBR 6118 [1]. Para isso, foram desenvolvidas expressões para o esforço normal, o momento fletor e para as deformações do concreto, das armaduras e dos elementos que compõem o perfil metálico em cada domínio de deformação. Com base nessas expressões criou–se um programa computacional denominado MDCOMP (2014). Neste trabalho utilizaram–se como valores limites das deformações do perfil metálico nos trechos comprimidos e tracionados, os mesmos estabelecidos pela ABNT NBR 6118 [1] para as deformações das armaduras de aço. Para verificar as implementações numéricas realizadas, as curvas de interação e os esforços máximos de plastificação da seção obtidos com o programa MDCOMP (2014) foram comparados com os determinados a partir das recomendações do EUROCODE 4 [2], da ABNT NBR 8800 [3] ou com respostas da literatura.

Palavras-chave: pilares mistos de aço e concreto, domínios de deformação, curva de interação, concreto armado.

[a] *Universidade Federal de Ouro Preto, Departamento de Engenharia Civil, Escola de Minas, Campus Morro do Cruzeiro.*

Received: 18 Nov 2014 • Accepted: 13 Apr 2015 • Available Online: 7 Aug 2015

1 Introdução

Considera–se como sistema misto de aço e concreto todo aquele no qual um perfil de aço laminado, dobrado ou soldado trabalha em conjunto com o concreto armado. Dentre os diversos sistemas existentes podem–se citar os pilares mistos, as vigas mistas, as lajes mistas e as ligações mistas.

As estruturas mistas surgiram nos Estados Unidos no final do século XIX, mais precisamente no ano de 1894, com o objetivo inicial de proteger os elementos metálicos contra a corrosão e o incêndio. Pesquisas realizadas por Faber [4] e Jones e Rizk [5] permitiram aferir a contribuição do concreto no desempenho estrutural de sistemas estruturais mistos sujeitos a cargas axiais (pilares mistos).

Como vantagens dos sistemas mistos podem–se citar, por exemplo, a considerável redução do consumo de aço estrutural, a possibilidade de dispensa de fôrmas e escoramentos, a redução do peso próprio e do volume da estrutura e o aumento da precisão dimensional da construção. Além disso, comparando–se as estruturas mistas com as estruturas de concreto e de aço, observa–se o aumento da rigidez e resistência da seção, a eliminação ou redução da flambagem local nos perfis metálicos, a proteção do perfil contra a corrosão, e por fim, o aumento da resistência ao fogo principalmente nos pilares totalmente revestidos com concreto.

Na Figura 1 são apresentadas duas seções transversais usuais de pilares mistos, uma parcialmente revestida com concreto e outra totalmente revestida com concreto.

A união do concreto ao aço em pilares mistos sujeitos à compressão simples ou à ação simultânea de força axial de compressão e de momentos fletores também é uma forma de potencializar as vantagens dos dois materiais, de modo a se encontrar a melhor solução estrutural.

Os primeiros estudos relativos a pilares mistos de aço e concreto datam da década de 60. Jones e Rizk [5] estudaram o comportamento de pilares mistos totalmente revestidos com concreto levando–se em consideração algumas variáveis como o comprimento do pilar, as dimensões da seção transversal e a quantidade de armadura na peça e a partir deste estudo concluíram que o revestimento do perfil de aço com concreto contribuiu muito para o aumento da sua capacidade de carga, se comparado com um pilar de aço.

Em [6] apresentam–se os resultados dos ensaios de 22 pilares mistos totalmente revestidos com concreto, submetidos à flexão em torno do eixo de menor inércia e com carregamento aplicado mediante a consideração de diferentes excentricidades. Os dois modos de falha observados, após certo nível de carga aplicada, foram o esmagamento do concreto em uma face próxima ao topo do perfil de aço e, o esmagamento do concreto em uma face e escoamento do aço em compressão, acompanhado por fissuras no concreto, na face oposta.

Naka *et al*. [7] apresentam os resultados da análise experimental de quatro pilares mistos com extremidades apoiadas e submetidos à flexão em relação ao eixo de maior inércia. Os resultados indicaram que o modo de falha dos pilares se dividiu em duas categorias: esmagamento do concreto e flambagem local da mesa do perfil metálico no lado comprimido; e esmagamento do concreto, flambagem das armaduras de aço em compressão e escoamento das armaduras no lado tracionado.

Yamada *et al*. [8] analisaram alguns pilares mistos submetidos à combinação de força axial com cargas transversais aplicadas nas extremidades da coluna considerando–se que o sistema estrutural apresentava flexão em relação ao eixo de maior inércia. Na maior parte dos modelos estudados houve uma redução na capacidade máxima de carga do pilar quando o concreto iniciou o processo de fissuração e as barras de reforço entraram em escoamento na região tracionada.

Ricles e Paboojian [9] mostram os resultados experimentais de oito pilares mistos totalmente revestidos com concreto, com dimensões da seção transversal iguais a 406mmx406mm e com conectores de cisalhamento. Os pilares foram submetidos à flexão em relação ao eixo de maior inércia e testados sob carga axial monotônica e carga lateral cíclica. Verificou–se que a carga máxima causou o escoamento da mesa do perfil metálico e das barras de reforço e que os conectores de cisalhamento não foram eficazes na melhoria da resistência à flexão.

Mirza *et al*. [10] estudaram o comportamento de dezesseis pilares com 4m de comprimento, totalmente revestidos com concreto,

Figura 1 – Seções mistas parcialmente e totalmente revestidas com concreto

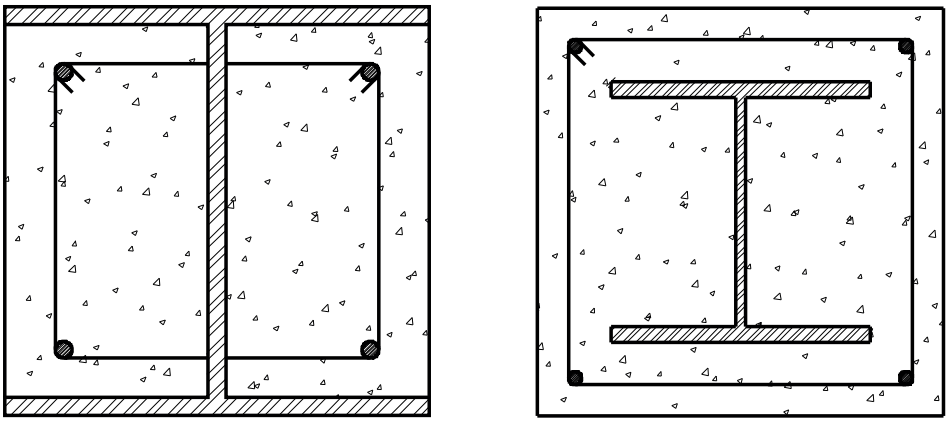

sujeitos à flexão em relação ao eixo de maior inércia e levando–se em consideração os efeitos de 2ª ordem nas análises. A partir dos ensaios realizados verificou–se que a deformação do concreto na fibra mais comprimida variou entre 0,0025–0,004 antes do colapso dos modelos e a presença de conectores de cisalhamento teve pouca influência na capacidade última do pilar misto.

Yokoo *et al*. [11] realizaram análises experimentais de dezenove pilares mistos curtos totalmente revestidos com concreto com $f_{ck} = 30MPa$. Neste programa experimental identificaram–se grandes fissuras na face inferior dos modelos e a falha ocorreu devido ao esmagamento do concreto. Concluiu–se, portanto que os pilares mistos curtos exibem um mecanismo de falha caracterizado por escoamento do aço e esmagamento do concreto e consequentemente não são influenciados pelos efeitos de segunda ordem.

Os pilares esbeltos, por sua vez, estão sujeitos a imperfeições geométricas capazes de amplificar os esforços atuantes, levando ao aparecimento de flambagem e caracterizando o chamado critério de estabilidade. Comportam–se inelasticamente e falham por inelasticidade parcial do aço, esmagamento do concreto na região comprimida e fissuração do concreto na região tracionada.

Outros efeitos importantes presentes nessas estruturas como a ductilidade e a capacidade de dissipação de energia de pilares mistos totalmente revestidos com concreto têm sido investigados e vêm sendo explorados no Japão e na América do Norte. Dentre alguns trabalhos importantes, podem–se comentar as pesquisas desenvolvidas por Wakabayashi *et al.* [12, 13].

Liew *et al.* [14] demonstraram, a partir de estudos realizados em pilares mistos parcialmente e totalmente revestidos com concreto, que os resultados do dimensionamento de pilares mistos definidos pelo EUROCODE 4 [2], pela norma britânica BS 5400 [15] e pelo AISC/LRFD [16] não convergiam necessariamente ao mesmo resultado. Tal fato foi atribuído aos diferentes valores dos coeficientes de ponderação da resistência e da solicitação e às considerações de dimensionamento relativas à deformação lenta do concreto e à excentricidade de carga.

Saw e Liew [17] apresentam a avaliação do projeto de pilares mistos de seções I parcialmente e totalmente revestidas com concreto e de seções tubulares preenchidas com concreto, com base nos critérios definidos pela parte 1.1 do EUROCODE 4 [2], pela parte 5 da norma britânica BS 5400 [15] e pela norma americana AISC/LRFD [16]. Nesta pesquisa estudaram–se parâmetros de projeto e realizaram–se comparações entre as resistências nominais previstas pelas três normas, bem como, com valores de resistências de campanhas experimentais disponíveis. Em alguns casos, os resultados obtidos a partir dos códigos normativos variaram consideravelmente, devido às diferentes considerações de projeto referentes a cada norma. No entanto, os procedimentos de projeto mostraram em geral respostas mais conservadoras quando comparadas com os resultados de campanhas experimentais. Por sua vez, o EUROCODE 4 [2] apresenta importantes fatores favoráveis em termos de sua abrangência e ampla gama de aplicação.

Para pilares sujeitos à compressão pura, a deformação limite do concreto é de 0,2%, sendo assim, para se evitar o colapso prematuro do concreto na peça, a deformação do aço do perfil e das armaduras também deve ser limitada a este valor [18].

Weng e Yen [19] investigaram as diferenças entre as abordagens dos códigos ACI 318 [20] e AISC/LRFD [16] para o projeto de pilares mistos de aço e concreto totalmente revestidos e avaliaram o quão os seus resultados se aproximam das respostas de uma coluna real. Isto foi comprovado a partir de uma série de comparações estatísticas.

Figura 2 – Domínios de deformação para seções de concreto armado

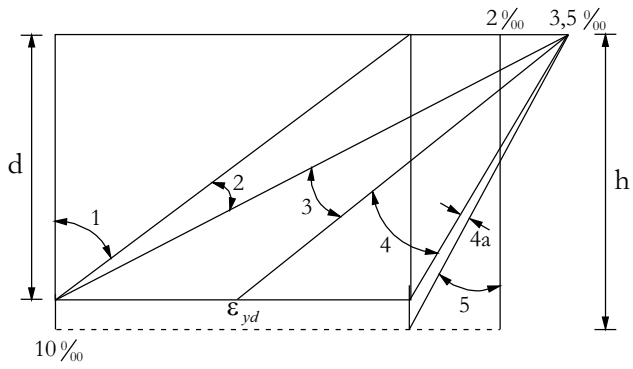

Os estudos foram realizados com o intuito de comparar os pontos fortes previstos usando as normas ACI 318 [20] e AISC/LRFD [16]. Estas abordagens foram comparadas com resultados de pilares mistos totalmente revestidos com concreto obtidos em pesquisas anteriores. Dentre as pesquisas podem–se citar os testes físicos realizados por Stevens [6], Naka *et al.* [7], Yamada *et al.* [8], Ricles e Paboojian [9], Mirza *et al.* [10], Yokoo *et al.* [11] e Wakabayashi *et al.* [12].

Dentre as modelagens numéricas de pilares mistos de aço e concreto, Fong [21] destaca que muitas normas tendem a recomendar o uso de uma análise de segunda ordem e um método de projeto de modo a obter resultados mais precisos e de maneira eficiente. Alguns trabalhos recentes têm como objetivo obter formulações numéricas para a análise avançada de estruturas mistas de aço e concreto, com base no método da rótula plástica refinado.

Um procedimento numérico eficiente para a construção da curva de interação de pilares mistos de aço e concreto é o método das fibras que consiste na subdivisão do domínio da seção transversal em pequenas regiões de material único, distribuídas ao longo do comprimento do pilar [22].

Neste trabalho propõe–se um procedimento de cálculo, baseado nos domínios de deformação de seções de concreto armado, conforme mostra a Figura 2, para a obtenção da curva de interação de pilares mistos totalmente revestidos com concreto de forma computacional. A adoção desta metodologia se deve às semelhanças observadas entre as curvas de interação de seções de concreto armado e seções mistas de aço e concreto. O pacote computacional desenvolvido denomina–se MDCOMP (2014) e foi implementado em linguagem FORTRAN. Os resultados obtidos a partir do MDCOMP (2014) são confrontados com as respostas definidas pela parte 1.1 do EUROCODE 4 [2], que é uma das mais importantes normas utilizadas para o dimensionamento desse tipo de elemento estrutural, e também com as respostas apresentadas nos trabalhos de Saw e Liew [17], Weng e Yen [19] e Naka *et al.* [7].

2. Curva de interação da seção transversal do pilar misto

A curva de interação é o lugar geométrico dos pares M–N que definem os valores limites de resistência da seção transversal de um elemento estrutural sujeito à flexão composta.

Figura 3 – Curva de interação segundo o EUROCODE 4 (2)

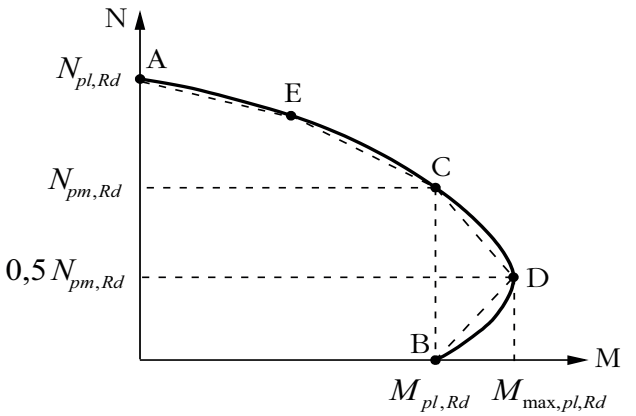

Na Figura 3 apresenta–se a curva adotada pela parte 1.1 do EUROCODE 4 [2], bem como, o diagrama poligonal simplificado adotado pela ABNT NBR 8800 [3], o qual é representado pela curva pontilhada da Figura 3. Neste caso, considera–se que há uma distribuição plástica total de tensões entre os pontos A, que corresponde ao esforço normal máximo, até o ponto D, que corresponde ao momento fletor máximo.

No ponto A da curva de interação, tem–se apenas a contribuição da força axial na peça, sendo assim, o concreto, o perfil metálico e as armaduras de aço estão sujeitos à compressão simples, com

$$N_A = N_{pl,Rd} \quad \text{e} \quad M_A = 0 \tag{1a}$$

No ponto B o pilar está submetido apenas à flexão pura sendo

$$N_B = 0 \quad \text{e} \quad M_B = M_{pl,Rd} \tag{1b}$$

No ponto C tem–se uma combinação destes dois esforços, isto é,

$$N_C = N_{pm,Rd} = \frac{0,85\,A_c\,f_{ck}}{\gamma_c} \quad \text{e} \quad M_C = M_{pl,Rd} \tag{1c}$$

e no ponto D, tem–se

$$N_D = 0,5\,N_{pm,Rd} = 0,5\,\frac{(0,85A_c\,f_{ck})}{\gamma_c} \quad \text{e} \quad M_D = M_{\max,pl,Rd} \tag{1d}$$

sendo o momento fletor máximo resistente de plastificação de cálculo, $M_{\max,pl,Rd}$, calculado com auxílio da soma das resistências plásticas de cada elemento que constitui a seção, a partir da seguinte expressão:

$$M_D = \frac{Z_{Pa}\,f_y}{\gamma_a} + \frac{Z_{Ps}\,f_s}{\gamma_s} + \frac{1}{2}\,\frac{Z_{Pc}(0,85\,f_{ck})}{\gamma_c} \tag{1e}$$

O ponto E está situado no ponto médio da curva entre os pontos A e C.

Nas equações anteriores $N_{pl,Rd}$ é o esforço normal resistente

Figura 4 – Seção mista e diagrama de deformações com esquema das resultantes de forças

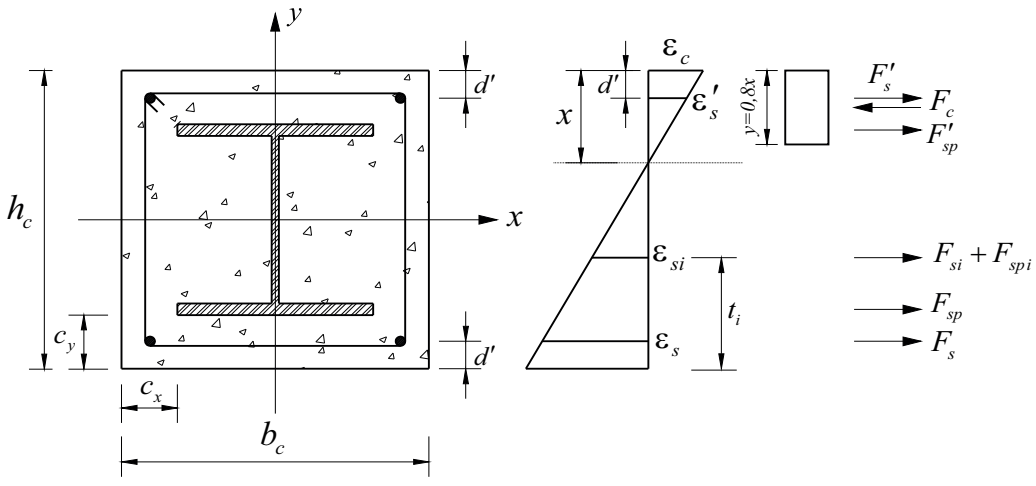

de cálculo da seção transversal à plastificação total, $N_{pm,Rd}$ é a resistência normal do concreto na seção mista, $M_{pl,Rd}$ é o momento fletor resistente de plastificação de cálculo da seção e Z_{Pa}, Z_{Ps}, Z_{Pc} são, respectivamente, os módulos de resistência plástico do perfil de aço, das barras de reforço e do concreto.

3. Definição das equações de equilíbrio e de deformações

Na Figura 4 apresenta–se esquematicamente o diagrama de deformações da seção mista totalmente revestida com concreto, bem como, as forças resultantes que atuam na seção.

Nesta figura F'_s, F'_{sp}, F_{si}, F_{spi}, F_{sp} e F_s são, respectivamente, as resultantes das forças nas armaduras superiores da seção mista, na mesa superior do perfil metálico, nas armaduras genéricas localizadas entre as mesas do perfil, na alma do perfil metálico, na mesa inferior do perfil metálico e nas armaduras inferiores da seção mista.

Considerando–se o equilíbrio de esforço normal e de momento fletor na seção chega–se a:

$$N_{Rd} = -F_c + \sum_{i=1}^{n} F_i \qquad (2)$$

$$M_{Rd} = N_d \frac{h}{2} + F_c\left(h - 0{,}4\,x\right) - \sum_{i=1}^{n} F_i\, t_i \qquad (3)$$

Os somatórios das equações anteriores correspondem às contribuições de forças e de momentos fletores do concreto, das armaduras e do perfil metálico.

A posição da linha neutra da seção mista (x) é definida a partir da relação

$$x = \frac{\varepsilon_c}{\varepsilon_c + \varepsilon_s} \qquad (4)$$

em que ε_c é a deformação do concreto, ε_s é a deformação do aço das armaduras inferiores e d' é a distância do centroide das armaduras de aço até a borda da seção mista de aço e concreto, a qual é dada por:

$$d' = c + \phi_t + 0{,}5\,\phi_l \qquad (5)$$

Na Eq. 5 c é o cobrimento da seção, ϕ_t é o diâmetro da armadura transversal (estribo) e ϕ_l é o diâmetro da armadura longitudinal.

As equações que relacionam as deformações das armaduras de aço e dos elementos que compõem o perfil metálico com a deformação do concreto são:

$$\varepsilon'_s = \frac{\varepsilon_c\,(x - d')}{x} \qquad (6a)$$

$$\varepsilon_s = -\frac{\varepsilon_c\,(d - x)}{x} \qquad (6b)$$

$$\varepsilon'_{sp} = \frac{\varepsilon_c\,(x - c_y - 0{,}5\,t_f)}{x} \qquad (6c)$$

$$\varepsilon_{sp} = -\frac{\varepsilon_c\,(h_c - x - c_y - 0{,}5\,t_f)}{x} \qquad (6d)$$

$$\varepsilon_{spi} = -\frac{\varepsilon_c\,(d - x + d' - 0{,}5\,h_c)}{x} \qquad (6e)$$

Nas equações anteriores ε'_s e ε_s são, respectivamente, as deformações das armaduras de aço superiores e inferiores, ε'_{sp} e ε_{sp} são as deformações da mesa superior e inferior do perfil metálico, respectivamente, ε_{spi} é a deformação da alma do perfil metálico, d é a altura útil da seção mista, c_y é a distância da face externa da mesa do perfil metálico até a borda da seção mista e h_c é a altura da seção mista (ver Fig. 4).

Neste trabalho as deformações das armaduras de aço e do perfil metálico foram limitadas a 1% na tração e a 0,35% na compressão, conforme estabelece a ABNT NBR 6118 [1], pois o concreto não acompanha deformações superiores a estes limites.

Como no domínio 5 a linha neutra se encontra fora da seção de concreto armado, ou seja, $h_c < x < +\infty$, fazendo–se o equilíbrio de forças e de momentos na seção, desconsiderando–se a parcela da resistência correspondente às armaduras, e igualando–se a equação de momentos a zero, chega–se ao valor limite da posição da linha neutra neste domínio que é igual a $x = 1{,}25h$.

O valor limite de x para a seção mista de aço e concreto foi obtido de forma semelhante ao descrito acima para a seção de concreto armado, porém considerando–se a parcela da resistência referente ao concreto e ao perfil metálico. Deste modo, o equilíbrio de forças e de momento na seção fornece:

$$N_{Rd} = -F_c + A_a\, f_{yd} \qquad (7)$$

Figura 5 – Curva de interação da seção transversal do pilar de concreto armado

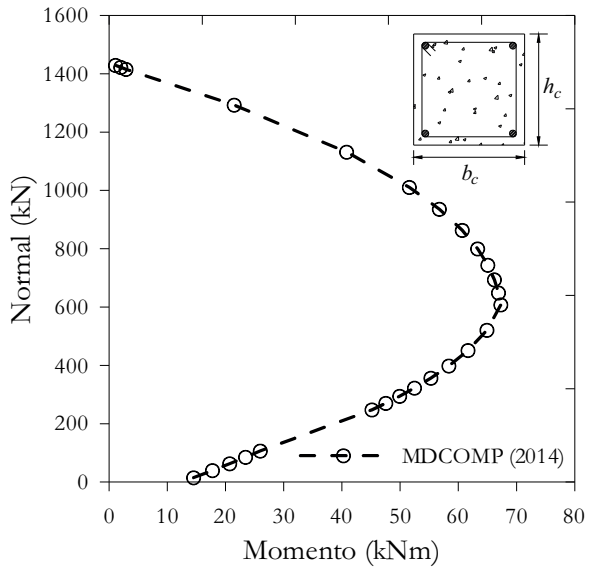

e

$$M_{Rd} = N_{Rd}\frac{h}{2} + F_c\left(h - 0{,}4\ x\right) \quad (8)$$

Substituindo–se (7) em (8) e fazendo $M_{Rd} = 0$, lembrando–se que $F_c = 0{,}85 f_{cd}\, b\, x$, se obtém a seguinte equação do 2º grau:

$$0 = 0{,}85 f_{cd}\, b\, 0{,}8\, x\,(0{,}5\, h - 0{,}4\ x) + A_a\ f_y\, 0{,}5\, h \quad (9)$$

A maior raiz da equação (9), $x = 2{,}305h$, corresponde a um valor nulo para o momento fletor e ao valor máximo para o esforço normal na seção e é, portanto o valor limite para a posição da linha neutra da seção mista de aço e concreto.

Tabela 1 – Dimensões da seção transversal de concreto

Seção mista	h_c (mm)	b_c (mm)	c_y (cm)	$\rho_s = \frac{A_a}{A_c}$ %
SM1	333	334	4,0	8,33
SM2	403	454	7,5	5,10
SM3	553	654	15,0	2,56

4. Exemplos

Nesta seção apresentam–se as curvas de interação da seção tranversal de um pilar de concreto armado e de diversas seções transversais de pilares mistos de aço e concreto obtidas numericamente a partir do programa computacional MDCOMP (2014). Comparações são feitas, quando possível, com as curvas obtidas com base em recomendações normativas vigentes e/ou com as respostas fornecidas por outros pesquisadores.

4.1 Curva de interação da seção transversal de um pilar de concreto armado

Neste exemplo faz–se a análise da seção transversal de um pilar de concreto armado com seção $33{,}3\,cm \times 33{,}4\,cm$. O concreto tem $f_{ck} = 20MPa$ e a armadura longitudinal é composta por quatro barras de aço CA50 de diâmetro $\phi_l = 10mm$, sendo $d' = 3{,}5cm$. Na Figura 5 apresenta–se a curva de interação momento x normal para a seção obtida a partir da variação das deformações do concreto e do aço nos seis domínios de deformação (ver Figura 2). O trecho da curva correspondente à flexo–tração, que inclui o domínio 1 e uma parte do domínio 2, foi suprimido, ou seja, apresentam–se apenas os trechos referentes ao comportamento da seção quando a mesma é submetida à flexo–compressão.

4.2 Curva de interação da seção transversal do pilar misto de aço e concreto

Neste exemplo tem–se a análise da seção transversal de um pilar misto de aço e concreto formada por um perfil metálico laminado

Figura 6a – Curvas de interação das seções transversais do pilar misto de aço e concreto

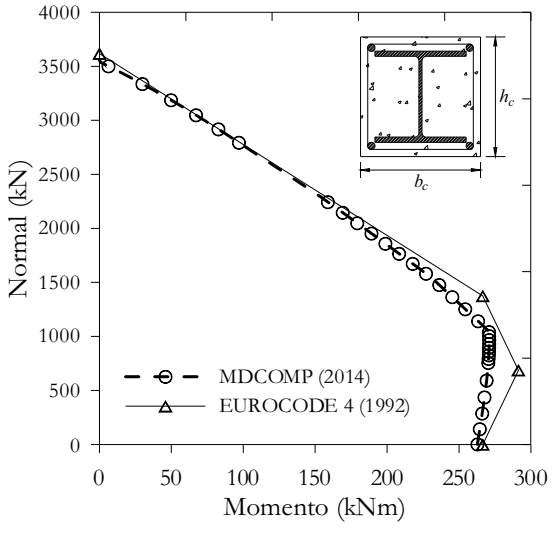

Figura 6b – Curvas de interação das seções transversais do pilar misto de aço e concreto

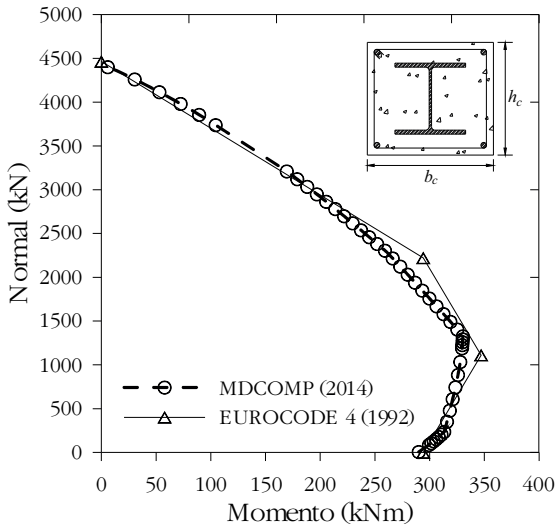

B Seção SM2

Figura 6c – Curvas de interação das seções transversais do pilar misto de aço e concreto

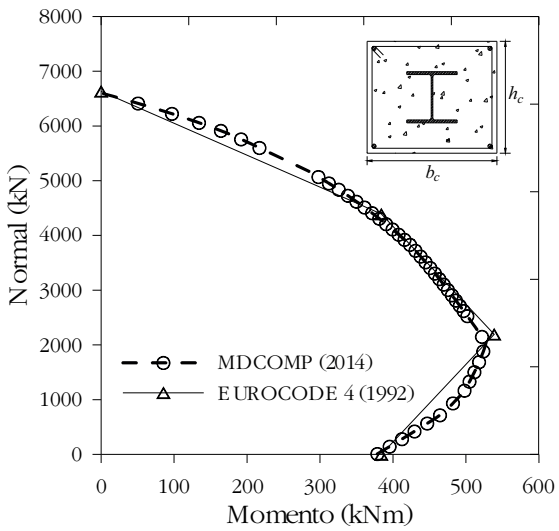

C Seção SM3

padrão *Gerdau W250x73kg/m* e considerando–se três valores diferentes para a altura e a largura da seção transversal de concreto, isto é, h_c e b_c, como mostra a Tabela 1.

Na Tabela 1 ρ_s é a relação entre a área da seção transversal do perfil de aço (A_a) e a área da seção transversal do concreto (A_c).

Adotou–se concreto com $f_{ck} = 20MPa$, quatro barras de aço CA50 de diâmetro $\phi_l = 10mm$ para a armadura longitudinal e $d' = 3,5cm$.

Nos gráficos da Figura 6 apresentam–se as curvas de interação momento x normal obtidas com o pacote computacional MDCOM (2014) para as três seções mistas de aço e concreto, sendo as mesmas comparadas com as curvas obtidas a partir das considerações do EUROCODE 4 [2].

Nas Tabelas 2 e 3 apresentam–se, respectivamente, os resultados numéricos dos momentos fletores e esforços normais resistentes para a seção mista de aço e concreto e as comparações com as respostas obtidas com base nas recomendações do EUROCODE 4 [2].

4.3 Comparação com resultados da literatura

Nesta seção faz–se um comparativo entre os resultados do programa computacional MDCOMP (2014) e as respostas obtidas por outros pesquisadores ou a partir de considerações normativas vigentes.

As primeiras curvas de interação apresentadas referem–se à seção transversal de um pilar misto de aço e concreto analisada anteriormente por Saw e Liew [17] de acordo com as recomendações do EUROCODE 4 [2]. A seção é formada por um perfil $UC\,254\times254\times107kg/m$ em aço com $f_y = 355MPa$, quatro barras de aço com $f_{yk} = 460MPa$ e $\phi_l = 12,5mm$ para armadura longitudinal, concreto com $f_{ck} = 20MPa$ e dimensões $b_c = h_c = 400mm$.

Tabela 2 – Momento fletor máximo resistente de plastificação de cálculo ($M_{max,pl,Rd}$) e Momento fletor resistente de plastificação de cálculo ($M_{pl,Rd}$)

Seção mista	$M_{max,pl,Rd}$ (kNm)			$M_{pl,Rd}$ (kNm)		
	EC4	MDCOMP	$\frac{M_{MDCOMP}}{M_{EC4}}$	EC4	MDCOMP	$\frac{M_{MDCOMP}}{M_{EC4}}$
SM1	291,28	270,44	0,93	291,28	270,44	0,99
SM2	346,98	330,31	0,95	346,98	330,31	0,99
SM3	538,63	527,49	0,98	538,63	527,49	0,99

Tabela 3 – Esforço normal resistente de cálculo da seção transversal à plastificação total ($N_{pl,Rd}$)

Seção mista	$N_{pl,Rd}$ (kN)		
	EC4	MDCOMP	$\frac{N_{MDCOMP}}{N_{EC4}}$
SM1	3618,22	3553,66	0,98
SM2	4465,09	4430,69	0,99
SM3	6635,02	6602,54	0,99

As curvas de interação obtidas nesta análise são apresentadas na Figura 7.

Na Tabela 4 apresentam–se as comparações entre as capacidades resistentes obtidas com o programa MDCOMP (2014) e as obtidas por Saw e Liew [17].

A segunda comparação foi feita com uma curva de interação obtida a partir das recomendações da norma americana ACI 318 [20]. Para essa análise utilizou–se uma seção com $b_c = h_c = 240mm$ ($f_{ck} = 25,6MPa$), que reveste totalmente um perfil metálico $H96\times100\times5,1\times8,6\,mm$ ($f_y = 311,2MPa$), e quatro barras de aço com $f_{yk} = 634MPa$ e $\phi_l = 10\,mm$ para armadura longitudinal. Tem–se $\rho_s = 3,7\%$ e $\rho_r = 0,5\%$, sendo ρ_r a taxa de aço da armadura longitudinal ($\rho_r = A_s / A_c$).

Os resultados obtidos são apresentados na Figura 8.

Na Tabela 5 mostram–se as comparações entre as capacidades resistentes obtidas com o programa MDCOMP (2014) e as definidas pela norma americana ACI 318 [20].

Na última análise fez–se novamente uma comparação dos resultados do programa MDCOMP (2014) com os obtidos a partir das recomendações da norma americana ACI 318 [20] e com os resultados experimentais apresentados por Naka *et al.* [7].

Tabela 4 – Momento fletor máximo resistente de plastificação de cálculo ($M_{max,pl,Rd}$), Momento fletor resistente de plastificação de cálculo ($M_{pl,Rd}$) e Esforço normal resistente de cálculo da seção transversal à plastificação total ($N_{pl,Rd}$) parametrizados

Esforço	EC4	MDCOMP	$\frac{MDCOMP}{EC4}$
$M_{max,pl,Rd}/M_u$	0,97	0,92	0,95
$M_{pl,Rd}/M_u$	0,90	0,89	0,99
$N_{pl,Rd}/N_u$	0,92	0,96	1,04

A seção transversal analisada é formada por um perfil de aço $H180\times120\times4,5\times12\,mm$ ($f_y = 344,8MPa$) revestido com concreto com $f_{ck} = 25,5MPa$ e dimensões $b_c = 240mm$ e $h_c = 300mm$. Adotaram–se quatro barras de aço com $f_{yk} = 461,3MPa$ e $\phi_l = 10\,mm$ para armadura longitudinal. Tem–se $\rho_s = 4,6\%$ e $\rho_r = 3,2\%$.

Nos gráficos da Figura 9 mostram–se as curvas de interação obtidas nesta análise.

5. Conclusões

No presente trabalho apresentou–se uma metodologia que permite a construção da curva de interação para seções mistas de aço e concreto, sujeitas à flexão composta normal, com base nos

Figura 7 – Curvas de interação – MDCOMP (2014) x Saw e Liew (2000)

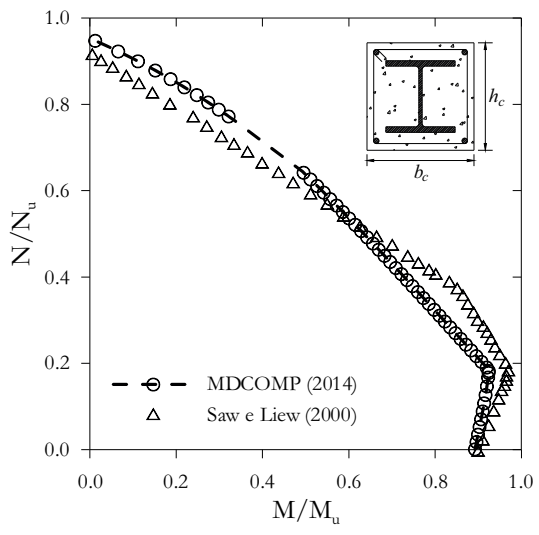

Figura 8 – Curvas de interação – MDCOMP (2014) x ACI 318 (1999)

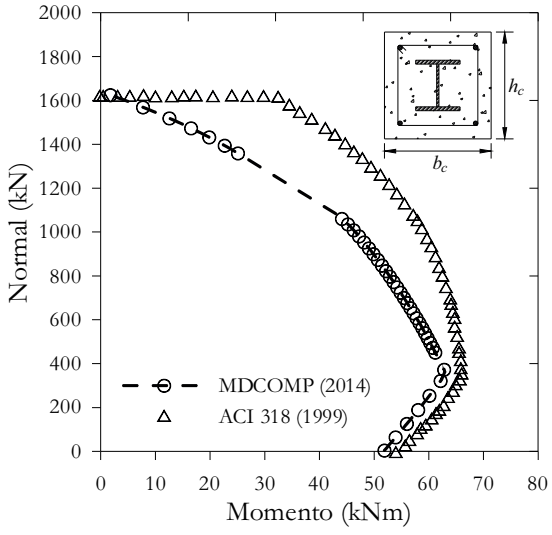

Tabela 5 – Momento fletor máximo resistente de plastificação de cálculo ($M_{max,pl,Rd}$), Momento fletor resistente de plastificação de cálculo ($M_{pl,Rd}$) e Esforço normal resistente de cálculo da seção transversal à plastificação total ($N_{pl,Rd}$)

Esforço	ACI 318	MDCOMP	MDCOMP / ACI 318
$M_{max,pl,Rd}$ (kNm)	66,00	62,91	0,95
$M_{pl,Rd}$ (kNm)	53,95	51,88	0,96
$N_{pl,Rd}$ (kN)	1622,19	1644,11	1,01

domínios de deformação de estruturas de concreto armado definidos pela ABNT NBR 6118 [1]. Para isso, foram escritas relações para as deformações das armaduras e dos elementos que compõem o perfil metálico em função da deformação do concreto, bem como equações para o esforço normal e para o momento fletor em cada domínio de deformação. A partir dessas expressões determinaram–se os pares M–N no estado limite último, necessários para a construção da curva de interação.

Observa–se nas Tabelas 2 a 5 que o esforço normal resistente de cálculo da seção transversal à plastificação total ($N_{pl,Rd}$), o momento fletor resistente de plastificação de cálculo ($M_{pl,Rd}$) e o momento fletor máximo resistente de plastificação de cálculo ($M_{\max,pl,Rd}$) obtidos a partir do programa computacional MDCOMP (2014), que se baseia nas relações definidas pela ABNT NBR 6118 [1], são muito próximos aos definidos tanto pelo EUROCODE 4 [2] quanto pelo ACI 318 [20]. A partir do gráfico da Figura 9 observa-se, na comparação feita com os resultados experimentais de Naka et al. [7], que a abordagem do ACI 318 [20] apresenta maior precisão que o procedimento baseado nos domínios de deformação preconizado pela ABNT NBR 6118 [1], embora os resultados correspondentes às resistências máximas ($N_{pl,Rd}$ e $M_{pl,Rd}$) sejam muito próximos pelos dois processos.

Figura 9 – Comparação entre curvas de interação

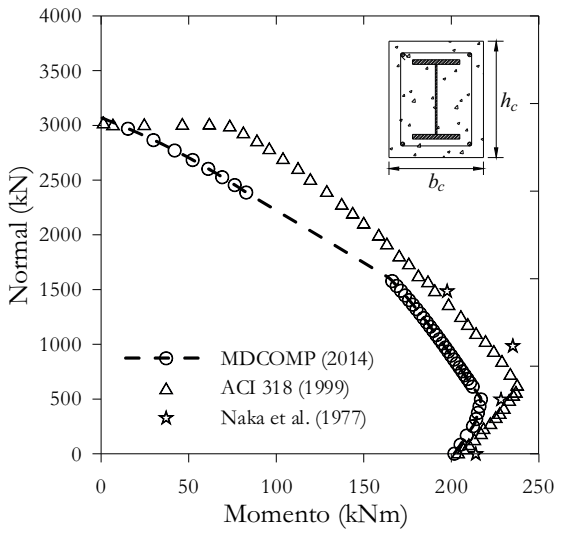

Com relação à variação da taxa de aço do perfil metálico na seção mista (ρ_s) pode–se verificar que quanto menor esse valor, mais a curva se aproxima do gráfico teórico para pilares mistos de aço e concreto definido pelo EUROCODE 4 [2] (ver Figura 6 e Tabelas 2 e 3). Isso fica evidente comparando–se a curva da Figura 6c com a curva da Figura 3.

Por fim, conclui–se a partir dos exemplos analisados que os resultados numéricos obtidos via MDCOMP (2014) apresentaram boa concordância com as curvas de interação definidas pelo EUROCODE 4 [2], porém verificaram–se algumas discrepâncias com as respostas definidas pelo ACI 318 [20] (ver Figuras 8 e 9). Isto se deve aos diferentes valores dos coeficientes de ponderação da resistência e da solicitação, bem como às considerações de dimensionamento relativas à deformação lenta do concreto e à excentricidade de carga adotadas por cada norma.

6. Referências bibliográficas

[1] ASSOCIAÇÃO BRASILEIRA DE NORMAS TÉCNICAS (2003), NBR 6118:2003. Projeto de estruturas de concreto armado. Rio de Janeiro, RJ.

[2] EUROPEAN COMMITTEE FOR STANDARDIZATION (1992), EUROCODE 4, Design of composite steel and concrete structures – Part 1.1: General rules and rules for buildings, CEN, Bruxelas, Belgium.

[3] ASSOCIAÇÃO BRASILEIRA DE NORMAS TÉCNICAS (2008), NBR 8800:2008. Projeto e execução de estruturas de aço e de estruturas mistas aço–concreto de edifícios: Projeto de revisão. Rio de Janeiro.

[4] Faber, O. (1956), Savings to be affected by the more rational design of encased stanchions as a result of recent full size tests, The Structural Engineer, vol. 34, pp. 88–109.

[5] Jones, R. and Rizk, A.A. (1963), An investigation on the behaviour of encased steel columns under load, The Structural Engineer, Vol. 41, N° 1, pp. 21–33.

[6] Stevens, R.F. (1965), Encased stanchions, The Structural Engineer, 43(2), pp. 59–66.

[7] Naka, T., Morita, K. and Tachibana, M. (1977), Strength and hysteretic characteristics of steel–reinforced concrete columns (in Japanese), Transaction of AIJ; 250, pp. 47–58.

[8] Yamada, M., Kawamura, H., and Zhang, F. (1991), Research on the elasto–plastic deformation and fracture behaviors of wide flange steel encased reinforced concrete columns subjected to bending and shear (in Japanese), Journal of Structural Construction Engineering, AIJ Architectural Institute of Japan); 420, pp. 63–74.

[9] Ricles, J.M. and Paboojian, S.D. (1994), Seismic performance of steel–encased composite columns, Journal of Structural Engineering, ASCE; 120(8), pp. 2474–2494.

[10] Mirza, S.A., Hyttinen, V. and Hyttinen, E. (1996), Physical tests and analyses of composite steel–concrete beam–columns, Journal of Structural Engineering, ASCE; 122(11), pp. 1317–1326.

[11] Yokoo, Y., Wakabayashi, M. and Suenaga Y. (1967), Experimental studies on steel concrete members with H–shape steel (in Japanese). Transaction of AIJ; 136, pp. 1–7.
[12] Wakabayashi, M., Shibata, M., Matsui, C. and Minami, K. (1974), A study on the behaviour of steel–reinforced concrete columns and frames. In: IABSE Symposium, pp. 53–60.
[13] Wakabayashi, M. (1987), A historical study of research on composite construction in Japan. In: Composite construction in steel and concrete. Proc. of eng. foundation conf. Henniker, New Hampshire: ASCE, pp. 400–427.
[14] Liew, J.Y.R., Saw, H.S. and Yu, C.H. (1998), Composite column design in buildings – Assessment of current methods and interim guidance. Research Report n. CE 026/98, National University of Singapore, May.
[15] BS 5400 (1979), Steel, concrete and composite bridges, Part 5, Code of practice for design of composite bridges. London: British Standards Institution.
[16] AISC/LRFD (1993), Load and Resistance Factor Design Specification for Structural Steel Buildings, 1st edn., American Institute of Steel Construction, AISC, Chicago, IL.
[17] Saw, H.S. e Liew, J.Y.R. (2000). Assesment of Current Methods for the Design of Composite Columns in Buildings. Journal of Constructional Steel Research, v. 53, p. 121–147.
[18] Queiroz, G., Pimenta, R.J. e Da Mata, L.A.C. (2001), Elementos das Estruturas Mistas Aço–Concreto, Belo Horizonte, 1ª edição, Editora O Lutador.
[19] Weng, C.C. e Yen, S.I. (2002). Comparisons of Concrete–encased Composite Column Strength Provisions of ACI Code and AISC Specification, v. 24, p. 59–72.
[20] Buildings code requirements for Structural Concrete (ACI 318–99) (1999). Detroit (MI): American Institute (ACI).
[21] Fong, M. (2012). Second–order analysis of imperfect light–weight and composite structures. Doctoral thesis, Department of civil and structural engineering, The Hong Kong Polytechnic University, Hong Kong, China.
[22] Sfakianakis, M.G. (2002). Biaxial bending with axial force of reinforced, composite and repaired concrete sections of arbitrary shape by fiber model and computer graphics. Advances in engineering software, v. 33, p. 227–242.

Volume 8, Number 4 (August 2015) p. 467-478 • ISSN 1983-4195
http://dx.doi.org/10.1590/S1983-41952015000400003

REVISTA IBRACON DE ESTRUTURAS E MATERIAIS
IBRACON STRUCTURES AND MATERIALS JOURNAL

Numerical and experimental analysis of the behavior of structural elements composed of double lattice panels filled with cast-in-place concrete

Análise numérica e experimental do comportamento de elementos estruturais compostos por painéis duplos treliçados preenchidos com concreto moldado no local




B. M. LACERDA [a]
benicio_lacerda@hotmail.com

M. C. V. LIMA [a]
macris@ufu.br

F. A. R. GESUALDO [a]
ngesualdo@ufu.br

V. C. CASTILHO [a]
castilho@feciv.ufu.br

Abstract

An experimental and numerical investigation was conducted into the factors that interfere in the shear strength of the concrete-concrete interface in structures composed of double lattice panels subjected to direct shear stress. The experimental program consisted of testing 26 direct shear models with varying widths of concrete filling of 7 cm, 9 cm and 13 cm, with smooth and rough interfaces, as well as different concrete compressive strengths in the filled region. The numerical modeling, which was performed with ANSYS software, employed solid finite elements, bar elements and contact elements, taking into account the non-linearity of the materials involved. The analyses of the experimental results under direct shear indicated that the transfer of stresses at the interface occurred with loss of adhesion. The numerical simulations indicated that the higher the geometric ratio of reinforcement the higher the direct shear strength of the structural model. In general, the slip of the models with smooth interfaces was 2 or 3 times greater than the models with rough surfaces. Numerically, the models with smooth interfaces showed a 36.61% gain in shear strength when the compressive strength in the region filled with concrete increased from 20 MPa to 28.4 MPa.

Keywords: numerical modeling, experimental analysis, double panels lattice, direct shear, nonlinear analysis.

Resumo

Este estudo apresenta uma investigação experimental e numérica dos fatores que interferem na resistência ao cisalhamento da interface entre concretos de estruturas formadas por painéis duplos treliçados, submetidos ao cisalhamento direto. O programa experimental foi realizado por meio do ensaio de 26 modelos submetidos ao cisalhamento direto, com a largura do concreto de preenchimento variando de 7 cm, 9 cm e 13 cm, com interfaces lisas e rugosas, além de diferentes resistências à compressão do concreto na região de preenchimento. A modelagem numérica foi feita com a utilização do software ANSYS e consistiu no emprego de elementos finitos sólidos, elementos de barras e elementos de contato, levando-se em conta a não linearidade física dos materiais envolvidos. A análise dos resultados experimentais mostra que, sob cisalhamento direto, a transferência de tensões na interface ocorre com perda de adesão. A simulação numérica indica que quanto maior a taxa de armadura que cruza a interface maior é a resistência ao cisalhamento direto. Em geral, o deslizamento relativo observado nos modelos com interface lisa é em torno de 2 a 3 vezes maior que nos modelos com interface rugosa. Numericamente, observa-se um ganho na resistência cisalhante de 36,61% ao elevar a resistência à compressão na região de preenchimento do concreto de 20 MPa para 28,4 MPa, para os modelos de interfaces lisas.

Palavras-chave: modelagem numérica, análise experimental, painel duplo treliçado, cisalhamento direto, análise não linear.

[a] *Universidade Federal de Uberlândia, Faculdade de Engenharia Civil, Uberlândia, MG, Brasil.*

Received: 25 Feb 2015 • Accepted: 22 May 2015 • Available Online: 7 Aug 2015

1. Introduction

Partial cross-section precast concrete structural elements have been employed in Brazil for the construction of small buildings, as a rational approach for using prefabricated components.

The Brazilian technical standard ABNT NBR 9062:2006 defines parts composed of partial cross-sections as concrete elements interconnected by separate forming systems, which act as a single part subjected to the loads imposed upon it after its solidification. Partial cross-section parts are used because they reduce the consumption of formwork and shoring and are an option for lower weight elements for small and medium-sized applications, which can be transported during their assembly.

The technical literature describes investigations of the shear transfer mechanism across new and existing concrete interfaces by many authors, e.g., Hofbeck, Ibrahim and Mattock (1969); Hsu, Mau and Chen (1987); Bass, Carrasquillo and Jirsa (1989), Araújo (1997, 2002) and Kabir (2005).The structural behavior of precast concrete sandwich panels has also been studied both experimentally and theoretically, as presented by Benayoune et al. (2008).

According to the ABNT NBR 6118:2014 standard, requirements that ensure the quality and structural strength, service performance and durability of concrete structures must be met during the construction and service stages.

In this context, this study aims to examine the structural behavior of precast concrete double lattice panels by means of numerical modeling and experimental analysis. The aim is to determine whether these components behave monolithically under direct shear. The interface bonds in concrete with different ages should be evaluated, once the mechanical behavior of the precast element is influenced by shear load transfer at the interface.

The structural response at the interface of the double lattice panel filled with cast-in-place concrete (CPC) is assessed taking into account the effect of variations in the width of filler concrete, the compressive strength of the concrete, and the surface roughness of the bonding interface.

Figure 1 – Details of a double lattice panel

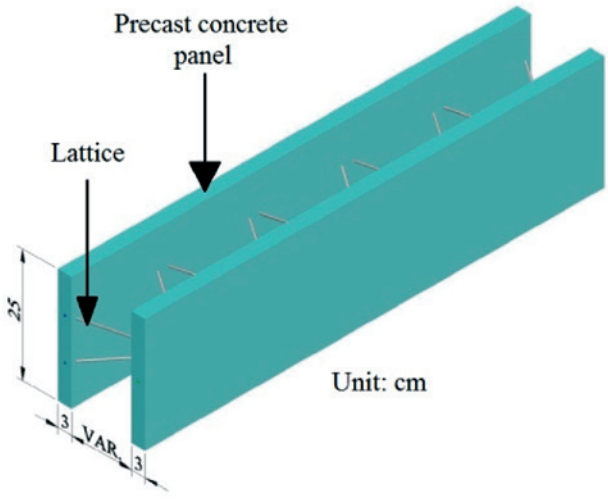

2. Double lattice panels

The double lattice panel consists of two precast concrete (PCC) plates about 3 cm to 3.5 cm thick and about 25 cm high. The plates are interconnected by means of an electro-welded lattice frame, with the distance between the plates varying according to the design requirement (Figure 1).

Some of the advantages of using this structural system at construction sites, according to El Debs (2000), are: faster production; lower consumption of concrete; lower expenses with riggers and carpenters, since the panel serves as formwork; substantial reduction in timber and scaffolding; and reduction of wastes generated during the construction phase, which ensures greater savings in construction site cleaning costs. In the case of precast partial cross-sections – the focus of this work, double lattice panels are an option for the use of the technique, preserving the overall characteristics of monolithic concrete structures.

However, structural elements composed of double lattice panels are limited in terms of shape, e.g., curved parts, and size, because they are built by hand; hence, a heavier component would make the construction process very difficult.

Double lattice panels are bonded with cast-in-place concrete, because this bond is simple to make.

According to Araújo (2002), the behavior of these interface bonds in concrete should be evaluated, because the fact that they have different ages and characteristics can influence their mechanical behavior, such as shear load transfer at the interface.

Precast panels are manufactured with fixed thicknesses, but their dimensions of height and width vary, and these panels can be used in various applications (Figure 2).

Each side of a double panel is concreted at an interval of 24 hours. After solidification, the structural behavior is influenced by shear load transfer at the interface. Solidification of the double lattice panel may lead to differential shrinkage and creep in the precast concrete (PCC) and cast-in-place concrete (CPC), since their ages and characteristics differ. Adherence between contact surfaces is an important parameter to be investigated, because it influences the transfer of shear stresses at the interface.

3. Shear transfer mechanisms between concrete surfaces

Shear transfer at the interface between different ages concrete can be divided into transfer through the contact surface and through the reinforcement transverse to this surface.

Shear load transfer at the contact surface between two concrete elements occurs by bonding and can be divided into:

- **Adhesion:** this is the first mechanism that is triggered at the interface between concrete components and is limited to low shear stress once it is removed by slip.
- **Friction:** after the breakup of the adhesive mechanism, the strength at the interface of the member can be ensured by the friction existing between the contact surfaces. This occurs when there is a small slip at the interface of the member due to the presence of transverse stresses. This portion of frictional load transfer at the interface is influenced directly by surface roughness.

Figure 2 – Application of double panels in shear wall, column, foundations and beams

Double panel shear wall

Column

Foundations

Beams

- **Mechanical:** mechanical load transfer occurs when there is relative slipping between two contacting surfaces. This type of transfer occurs by mechanical engagement when these slips are shear loaded. On rough surfaces, mechanical engagement is ensured by the coarse aggregate at this interface.

When slip occurs on a surface, the transverse reinforcement at the interface contributes to transfer shear stresses by dowel action. According to Araújo (2002), the shear resistance by dowel action due to the transverse reinforcement generally presents lower values than the frictional and mechanical action. The transverse reinforcement increases the frictional resistance between the surfaces in response to a load normal to the interface. If the surface is rough, transverse clearance may occur, which, added to the slip between the surfaces, may cause elongation of the rebar (Figure 3).

The frictional resistance between the contact surfaces increases due to rebar reactions, creating normal compressive stress at the interface. Araújo (2002) explains that an interface must be clearly defined for concrete members with a high concentration of rebars normal to the plane of the interface and subjected to tangential loads. Otherwise, cracks inclined towards the shear plane are formed (Figure 4).

4. Experimental program

The experimental program consisted of testing 26 direct shear models, in the form of 50 cm high prismatic models, under increasing loads. The variables considered in the analysis of these models were: internal thickness of the panel, corresponding to the width of the concrete filling, roughness of the concrete-concrete interface (smooth or rough), and compressive strength of the cast-in-place concrete (CPC). The widths of the region filled with CPC were 7 cm, 9 cm and 13 cm. The compressive strengths of the CPC were

Figure 3 – Contribution of reinforcement to shear strength. (Risso (2008))

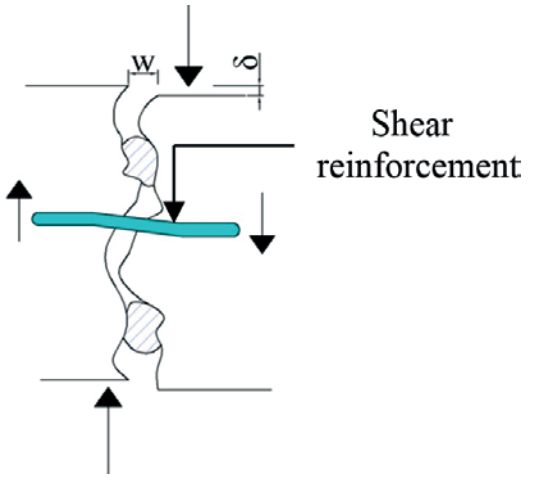

Figure 4 – Cracks inclined toward the shear plane at the interface. (Araújo (2002))

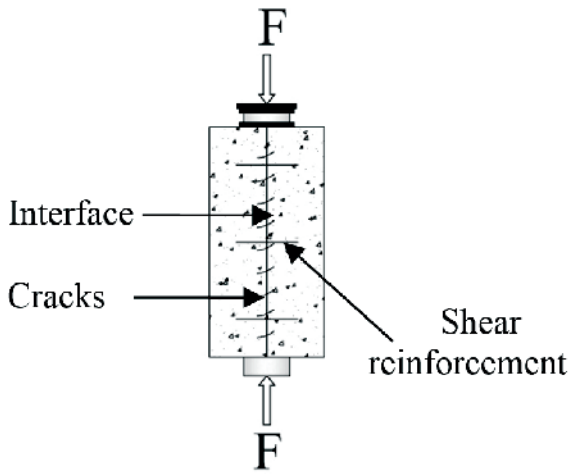

20 MPa, 29 MPa, and 28.4 MPa. The precast concrete (PCC) panels showed a compressive strength of 27.5 MPa. The surfaces of the interfaces were considered smooth (S) and rough (R).

4.1 Direct shear test of the double panels

The external sides of the panels were on average 3 cm thick. One of the sides of the panel was cast first (Figure 5a), and the other side was cast three days later (Figure 5b). The precast concrete elements are interconnected by means of electro-welded lattices and stirrups.

The second step consisted of filling the models with CPC between the PCC layers of the panel, resulting in a structural element with concrete of different ages. This step was performed in the Structures Laboratory of the Federal University of Uberlandia (Brazil).

The surface of the PCC-CPC interfaces of one of the tested series was roughened by waterblasting the aggregates and then cleaning them (Figure 6). The interfaces of the other series were left untouched after concreting the panel, i.e., without water blasting, and were considered smooth in this study. Figure 7 shows details of the reinforcement and dimensions of the models.

In the direct shear tests, an increasing load was applied upon the central element in the longitudinal direction of the CPC surface in the filled region. Wooden apparatuses were built and fixed onto

Figure 5 – Molding of the outer surfaces of the precast concrete panel

Concreting of the upper side of the panel

Concreting of the opposite side

Figure 6 – Panel with exposed coarse aggregate

the PCC to measure the displacement at the concrete-concrete interface. Loading was applied in a universal testing machine with 600 kN capacity.

The identification of each model of the tested series is identified as follows: XS/Y-Exp # for smooth interfaces and XR/Y-Exp # for rough interfaces. The value of X corresponds to the width of the concrete filled region (CPC). The letters S (smooth) or R (rough) correspond to the type of interface. This is followed, after the slash, by the Y value of the compressive strength of the CPC. Lastly, the experimental model is designated Exp #, as indicated in Table 1. The compressive strength of the PCC was about 27.5 MPa in all the tests.

Figure 8 shows a schematic diagram of the positioning of the wooden apparatus and the area where loads were applied, while Figure 9 shows the positioning of the transducers during the test.

5. Numerical modeling

The numerical modeling of the direct shear models was performed using the elements SOLID65, SOLID185, LINK8, TARGE170 and CONTA174, which are available in the ANSYS software library to simulate the constituent parts of physical models. These elements were applied to simulate the behavior of concrete, steel, and the region of contact between the surfaces of concrete of different ages and of the contact with the steel plate on which double lattice panel was supported.

The element SOLID65 was used to simulate the PCC and CPC. This element consists of eight nodes with three degrees of freedom per node: translation in the nodal x, y and z directions, and it can undergo tensile cracking, compressive crushing and plastic deformation.

LINK8 was applied to simulate the longitudinal framing and stirrups of the physical models. LINK8 has three degrees of freedom per

Figure 7 – Reinforcement details of models under direct shear

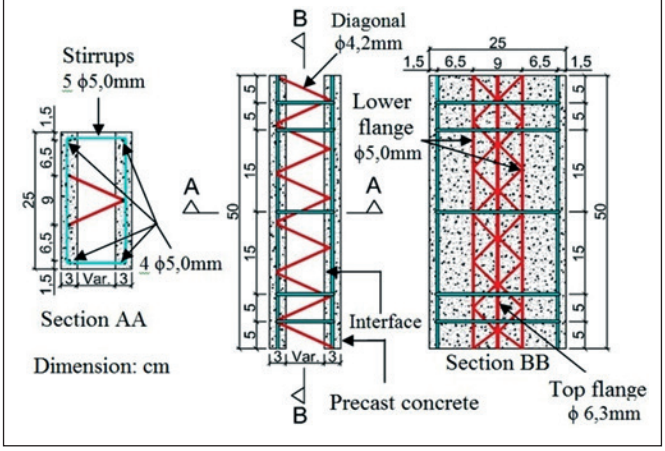

Figure 8 – Positioning scheme of displacement transducer

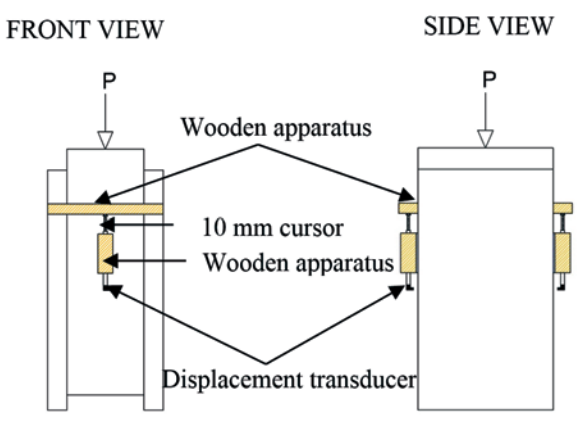

Table 1 – Identification of the direct shear tested models

Series	Model	Internal width (cm)	Type of surface shear	f_c (MPa)
A	7S/20 - Exp #	7	Smooth	20
B	9S/20 - Exp #	9	Smooth	20
C	13S/20 - Exp #	13	Smooth	20
D	7R/29 - Exp #	7	Rough	29
E	9R/29 - Exp #	9	Rough	29
F	13R/29 - Exp #	13	Rough	29
G	7S/28.4 - Exp #	7	Smooth	28.4
H	9S/28.4 - Exp #	9	Smooth	28.4
I	13S/28.4 - Exp #	13	Smooth	28.4

node, i.e., translation in the nodal directions x, y and z. This element can only simulate tension and compression forces, and can undergo plastic deformation, elongation and large displacements.

The finite element TARGE170 was used to represent various "target" surfaces of contact surface elements associated with the element CONTA174. These elements simulate the contact of the surface at the interface of the concrete-to-concrete bond of the models. The pair of contacts represented by the elements TARGE170 and CONTA174 allows friction and cohesion to be considered, as well as slipping between the bond surfaces. The friction coefficient considered in the numerical analysis was 0.6 for smooth surfaces and 1.0 for rough surfaces.

Figure 10 illustrates the discretization of the finite element used in the models subjected to direct shear, showing the indispensable condition of matching nodes with the nodes of the solid elements (CPC and PCC) to generate a stable model, using LINK8 (pinned nodes).

With regard to the physical nonlinearity of concrete, the *concrete* model was used to represent the behavior of CPC and PCC,

Figure 9 – Positioning of displacement transducer in direct shear test

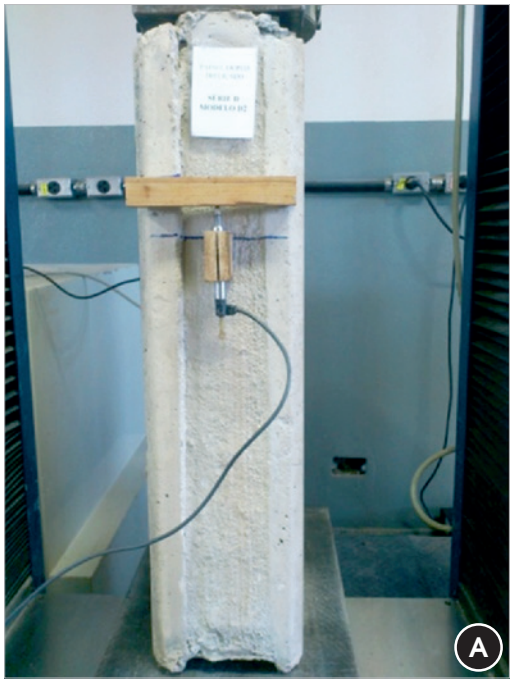

Transducer positioned on side A (front view)

Transducer positioned on side B (back view)

Figure 10 – Direct shear model simulated with ANSYS

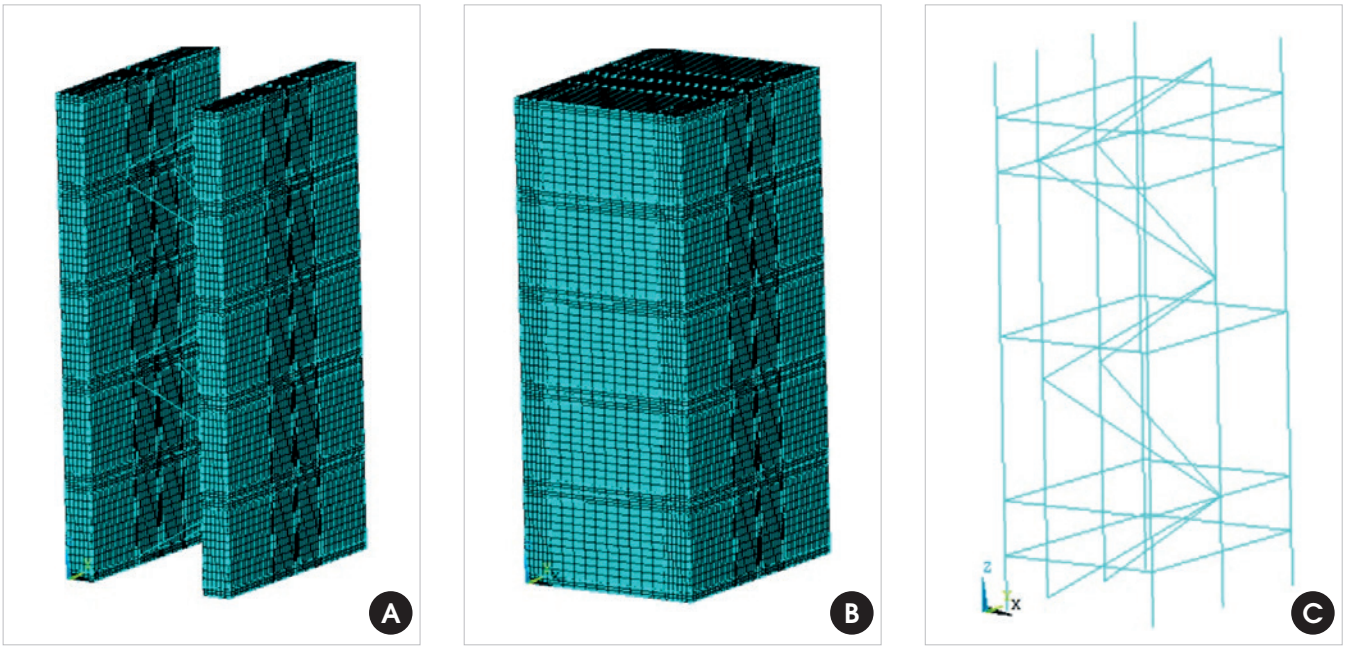

Solid and truss finite elements between PCC | Precast and cast in place concrete mesh | Link8 elements

because it allows the material's failure to be predicted, presenting yielding, cracking and crushing based on Willam-Warnke criterion (Figure 11). The bilinear isotropic hardening model is adopted for steel behaviour (Figure 12). This model applied in LINK8 follows the von Mises yield criterion and lists the yield stress of steel, its modulus of elasticity and its density.

The convergence method for solving the nonlinear system applied here was the full Newton-Raphson method, which, according to Oliveira (2007), allows the tangent stiffness matrix to be updated at each iteration. The adaptive descent feature was activated simultaneously to the full Newton-Raphson process. This feature should be used when applying elements of surface contact and is only valid when the full Newton-Raphson process is applied. In order to improve the convergence for the physical nonlinear analysis, the line search feature was enabled. This feature multiplies the incremental displacement vector by a scale factor between 0 and 1.

Figure 11 – Stress x strain concrete behavior (Unit: kN; cm) (Ansys v.11)

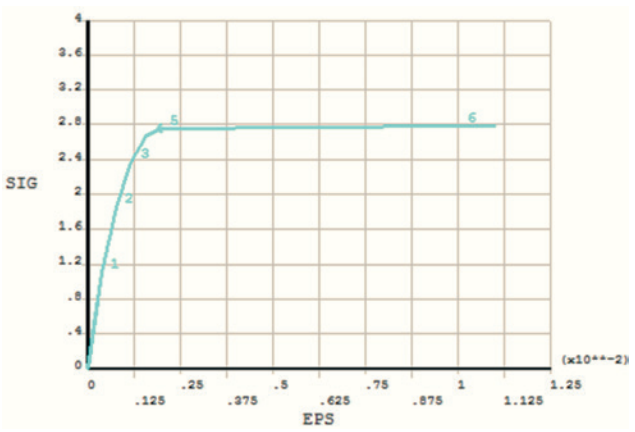

Figure 12 –Stress x strain steel behavior (Unit: kN; cm) (Ansys v.11)

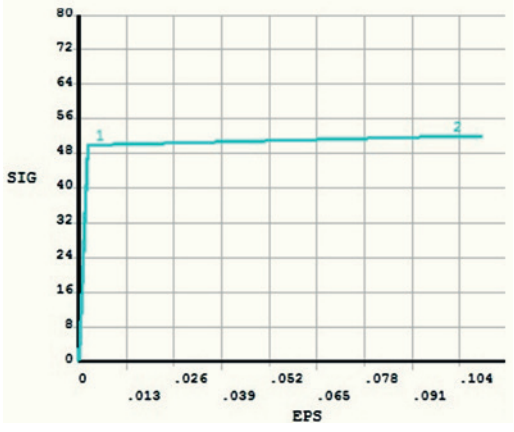

Figure 13 – Diagram of force vs. relative slip at the interface in Series C, F and I (13 cm)

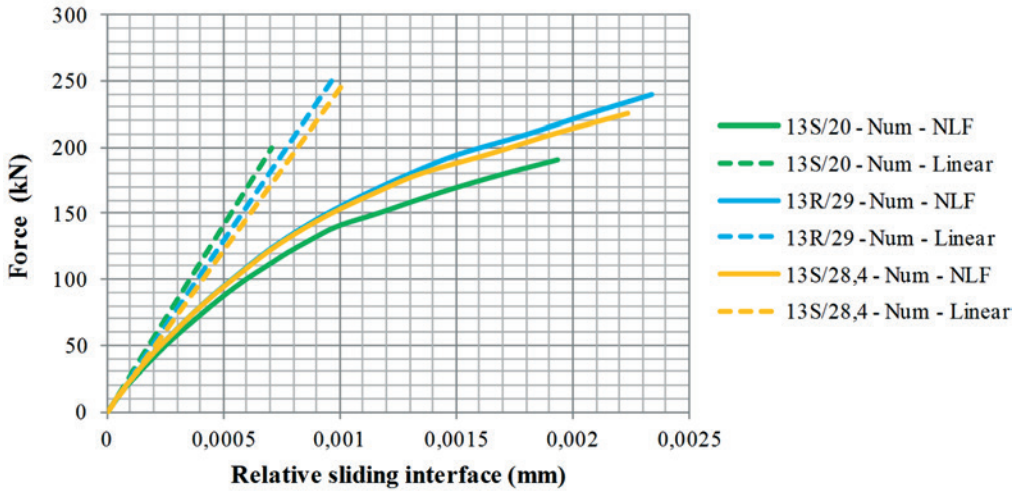

5.1 Results of numerical simulations of the models subjected to direct shear stress

The next sections describe the numerical results of direct shear strength as a function of the influence of interface roughness, of width and strength of concrete in the filled region, and of the dowel effect.

5.1.1 Influence of interface roughness and strength of concrete fill

Figure 13 illustrates the linear and nonlinear physical behavior (NLF) of series C, F and I (13 cm) with respect to the influence of interface roughness and strength of concrete fill. Series A, D and G (7 cm) and B, E and H (9 cm) showed the same behavior pattern.
For the same loading level, models C and I, with smooth interfaces, show a higher relative displacement than series F with rough interface. It is worth noting that, for the same interface surface, the model with the lowest compressive strength in the filled region (CPC) showed higher displacements.

The numerical rupture force also increases due to roughness of the interface and the concrete compressive strength, varying between 18 and 26% of changing. The roughness interface contribution is less than the concrete compressive strength in the filled region (CPC), about 7%.

5.1.2 Influence of the variation in width of the CPC filled region

Figure 14 compares the results of the influence of the width of the region filled with CPC. For the same amount of relative displacement, it was found that the loading level achieved was higher in the models with smaller widths of CPC.
This behavior is explained by the fact that the model with the smaller internal width shows lower stress normal to the interface distributed throughout the section. Conversely, the models that show higher stresses normal to the interface are those with greater widths in the CPC filled region, failing under lower loading. It should be noted that both the higher roughness and higher strength of the concrete fill contribute to the tendency for greater ultimate loading capacity of the model.

Figure 14 – Effect of varying the width of the concrete filled region CPC

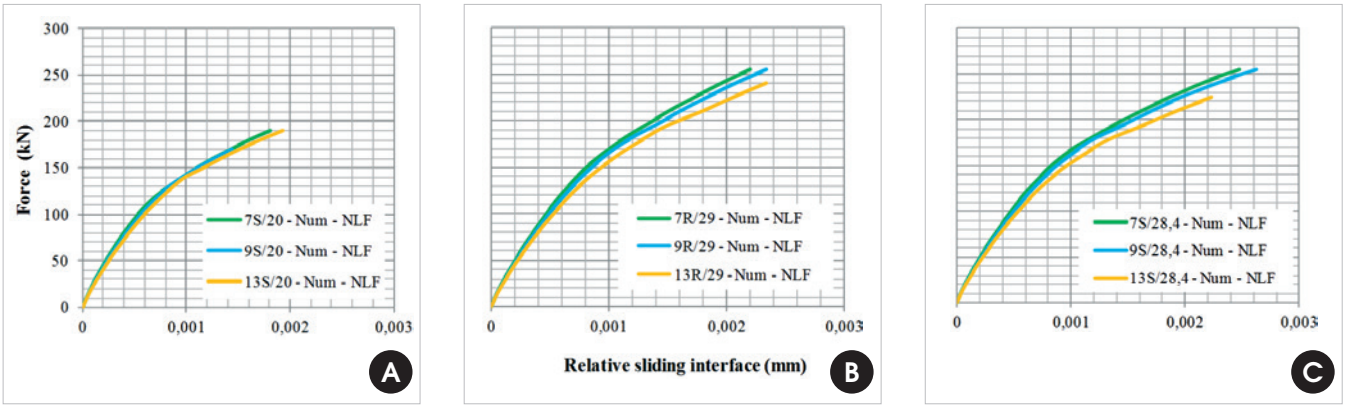

Series A, B and C | Series C, D and F | Series G, H and I

Figure 15 – Contribution of reinforcement throughout the interface of series G, H and I

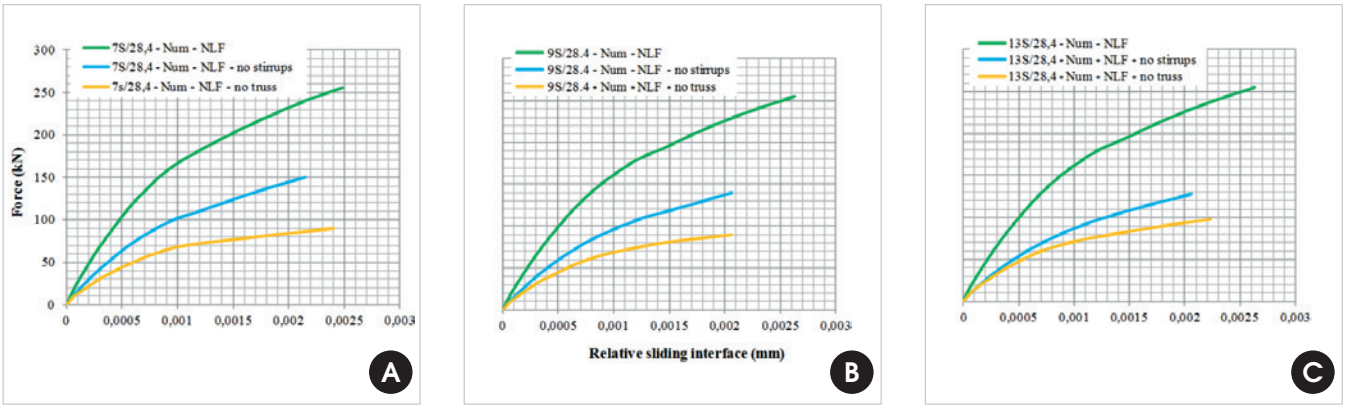

Series G | Series H | Series I

5.1.3 Influence of the dowel effect

To evaluate the influence of the reinforcement that crosses the interface, or the dowel effect on shear strength, three types of situations were analyzed numerically: without stirrups, without lattice, and with lattice and stirrups (Figure 15).

Models with stirrups and lattice withstand a higher level of loading than the other cases. Thus, it is possible to observe the influence of the dowel effect on the shear strength. Models with lattice and without stirrups withstand on average 71% of the breaking strength of the models with all the reinforcements. Models with stirrups but without lattices reach only 40% of the ultimate strength of the models with stirrups and lattices. As the width of the region of CPC (13 cm) increases, the effect of the absence of the stirrups becomes more significant (Figure 15c).

5.2 Cracking of the double lattice panels under direct shear

Cracking in the panels subjected to direct shear stress was analyzed in this study for the B Series, since almost all the numerical models showed the same type of cracking. The first crack occurred at the interface of the model under a load of approximately 25 kN. In general, the same type of cracking and mechanical behavior obtained in the numerical modeling was observed experimentally (Figure 16).

6. Comparison of numerical and experimental results

The numerical and experimental results of the models revealed

Figure 16 – Rupture of the experimental Series B model

Cracks at rupture (front and lateral face)

Details of slipping at the concrete interface (PCC and CPC)

Shear deformation of reinforcement

Figure 17 – Comparison of the numerical and experimental results for Series B, D, E, F, G and I

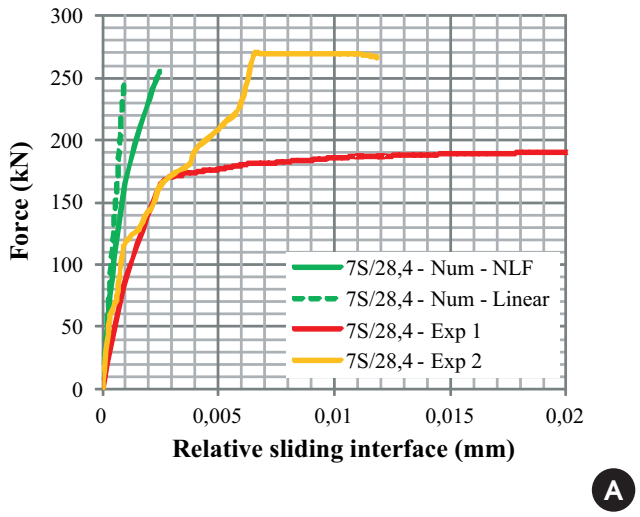

Series G: Smooth interface-7cm-CPC 28.4 MPa

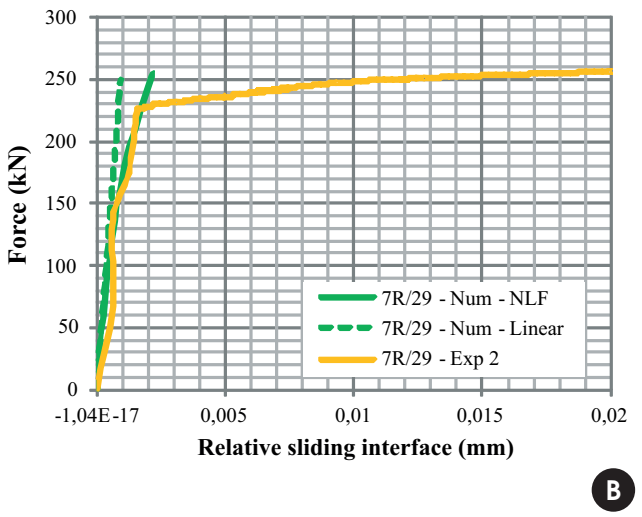

Series D: Rough interface-7cm-CPC 29 MPa

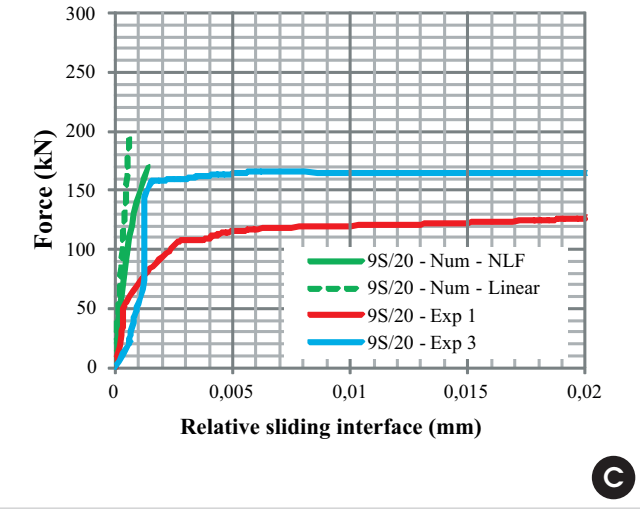

Series B: Smooth interface-9cm-CPC 20MPa

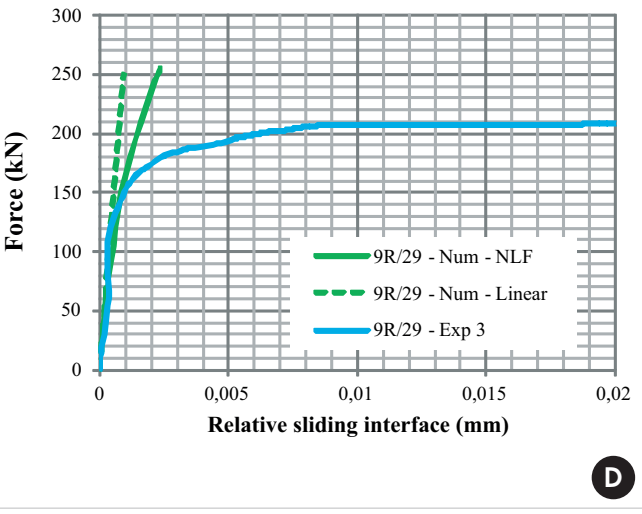

Series E: Rough interface-9cm-CPC 29MPa

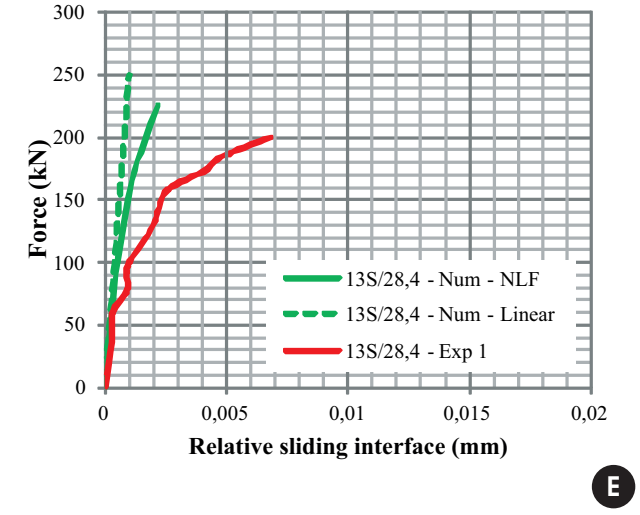

Series I: Smooth interface-13cm-CPC 28.4MPa

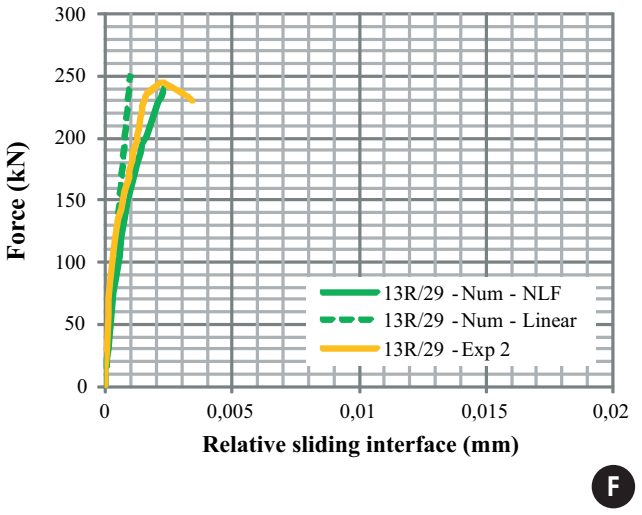

Series F: Rough interface-13cm-CPC 29MPa

low values of interface slipping and shear failure without yielding of reinforcing bars. The linear and nonlinear responses of the models are presented numerically. The rupture strength achieved experimentally for the series varied widely in the tested models. However, this variation was attributed to the small number of prototypes tested for each series. As a matter of fact, a tendency of the increasing of the load-bearing capacity of the models under direct shear stress was observed due the increase in compressive strength of the concrete in the filled region.

Figure 17 illustrates the ratio of force vs. relative slip at the interface indicated by the numerical and experimental results of models under direct shear stress of Series B, D, E, F, G and I. Other series showed very similar results.

The models with smooth interfaces showed higher relative slip than the models with rough interfaces, in order of 2 or 3 times greater (Figure 17a,b and Figure 17e,f). In general, the models with rough interfaces presented relative slipping in the order of $2x10^{-3}$ mm.

The numerical response of the relative sliding interface for the smooth interface tested series showed conservative values compared to the experimental tests. The rough interface series showed a good agreement between experimental and numerical response.

7. Conclusions

In general, the results show that the structural set works without significant slip at the interface. The main conclusions are described below.

The analyses of the experimental results under direct shear indicated that the transfer of stresses at the interface occurred with loss of adhesion. This was caused by detachment between the surfaces, frictional and mechanical forces, and the contribution of the dowel effect, until concrete-to-concrete slippage and rupture occurred, with crushing of the precast concrete in the region of the supports.

The surface roughness of the interface bonding region was an important factor in the increase in direct shear strength. In general, the smooth models with lower compressive strength in the filled region showed slippage 2 or 3 times greater at rupture than the relative slip at the interface of the models with rough surfaces;

As for the contribution of the compressive strength of the concrete in the filled region, an increase was observed in the direct shear strength of concrete with higher compressive strengths. Due to the wide dispersion of results for the experimental models, the average value of this contribution could not be determined. In numerical terms, the models with smooth interfaces showed a 36.61% gain in shear strength in response to the increase in compressive strength of the concrete in the filled region from 20 MPa to 28.4 MPa.

The numerical study indicated that the direct shear strength at the interface was higher in models of smaller width, since they presented lower normal stresses distributed at the interface, thus withstanding higher loading than the other models. Experimentally, due to the small number of tests performed for each variable under analysis, the values of rupture strength varied significantly.

Considering the contribution of each portion of reinforcement crossing the interface, the numerical simulations indicated that the higher the geometric ratio of reinforcement the higher the direct shear strength of the structural model. The models with lattices but without stirrups showed 71% of the rupture strength of the models with complete reinforcement. This rate dropped to 40% in the models with only stirrups and without lattices. At break, the stirrup reinforcement of the numerical models under direct shear did not reach the yield point.

8. Acknowledgements

The author gratefully acknowledges the Brazilian research funding agency CAPES (Federal Agency for the Support and Improvement of Higher Education) for a master's scholarship awarded for this research and the company PREMON the donation of precast concrete components.

9. References

[1] ANSYS RELEASE. Version 11.0 Documentation. SAS IP, Inc©; 2007.

[2] ASSOCIAÇÃO BRASILEIRA DE NORMAS TÉCNICAS. NBR 6118: Projeto de estruturas de concreto – Procedimento. Rio de Janeiro: ABNT, 2014.

[3] ASSOCIAÇÃO BRASILEIRA DE NORMAS TÉCNICAS. NBR 9062: Projeto e execução de estruturas de concreto pré-moldado. Rio de Janeiro: ABNT, 2006.

[4] ARAÚJO, D. L. Cisalhamento na interface entre concreto pré-moldado e concreto moldado no local em elementos submetidos à flexão. Thesis (Master Science). Escola de Engenharia de São Carlos, Universidade de São Paulo, 1997.

[5] ARAÚJO, D. L. Cisalhamento Entre Vigas e Lajes Pré-Moldadas Ligadas Mediante Nichos Preenchidos com Concreto de Alto Desempenho. Thesis (Doctor Science). Escola de Engenharia de São Carlos, Universidade de São Paulo, 2002.

[6] BASS, R. A., CARRASQUILLO, R. L., JIRSA, S. O. Shear Transfer Across New and Existing Concrete Interfaces, ACI Structural Journal, v. 86, n. 4, p. 383-393, jul./aug. 1989.

[7] BENAYOUNE, A., et al. Flexural Behaviour of Pre-cast Concrete Sandwich Composite Panel – Experimental and Theoretical Investigations. Construction and Building Materials, v. 22, p. 580-592, 2008.

[8] EL DEBS, M. K. Concreto Pré-Moldado: Fundamentos e Aplicações. Universidade de São Paulo. São Carlos: EDUSP, 2000.

[9] HOFBECK, J. A., IBRAHIM, I. O., MATTOCK, A. H. Shear Transfer in Reinforced Concrete, ACI Journal, Proceedings, v. 66, n. 2, p. 119-128, feb. 1969.

[10] HSU, T. T. C., MAU, S. T., CHEN, B. Theory of Shear Transfer Strength in Reinforced Concrete, ACI Structural Journal, v. 84, n. 2, p. 149-160, mar./apr. 1987.

[11] KABIR, M. Z. Structural Performance of 3-D Sandwich Panels Under Shear and Flexural Loading. Scientia Iranica, v. 12, n. 4 p. 402-408, oct. 2005.

[12] LACERDA, B. M. Estudo Numérico e Experimental do Comportamento de Painéis Duplos Treliçados Preenchidos com Concreto Moldado no Local. Thesis (Master Science). Universidade Federal de Uberlândia, 2013.

[13] LEONHARDT, F., MÖNNIG, E. Construções de Concreto: princípio básico do dimensionamento de estruturas de concreto armado. Rio de Janeiro: Interciência, 1982.

[14] OLIVEIRA, D. M. Estudo dos Processos Aproximados Utilizados para a Consideração das Não-linearidades Física e Geométrica na Análise Global das Estruturas de Concreto Armado. Thesis (Doctoral Science). Universidade Federal de Minas Gerais, 2007.

[15] RISSO, M. A. C. Resistência ao Cisalhamento de Ligações de Concreto de Diferentes Idades Providas de Chumbadores de Expansão. Thesis (Master Science). Universidade Federal do Rio de Janeiro, 2008.

Volume 8, Number 4 (August 2015) p. 479-490 • ISSN 1983-4195
http://dx.doi.org/10.1590/S1983-41952015000400004

REVISTA IBRACON DE ESTRUTURAS E MATERIAIS
IBRACON STRUCTURES AND MATERIALS JOURNAL

Influence of reinforcement's corrosion into hyperstatic reinforced concrete beams: a probabilistic failure scenarios analysis

Influência da corrosão de armaduras em vigas hiperestáticas em concreto armado: uma análise probabilística dos cenários de falha



G. P. PELLIZZER [a]
gpais@usp.br

E. D. LEONEL [a]
edleonel@sc.usp.br

C. G. NOGUEIRA [b]
cgnogueira@feb.unesp.br

Abstract

This work aims to study the mechanical effects of reinforcement's corrosion in hyperstatic reinforced concrete beams. The focus is the probabilistic determination of individual failure scenarios change as well as global failure change along time. The limit state functions assumed describe analytically bending and shear resistance of reinforced concrete rectangular cross sections as a function of steel and concrete resistance and section dimensions. It was incorporated empirical laws that penalize the steel yield stress and the reinforcement's area along time in addition to Fick's law, which models the chloride penetration into concrete pores. The reliability theory was applied based on Monte Carlo simulation method, which assesses each individual probability of failure. The probability of global structural failure was determined based in the concept of failure tree. The results of a hyperstatic reinforced concrete beam showed that reinforcements corrosion make change into the failure scenarios modes. Therefore, unimportant failure modes in design phase become important after corrosion start.

Keywords: reinforcements corrosion, chlorides ingress, Fick's law, reliability, reinforced concrete, failure scenarios.

Resumo

Este trabalho tem como principal objetivo analisar os efeitos da corrosão de armaduras em vigas em concreto armado na alteração dos possíveis cenários de falha individuais e na falha global da estrutura ao longo do tempo. As equações de estado limite consideradas descrevem analiticamente a resistência à flexão e ao esforço cortante em seções transversais retangulares em concreto armado. Foi também incorporada uma lei que penaliza a resistência ao escoamento do aço em função da evolução da corrosão em conjunto com a lei de Fick, a qual modela a penetração de íons cloreto no interior dos poros do concreto. Equações empíricas baseadas na lei de Faraday foram utilizadas para a determinação da nova área de armadura a cada instante de tempo na análise. A teoria da confiabilidade foi aplicada adotando-se o método de simulação de Monte Carlo para a avaliação das probabilidades individuais dos modos de falha considerados. A determinação da probabilidade de falha global da estrutura seguiu um procedimento baseado no conceito de árvore de falhas. Os resultados da análise de uma viga hiperestática em concreto armado demonstram que a corrosão das armaduras pode alterar os cenários de falha, de forma que, modos de falha não importantes na fase de projeto se tornam importantes à medida que o processo corrosivo evolui.

Palavras-chave: corrosão de armaduras, ingresso de cloretos, leis de Fick, confiabilidade, concreto armado, cenários de falha.

[a] *Universidade de São Paulo, Departamento de Engenharia de Estruturas, Escola de Engenharia de São Carlos, São Carlos-SP, Brasil;*
[b] *Universidade Estadual Paulista, Departamento de Engenharia Civil e Ambiental, Faculdade de Engenharia, Bauru-SP, Brasil.*

Received: 27 Jan 2015 • Accepted: 25 May 2015 • Available Online: 7 Aug 2015

1. Introduction

Reinforced concrete is one of the most used types of construction material around world. There are several advantages on using this type of solution such as its relative low production cost, facility to obtain its components, adaptability to complex geometries, high strength capacity and chemical properties [1].

The mechanical properties such as strength and stiffness have major importance in the context of reinforced concrete design as it is related to the resistance limit state. However, the interest on structural durability had a considerable advance in the last few years due to the large cost associated to structure repair and maintenance. NBR 6118 [2] prescribes rigorous design criteria in order to ensure durability in reinforced concrete structures. To improve the durability of reinforced concrete structures, engineers have to design taking into account the water/cement ratio adopted into concrete mixture, concrete cracking control, the environment aggressiveness and the prescribed cover depth. However, design codes do not present further recommendations aiming the structural durability analysis. It provides only guidelines that should be considered without information concerning the assessment of durability problems, which justifies the development of the present research.

Among the processes that reduce the durability of reinforced concrete structures, reinforcement's corrosion is mentioned as the major cause. The corrosion process produces the concrete cracking, cover spalling, loss of steel rebar cross section and yield stress and, consequently, the decrease of the mechanical strength along time. The corrosion process may derive from carbonation and/or high content of chloride ions, for instance, [3-5]. However, among such processes, the chloride penetration is the most important process that triggers the reinforcements corrosion [6]. Therefore, the modelling of chloride penetration and reinforcements corrosion lead to the accurate assessment of reinforced concrete durability.

The rebar corrosion phenomenon in reinforced concrete structures due to chloride penetration starts when the chloride concentration at the rebar/concrete interface reaches a threshold value. At this moment, the amount of hydroxyl into concrete pores exceeds the chemical threshold, causing the depassivation of the chemical layer protection around the steel rebar [7]. The chloride concentration at reinforcements interface grows along time and reaches the threshold value due to the ions transport from the external structural surface into it. The chloride ingress into concrete pores is a complex phenomenon governed by complex physical and chemical mechanisms. However, the representation of this phenomenon may be simplified considering only the chloride ions diffusion along the concrete cover. In this context, several models have been proposed in literature. Among them, it is worth to mention [8], which presents mathematical models to represent the particles movement in saturated concrete. Samson and Marchand [9] studied the influence of temperature on the chloride transport into concrete pores. Bastidas-Arteaga et al. [10] presented a study on the mechanical degradation processes caused by reinforcement's corrosion, concrete cracking and bio deterioration, as well as their combined influence on the strength reduction of reinforced concrete elements along time. Zhao et al. [11] analysed the mechanical degradation on the concrete cover from corrosion processes in non-cracked stages, initially, and then in partially cracked stages.

In spite of many proposed models in literature, such models deals the reinforcement's corrosion considering deterministic approaches, i.e., the influence of the inherent randomness is not accounted. As the corrosion involves chemical, mechanical and environmental parameters, which are uncertain, the randomness influence is widely significant. Therefore, this mechanical problem is represented consistently and realistically when the randomness is properly addressed. As a result, deterministic variables become probabilistic and uncertainties are accounted.

There are studies in literature using simple mathematical models to represent the chloride diffusion phenomenon into concrete pores combined with statistical approaches to model the uncertainties influence on the prediction of structural safety along time. Frangopol et al. [12], for instance, proposed a model to represent the mechanical behaviour of reinforced concrete girders as a function of time. In this model, the Fick's law was applied to represent the chloride diffusion process along time, empirical laws were adopted for the quantification of reinforcement's cross section loss and the Monte Carlo simulation method was used to carried out the probabilistic analysis. Nogueira et al. [13] performed a study on the determination of corrosion start using a probabilistic approach by the coupling between Fick's law and reliability theory. In this work, the influence of uncertainties associated with concrete cover depth and water-cement ratio on the probability of structural life failure was analysed. Nogueira and Leonel [14] proposed a simplified method to determinate the optimal maintenance time as a function of water-cement ratio, cover depth and environment aggressiveness. Interaction abacuses were proposed in order to determine optimum values of concrete cover according to maintenance time fixed a priori. Liberati et al. [15] proposed the coupling among Fick's law, reliability algorithms and damage mechanics to predict the structural life based on a robust finite element code. Such model allowed the elastoplastic behaviour of reinforcements and quasi-brittle behaviour of concrete.

In spite of several studies presented in literature concerning reinforcement corrosion modelling, aggressive mechanisms and chloride transport modelling, few studies have been observed focusing in the influence of corrosion on the global mechanical behaviour of reinforced concrete elements along time. Especially in the context of hyperstatic structures where effort distribution must be accounted. Normally, bending failure tends to be ductile whereas shear failure exhibits brittle behaviour in reinforced concrete structures. Therefore, brittle failures must be avoided and ductile failures must be predicted in design. However, change on the structural failure mode may occur due to reinforcements corrosion effects. Ductile failure, initially predicted in design, may not be the major weak structural link after corrosion start. As reinforcements area is lost during corrosion, effort distribution is observed and failure configurations different from those predicted in design may appear.

In such context, the present research aims to study the influence of reinforcement's corrosion phenomenon on the mechanical strength of hyperstatic reinforced concrete beams. One goal of this study concerns the determination of structural failure scenarios change along time. The mechanical modelling of corroded reinforced concrete structures is performed by coupling Fick's law, for chloride diffusion representation, to analytical approaches based on [2], to predict bending and shear structural resistance along time. The reduction on the reinforcements area and yield stress due to corrosion is modelled by empirical approaches. In addition to that, reliability theory is coupled to mechanical model in order to consider the inherent uncertainty on the physical problem. The

Monte Carlo simulation method is applied to assess the probability of each individual failure mode. The probability of global structural failure is achieved based in the concept of failure tree. Consequently, the applied model performs mechanical analyses in the probabilistic domain. A hyperstatic beam is analysed in this study and the change on the failure modes, individual and global, according to the corrosion evolution is represented, which is the main contribution of this work. Moreover, the evolution of the probability of failure, for global and each individual failure mode, is assessed, which is another contribution of this study.

2. Mechanical model

2.1 Simple bending and shear strengths

The evaluation of strength in reinforced concrete members considering simple bending and shear cases is performed based on classical hypothesis and models described by the Brazilian standard [2]. Figure 1 illustrates the cross section of a rectangular beam subjected to bending moment M, containing width b_w, height h, effective depth d, tensile steel area A_s, compression steel area A_s', neutral axis position x and strength of compression concrete f_{ck}.

The neutral axis is defined by the distance x, which value is null at the cross-section end, at is more compressive fibre. By adopting the simplification of plastic depth allowed by the parabolic-rectangle diagram for compression concrete, given by y = 0.8x, and enforcing the cross section equilibrium the bending design moment and neutral axis position are obtained. In such equilibrium condition, the external bending moment is equilibrated by the resistant bending moment, which is due to reinforcements and concrete. By performing the equilibrium in terms of bending moment, the following equation is obtained:

$$M_d = 0.68 b_w x f_{ck} \left(d - 0.4x\right) \quad (1)$$

in which M_d is the external bending moment applied into the cross-section, normally denominated as bending design moment.

The neutral axis position is determined from Equation 1. Solving such equation for x variable one obtains:

$$x = 1.25 d \left[1 - \sqrt{1 - \frac{M_d}{0.425 b d^2 f_{ck}}}\right] \quad (2)$$

After the design of the reinforced concrete element, in which the tensile steel area is determined, the associated resistant bending moment, M_{resist}, is calculated by equilibrium conditions. Such equilibrium results in:

$$M_{resist} = 0.408 b_w x^2 f_{ck} + A_s f_{sk} \left(d - x\right) \quad (3)$$

in which: f_{sk} is the yield steel for longitudinal reinforcements.

The determination of shear strength in reinforced concrete structures assumes as valid the hypothesis of generalized truss. It assumes stirrups positioned at 90º with the beam axis and spaced at each s. In addition to that, the shear resistance is determined considering the values of transversal reinforcement area A_{sw}, concrete compressive characteristic strength f_{ck} (MPa), steel yield for transversal reinforcement f_{yw} (MPa), b_w and d given in metre. The shear resistance of a rectangular cross section, V_{resist} (kN), belonging to a reinforced concrete beam is calculated by [16], considering the parameters described in the present paragraph, as follows:

$$V_{resist} = 644 b_w d \left(\frac{A_{sw}}{b_w s} f_{yw} + 0.10 f_{ck}^{2/3}\right) \quad (4)$$

Figure 1 – Rectangular cross-section of a rectangular reinforced concrete beam. Hypothesis, stress and strain distributions for failure limit state

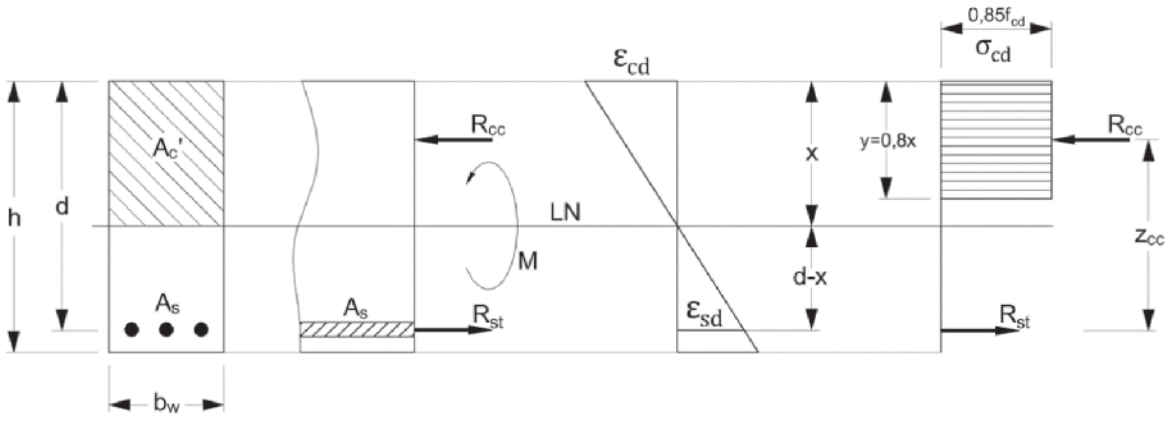

It is important to mention that during the durability analysis, in which steel reinforcements area is lost along time, the neutral axis position, Equation 2, is updated at each time step. Therefore, as the reinforcements are corroded the neutral axis is recalculated.
Another important remark that must be mentioned concerns the safety coefficients for design. The hyperstatic beam analysed in this study was designed considering safety coefficients. Then, the steel reinforcements areas were determined considering safety coefficients on the concrete and steel strengths and on the loading actions. Nevertheless, the probabilistic analyses were carried out disregarding such safety coefficients. Therefore, the characteristic values for all variables were considered during the probabilistic analyses.

2.2 Fick's law

Reinforcement's corrosion due to chloride ingress occurs in the presence of oxygen. Such process stars when the chloride concentration at the rebar contours exceeds a threshold level causing depassivation. Even for well-constructed and controlled reinforced concrete structures, a gradual ingress of chloride content from the external surface into concrete pores may occur according to the environmental conditions of aggressiveness. The transport mechanisms responsible for chlorides movement into concrete are capillary absorption, permeability under pressure, ion migration and ionic diffusion [4]. Among them, the most significant contribution is attributed to the ionic diffusion. Therefore, the proposed models, in literature, to represent such phenomenon are based, normally, only into ionic diffusion.
Fick's law [17] is an approach that has been widely used to simulate chloride penetration and its transport through concrete pores [7, 14, 15, 18, 19, 20]. It is important to mention that Fick's laws for diffusion assumes the media in which the flow occurs as homogeneous, isotropic and chemically inert. In addition to that, the chloride flow is assumed to be identical along all directions and constant along time. Considering concrete, these hypotheses are not completely satisfied, because concrete is well known as heterogeneous, anisotropic and chemically reactive (continued hydration and micro-cracking process) material. However, the methods commonly adopted for chlorides transportation modelling in concrete consider this process governed only by ionic diffusion. Then, it assumes that the concrete cover is completely saturated. Therefore, it makes the hypotheses of Fick's laws acceptable for the chloride ingress modelling, because, in this case, the material is assumed completely saturated, with unidirectional chloride flux, i.e., from the exterior surface into the concrete depth. When chloride diffuses into concrete, a change in chloride concentration, C, occurs at any time, t, in every point, y, of the concrete, i.e., it is a non-steady state of diffusion. To simplify its analysis, the diffusion problem is considered as one-dimensional. Many engineering problems of chloride ingress, as those discussed in this study, can be solved considering this simplification.
For a semi-infinite domain with an uniform fluid concentration at the external surface, the second Fick's law can be written as follows [13-15, 17]:

$$C(y,t) = C_0\, erfc\left[\frac{y}{2\sqrt{D_0\, t}}\right] \quad (5)$$

In which: $C(y,t)$ is the chloride concentration at a given depth y and at a time t; C_0 is the chloride concentration at the external surface assumed constant in time; *erfc* is the complementary Gauss error function; D_0 is the material diffusion coefficient considered constant along time.
From Equation 5, assuming that y is the concrete cover thickness and $C(y,t)$ the chloride concentration threshold, required to eliminate the chemical protective layer of reinforcements, it is possible to determine the time for corrosion start t_r as follows:

$$t_r = \frac{1}{D_0}\left\{\frac{y}{2\,erfc^{-1}\left[C(y,t)/C_0\right]}\right\}^2 \quad (6)$$

During the corrosion process caused by chloride diffusion, two different phases are observed. The first one, called initiation period, is defined from the construction until the rebar depassivation. The second phase, denominated propagation period, involves the end of initiation period until the structural collapse. The boundary between these two phases is the point characterized by the time of corrosion starts, which is evaluated by Equation 6 [14, 15].

2.3 Steel area reduction as a function of time

After the start of reinforcement corrosion, the rebar cross-section area reduces until its complete deterioration defining the propagation period. In literature, there are few mathematical models to represent such period as most researches consider as structural life only the initiation period. However, the propagation period can be modelled by empirical equations based on Faraday's laws. According to this approach, the reduction on the rebar cross-section area along time, assuming uniform corrosion process, is determined by the following equation [7, 21]:

$$d(t) = \begin{cases} d_{initial} & se\ t \le t_r \\ d_{initial} - 0.0232\, i_{corr}\,(t - t_r) & se\ t > t_r \end{cases} \quad (7)$$

In which: $d(t)$ and $d_{initial}$ are the rebar diameter given in millimetres for actual and initial configurations, respectively; i_{corr} is the corrosion ratio given in μA/cm²; t_r is the time for corrosion initiation given in years and calculated according to Equation 6; t is the diffusion time, given in years.
Different parameters have influence on the intensity of corrosion or into its rate. Among them, the water-cement ratio *w/c* and the cover depth y have to be mentioned. In order to account the influence of such parameters, the corrosion ratio is expressed according to [22] as follows:

$$i_{corr} = \frac{37.8\,(1 - w/c)^{-1.64}}{y} \quad (8)$$

2.4 Steel yield strength reduction as a function of time

In addition to the rebar cross-section area reduction during propagation period, the yield stress of reinforcements is also reduced

during corrosion process. Du et al. [23] performed an experimental study aiming to determine the mechanical residual strength of corroded steel rebar located into reinforced concrete elements. The researchers observed that the decrease on the yield stress occurs faster than the reduction of rebar diameter. According to [23], the reduction of the steel yield stress along time can be evaluated based on the following empirical expression:

$$f_{y,t} = (1.0 - 0.005 Q_{corr}) f_{y,o} \quad (9)$$

in which: $f_{y,t}$ e $f_{y,0}$ are the yield stress for corroded and non-corroded steel rebar at a given time, respectively; Q_{corr} is the amount of reinforcements corrosion given as a percentage of material mass loss. The amount of corrosion is calculated, according [23], as follows:

$$Q_{corr} = \frac{0.046\, i_{corr}}{d_{initial}} (t - t_r) \quad (10)$$

In which: i_{corr} is given in μA/cm² and calculated by Equation 8; the diameter is provided in millimetres and the times in years.

3. Reliability model

3.1 General Concepts

The reliability analysis aims at calculating the probability of failure regarding a specific failure scenario, known as limit state. It is worth to note that reliability R and probability of failure Pf are complementary concepts, in which R=1- Pf.

The first step in the reliability assessment is to identify the basic set of random variables $X = [x_1, x_2, ..., x_n]^T$ for which uncertainties have to be considered. For all these variables, probability distributions are attributed to model its randomness. These probability distributions may be defined by physical observations, statistical studies, laboratory analysis and expert opinion. The number of random variables is an important parameter to determine the computing time consumed during the reliability analysis. To reduce the size of the random variable space, it is strongly recommended to consider as deterministic all variables whose uncertainties lead to minor effects on the value of the probability of failure.

The second step consists in defining a number of potentially critical failure modes. For each of them, a limit state function $G(X)$ separates the space into two regions: the safe domain, where $G(X) > 0$ and the failure domain, where $G(X) < 0$. The boundary between these two domains is defined by $G(X) = 0$, known as the limit state itself.

The probability of failure is evaluated by integrating, over the failure domain, the joint density function, [21]:

$$P_f = \int_{G \le 0} f_X(x_1, x_2, \ldots, x_n)\, dx_1, dx_2, \cdots dx_n \quad (11)$$

In which $f_X(x_1, x_2, \ldots, x_n)$ is the joint density function of the variables X. As the evaluation of the above integration is impossible in practice, as the joint density function has not an explicit form, alternative procedures have been developed on the basis of the concept of reliability index, β, or simulation methods [24, 25].

In the present study, the Monte Carlo simulation method was applied to evaluate the probability of structural failure for each individual failure mode. Such approach will be presented in the following section.

3.2 Monte Carlo simulation

Monte Carlo method is a numerical simulation procedure widely used in reliability problems. In this method, a sampling of random variables is used to construct a set of values aiming to describe the failure and safe spaces in order to calculate Eq. (11). The sampling is constructed based on the statistical distribution assigned for each random variable considered in the problem. As this method deals with simulation of the limit state function, as bigger be the sampling adopted more accurate will be the spaces' description and more accurate will be the probability of failure achieved. The kernel of this method consists on the construction of a sampling for the random variables involved in the problem, as described in Figure 2.

Figure 2 presents a general sampling scheme assuming two random variables and two limit state functions. The simulation leads to the structural failure when the considered point is located at the failure domain. Otherwise, safety condition is observed. Series schemes consider failure if at least one limit state function be violated. On the other hand, parallel schemes assume failure condition when a set of critical limit state functions are violated. Such set of limit state functions are defined according to the structural system analysed and the failure paths available.

In spite of simulation methods be applicable for reliability analysis, optimization approaches such as First Order Reliability Methods (FORM) and Second Order Reliability Methods (SORM) are also available. FORM and SORM are based on the determination of the reliability index, which is associated to the probability of failure.

The probability of failure is calculated, for Monte Carlo simulation, using the following equation:

$$P_f = \int_{G<0} f_X(x_i)\, dx_i = \int_{G<0} I(x_i) f_X(x_i)\, dx_i = E[I(x_i)] \quad (12)$$

The function $I(x_i)$ can be estimated as follows:

$$I(x_i) = \begin{cases} 1 \rightarrow G \le 0 \\ 0 \rightarrow G > 0 \end{cases} \quad (13)$$

By simulating the limit state function for a convenient range of sampling, the mean value of $I(x_i)$ will be an estimator for the probability of failure. Therefore:

Figure 2 – Monte Carlo simulation method. General scheme considering two random variables and two limit state functions

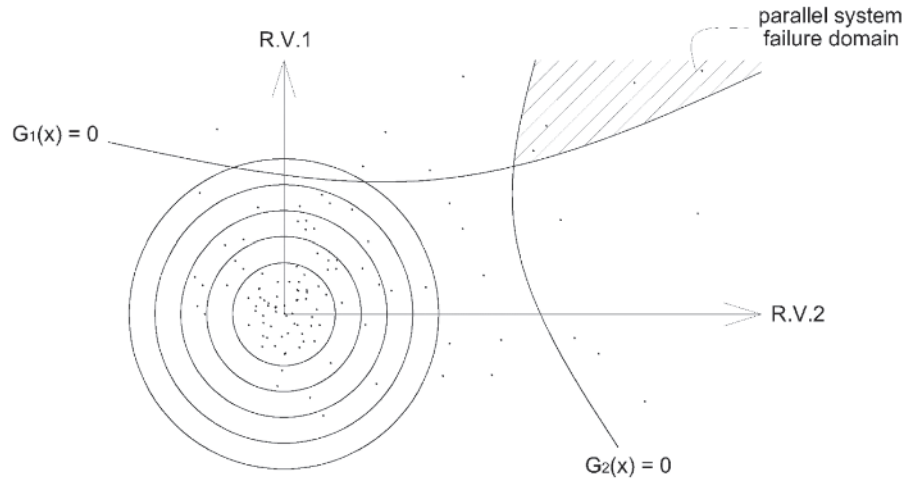

$$\overline{P}_f = E\left[I(x_i)\right] = \frac{1}{N}\sum_{i=1}^{N} I(x_i) \quad (14)$$

The disadvantage of this method is related to the high number of simulations required to compute accurately the probability of failure. Normally, in order to estimate accurately the probability of failure of 10^{-n}, the number of simulations must be higher than 10^{n+2} or 10^{n+3}. It means, in engineering structures, where the probability of failure is in between 10^{-3} to 10^{-6}, it is required 10^{5} to 10^{9} realizations of the limit state function. When complex numerical mechanical models are involved, which lead to high computational time, this method may be not reliable. However, theoretically, when the number of simulations tends to infinity, the probability of failure calculated tends to its real value. Other details about Monte Carlo simulation can be found in [24-27].

4. Studied problem

4.1 Structure definition

The presented methodology was applied to the probabilistic analysis of a hyperstatic beam. Such beam is supported into three points, and the external load is composed by an uniform distributed load. Figure 3 illustrates the static scheme of the beam. The bending moment and shear effort diagrams are also presented.

The reliability analyses were carried out considering the critical efforts presented in Figure 3. The intensity of such efforts is defined as follows:

$$M_1 = \frac{(q+g)L^2}{8};\ M_2 = \frac{9(q+g)L^2}{128};$$
$$V_1 = \frac{5(q+g)L}{8};\ V_2 = \frac{3(q+g)L}{8} \quad (15)$$

The analysed beam was designed, i.e. the reinforcements areas were determined, assuming a cross section of 20 cm x 40 cm (width x high); permanent load g = 3 kN/m; accidental load q = 20 kN/m; f_{ck} = 30 MPa; f_{yk} = 500 MPa; concrete Young's modulus E_c = 26071 MPa. The design procedure recommended by [2] was followed. In addition to that, the following parameters were considered for durability analysis: environmental aggressiveness class III (industrial type with high risk of structure deterioration [2]); concrete cover thickness 4 cm. It is important to stress that the structural design considered safety factors. However, the probabilistic analyses were carried out disregarding all safety factors on the load and material properties.

After such considerations, the structure was designed and detailed as shown in Figure 4.

It is worth to mention that in this study serviceability limit states were not accounted.

4.2 Safety Evaluation. Mixed model considered and effort redistribution

The reliability theory describes hyperstatic structural systems as redundant systems. Such description appears since the system failure, in this case, occurs after the failure of a number of individual modes equal to the structural hyperstatic degree. Consequently, as more than one limit state must be violated to the global failure be observed, such systems are subjected to load distribution, ensuring higher safety level when compared to simple isostatic schemes.

Considering the studied beam, the global collapse occurs after the consecutive failure of at least two individual failure modes. The failure is assumed when the effort due to the external load, Equation 15, exceeds the structural mechanical capacity given by Equations 3 and 4, in a given cross-section.

It is important to mention that hyperstatic structures presents more than one failure path, i.e. due to the load distribution and the combination of different random variables, the global failure can occur according to different sequences of individual failure modes. In such cases, the reliability theory based on system approach aims to determine the probability of each individual failure mode as well as the probability of global structural failure. As a result, this approach predict the most probable failure path and the most probable mechanical mechanism of failure.

In order to apply the reliability theory based on system approach it

Figure 3 – Static scheme considered and internal efforts

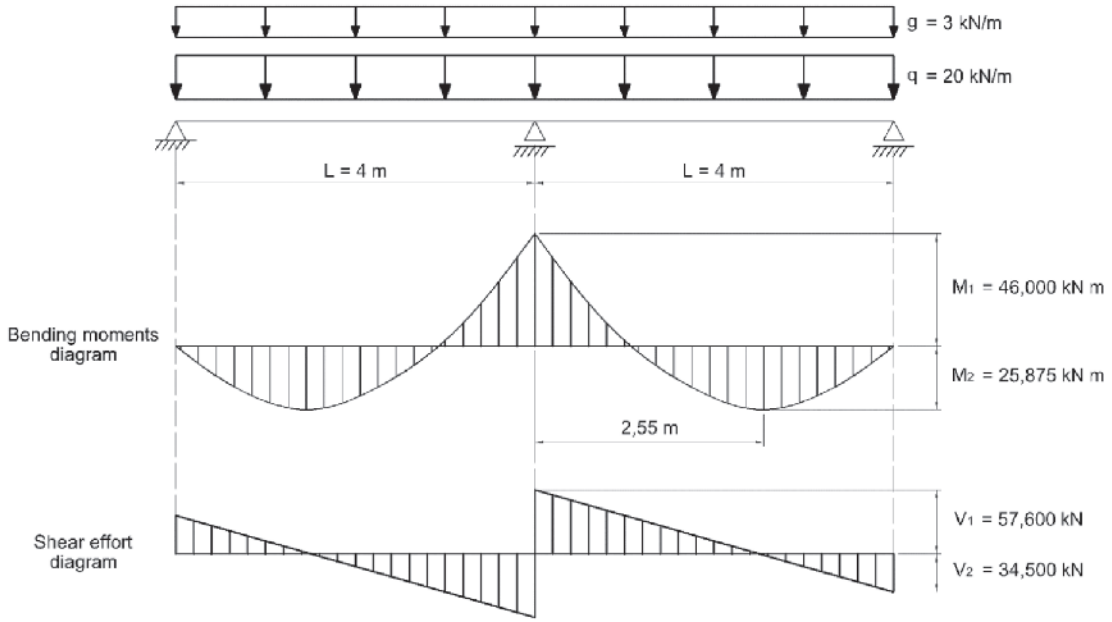

is convenient to construct a tree of failure. The strategy of tree of failure is commonly used in literature to indicate all possible failure paths. Therefore, by determining the probability of failure on each branch, the probability of global failure is determined as well as the most probable failure path.

To construct the tree of failure, individual failure modes must be defined. In the present study, three individual failure modes were considered. Two failure modes are related to bending whereas one relates shear. The bending failures are due to the maximum negative and positive bending moments M_1 and M_2, respectively. Such bending moments are represented in Figure 3 and occur at the central support (negative moment) and along the beam's span (positive moment). The shear failure is due to V_1, which occur at the cross-section next to the central support.

Therefore, the tree of failure was constructed considering three limit states: failure [A] defined by the bending failure on point A,

Figure 4 – Analysed beam. Reinforcement scheme

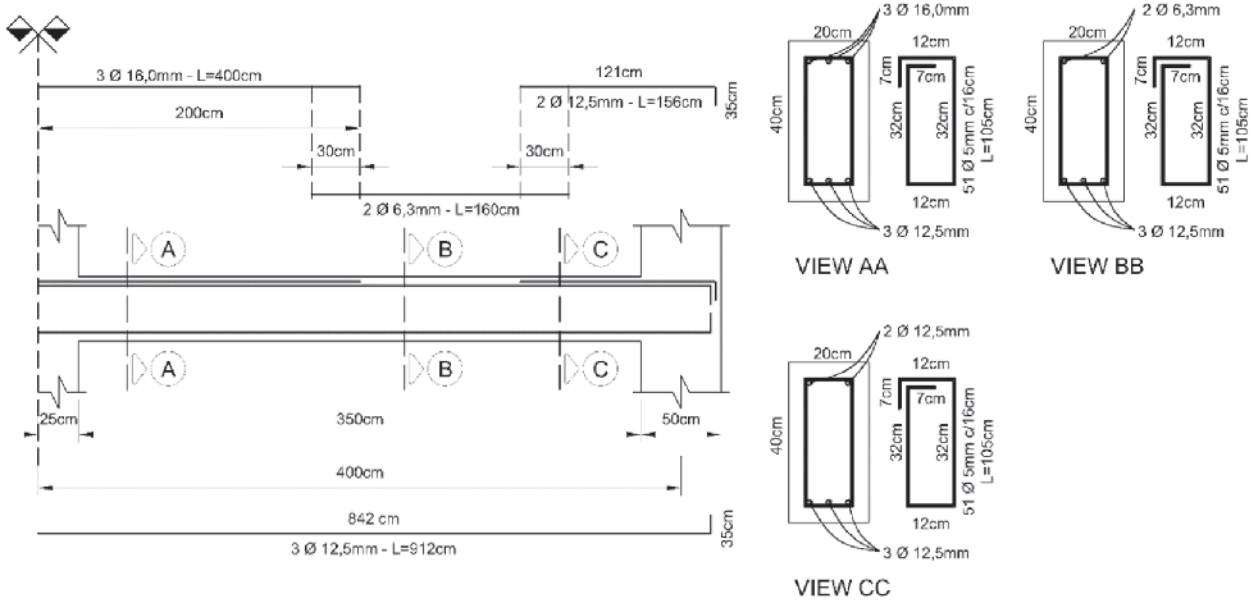

Figure 5 – Failure modes defined by the respectively cross-sections

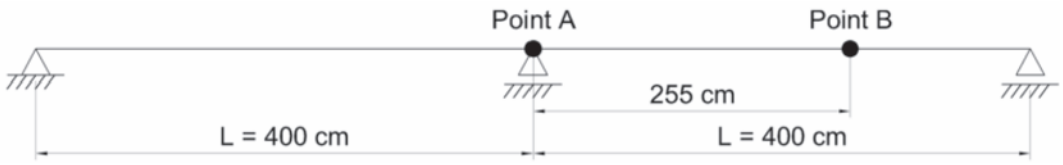

failure [B] defined by the bending failure on point B and failure [C] defined by shear failure on point A. The points A and B are illustrated in Figure 5 whereas Figure 6 presents graphically the tree of failure.

The first level of the tree presented in Figure 6 describes only individual failure modes [A], [B] and [C]. The second level accounts the conditional failure modes, i.e. the modes observed only after the occurrence of one individual mode. Therefore, in the second level, the conditional failure modes are written as follows: [B|A], [C|A], [A|B] and [C|B]. As observed in Figure 6, it is assumed that the individual failure mode [C] leads to the global failure. As previously commented, shear failure has brittle mechanical behaviour. Then, the occurrence of such individual failure mode leads to the mechanical collapse of some structural components; the effort redistribution is not available in such cases and collapse is observed. The tree of failure, which is used to illustrate the system approach with reliability theory, may be composed by failure mechanisms associated in parallel or series manner. The system adopted in the beam analysed in this study is mixed, as it is composed by a parallel sequence (initial failure by bending) connected to a series sequence (initial failure due to shear effort), [27]. Assuming that each failure path is a mutually exclusive event, the probability of global failure $P_{f,syst}$ is obtained by the sum of the probabilities of failure on each path, as follows:

$$P_{f,syst} = P[A]xP[B|A] + P[A]xP[C|A] + P[B]xP[A|B] + P[B]xP[C|B] + P[C] \quad (16)$$

To formulate the reliability problem, the following limit state functions were considered:

$$G_1(x) = M_r^A - M_a^A$$
$$G_2(x) = M_r^B - M_a^B$$
$$G_3(x) = V_r^A - V_a^A \quad (17)$$

In which: M_r and M_a are, respectively, the resistant bending moment and the bending moment due to the loading. concerns the limit state function, in terms of bending moments, for point A, whereas indicates the limit state function, in terms of bending moments, for point B. V_r and V_a are the resistant shear effort and the shear force due to the loading, respectively. indicates the limit state function, in terms of shear, for point. The resistant efforts are obtained considering Equations 3 and 4. The efforts due to the applied load are obtained using Equations 15.

4.3 Effort redistribution. Hypothesis assumed

It is important to mention that the initial static scheme presented in Figure 3 is valid for the determination of the first individual failure mode, i.e. events [A], [B] and [C] on the tree of failure. After the first individual failure mode be violated, effort redistribution may be assumed.

As previously mentioned, shear failure is brittle and normally leads to the structural collapse. Therefore, when the first individual failure mode violated is the mode [C], structural failure is assumed. However, the first individual failure being modes [A] and [B], which characterize bending failures, effort redistribution has to be performed.

If individual failure mode [A] is firstly observed, a perfect plastic hinge is assumed to appear at point A. The mechanical effect of such new condition is introduced by reapplying the difference between the bending moment due to the external load and the resistant bending moment at point A, which characterizes a new static scheme. Then, in this new static scheme, the positive bending moments and shear efforts considering the exceeding bending moment at point A are recalculated along the beam and the failure of the conditional failure modes is assessed.

When the first individual failure mode observed is [B], first level on the tree of failure, a perfect plastic hinge is introduced at point B.

Figure 6 – Tree of failure for the beam analysed

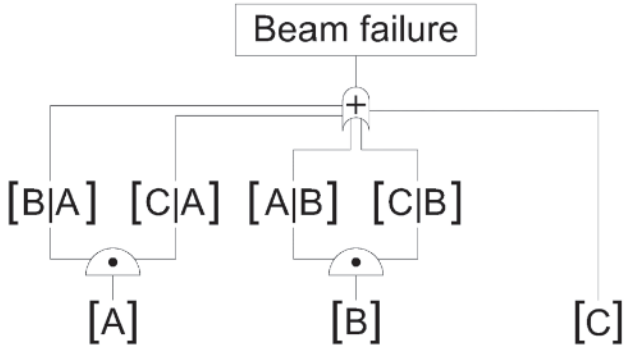

Table 1 – Statistic properties for random variables

V.A.	Distribution	Mean	Std. deviation	Unit
f_{ck}	Normal	30000.0	8000.0	kN/m²
f_{yk} (longitudinal reinforcements)	Lognormal	500000.0	50000.0	kN/m²
f_{yk} (transversal reinforcements)	Lognormal	600000.0	60000.0	kN/m²
q	Normal	3.0	0.345	kN/m
g	Gumbel	20.0	4.3	kN/m

Analogously to performed for point A, the difference between the bending moment due to the external load the resistant bending moment is reapplied into the structure. Then, considering this new static scheme, the bending moment at point A and the shear efforts along the beam span are recalculated in order to assess the violation of the conditional failure modes.

The corrosion modelling was performed considering the propagation phase, i.e. the reinforcements area and yield stress are penalised after the corrosion time initiation. For each time step increment, the rebar area and yield stress are determined using Equation 7 and 9, respectively. After applying the corrosion effects, the limit state functions are recalculated in order to determine the failure path at each time increment (first individual failure mode and the conditional mode). As a result of such procedure, the individual probabilities of failure and the probability of global failure are assessed. Is important to emphasize that the internal stresses derived from the expansive corrosion reactions and the adherence loss between steel were not considered in the present study.

5. Results and discussion

The random parameters adopted in the probabilistic analyses are presented in Table 1. In addition to such parameters, it was also considered the following information, which were assumed as deterministic:

- Water-cement ratio: 0.50;
- Chloride concentration for reinforcements depassivation, C(y,t): 0.90 kg/m³ [22];
- Chloride concentration at the beam surface, C_0: 2.95 kg/m³ [22];
- Concrete diffusion coefficient: [22];
- Total time considered in the analysis: 20 years;
- Time increment to evaluate the strength capacity due to corrosion: 0.1 years;
- Total number of Monte Carlo simulations: $3x10^6$.

Figure 7 illustrates the evolution of reinforcement area along time. Due to corrosion phenomena, reinforcement area is lost along time. As illustrated in this figure, the reinforcement depassivation occurs after 11 years of the beam construction. From that time, denominated time for corrosion initiation, the corrosion propagation period starts. Then, the reinforcement area is penalized according to Equation 7. It is important to stress that reinforcement diameter reduction along time has linear behaviour, as presented in Equation 7. Consequently, the area reduction along time has quadratic behaviour.

Figure 8 presents the evolution of the probability of failure considering each individual failure mode along time. In this figure, the probabilistic analyses were carried out accounting and disregarding the yield stress penalization on reinforcements along time.

Figure 7 – Evolution on the rebar cross-section during the corrosion process

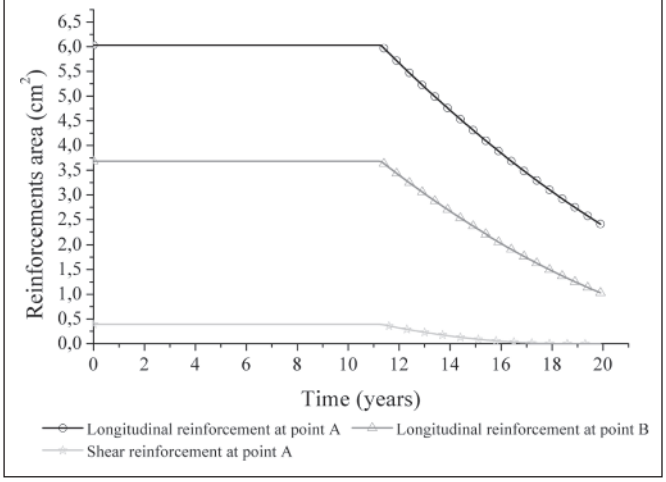

Figure 8 – Evolution on the probability of failure considering individual failure modes

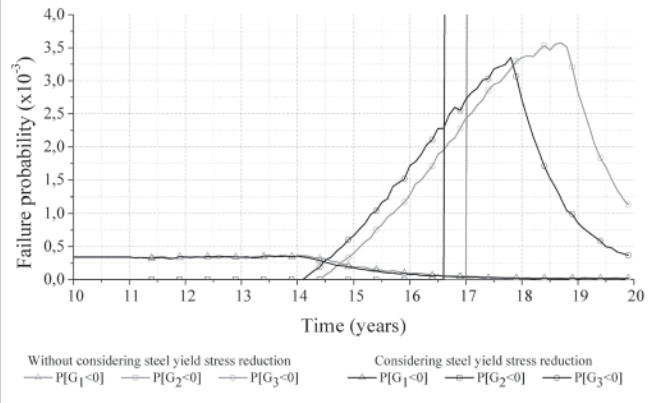

Figure 9 – Evolution of the probability of failure considering only the most probable failure path. Penalization of the reinforcement yield stress disregarded

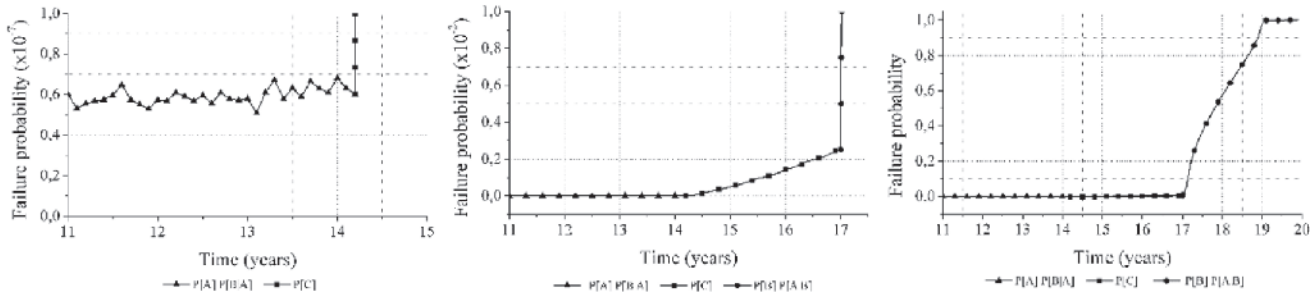

In order to do not disserve the visualization of the results illustrated in Figure 8, the probabilities of failure only in the range 10 to 20 years are considered.

It is important to emphasize that, regarding Figure 8, the probability of failure of each initial failure mode changes along time. Therefore, the most probable failure path is not the same during all the time, as the most probable initial individual failure mode changes along time.

In the beginning of the propagation time, the most probable initial failure mode is [A]. Such type of failure is, initially, obvious as the cross-section positioned at point A required the higher amount of reinforcement's area. However, as the corrosion process proceeds along time, the most probable failure scenario change. As presented in Figure 8, after 14 years of the beam construction, the failure mode [C] becomes the most probable initial failure mode. Such probabilistic behaviour is explained due to the stirrups diameter be lower than the longitudinal reinforcements diameter. Therefore, as presented in Equation 7, the stirrups lose cross-section area faster than longitudinal reinforcements along time. As a result of such cross-section lost, the failure on stirrups become more probable. This type of probabilistic behaviour illustrates the relevance/importance of the present study. It shows that the mechanical behaviour intended during design phase may not be observed during the structural life. The mechanical structural behaviour can change drastically when corrosion effects are accounted. As presented in Figure 8, sudden brittle failures due to shear effort may appear before the expected ductile bending failures.

After 16.5 years from the beam construction, the individual failure mode [B] becomes the most probable initial failure mode, as presented in Figure 8. Such change is explained due to the longitudinal reinforcements cross-section lost along time caused by corrosion. Thus, the faster decrease of the longitudinal reinforcement's cross-section along time at point B in comparison with point A and stirrups increases significantly the importance of such initial failure mode. As the reinforcement area along the beam change due to the corrosion, the structural configuration change, the resistant mechanisms change and, consequently, the failure modes also change.

Another important behaviour that must be commented concerns the reduction of the probabilities of failure in individual modes [A] and [C]. The probabilities of failure presented in Figure 8 relate only the probability of failure of each individual failure mode. Therefore, conditional probabilities of failure were not considered in the construction of such figure. Then, it explains the reduction on individual failure modes [A], after 14.5 years, and [C], after 18.5 years. It is important to emphasize that at each time increment at least one individual failure mode had its individual probability of failure increased (during the propagation period obviously). It is consistent regarding probabilistic analyses and make consistent the analyses performed.

Figure 10 – Evolution of the probability of failure considering only the most probable failure path. Penalization of the reinforcement yield stress accounted

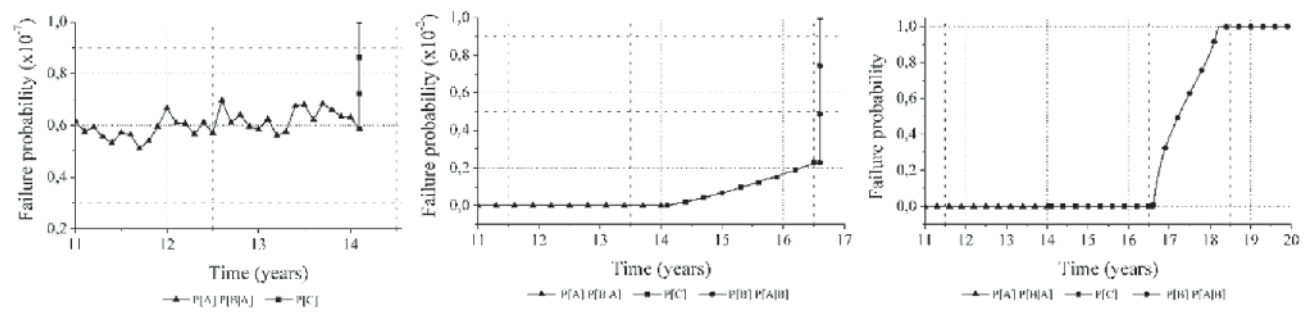

The penalization of the reinforcement yield stress as a function of time did not introduce significant change into the probabilistic mechanical behaviour of the beam along time. The subtle difference concerns the time in which the mechanical effects due to the corrosion are observed. Considering the penalization of reinforcement yield stress, the mechanical effects of corrosion are observed earlier in comparison with analyses where such penalization was disregarded.

The behaviour of the probability of failure evolution along time regarding only the most probable failure path can also be analysed, leading to interesting results. Figure 9 presents the evolution of the probability of failure along time considering only the most probable failure path and disregarding the penalization of the reinforcements yield stress. Figure 10 presents similar results but accounting the penalization of the reinforcements yield stress.

The main difference among the results presented in Figure 9 and 10 relates the time in which the mechanical corrosion effects are observed. When the penalization of the reinforcements yield stress is accounted, the mechanical corrosion effects are earlier observed, as expected. However, any change is observed into the most probable failure paths, which are the same.

Figure 11 illustrates the evolution of the probability of global failure along time. According to this figure, it can be observed important increase on the probability of global failure from, approximately, 16 years. Such global probabilistic behaviour indicates, as presented in Figures 9 and 10, that in this age, the mechanical effects due to the corrosion change the most probable failure path. The reduction on the reinforcements cross-section provided by corrosion phenomenon reduces the structural resistance. Consequently, the probability of global failure grows. It is important to observe that the probability of global failure always increase during the propagation period, which is consistent.

Figure 11 – Evolution on the probability of failure considering global failure

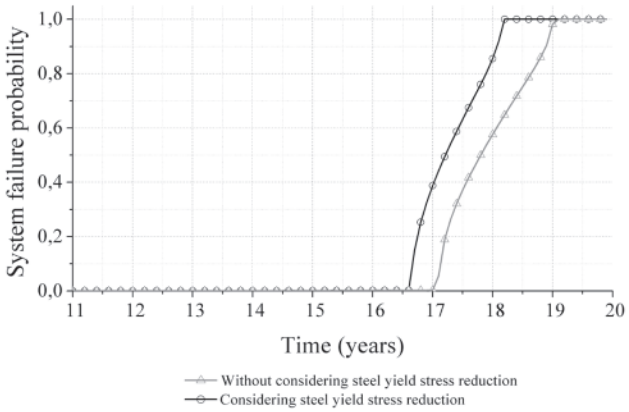

6. Conclusions

The main conclusions of the present study are the following:

- The penalization on the reinforcement yield stress along time introduces mechanical degradation earlier than the case in which such penalization is disregarded. However, any change was observed regarding the structural global failure path. Then, the importance of considering such penalization concerns the extension of propagation period, which is lower when penalization is considered. In spite of its simplicity as the penalization model is based on empirical observations, the coupling of this approach in a nonlinear mechanical framework may lead to important changes into the mechanical structural behaviour.
- The main conclusion of the present study concerns the change on the structural failure mode along time. The corrosion process provides reduction on the reinforcement's cross-section area along time. Then, the structural resistance changes along time as well as the initial failure mode and the structural collapse path. The knowledge about the most probable failure mode has major importance into a structural design, especially if maintenance, safety and failure prevention are focused. Considering a reinforced concrete structural design, bending moments and shear efforts lead to the determination of longitudinal reinforcements and stirrups areas, respectively. Then, the structural cross-sections more requested by the external load receive higher reinforcement area. The structural engineer, intuitively, expects that the first failure mode occurs at the cross-section with higher reinforcement ratio, as such cross-sections are more requested. However, during the corrosion process, reinforcements area are lost, as previously mentioned. In addition to that, the corrosion process has more severe consequences in cross-sections with lower reinforcement ratios, as presented in the results of the present study. Then, during the corrosion phase, failure modes expected during design phase normally does not occur and failure modes in cross-section with lower reinforcement ratio appear. Therefore, the change on the failure modes during the propagation period is an important phenomenon that must be accounted in durability analyses in reinforced concrete structures in order to avoid unexpected failure modes.

Finally, the present study supports further investigations that incorporates nonlinear mechanical models for concrete and steel, in order to consider realistic approaches to the efforts redistribution. Furthermore, the coupling of the probabilistic model to an optimization approach may also be interesting to determinate the optimal design solution that includes initial costs, maintenance and repair costs due to the change on the failure modes along time.

7. Acknowledgment

Sponsorship of this research project by São Paulo Research Foundation (FAPESP), grant number 2014/18928-2 is greatly appreciated. This research is a part of the activities scheduled by the research project USP/COFECUB 2012.1.672.1.0.

8. Bibliography

[1] MEHTA, P. K.; MONTEIRO, P. J. M. Concreto: microestrutura, propriedades e materiais. Ibracon, São Paulo, 3ed., 2008, 674 p.

[2] ASSOCIAÇÃO BRASILEIRA DE NORMAS TÉCNICAS. NBR 6118. Projeto de estruturas de concreto, Rio de Janeiro, 2014.

[3] HELENE, P. R. L. Corrosão em armaduras para concreto armado. Pini/IPT, São Paulo, 1986.
[4] CASCUDO, O. O controle da corrosão de armaduras em concreto: inspeção e técnicas eletroquímicas. São Paulo: Pini; Goiânia: Editora UFMG, 1997.
[5] APOSTOLOPOULOS, C. A.; PAPADAKIS, V. G. Consequences of steel corrosion on the ductility properties of reinforcement bar. Construction and Building Materials, v. 22, n. 12, 2008, p. 2316-2324.
[6] BASTIDAS-ARTEAGA, E.; SCOEFS, F.; STEWART, M. G.; WANG, X. Influence of global warming on durability of corroding RC structures: a probabilistic approach. Engineering Structures, v. 51, 2013, p. 259–266.
[7] VAL, D. V.; STEWART, M. G. Life-cycle cost analysis of reinforced concrete structures in marine environments. Structural Safety, v. 25, 2003, p. 343–362.
[8] SAMSON, E.; MARCHAND, J.; SNYDER, K. A. Calculation of ionic diffusion coefficients on the basis of migration test results. Materials and Structures, v. 36, 2003, p. 156–165.
[9] SAMSON, E.; MARCHAND, J. Modeling the effect of temperature on ionic transport in cementitious materials. Cement and Concrete Research, v. 37, 2007, p. 455–468.
[10] BASTIDAS-ARTEAGA, E.; SÁNCHEZ-SILVA, M.; CHATEAUNEUF, A.; RIBAS-SILVA, M. Coupled reliability model of biodeterioration, chloride ingress and cracking for reinforced concrete structures. Structural Safety, v. 30, 2008, p. 110-129.
[11] ZHAO, Y.; YU, J.; JIN, W. Damage analysis of cracking model of reinforced concrete structures with rebar corrosion. Corrosion Science, v. 53, 2011, p. 3388–3397.
[12] FRANGOPOL, D. M.; LIN, K-Y.; ESTES, A. C. Reliability of reinforced concrete girders under corrosion attack. Journal of Structural Engineering, ASCE, v. 123, n. 3, 1997, p. 286–297.
[13] NOGUEIRA, C. G.; LEONEL, E. D.; CODA, H. B. Reliability algorithms applied to reinforced concrete structures durability assessment. IBRACON Structures and Materials Journal, v. 5, n. 4, August, 2012, p. 440-450.
[14] NOGUEIRA, C. G.; LEONEL, E. D. Probabilistic models applied to safety assessment of reinforced concrete structures subjected to chloride ingress. Engineering Failure Analysis, v. 31, 2013, p. 76–89.
[15] LIBERATI, E. A. P.; NOGUEIRA, C. G.; LEONEL, E. D.; CHATEAUNEUF, A. Nonlinear formulation based on FEM, Mazars damage criterion and Fick's law applied to failure assessment of reinforced concrete structures subjected to chloride ingress and reinforcements corrosion. Engineering Failure Analysis, v. 46, 2014, p. 247-268.
[16] CARVALHO, R. C.; FIGUEIREDO FILHO, J. R. Cálculo e detalhamento de estruturas usuais de concreto armado segundo a NBR 6118:2003 – 3ed. – São Carlos: EdUFSCar, 2009.
[17] CRANK, J. The mathematics of diffusion. 2ed. Oxford (London): Clarendon Press; 1975, 414 p.
[18] GUZMÁN. S.; GÁLVEZ, J. C.; SANCHO, J. M. Cover cracking of reinforced concrete due to rebar corrosion induced by chloride penetration. Cement and Concrete Research, v. 41, 2011, p. 893–902.
[19] BASTIDAS-ARTEAGA, E.; CHATEAUNEUF, A.; SANCHEZ-SILVA, M.; BRESSOLETTE, P.; SCHOEFS, F. A comprehensive probabilistic model of chloride ingress in unsaturated concrete. Engineering Structures, v. 51, 2011, p. 259–66.
[20] VAL, D. V.; CHERNIN, L.; STEWART, M. G. Experimental and numerical investigation of corrosion-induced cover cracking in reinforced concrete structures. Journal of Structural Engineering, ASCE, v. 135, 2009, p. 376–385.
[21] VAL, D. V.; MELCHERS, R. E. Reliability of deteriorating RC slab bridges. Journal of Structural Engineering, ASCE, v. 123, n. 12, 1997, p. 1638–1644.
[22] VU, K. A. T.; STEWART, M. G. Structural reliability of concrete bridges including improved chloride-induced corrosion models. Structural Safety, v. 22, n. 4, 2000, p. 313-333.
[23] DU, Y. G.; CLARK, L. A.; CHAN, A. H. C. Residual capacity of corroded reinforcing bars. Magazine of Concrete Research, v. 57, n. 3, April, 2005, p. 135-147.
[24] NOWAK, A. S.; COLLINS, K. R. Reliability of structures, Boston: McGraw-Hill, 2000.
[25] ANG, A. H-S.; TANG, W. H. Probability Concepts in Engineering: Emphasis on Applications to Civil and Environmental Engineering, 2nd Edition. New York: John Wiley & Sons, 1984.
[26] SANTOS, K. R. M. Técnicas de amostragem inteligente em simulação de Monte Carlo. São Carlos, 2014, Dissertação (Mestrado) – Escola de Engenharia de São Carlos, Universidade de São Paulo, São Paulo, 191 p.
[27] DITLEVSEN, O.; MADSEN, H. O. Structural reliability method, New York: John Wiley and Sons, 1996.

Volume 8, Number 4 (August 2015) p. 491-506 • ISSN 1983-4195
http://dx.doi.org/10.1590/S1983-41952015000400005

REVISTA IBRACON DE ESTRUTURAS E MATERIAIS
IBRACON STRUCTURES AND MATERIALS JOURNAL

Weighing in motion and characterization of the railroad traffic with using the B-WIM technique

Pesagem em movimento e caracterização do tráfego ferroviário com uso da técnica B-WIM

J. A. DE CARVALHO NETO [a]
decarvalho@ufpa.br

L. A. C. M. VELOSO [a]
lveloso@ufpa.br

Abstract

The knowledge on the active moving load of a bridge is crucial for the achievement of the information on the behavior of the structure, and thus foresee maintenance, repairs and better definition of the logistics of its active vehicles. This paper presents the development of the algorithms for the application of the Bridge-Weigh In Motion (B-WIM) method created by Moses for the weighing of trains during motion and also for the characterization of the rail traffic, allowing the obtainment of information like passage's train velocity and number and spacing of axles, eliminating the dynamic effect. There were implemented algorithms for the determination of the data referring to the geometry of the train and its loads, which were evaluated using a theoretical example, in which it was simulated the passage of the train over a bridge and the loads of its axles were determined with one hundred percent of precision. In addition, it was made a numerical example in finite elements of a reinforced concrete viaduct from the Carajás' Railroad, in which the developed system reached great results on the characterization and weighing of the locomotive when the constitutive equation of the Brazilian Standards was substituted by the one proposed by Collins and Mitchell.

Keywords: B-WIM, axle loads, bridges, numerical modeling, gross vehicle weight.

Resumo

O conhecimento do carregamento móvel atuante em uma ponte é de grande importância para obter a informação do comportamento da estrutura, e assim prever manutenção, reparos e definir melhor a logística dos veículos que circulam sob a mesma. Este trabalho apresenta o desenvolvimento dos algoritmos para aplicação do método Bridge-Weigh In Motion (B-WIM) criado por MOSES (1979) para a pesagem em movimento de trens e também para a caracterização do tráfego ferroviário, permitindo-se obter informações sobre a velocidade de passagem dos trens, número e espaçamento entre eixos, eliminando o efeito dinâmico. Foram implementados os algoritmos para a determinação dos dados referentes a geometria do trem e das cargas, que foi validado a partir de um exemplo teórico, onde se simulou a passagem do trem sobre a ponte e as cargas por eixos foram determinadas com 100% de exatidão. Além disso, foi feito um exemplo numérico em elementos finitos, de um viaduto em concreto armado para aplicações do método, onde foi feita a determinação das cargas por eixo para diferentes velocidades de passagem do trem. Finalmente, o método foi testado em um caso real a partir de monitorações realizadas em um viaduto de concreto armado da Estrada de Ferro Carajás, onde o sistema desenvolvido conseguiu atingir ótimos resultados na caracterização e pesagem da locomotiva quando se substituiu a equação constitutiva da ABNT NBR 6118 (2007) pela equação proposta por Collins e Mitchell (1991).

Palavras-chave: B-WIM, carga por eixo, pontes, modelo numérico, peso bruto total.

[a] *Institute of Technology, Civil Engineering College, Universidade Federal do Pará, Belém, PA, Brazil.*

Received: 29 Nov 2014 • Accepted: 18 May 2015 • Available Online: 7 Aug 2015

1. Introduction

The studies on railroad bridges have led to great improvements regarding the understanding of their dynamic behavior. Furthermore, many researches are carried aiming the evaluation of the real characteristics of its active traffic.

Every structure must be conceived and designed so that it is able to support, with an appropriate margin of safety, the loads and deformations predicted during its operating life. In this context, there is a special interest on the development of methodologies that allow the measurement of the real effects of the traffic on the railroad's structures, in a manner that, in the future, to be possible, in a relatively simple way, to increase the axle loads and speed of traffic, with no need of big investments in infrastructure.

The acquisition of information on the axles and gross weight of the vehicles have been object of studies around the world since the 70's, having their origin in a research which took place in a road bridge near Cleveland, Ohio (Moses [1]). This kind of data is essential in the design of new structures and maintenance of old bridges and viaducts.

The weigh-in-motion methods were created to determine the axle's loads and gross weight of vehicles during highway trips, avoiding the vehicles to stop. These methods were called Weigh-In-Motion (WIM) and divided in two categories based on the type of instrumentation used, which could be assembled on the pavement (WIM) or in bridges (Bridge Weigh-In-Motion – B-WIM) (Moses[1]), see Figure [1].

2. Experimental determination of moving loads (Moses' algorithm)

Studies on the loads of traffic are a normal practice in respect of road traffic worldwide. The fact comes from the great expansion of the road transport of goods in the second half of the twentieth century. It was verified that the recent growth of the loads transported by vehicles led to the deterioration of the pavements and bridges, what induced the need of control of these loads. Initially, the control was done through static weighing systems. Despite their high precision, the reduced number of heavy vehicles, as well as the delay caused by the process, increased the interest on the development of dynamic methods of weighing.

In order to satisfy the necessity of studying the traffic load on roads, were developed many systems of weighing during motion, which take measurements through sensors installed on the pavement. These systems can determine with high precision the load of vehicles.

The B-WIM differs from other systems due the use of measurements of deformation from the bridges, not the pavement, during the passage of vehicles. The advantage of this system is that it allows the weighing along the length of the bridge, while the others weigh a single lane of the pavement. Moreover, it is possible to filter the signal to take the dynamic effect caused by flaws in the wheels and irregularities on the lane. The method can be applied both in characterization of the traffic of highways and railroads.

The characteristics of the structures in which the B-WIM algorithms will be used have particular significance for obtaining good results, specially the length of the free span and the dynamic properties of the structure (Pimentel [4]). The bridges of short free span are more frequently used in the application of the algorithm, once a large free span bridge would have several axles acting on the same span, condition that would forbid the determination of the load per axle, but permits to detect the trucks with better precision.

Regarding the dynamic properties of these bridges, the dynamic effects due the passage of the train must be filtered, so the frequencies of the vehicles, derived from the relation between the velocity (which must be constant) and their axle's spacing, see Equation [1], are isolated. The feature that makes these structures able

Figure 1 – WIM methods: a) Measurements on the pavement, WIM; b) B-WIM, complete system (Znidaric e Baumgärtner, (2) apud Quilligan, (3))

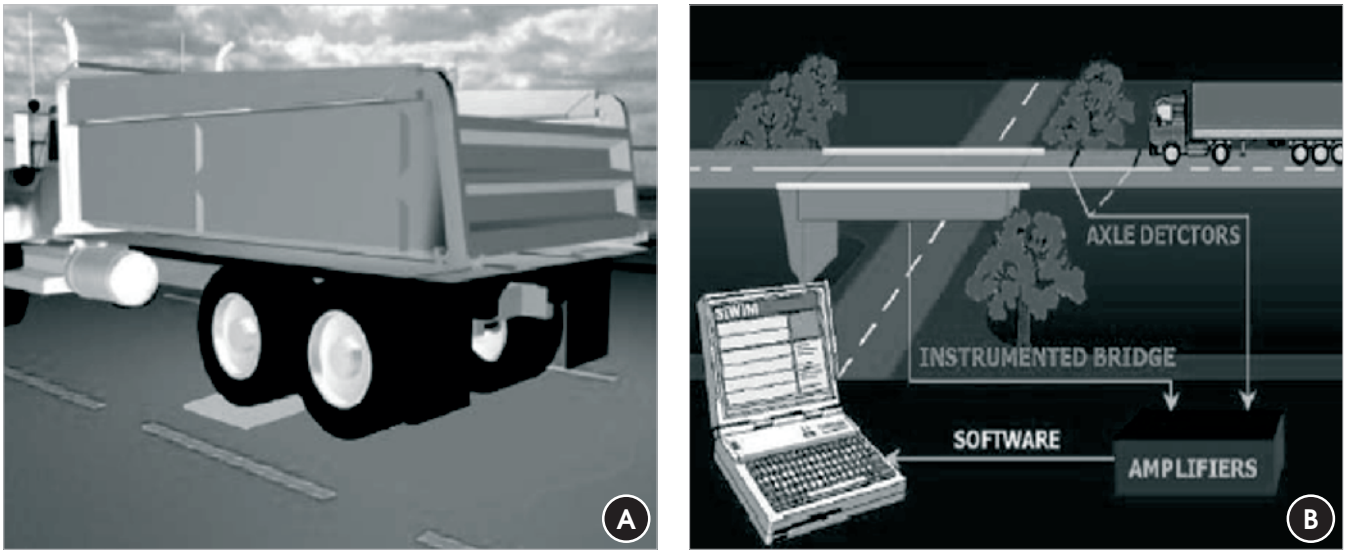

Figure 2 – a) Position of the axles along the bridge; b) Influence line of the bending moment

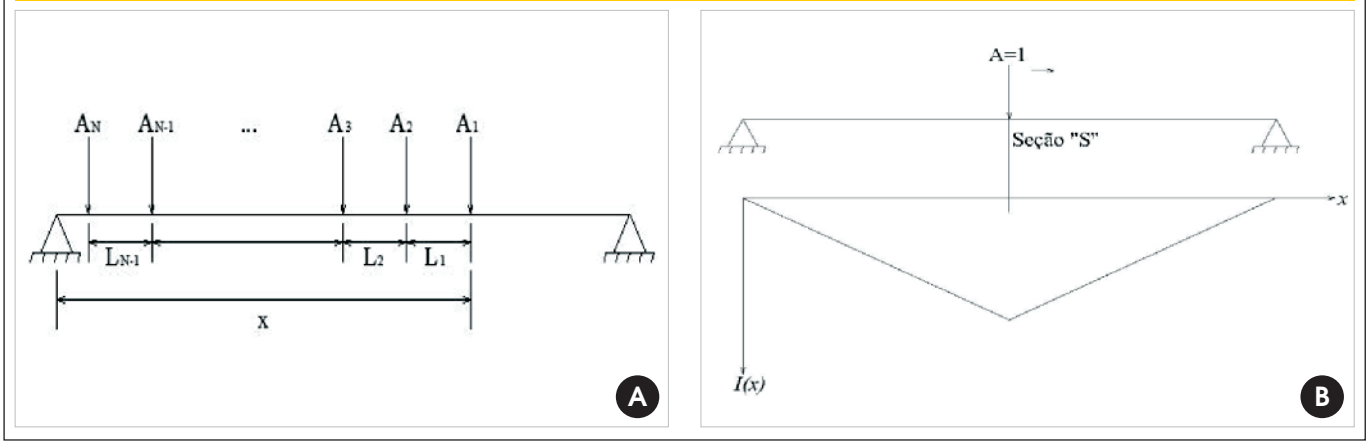

for the application of the algorithm is the gap between their natural frequency and the frequency of passage of each axle.

$$f = \frac{V}{d_{axles}} \quad (1)$$

There are other factors that may decrease the precision of the method, such as the difficulty in the determination of a proper influence line and the variation in the velocity during the passage of the vehicle.

The influence line must take into account the elements of the bridge, like sleepers, ballast, tracks and load spreading. Therefore, it is necessary, for a numerical or experimental verification, that the most appropriate influence line is achieved.

The algorithm has two inputs: the time-series of the bending moment of a determined transversal section of the bridge and its respective influence line. The time-series is obtained from the deformations measured with strain-gages, fixed on the main girders of the bridge, and the influence line at that same section.

2.1 B-WIM Algorithm

The algorithm of Moses (Moses [1]) is based on the concept of influence line, in which a moving load over a structure causes reactions proportional to the product of the influence line's ordinate and the magnitude of the respective load. Assuming that the structure has *n* longitudinal girders, each girder must be instrumentalized in the longitudinal direction at mid-span. For a determined static position of a vehicle, the total bending moment is equal to the summation of the bending moments in each of the girders. Assuming that the structure is under elastic regime, the bending moment may be formulated as a function of its deformation.

$$M_i = f(\varepsilon_i) \quad (2)$$

Where:

$f(\varepsilon_i)$ is the deformation measured in the girder *i*.

The algorithm B-WIM is an inverse problem, in which the response is known, being necessary to determine one the variables. Knowing the characteristics of the vehicle, the number of variables of the problem corresponds to the number of axles (N), which can be obtained through the N different values of the bending moment in k different positions of the vehicle on the bridge, see Figure [2]-a. Considering a sampling for the passage of the vehicle over the structure, it is possible to define the bending moment as a function of the time or number of readings. In the same way, knowing the velocity and the spacing between axles, it is possible to define the ordinate of the influence line for each axle as a function of time, see Figure [2]-b. Considering the principle of superposition of effects, the theoretical bending moment is given by:

$$M_k(t_k) = \sum_{i=1}^{N} A_i I_i(t_k) \quad (3)$$

Where:

$M_k(t_k)$ is the theoretical bending moment at time *k*;

A_i is the load of the axle *i*;

$I_i(t_k)$ is the ordinate of the influence line to the axle *i* at time *k*.

The results collected from the structure's monitoring are obtained in function of time. By matching the readings of bending moment in the instant k as M_k^*, it is possible to settle the quadratic deviation function *E* between the theoretical value and the measured value of the bending moment using equation [4].

$$E = \sum_{k=1}^{t_f} \left[M_k(t_k) - M^*(t_k) \right]^2 \quad (4)$$

Where:

t_f is the vehicle's total passage time, or the total time of the signal time increments;

Figure 3 – Numerical model of the WOA 01 (half section)

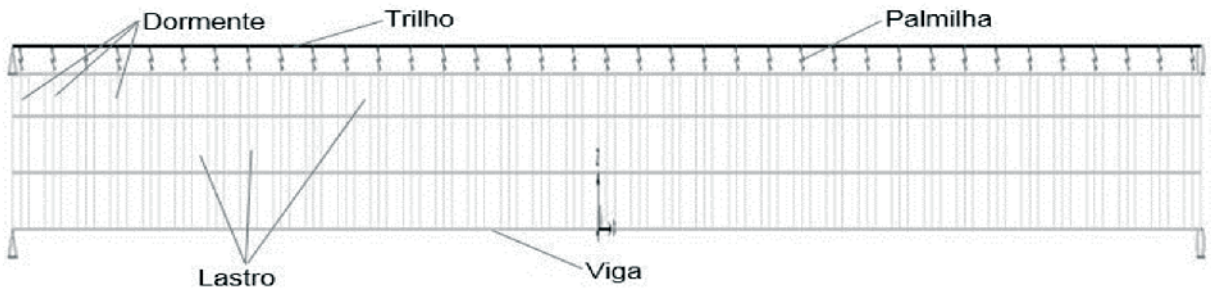

$M^*(t_k)$ is the bending moment at the instant *k*.
Since it is willing to calculate the loads, it is needed that the error related to the loads be minimized, verging zero. For this, the partial derivatives of *E* in relation to each load A_j are set equal to zero, and the matrices *[F]* and *{M}* are then obtained.

$$[F]=\left[F_{ij}\right]=\sum_{k=1}^{T} I_i(t_k)I_j(t_k) \quad (5)$$

$$\{M\}=\{M_j\}=\sum_{k=1}^{T} M^*(t_k)I_j(t_k) \quad (6)$$

Where:
$[F]$ is the matrix of the influence line of the bending moments;
$\{M\}$ is built with the bending moments calculated in function of the deformations measured and the influence lines;

T is the total number of instants of time after the reading analysis.
In matrix form, the axle loads, A, are given by equation [7]. The gross vehicle weight (GVW) is the summation of the vector {A}.

$$\{A\}=[F]^{-1}\{M\} \quad (7)$$

3. Implementation and numerical validation

Having the algorithm ready, it was needed to validate it, so a bidimensional numerical example was performed. The chosen structure was a reinforced concrete viaduct belonging to the Estrada de Ferro Carajás, managed by the minning company VALE, located near São Luís. The structure was modelled in finite elements using the software SAP2000® [5].
The analysis considered only half of the cross-section of the bridge due its symmetry, see Figure [4]-b, using beam, membrane and spring elements, see Figure [3].

Figure 4 – a) Overview of the viaduct over the CFN 1st crossing (Carvalho Neto et al (6)); b) Half cross-section of the viaduct

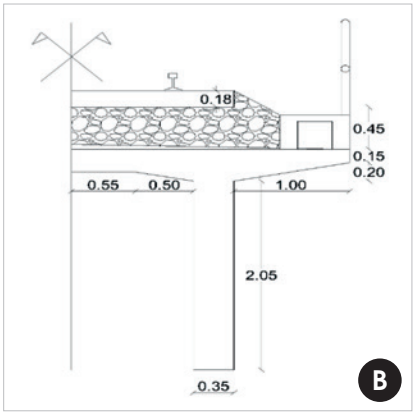

Table 1 – Natural frequencies obtained from the numerical model

Mode	Frequency (Hz)	Mode shape
1	8.42	Vertical flexure
2	30.21	Vertical flexure
3	36.23	Transversal flexure
4	61.88	Vertical flexure
5	82.63	Transversal flexure

3.1 Description of the viaduct

The viaduct over the CFN 1st crossing corresponds to the work of art number 01 (WOA 01) of the Carajás Railroad, located at the km 4+900. It is a reinforced concrete viaduct with 44.90 m long, constituted by an isostatic span of 18.00 m, a left abutment of 15.25 m and the right one measuring 11.65 m. In Figure [4]-a it is presented an overview of the structure and the cross-section used for data acquirement. Due the symmetry, it was adopted only half cross-section for the modeling in finite elements, as can be seen in the Figure [4]-b.

3.2 Modal analysis

In order to apply the B-WIM system, it is necessary to initially run a modal analysis of the viaduct to determine the modal parameters, which will help the modeling and application of the method.
Having the fundamental natural frequencies of the structure, it can be determined if the B-WIM is applicable, because the existence of regularly spaced axles may cause the phenomenon of resonance or excessive vibration in the structure, where the increasing of velocity is a basic factor for the growth of this frequency, as seen in equation [1].

The modal characteristics of the structure were determined and the first five natural frequencies, referring to the vertical and transversal flexure modes, are presented in Table [1].
Preliminary analysis were made aiming the detection of the most relevant vibration modes of the model, having as parameter the modal influence of the mass, once many modal shapes identified refer to the pads. Figure [5] shows the first two vibration modes obtained.

3.3 Determination of the influence line and the vehicle

For the implementation of the algorithm it was also needed to determine an influence line able to faithfully represent the numerical model and to build the vehicle with axles spacing and loads similar to the operational ones. Thus, it was developed an algorithm that generates linear functions that correspond to the passage of a vehicle in each node of the beam element representing the trail.
The algorithm works by loading the nodes with unitary forces and applying displacements in function of the velocity and the adopted increment. This way, the equivalent functions of these loads due the passage of the loads are obtained. The algorithm assigns the unitary loads through a vector with coefficients related to the axles of the locomotive and wagons, which use the weight variation of the axles.
This algorithm helps in the determination of the influence line in a numerical form, if applied as a vector of unitary coefficients.
Lastly, a time history analysis was performed using the direct linear integration method.

3.3.1 Influence line

The influence line of the bending moment was drawn for the cross-section where the strain-gages were installed, distant 1 meter from the mid-span to velocity of 1 m/s. After the analysis of the model, the results were processed and the influence line in space domain was obtained. Then, the polynomial coefficients used to represent the influence line were determined, see Figure [6].

Figure 5 – a) First vibration mode (f=8.42 Hz); b) Second vibration mode (f=30.21 Hz)

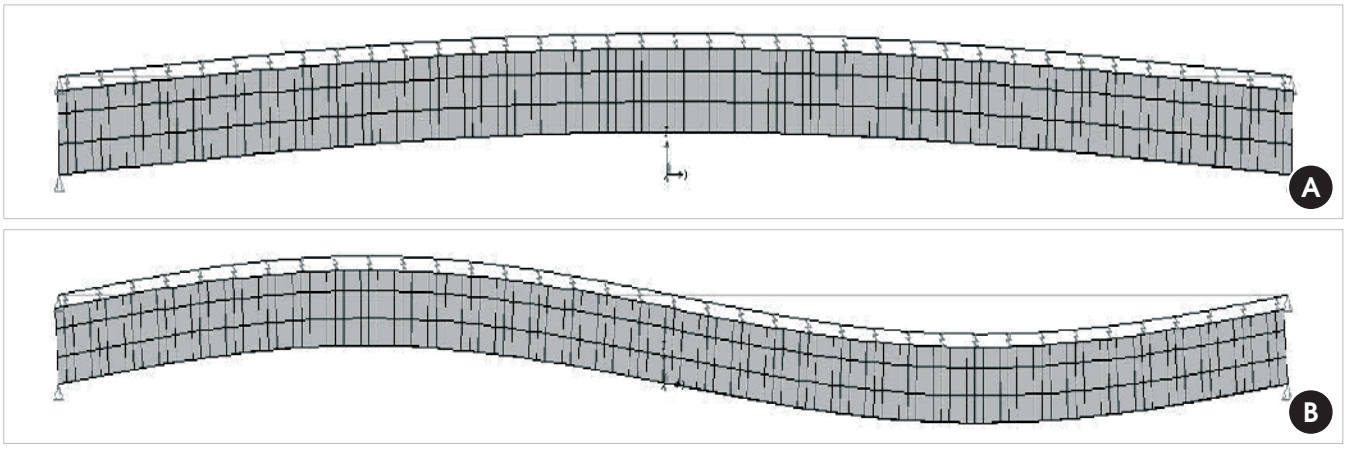

Figure 6– Influence line obtained and curve of the influence line determined

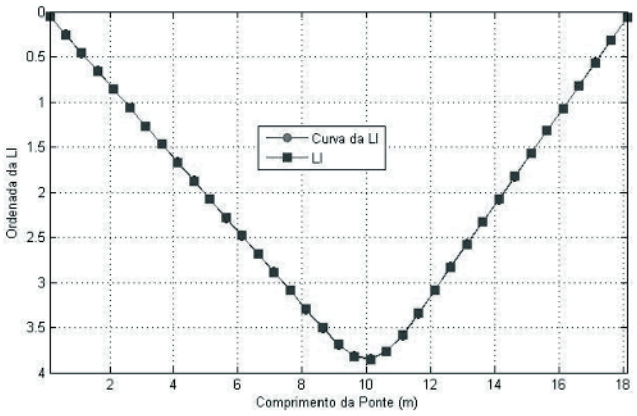

3.3.2 Vehicle

The simulations were made using 6 different velocities (1 m/s, 5, 10, 40, 60 and 80 km/h) for an arrangement of 2 locomotives and 4 wagons, see Figure [7], with axles weighing 300 kN and 325 kN, respectively. It was used the algorithm "Calcula_TimeHistory" to generate the corresponding functions and this way to load the nodes of the computational model in order to obtain a time series of the bending moments of the section equivalent from which was withdrawn at the influence line.

Once in possession of the time-histories, it is important to verify the difference between the natural frequencies and the static part of the response, since the frequencies related to the axles spacing must not be within the natural frequencies. Table [2] presents the maximum calculated frequencies for the adopted number of passages and, thus, it is concluded that there is no dynamic interference between the natural frequencies and the ones determined.

In Figure [8], the treated time history is presented in which a moving average of seventh order and a low-pass digital filter with threshold of 8 Hz was used, inferior to the first natural frequency (8.42 Hz).

3.4 Results

In possession of the bending moment's time-series and the influence line, the axle loads for the previously mentioned velocities were calculated (Figure [9]). For better analysis of the results, the mean errors for the axle loads (Figure [10]) and GVW (Table [3]) were calculated.

Table [3] presents the calculated values for gross vehicle weight (GVW), which achieved minimum differences in comparison with the vehicle's actual value (8800 kN), even in face of larger discrepancies between the axle loads. Regarding the axle loads of Figure [9], they presented a small variance in comparison with their real values, stressing that the results for a passage of the train for the velocities of 60 km/h and 80 km/h showed values around the actual ones.

The average error of the loads and the error of the total gross weight were calculated using the Equations [8] and [9], respectively.

In Figure [10], it is verified that the relative error is smaller for lower velocities due the reduced dynamic effects. For velocities up to 40 km/h, the maximum error reached 10 %, referring to the fourth axle of the first locomotive of the arrangement (2 locomotives and 4 wagons). The maximum relative errors found for 60 km/h and 80 km/h were 12 % and 18 %, respectively. From Figures [9] and [10], it is observed that the calculated axle loads were distributed unequally, producing average mean errors varying from 3.16% (1m/s) to 9.82 % (80 km/h). However, the achieved GVWs presented errors smaller than 1% for every velocity.

Figure 7 – Arrangement of 2 locomotives and 4 wagons adopted in the numerical example

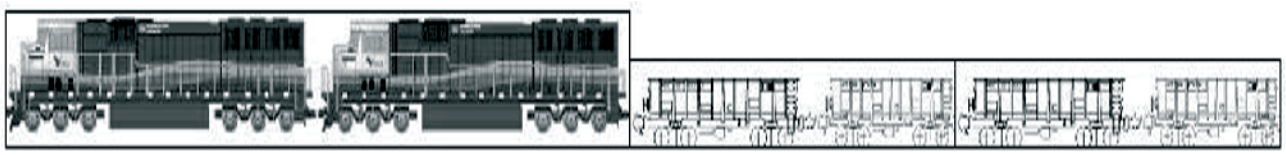

Table 2 – Frequencies related to the distance between axles for varying traffic velocities

	Frequencies (Hz)					
Vehicle	80 km/h	60 km/h	40 km/h	10 km/h	5 km/h	1 m/s
Locomotive	1.56	1.17	0.78	0.19	0.10	0.07
Wagon	4.15	3.11	2.07	0.52	0.26	0.19

Figure 8 – Time-histories of the bending moment in the girder: a) 1 m/s; b) 5 km/h; c) 10 km/h; d) 40 km/h; e) 60 km/h; f)80 km/h

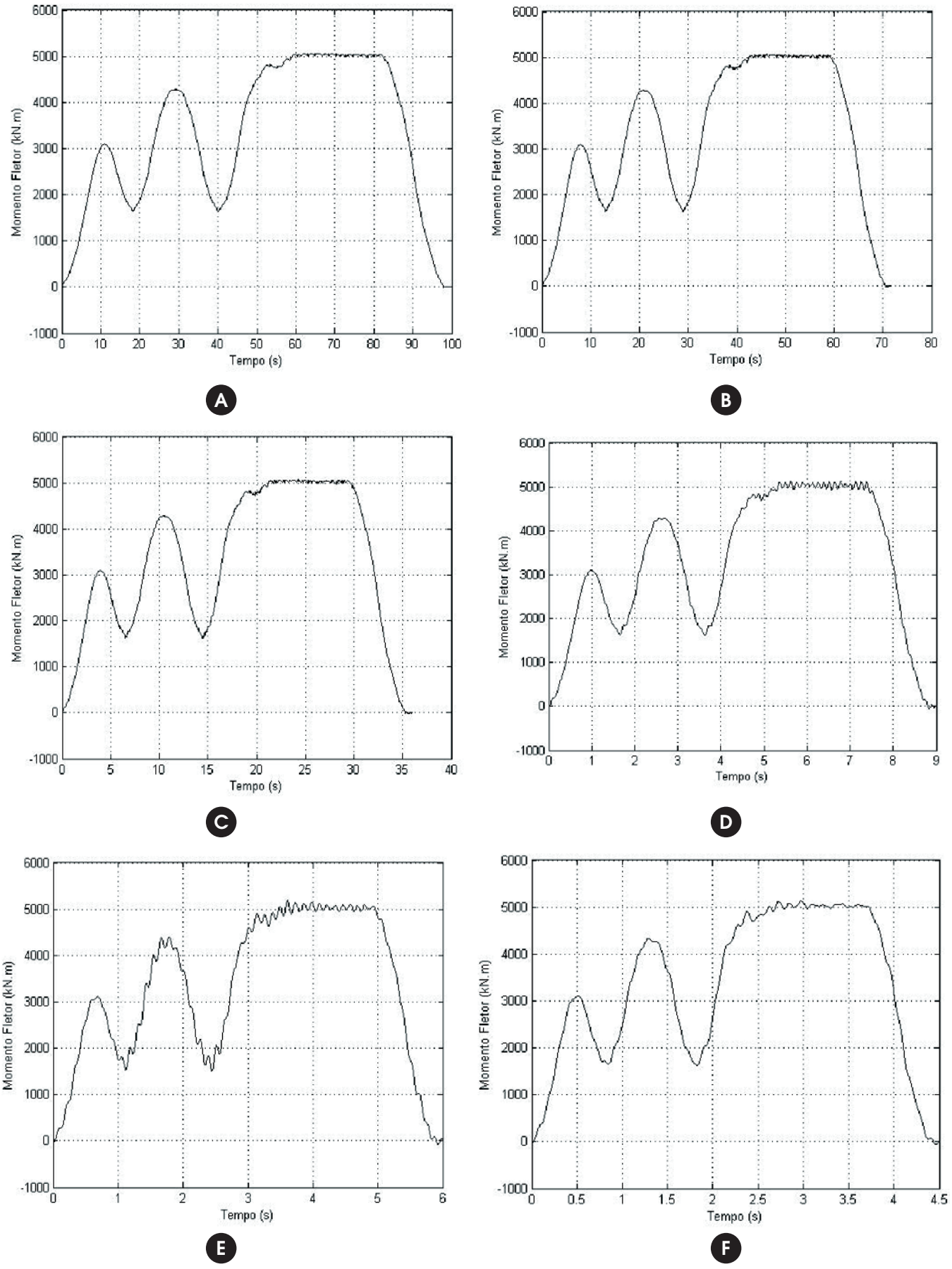

Figure 9 – Axle loads determined by the algorithm of Moses (1) for velocities: a) 1 m/s; b) 5 km/h; c) 10 km/h; d) 40 km/h; e) 60 km/h; f) 80 km/h. Values in kN

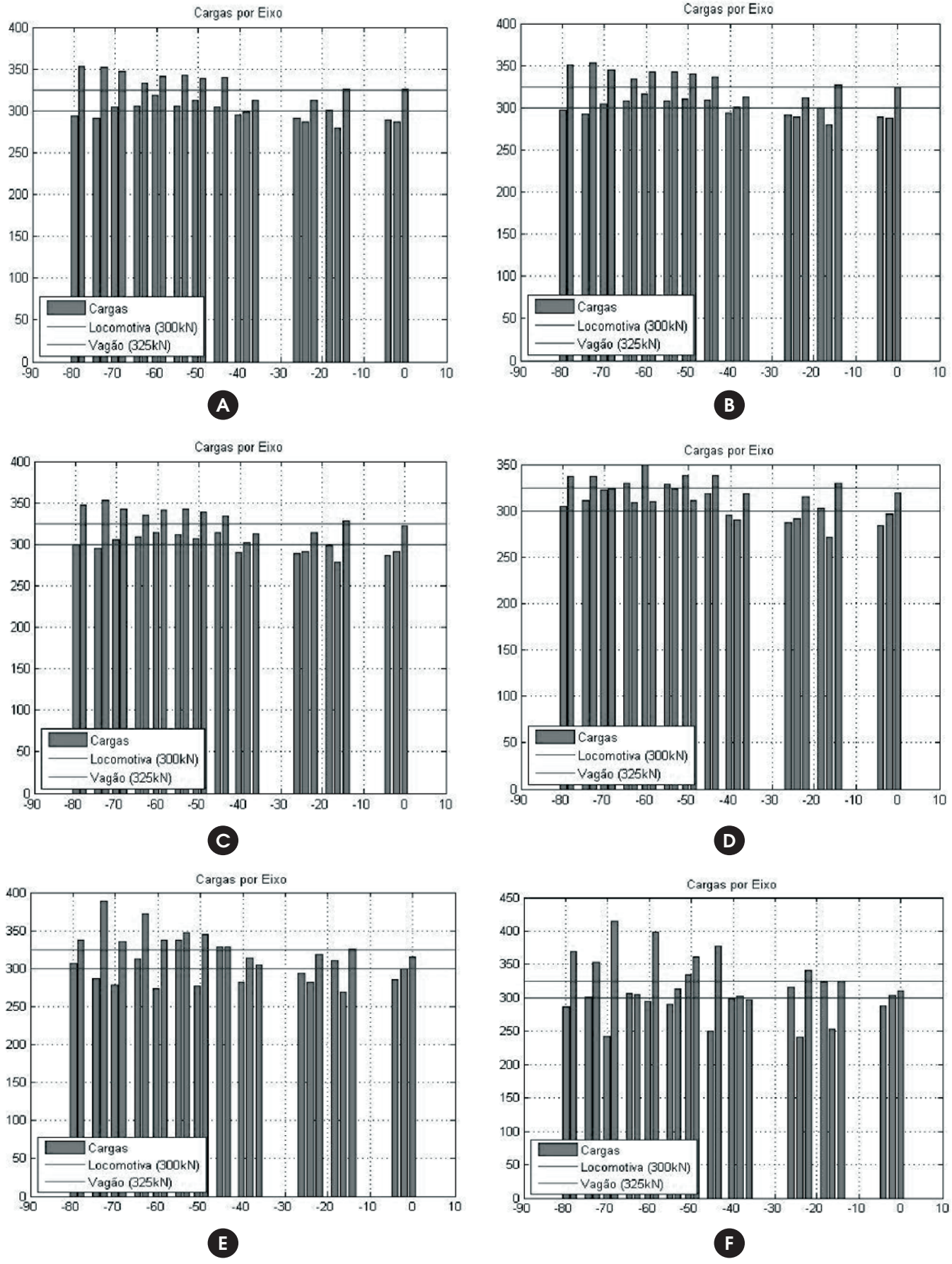

Figure 10 – Errors per axle determined for varying velocities: a) 1m/s; b) 5km/h; c) 10km/h; d) 40 km/h; e) 60 km/h; f) 80 km/h

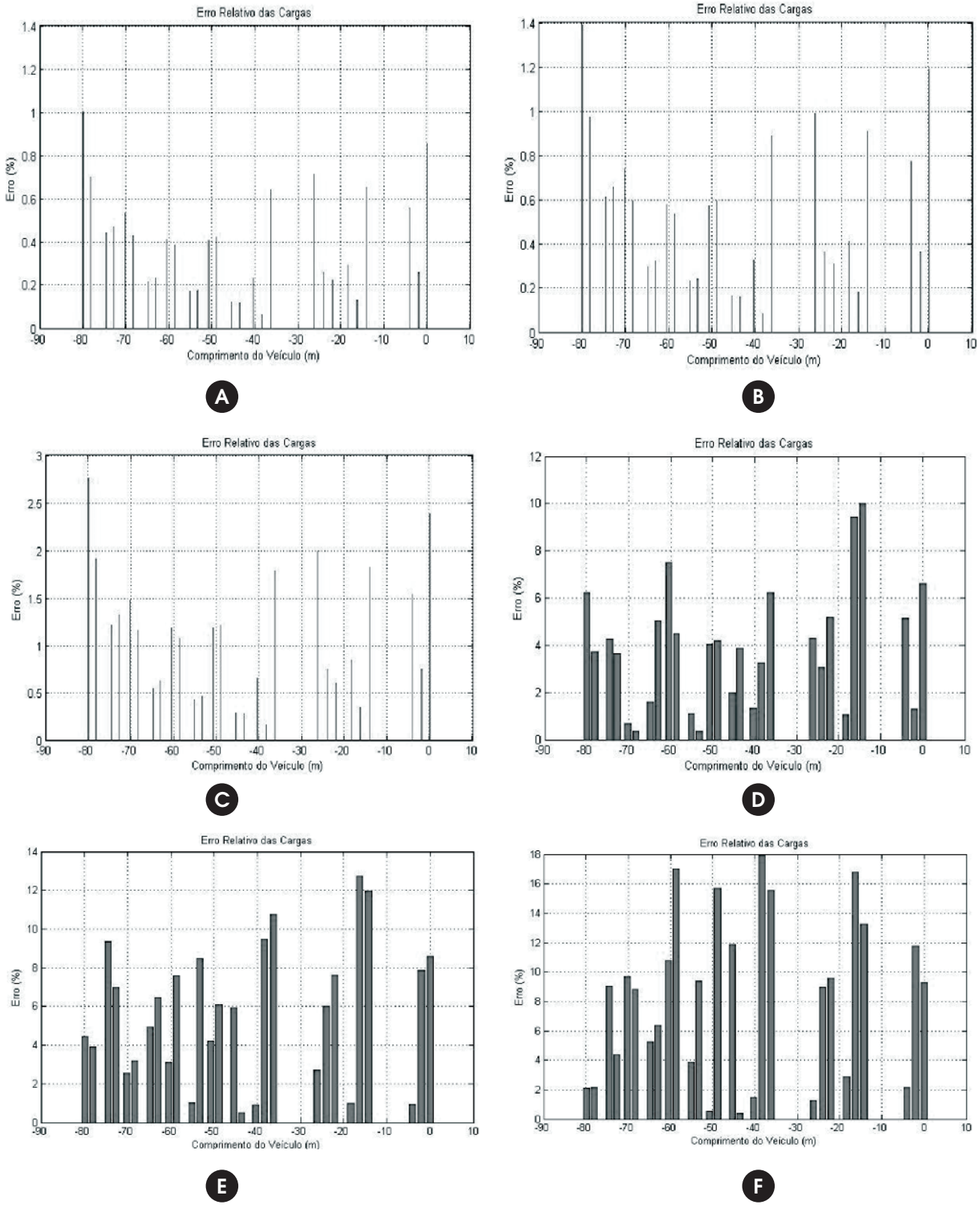

Table 3 – Total gross weight error and average axle load error for varying velocities

Total gross vehicle weight error and average axle load error (%)						
Error/Velocity	80km/h	60km/h	40/km/h	10km/h	5km/h	1m/s
GVW	0.05	0.05	0.06	0.07	0.08	0.11
Average	9.82	6.24	4.73	4.44	4.22	3.16

4. Characterization and weighing of a locomotive from experimental data

After benchmarking the algorithm, a field trip was done to weigh and characterize the train from experimental data. The actual structure used in the procedure was the same one used in the numerical model, see Figure [4]-a.

4.1 Instrumentation of a viaduct

The instrumentation of the viaduct was made near its midspan and at the expansion joints, see Figure [11], located at its entrance and exit. Due the presence of a girder at midspan, two strain-gages were installed far 1m from it in the longitudinal direction, in the lower reinforcement and over the viaduct, directly on the concrete surface, see Figure [11]. The models were KFG, from KYOWA, which are proper for outdoor use.

In order to fix the strain-gage on the concrete, it was necessary to remove parts of the mortar layer and ballast of the railroad, and to fix another on the lower reinforcement, part of the concrete was removed.

4.2 Data acquisition

The ADS-2000® system was used to collect the data from the strain-gages. An ethernet network was set up between the system and a computer, see Figure [12]. The data was collected under a 100 Hz rate.

Figure 11 – Strain-gages fixed on the trails and girders

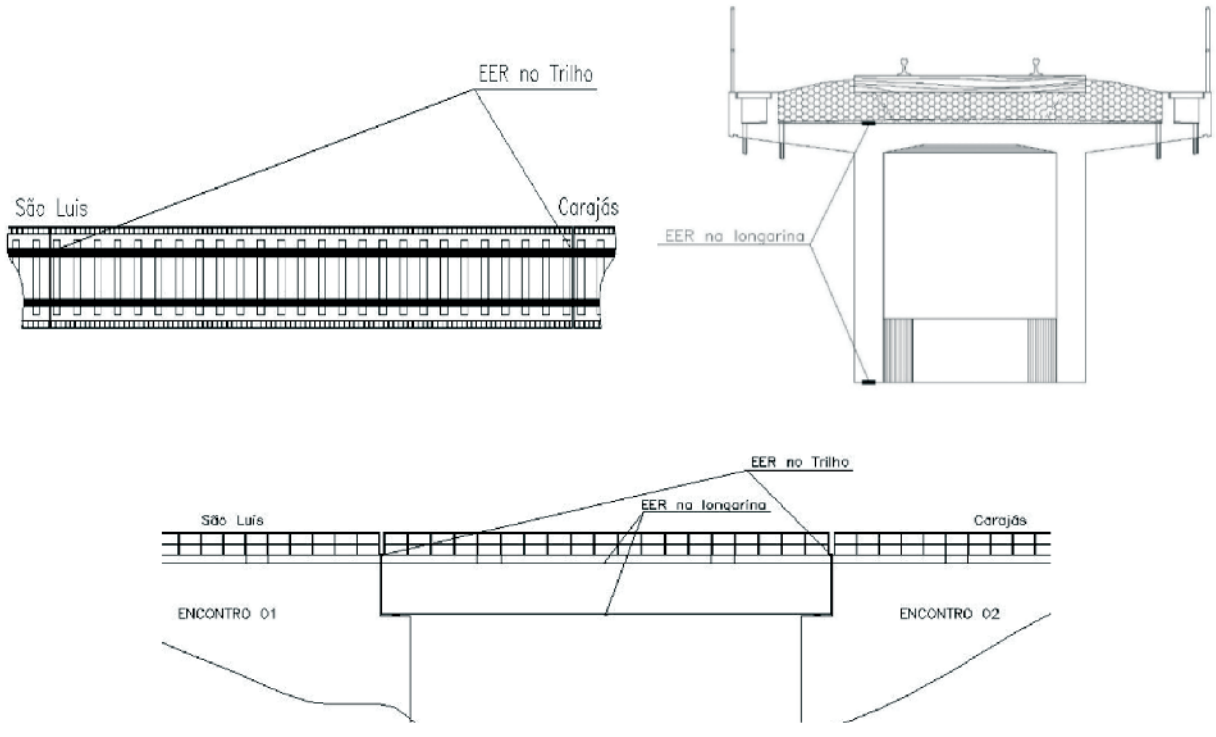

Figure 12 – Draft of the data acquisition's setup

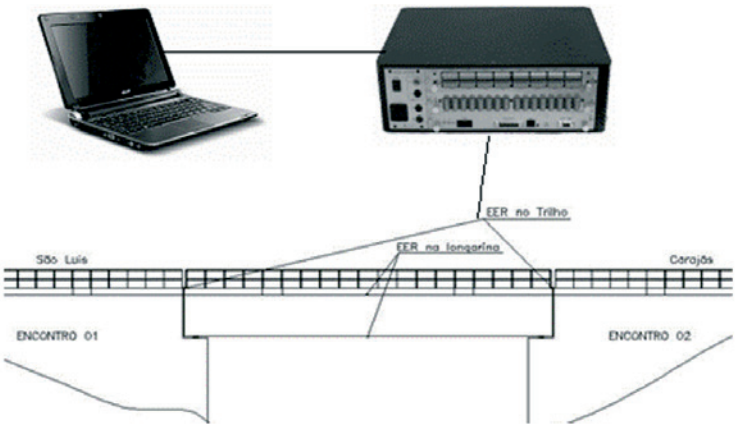

4.3 Peak Detection

The peak detection is a crucial step for the definition of the vehicle's geometry. The passage of a vehicle's axle over an instrumentalized section creates a peak in the time-series of deformation, which allows the knowledge of the quantity and spacing of axles. Thus, it is needed to distinguish what is a peak. For that, it was used the algorithm "peakfinder" (Yoder [7]), developed in MATLAB language (MATLAB [8]), which has inputs:

a) The time-series vector;
b) A threshold;
c) An extreme: 1 when searching for maximum, -1 when searching for minimum.

The outputs are the peak values and their respective time of

Figure 13 – Maximum detected in the time-series of deformation of the trail under the passage of a locomotive a) Strain-gage installed on São Luis' side; b) Strain-gage fixed on the Carajás' side

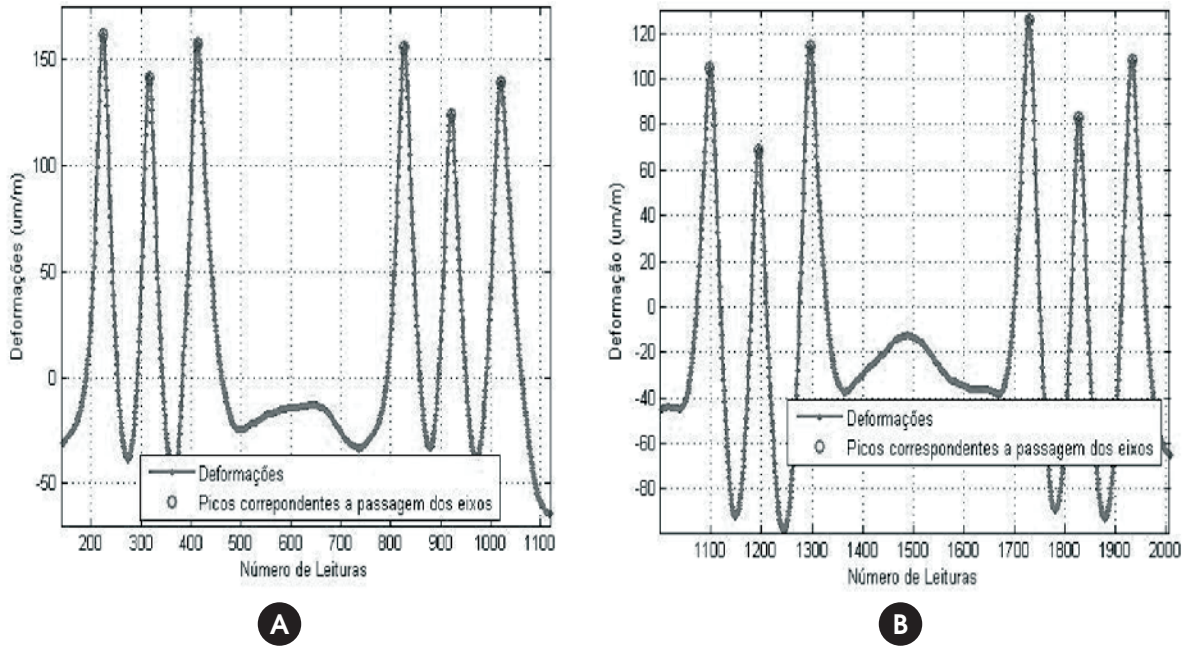

Figure 14 – Speed per axle obtained from a deformation time-series due the passage of a DASH-9 locomotive at midspan

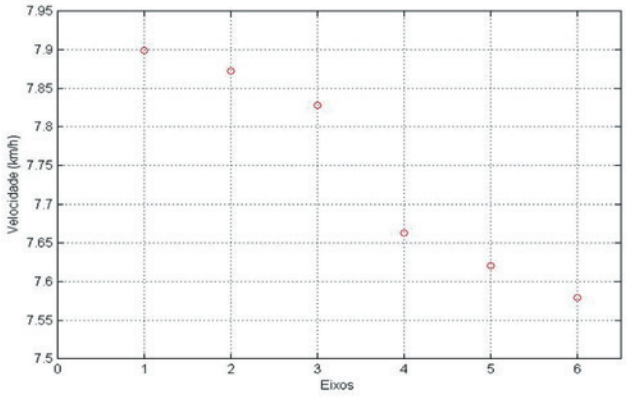

occurrence (in seconds). Figure [13] presents the peaks, or axles, obtained from the experimental data. It is clear the presence of six peaks, corresponding to the passage of the six axles of the locomotive over the trails instrumentalized on the sides of São Luis and Carajás, respectively.

The time interval between the passages of the same axle over distinct sections is calculated based on the variation of the reading numbers among the samples divided by the sampling rate of the data acquisition, fixed in 100 Hz.

4.4 Calculation of axles' speed and spacing

The speed calculation per axle was made using the Rectilinear Motion formulation. Then, the average speed of the locomotive was achieved, see Figure [14].

The average speed obtained was 7.74 km/h for the analyzed signal. Using the average speed and the maximum peaks, it was possible to calculate the locomotive axle spacing. In Table [4], the values of the calculated axle spacing and their actual values are presented. The values obtained are close to the actual ones. To perform this analysis, it were used the axle spacing of the locomotive type DASH-9, the most used by the VALE mining company, although it also works with locomotives with varying axle spacing.

4.5 Obtaining the Bending Moment's Time-Series

The obtainment of the bending moment's time-series was performed using constitutive models for the bridge materials and the Navier-Bernoulli Hypothesis.

4.5.1 Constitutive models

The deformation's time-series provided by the strain-gages must be converted in bending moment's time-series. For that, it was necessary to study the mechanical behavior of reinforced concrete and to define the relations between its stresses and deformations. These relations were defined based on the constitutive models for the steel and concrete and the Navier-Bernoulli Hypothesis.

Table 4 – Comparison of actual and calculated axle spacing

Real distance (m)	Obtained distance (m)	Difference (m)
0	0	0
2.0193	2.0324	0.0131
2.1209	2.1198	0.0010
10.0838	9.0475	1.0362
2.1209	2.0542	0.0666
2.0193	2.1854	0.1661

4.5.1.1 Constitutive models for the concrete

There are several models to represent the mechanical behavior of concrete, consisting in relations between its stresses and strains. The linear-elastic model is the simplest. The plastic model is another very used one, been characterized by the occurrence of residual deformations when unloaded. In this paper, it were adopted elastic non-linear models.

4.5.1.1.1 Constitutive model for the concrete (ABNT NBR 6118 [9])

a) Compression

Under compression, to analyze the ultimate strength limit, it may be used the idealized stress-strain diagram presented in Figure [15].

The constitutive equation for the concrete under compression is presented in equation [8].

Figure 15 – Idealized Stress-strain diagram (ABNT NBR 6118 (9))

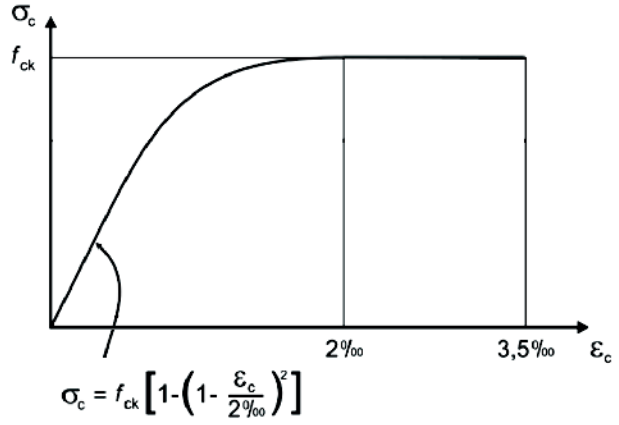

$$\sigma_c = 0{,}85\, f_{ck}\left[1-\left(1-\frac{\varepsilon_c}{0{,}002}\right)^2\right] \text{ if } 0=\varepsilon_c=0.002$$

$$\sigma_c = 0{,}85\, f_{ck} \text{ if } 0{,}002<\varepsilon_c=0.0035$$

$$\sigma_c = 0 \text{ if } \varepsilon_c>0.0035 \qquad (8)$$

Where:
σ_c Is the compression stress;
f_{ck} Is the compression's ultimate strength of the concrete obtained from specimen compression tests;
ε_c Is the concrete's strain.

b) Tension
Under tension, the brazilian standard considers the strength of the concrete equals 0 (zero), when cracked. In the algorithm, the main girders were considered all cracked along their longitudinal direction, causing the concrete's resistance in tension to be null.

4.5.1.1.2 Constitutive models (Collins and Mitchell [10])

a) Compression
The model proposed presents a family of curves for the behavior of concrete under compression and tension (Collins and Mitchell [10]). The performance of the concrete under compression is described by the equation [9].

$$\sigma_c = f_{ck}.\left[\frac{n\left(\frac{\varepsilon_c}{\varepsilon_{ck}}\right)}{n-1+\left(\frac{\varepsilon_c}{\varepsilon_{ck}}\right)^{nk}}\right] \text{ if } \varepsilon_c=0 \qquad (9)$$

Where:
σ_c Is the compression stress;
f_{ck} Is the compression's ultimate strength of the concrete obtained by sample tests;

$n = 0{,}8+\frac{f_{ck}}{17}$ With fck in MPa;

ε_c Is the concrete's strain;

$\varepsilon_{ck} = \frac{f_{ck}}{E_c}.\frac{n}{n-1}$ Is the deformation of the concrete corresponding to its maximum stress;

$k = 0{,}67+\frac{f_{ck}}{62}\geq 1$ With fck in MPa.

b) Tension
The curve that represents the concrete behavior under tension simulates the resistance contribution between cracks ("tension-stiffening" effect). When over the cracking strain (ε_{cr}), the concrete still presents strength due the bond between its intact portions and the reinforcement, which transfers to the concrete its stress through radial forces. The post-cracking response of the tensioned material is considered in a way that the axial load is shared by both concrete and steel along the length of the element, (Rêgo [11]). The tension stress in the reinforcement will be greater in the cracked section than in its neighborhood, once the strees in the concrete is null on that section. In the traditional processes, this superposition is neglected, than the reinforcement's response is taken as if it was uncovered in its extension. The model estimates the average contribution of the concrete in tension, following many other papers, which also propose constitutive equations based on experimental results.
The performance of the concrete under tension is described by the equation [10].

$$\sigma_c = \frac{\alpha_1\alpha_2}{1+\sqrt{500.(-\varepsilon_c)}} \text{ if } \varepsilon_c<0 \;\&\; \varepsilon_c<\varepsilon_{cr}$$

$$\sigma_c = E_c.\varepsilon_c \text{ if } \varepsilon_c<0 \;\&\; \varepsilon_c=\varepsilon_{cr} \qquad (10)$$

Where:
σ_c Is the compression stress;
ε_c Is the concrete's strain;

$E_c = 3320+\sqrt{f_{ck}}+6900$, In MPa, is the elastic modulus proposed;
α_1 Is a coefficient relative to the bonding between the reinforcement and the concrete (equals 1.0 for ribbed, 0.7 for smooth bars or strands and 0 for loose bars);
α_2 Is a coefficient relative to the type of load (equals 1.0 for monotonic loading of small duration and 0.7 for cyclic or long duration loading).

4.5.1.2 Constitutive model for the steel

In reinforced concrete structures, the reinforcement is used to contribute only for axial loading, and so it is only needed to know the uniaxial properties of the material in order to properly model it. The presence of a constant yielding stress in the stress-strain curve depends on the manufacturing process of the steel. The present model possession it (Teixeira [12]).

4.5.1.2.1 Perfectly elastoplastic model

The perfectly elastoplastic behavior is presented in Figure [16]. The relation is given by the equation [11].

$$\sigma_s = E_s.\varepsilon_s \text{ if } \varepsilon_s=\varepsilon_y$$

$$\sigma_s = f_y \text{ if } \varepsilon_s=\varepsilon_y \;\&\; \varepsilon_s=\varepsilon_u$$

$$\sigma_s = 0 \text{ if } \varepsilon_s=\varepsilon_u \qquad (11)$$

4.5.1.3 Experimental load acquisition

To determine the bending moment's time-series, it was performed the methodology based on the Navier-Bernoulli beam hypothesis,

Figure 16 – Steel's stress-strain diagram in reinforced concrete

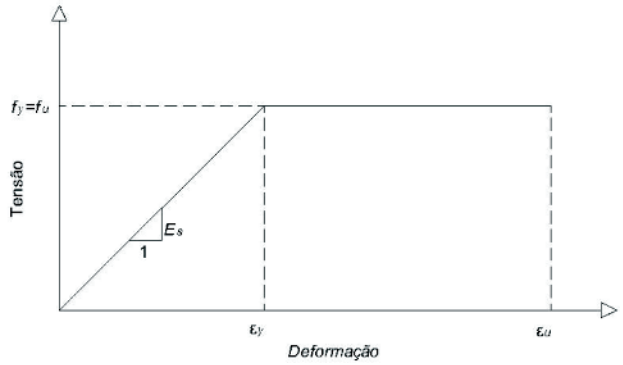

which considers that the initial parallel sections of the beam remain parallel after the load is applied and normal to the beam's axis (Pureza [13]). Adopting the joint behavior of steel and concrete, then the strain in some point of the section is equal for both materials. Using this result and by assigning the centroid (centre of gravity) of the section as a fixed reference line, it is possible to determine the deformation in every point of the section, see Figure [17]. For the evaluation of the concrete, it was used the model beams with section discretization in fiber, consisting on the discretization of the cross-section in fibers parallel to a reference axis of constant thickness, see Figure [18], considering that the strain on every point of a fiber is constant. The stresses were obtained from the constitutive material equations previously described. With the stress in each fiber and reinforcement layer *j*, we are able to calculate the loads in every instant *i*, and the bending moment's time-history will be the summation of the bending moments of each fiber and reinforcement layer.

$$M_{i,j} = A_{f_j} . \sigma_{f_{i,j}} . y_{f_j} \quad (12)$$

Where:
A_f Is the area of the fiber;

Figure 17 – Strain distribution along the height of the section (Pureza, (13))

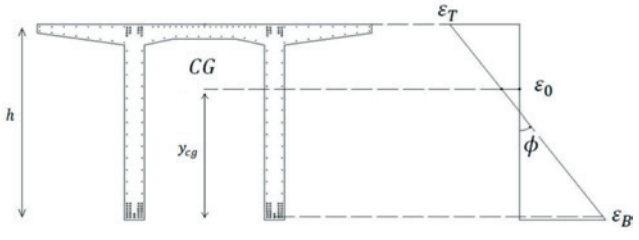

Table 5 – Comparison of calculated and actual "GVW" of the locomotive

PBT real	PBT (NBR 6118/2007 (9))	PBT (Collins & Mitchell (10))
1800 kN	1425.57 kN	1768.61
Erros	20.80%	1.74%

σ_f is the stress on the fiber;
y_f is the height of the fiber *j*
Figure [19] presents the flowchart for the calculation and storage of the loads used.
Figure [20] presents the bending moments' time-series from the adopted constitutive equations.

4.6 Axle loads and gross-vehicle-weight

Having all the inputs, the locomotive's axle loads were calculated using both constitutive equations. Due the absence of an experiment with a known weight vehicle, it was adopted an influence line for a 1 m/s speed, once it causes a negligible dynamic effect.
In two occasions, negative axle loads were found. Even when considering their absolute values, they present great distance from the actual ones (300 kN/axle). By observing Table [5], it is concluded the calculated gross weight are much closer to its actual values when the constitutive equations are used (Collins and Mitchell [10]).

Figure 18 – Cross-section in fibers and reinforcement

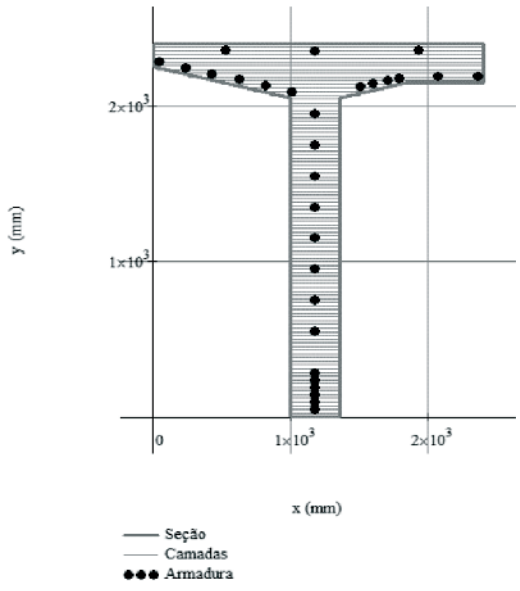

Figure 19 – Flowchart of the calculation and storage of the experimental loads

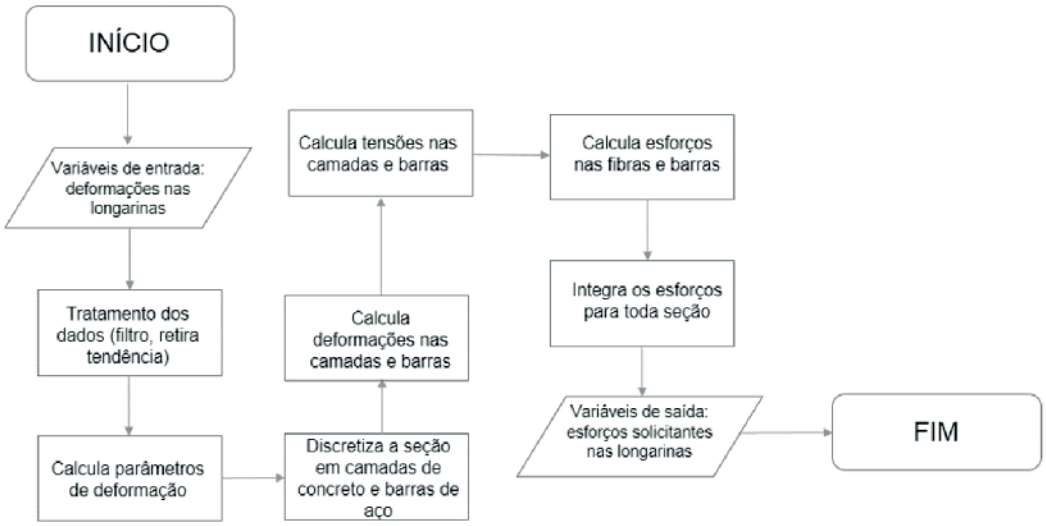

5. Conclusion

The axle detection proved very effective, easily identifying the passage of all the axles expected from the time-series.

The bending moments time-series allow the evaluation of the performance of the constitutive equations adopted for the concrete. The best results were achieved using the constitutive model (Collins and Mitchell [10]), proving that it is the most appropriate model for the present problem.

The algorithm used for the identification of axle loads revealed itself very sensitive, once small variations in the inputs lead to large output errors, leading to an average variation of 7.11% for axle loads and 0.03% for the GVW in the numerical example. For the experimental case, the results vary greatly from the actual values, even reaching negative values, but the total gross weight achieved presented an error of only 1.74%.

6. Acknowledgement

The authors wish to express their gratitude to PROPESP/UFPA, FADESP and CNPq for their financial support.

Figure 20 – Bending moments' time-series at midspan. a) Using the equation proposed by ABNT NBR 6118 (9); b) Using the equation proposed (Collins e Mitchell (10))

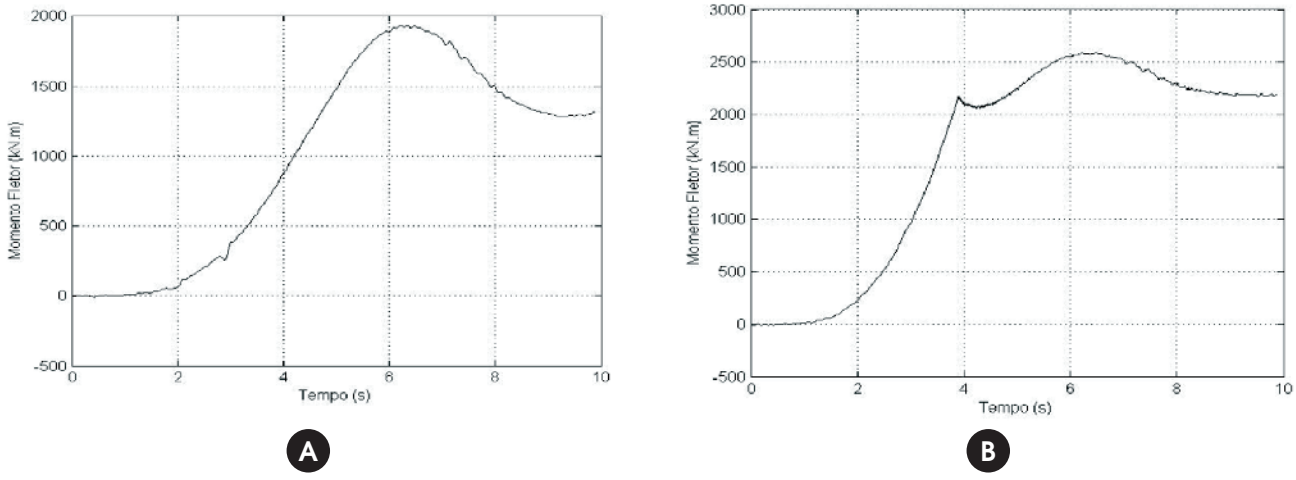

7. References

[1] MOSES, F. Weigh-in-Motion System Using Instrumented Bridges. Transportation Engineering Journal, v. 105, n. TE3, 233-249, May 1979.

[2] ZNIDARIC, A.; BAUMGÄRTNER, W. Bridge Weigh-in-Motion Systems – an Overview. In: PRE-PROCEDINGS OF 2nd EUROPEAN CONFERENCE ON WEIGH-IN-MOTION OF ROAD VEHICLES, 1998, Lisbon.

[3] QUILLIGAN, M. Bridge Weigh-In-Motion - Development of a 2-D Multi-Vehicle Algorithm. 2003. 162 f. Licentiate Thesis – Department of Civil and Architectural Engineering, Structural Design and Bridge Division, Royal Institute of Technology, Stockholm, 2003.

[4] PIMENTEL, R. M. C. M. Caracterização do Tráfego Ferroviário e dos seus Efeitos em Pontes de Pequeno Vão. 2008. 188 f. Dissertação (Mestrado em Estruturas de Engenharia Civil) - Faculdade de Engenharia, Universidade do Porto, Porto, 2008.

[5] SAP2000 Advanced 14.1.0 – Structural Analysis Program, ©1976 – 2009, Computers and Structures, Inc, University Ave. Berkeley, CA, EUA.

[6] CARVALHO NETO, José A. de; PUREZA, Dennis Q.; COSTA, Fábio I. B. da; VELOSO, L. A. C. M.; SAMPAIO, Regina A. C.; RODRIGUES Jr, Sandoval J.; BARICHELLO, César V. M.; MOREIRA, Jouberson L. da R. Desenvolvimento de Metodologia para Avaliação da Integridade Estrutural de Pontes e Viadutos Ferroviários ao Longo da Estrada de Ferro Carajás. Pará: NICAE-UFPA, 2009. 143 p. (Relatório Técnico Segunda Etapa: Obra de Arte Especial n. 01 - Viaduto sobre a Primeira Travessia).

[7] YODER, N. PeakFinder. http://www.mathworks.com, acessado no dia 19 de Abril de 2013.

[8] MATLAB - Matrix Laboratory R2012b 8.0.0.783 ©1984 - 2012, Mathworks, Inc, 3 Apple Hill Drive, Natick - MA, EUA.

[9] ASSOCIAÇÃO BRASILEIRA DE NORMAS TÉCNICAS. NBR 6118: Projetos de Estruturas de Concreto Armado. Rio de Janeiro, 2007.

[10] COLLINS, M. P.; MITCHELL, D. Prestressed Concrete Structures. New Jersey, Prentice Hall, 1991.

[11] RÊGO, G. M. Desempenho dos Modelos da NBR 6118 para Análise de Vigas Contínuas em Concreto Armado. (Dissertação de Mestrado). Programa de Pós-graduação em Engenharia Civil, Universidade Federal de Pernambuco, Recife, 2005.

[12] TEIXEIRA, Ritermayer M. Estudo Teórico-Experimental do Comportamento Estrutural de uma Ponte Ferroviária em Concreto Armado. 2009. 199 f. Dissertação (Mestrado em Engenharia Civil) – Coordenação dos Programas de Pós-Graduação de Engenharia, Universidade Federal do Pará, Belém, 2009.

[13] PUREZA, Dennis Q., Avaliação de Segurança de Longarinas de Pontes Ferroviárias em Concreto Armado a partir de Dados Experimentais. 2013. 71 f. Dissertação (Mestrado em Engenharia Civil) – Coordenação dos Programas de Pós-Graduação de Engenharia, Universidade Federal do Pará, Belém, 2013.

[14] ASSIS, W.S.; TRAUTWEIN, L. M.; BITTENCOURT, T. N.; CONCEIÇÃO NETO, A. P. Structural health monitoring of a steel railway bridge on the river Suaçuí. In: IABMAS 2012 - 6th International Conference on Bridge Maintenance, Safety and Management, Stresa - Itália. Bridge Maintenance, Safety and Management. Leiden - Holanda: CRC Press, 2012. v. 1.

[15] CHOPRA, Anil K. Dynamics of Structures: theory and applications to earthquake. Englewood Cliffs: Prentice Hall, 1995.

[16] CLOUGH, Ray W.; PENZIEN, Joseph. Dynamics of Structures. Berkeley: Computers & Structures, 2003.

Volume 8, Number 4 (August 2015) p. 507-528 • ISSN 1983-4195
http://dx.doi.org/10.1590/S1983-41952015000400006

REVISTA IBRACON DE ESTRUTURAS E MATERIAIS
IBRACON STRUCTURES AND MATERIALS JOURNAL

Finite element analysis of composite concrete-timber beams

Análise de vigas mistas de concreto e madeira pelo método dos elementos finitos

N. C. S. FORTI [a]
nadia.cazarim@puc-campinas.edu.br

T. L. D. FORTI [b]
forti@simworx.com.br

A. E. P. G. A. JACINTHO [a]
anajacintho@puc-campinas.edu.br

L. L. PIMENTEL [a]
lialp@puc-campinas.edu.br

Abstract

In the search for sustainable construction, timber construction is gaining in popularity around the world. Sustainably harvested wood stores carbon dioxide, while reforestation absorbs yet more CO2. One technique involves the combination of a concrete slab and a timber beam, where the two materials are assembled by the use of flexible connectors. Composite structures provide reduced costs, environmental benefits, a better acoustic performance, when compared to timber structures, and maintain structural safety. Composite structures combine materials with different mechanical properties. Their mechanical performance depends on the efficiency of the connection, which is designed to transmit shear longitudinal forces between the two materials and to prevent vertical detachment. This study contributes with the implementation of a finite element formulation for stress and displacement determination of composite concrete-timber beams. The deduced stiffness matrix and load vector are presented along to numerical examples. Numerical examples are compared to the analytical equations available in Eurocode 5 and to experimental data found in the literature.

Keywords: composite structures, finite element method and sustainable structures.

Resumo

A madeira tem se destacado na produção de edificações sustentáveis, principalmente pela possibilidade de emprego de madeiras provenientes de florestas plantadas. A combinação de vigas de madeira com um tabuleiro de concreto armado ligados entre si por conexões flexíveis é uma alternativa que traz aumento de rigidez à estrutura, ameniza problemas de durabilidade, quando exposta às intempéries, e melhora seu desempenho acústico, se comparada à uma estrutura em madeira. As estruturas mistas são constituídas pela associação de materiais com diferentes propriedades mecânicas e seu desempenho mecânico depende da eficiência da ligação entre eles. Os conectores flexíveis são responsáveis pela transmissão de forças de cisalhamento entre os dois materiais e por evitar o desprendimento vertical. Esta pesquisa desenvolveu e implementou uma formulação de elementos finitos para cálculo dos esforços internos da estrutura mista de concreto e madeira. A matriz de rigidez e o vetor de carga deduzidos são apresentados juntamente com exemplos numéricos e seus resultados são comparados com as equações analíticas do Eurocode 5 e resultados experimentais da literatura.

Palavras-chave: estruturas mistas, elementos finitos e estruturas sustentáveis.

[a] *School of Civil Engineering - PUC Campinas, Campinas, SP, Brasil;*
[b] *Simworx Engenharia, Pesquisa e Desenvolvimento, Campinas, SP, Brasil.*

Received: 03 Sep 2014 • Accepted: 22 May 2015 • Available Online: 7 Aug 2015

1. Introduction

Composite structures combining materials with different mechanical properties offer an alternative to the civil construction industry. The technique provides reduced costs, environmental benefits and a better acoustic performance when compared to timber structures, while maintaining structural safety.

Concrete-timber composite systems may be applied to the construction of bridges, improving the bridge stiffness, resulting in smaller displacements and increasing natural frequencies of vibration.

The deck floor is composed of a concrete slab connected to timber beams aiming for the two materials to work together. The level of stress transfer between the concrete slab and the timber beam defines the mechanical behavior of the composite structure. It may be considered as a monolithic structure, when there is no slip in the region of contact, or it may behave as a non-monolithic structure when relative longitudinal displacement is observed.

The concrete slab protects the timber beams against direct weathering, surface abrasion and fire, improves the vibration performance and its maximum load when compared to timber bridges. The maximum load may increase by a factor of the order of two and the stiffness by three or four times according to CECCOTTI [1]. The relative lightness of composite materials and the possibility of using glued laminated timber (GLULAM) are factors that contribute to its prefabricated production.

1.1 Connection systems for concrete-timber composite structures

TARANTINO and DEZI [2] describes the necessity of studying the connection systems, which are responsible for transmitting the longitudinal shear forces in the interface of the two combined materials along the length of the beam.

Analyzing the connection of timber components, RACHER [3] highlights the major importance of the connection system, since its behavior directly affects the distribution of forces in the components and, as a consequence, in the structure deformations.

According to SORIANO [4] the connection system may be characterized as rigid or semi-rigid (flexible), Figure [1]. An example of rigid connection is the use of epoxy structural adhesive throughout the entire contact surface between the two materials, GIRHAMMAR and GOPU [5]. The rigid connection consists of the full integration of the cross section and the structure behaves as a monolithic structure. Studies developed in Brazil, by directly gluing timber beams to structural elements of reinforced concrete, were presented by NICOLAS [6]. SORIANO [4] also tested T-shaped timber-concrete beams, where the timber web was glued to the concrete slab.

In the semi-rigid connection system, the attachment between the two materials may be done using steel pins, nails, screws, bolts or metal profiles. The semi-rigid connection performs a partial interaction of the cross section, with a relative displacement (slip) between the two materials.

1.2 Models for the analysis of composite beams

The main mathematical models for describing the mechanical behavior of composite structures proposed in the literature are based on the equilibrium equations and on energy principles. Unlike concrete-steel composite structures, there is insufficient standard specification for concrete-timber structures. For concrete-steel structures, it can be cited the BS 5400 [7] or the Brazilian NBR8800/02 [8]. However, there is no Brazilian standard regarding the design of concrete-timber structures. An international standard that can be cited is the EUROCODE 5 [9].

1.2.1 The EUROCODE 5 model for the analysis of composite beams

Both the EUROCODE 5 [9] and the DIN 1052 [10] consider the flexibility of the connection system, and the relative displacement between the materials, by adopting an effective bending stiffness parameter $(EI)_{ef}$ which is calculated according to Equation [1]. Equation [1] is a function of the shape of the cross section, the Young's modulus of the materials, the spacing of connectors and its slip modulus.

$$(EI)_{ef} = E_c I_c + y_c E_c A_c a_c^2 + E_w I_w + y_w E_w A_w a_w^2 \quad (1)$$

In Equation [1] E_c, E_w, I_c, I_w, A_c and A_w are Young's modulus, the moment of inertia and the cross section areas of the concrete

Figure 1 – Vertical displacement of a composite beam

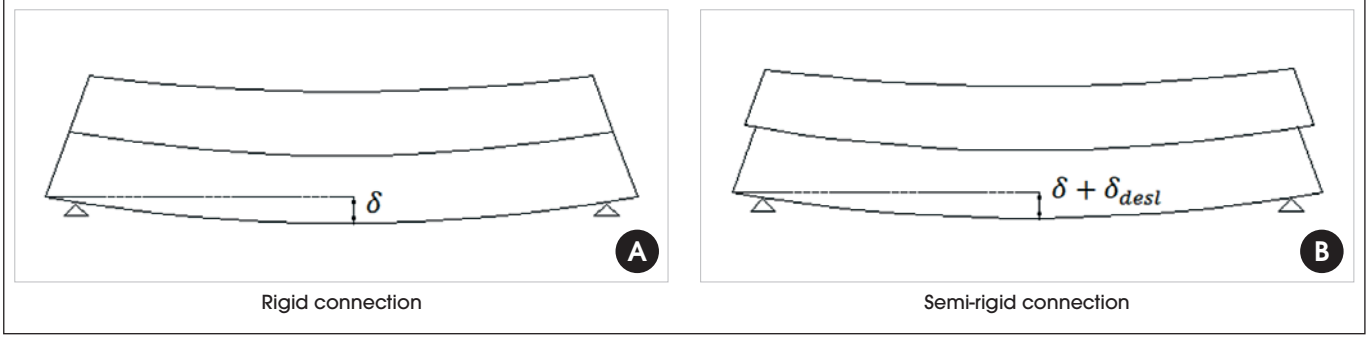

Rigid connection

Semi-rigid connection

Figure 2 – Cross section of a T-shaped composite beam and normal stresses on bending. Source: adapted from the EUROCODE 5 (9)

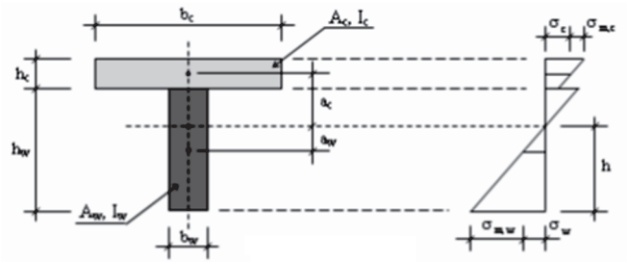

and timber elements respectively; y_c is the partial factor of the slab, calculated according to Equation [2]; $y_w = 1,0$ is the partial factor of the web; a_c and a_w are the distances indicated in Figure [2] calculated by Equations [3] and [4]; l is the length of the beam, s is the spacing of connectors and K is the connector slip modulus.

$$y_c = \left(1 + \frac{\pi^2 E_c A_c s}{K \cdot l^2}\right)^{-1} \quad (2)$$

$$a_c = \frac{(h_c + h_w)}{2} - a_w \quad (3)$$

$$a_w = \frac{y_c E_c A_c (h_c + h_w)}{2(y_c E_c A_c + y_w E_w A_w)} \quad (4)$$

1.2.2 A variational formulation for concrete-timber composite beams

In the present work, the formulation presented in FORTI [11] and MASCIA et al. [12] was adopted. The formulation is based on the principle of virtual works. Therefore, it can be easily implemented in a computer solver using both the Finite Element Method (ODEN et al. [13]) and the Direct Stiffness Method (GERE and WEAVER [14]). Two consolidated theories for the analysis of beams are the Euler-Bernoulli's beam theory and the Timoshenko's beam theory (SLHESSARENKO [15]). In this work, the Euler-Bernoulli's beam theory in two dimensions was adopted.

1.2.2.1 Principle of virtual work

The principle of virtual work is adopted to formulate the problem. The composite beam is considered as two independent beams connected (one made of concrete and the other of wood). The strain energy of the composite structure is given as the sum of the strain energy of the two beams and the strain energy of the connectors. Thus, the internal

Figure 3 – Kinematics of a composite beam

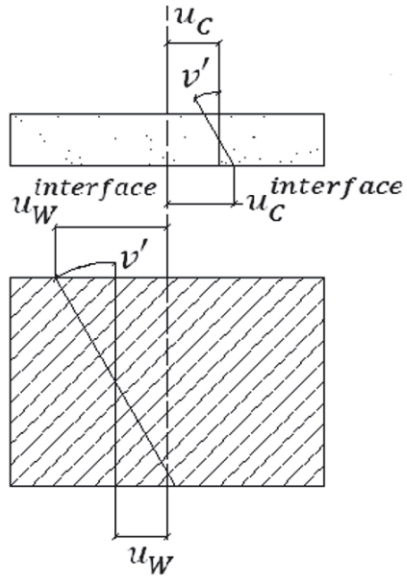

virtual work of the structure is the sum of the three individual internal virtual work, i.e., $TV_{int}^C + TV_{int}^W + TV_{int}^S = TV_{ext}$, where indices C, W e S refer to concrete, wood, and connectors, respectively.

It is assumed the vertical displacement ($v(x)$) of the two beams are equal and therefore, their derivatives are equal too. Under Euler-Bernoulli's beam theory assumptions, the derivative of the vertical displacement is equal to the rotation of the cross section, and both beams have the same rotation $\theta^C = \theta^W = v'(x)$. The shear force (force per unit of length) of the connectors is given as $Ts = K\Delta u$, where K is the slip modulus of the connectors and Δu is the relative displacement between the lower fiber of the concrete beam and the upper fiber of the timber beam. Figure [3] illustrates this relative displacement.

The relative displacement (Δu)is calculated as:

$$\Delta u = u_C^{interface} - u_W^{interface}$$

with

$$u_C^{interface} = u_C + \theta_C \frac{h_C}{2}$$

$$u_C^{interface} = u_C + \theta_C \frac{h_C}{2} \quad u_C^{interface} = u_C + \theta_C \frac{h_C}{2}$$

$$u_W^{interface} = u_W - \theta_W \frac{h_W}{2} \quad (5)$$

Since the rotation of both beams are equal, then:

$$\Delta u = u_C - u_W + v'\left(\frac{h_C + h_W}{2}\right) \quad (6)$$

Figure 4 – A set of piecewise linear base functions

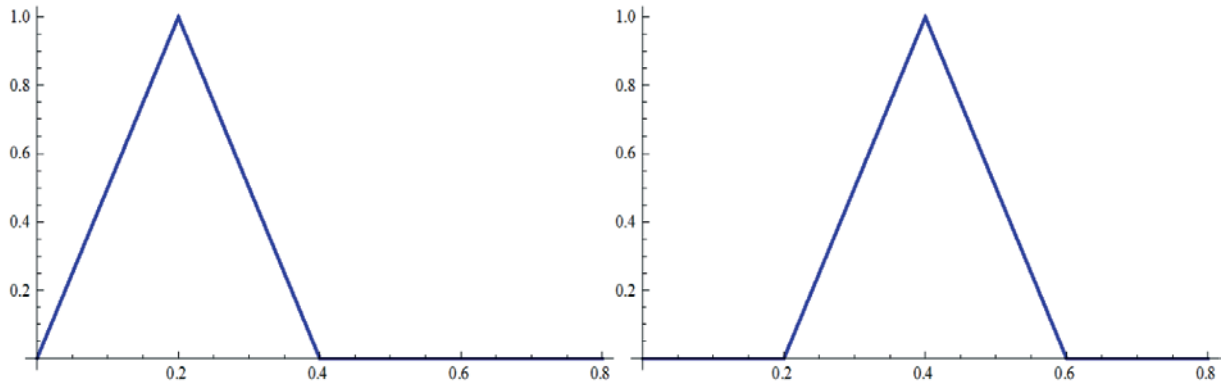

Defining r the distance between the gravity center of the beams, it comes that:

$$r = \left(\frac{h_C + h_W}{2} \right).$$

$$\text{and} \quad T_S = K\left(u_C - u_W + v'r\right) \tag{7}$$

The internal virtual work of the connector is then given as:

$$TV_{int}^{S} = \int_0^L T_S \, \delta\Delta u \, ds$$

$$TV_{int}^{S} = \int_0^L K\left(u_C - u_W + v'r\right)\left(\delta u_C - \delta u_W + \delta v'r\right) ds \tag{8}$$

Adding the internal virtual work of the connector to those of concrete and timber beams, the composite beam formulation is stated as:

$$TV_{int}^{C} + TV_{int}^{W} + TV_{int}^{S} = TV_{ext}$$

with

$$TV_{int}^{C} = \int_0^L \left(E_C A_C u_C' \delta u_C' + E_C I_C v'' \delta v'' \right) ds$$

$$TV_{int}^{W} = \int_0^L \left(E_W A_W u_W' \delta u_W' + E_W I_W v'' \delta v'' \right) ds$$

$$TV_{int}^{S} = \int_0^L K\left(u_C - u_W + v'r\right)\left(\delta u_C - \delta u_W + \delta v'r\right) ds$$

$$TV_{ext} = \int_0^L q\,\delta v\, ds + \sum_{i=1}^{N} P_i \, \delta v\left(x_i\right) \tag{9}$$

where the unknowns are the horizontal displacement of the fiber in the gravity center of the elements $u_c(x)$ and $u_w(x)$ and the vertical displacement $v(x)$; δu_C, δu_W and δv are their respective virtual dsiplacements.

In FORTI [11], the variational formulation (Equation [9]) is solved using the Rayleigh-Ritz method. However, the Finite Element Method permits the application of this formulation to different types of load and geometries of beams in a more general fashion and simplicity of use. Moreover, this approach is more suited to be inserted in other software of structural analysis already available.

2. The finite element method

The Finite Element Method consists in adopting functions to approximate the displacements $u_c(x)$, $u_w(x)$ and $v(x)$ and also the virtual displacements $\delta u_c(x)$, $\delta u_w(x)$ and $\delta v(x)$. Adopting approximating base functions, permits the calculation of an approximate solution to the variational problem of Equation [9]. In this work, two families of functions are employed: the piecewise linear functions and the cubic Hermite polynomials.

The piecewise linear base functions are defined as being linear functions that take value of 1 in one of the nodes of the mesh and zero in all the other nodes. Also known as hat functions, one example of two base functions is presented in Figure [4].

It can be noted the function has values different from zero in a

Figure 5 – Linear shape functions of an element

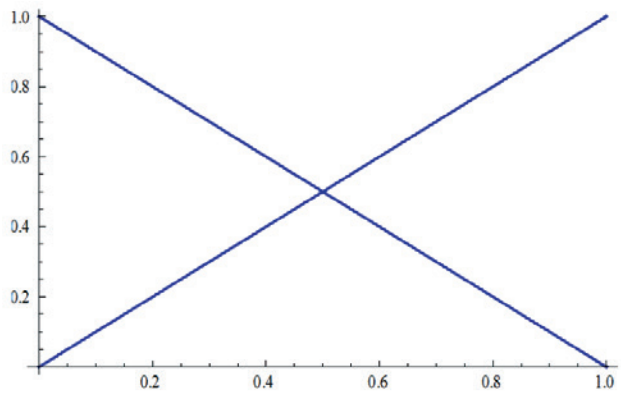

Figure 6 – Cubic Hermite shape functions of an element

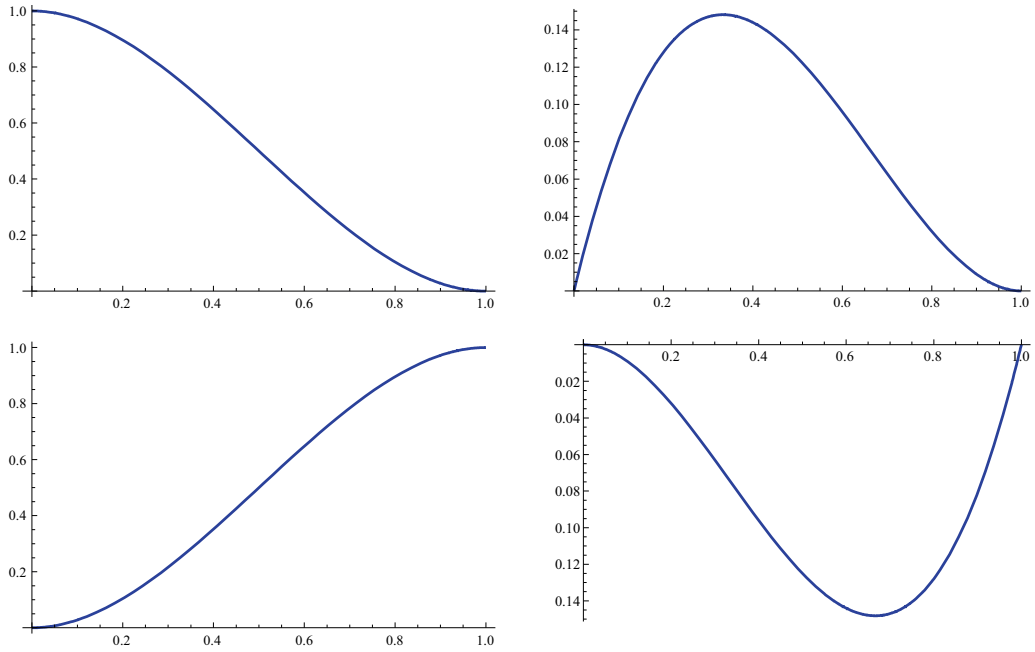

region formed by 3 nodes and has zero value in the rest of the domain. If each element of the mesh is formed by 2 nodes, then the function has local support to 2 neighbor elements and each element contributes with 2 functions, which are called shape functions of the element (Figure [5]). The local support property of the functions is employed in the construction of the element stiffness matrix.

The combination of the elements shape functions builds the approximate base functions. The defined linear functions has derivatives with piecewise constant values. Thus, the derivative of the function is discontinuous between elements. It means the first derivative of the piecewise linear function is integrable over the domain, but its second derivative would not be defined in the nodes of the mesh.

The cubic Hermite functions also have local support to the element and its neighbors. The properties of the Hermite functions involve the value of the function and its derivatives. The shape functions of one element are plotted in Figure [6].

The first function has the property of having value equal to 1 in the initial node of the element and zero in the final node. Additionally, its first derivative has zero value in both initial and final node. The second function has zero value in both nodes and its first derivative has value equal to 1 in the initial node and zero in the final node. The third function has value equal to 1 in the final node and the fourth function has value 1 for the first derivative in the final node, with zero value for the remaining values of function and first derivatives in the nodes. These functions are particularly important because they construct, in association to the neighbor elements, functions having the first derivative continuous over the whole domain. Thus, these functions are integrable up to their second derivatives.

The finite element formulation is obtained substituting the displacement functions by the approximating functions, i.e., $u_w \cong \sum_{j=1}^{n} \alpha_j \varphi_j$, $u_w \cong \sum_{j=1}^{n} \beta_j \varphi_j$, and $v \cong \sum_{j=1}^{m} \gamma_j \phi_j$. In the same manner, the virtual displacements are approximated by the same functions. Thus, the virtual displacement δu_c is adopted as equal to each function φ_i and so on. Then, the finite element formulation is given as:

$$TV_{ini}^{C} + TV_{ini}^{W} + TV_{ini}^{S} = TV_{ext}$$

where

$$TV_{ini}^{C} = \int_0^L \left(E_C A_C \left(\sum_{j=1}^{n} \alpha_j \varphi_j' \right) \varphi_{i,c}' + E_C I_C \left(\sum_{j=1}^{m} \gamma_j \phi_j'' \right) \phi_i'' \right) ds$$

$$TV_{ini}^{W} = \int_0^L \left(E_W A_W \left(\sum_{j=1}^{n} \beta_j \varphi_j' \right) \varphi_{i,w}' + E_W I_W \left(\sum_{j=1}^{m} \gamma_j \phi_j'' \right) \phi_i'' \right) ds$$

$$TV_{ini}^{S} = \int_0^L K \left(\left(\sum_{j=1}^{n} \alpha_j \varphi_j \right) - \left(\sum_{j=1}^{n} \beta_j \varphi_j \right) + \left(\sum_{j=1}^{m} \gamma_j \phi_j' \right) r \right) \left(\varphi_{i,c} - \varphi_{i,w} + \phi_i' r \right) ds$$

$$TV_{ext} = \int_0^L q \phi_i \, ds + \sum_{i=1}^{N} P_i \phi_i(x_i)$$

(10)

The variational formulation requires the calculation of integral that involves the first derivatives of the horizontal displacements u_c and u_w. Thus, one can observe the piecewise linear functions (hat functions) satisfy the necessary requirements to approximate the horizontal displacements, since its first derivatives are integrable over the whole domain. Therefore, we adopted φ_j as being hat functions, with the index j indicating the node of the mesh where the function has value equal to 1. The vertical displacement, however, requires the second derivative to be integrable in order to satisfy the variational formulation. Thus, the cubic Hermite functions are candidates to ϕ_j, since their second derivatives are integrable

over the domain. In this work, the Hermite functions are adopted as shape functions to approximate the vertical displacement $v(x)$. It is interesting to observe that in the Euler-Bernoulli's formulation, the rotation of the cross section is equal to the first derivative of the vertical displacement, i.e., $\theta(x) = v'(x)$. Then, one may note that the first and third Hermite functions plotted in Figure [6] refer to the vertical displacement, while the second and fourth are related to the section rotation because they have first derivatives with values equal to 1 in the nodes.

Since the approximating functions have local support to the 2 neighboring elements connected to a node, the integrals over the domain $(0, L)$ are indeed calculated only over the elements of support of the function. The formulation can be written, in matrix form, as:

$$[K]\{u\} = \{F\} \tag{11}$$

where the matrix K is composed by the sum of the matrices of each element. The solution vector u is given as:

$$u = \left\{u_c^1, u_w^1, v^1, v'^1, u_c^2, u_w^2, \ldots, u_c^n, u_w^n, v^n, v'^n\right\}^T \tag{12}$$

which is the union set of the horizontal and vertical displacements and rotation of each node of the mesh $\{u_c, u_w, v, v'\}$. The matrix of each element is described in the sequel.

2.1 Element stiffness matrix

The stiffness matrix is presented in parts, one for each term of the internal virtual work: concrete, wood and connector.

The stiffness matrix associated to the concrete element is given by the expression:

$$K_{ij}^c = \int_0^L \left(E_C A_C \varphi_j' \varphi_{i,c}' + E_C I_C \phi_j'' \phi_i''\right) ds \tag{13}$$

which gives, for each element of the mesh of length L_e:

$$k_{ij}^c = \int_0^{L_e} \left(E_C A_C \varphi_j' \varphi_{i,c}' + E_C I_C \phi_j'' \phi_i''\right) ds\,. \tag{14}$$

or

$$k_e^c = \begin{bmatrix}
\frac{A_c E_c}{L_e} & 0 & 0 & 0 & -\frac{A_c E_c}{L_e} & 0 & 0 & 0 \\
0 & 0 & 0 & 0 & 0 & 0 & 0 & 0 \\
0 & 0 & \frac{12E_c I_c}{L_e^3} & \frac{6E_c I_c}{L_e^2} & 0 & 0 & -\frac{12E_c I_c}{L_e^3} & \frac{6E_c I_c}{L_e^2} \\
0 & 0 & \frac{6E_c I_c}{L_e^2} & \frac{4E_c I_c}{L_e} & 0 & 0 & -\frac{6E_c I_c}{L_e^2} & \frac{2E_c I_c}{L_e} \\
-\frac{A_c E_c}{L_e} & 0 & 0 & 0 & \frac{A_c E_c}{L_e} & 0 & 0 & 0 \\
0 & 0 & 0 & 0 & 0 & 0 & 0 & 0 \\
0 & 0 & -\frac{12E_c I_c}{L_e^3} & -\frac{6E_c I_c}{L_e^2} & 0 & 0 & \frac{12E_c I_c}{L_e^3} & -\frac{6E_c I_c}{L_e^2} \\
0 & 0 & \frac{6E_c I_c}{L_e^2} & \frac{2E_c I_c}{L_e} & 0 & 0 & -\frac{6E_c I_c}{L_e^2} & \frac{4E_c I_c}{L_e}
\end{bmatrix}$$

The stiffness matrix associated to the timber element is given as:

$$k_e^w = \begin{bmatrix}
0 & 0 & 0 & 0 & 0 & 0 & 0 & 0 \\
0 & \frac{A_w E_w}{L_e} & 0 & 0 & 0 & -\frac{A_w E_w}{L_e} & 0 & 0 \\
0 & 0 & \frac{12E_w I_w}{L_e^3} & \frac{6E_w I_w}{L_e^2} & 0 & 0 & -\frac{12E_w I_w}{L_e^3} & \frac{6E_w I_w}{L_e^2} \\
0 & 0 & \frac{6E_w I_w}{L_e^2} & \frac{4E_w I_w}{L_e} & 0 & 0 & -\frac{6E_w I_w}{L_e^2} & \frac{2E_w I_w}{L_e} \\
0 & 0 & 0 & 0 & 0 & 0 & 0 & 0 \\
0 & -\frac{A_w E_w}{L_e} & 0 & 0 & 0 & \frac{A_w E_w}{L_e} & 0 & 0 \\
0 & 0 & -\frac{12E_w I_w}{L_e^3} & -\frac{6E_w I_w}{L_e^2} & 0 & 0 & \frac{12E_w I_w}{L_e^3} & -\frac{6E_w I_w}{L_e^2} \\
0 & 0 & \frac{6E_w I_w}{L_e^2} & \frac{2E_w I_w}{L_e} & 0 & 0 & -\frac{6E_w I_w}{L_e^2} & \frac{4E_w I_w}{L_e}
\end{bmatrix}$$

It is interesting to observe that the stiffness matrices of the concrete and timber elements are, in fact, the same matrices one would obtain from the Direct Stiffness Method. Adding the two matrices, we would have the stiffness matrix in the case the elements were disassembled, where the bending stiffness would be added while the horizontal displacements would remain independent. The interaction between the two materials, with a consequent increase in the bending stiffness of the composite beam, is represented by the connector stiffness matrix. The connector matrix is calculated from the equation of internal virtual work of the connector:

$$TV_{int}^S = \int_0^L K\left(u_C - u_W + v'r\right)\left(\delta u_C - \delta u_W + \delta v'r\right) ds \tag{15}$$

which, being integrated over the domain of one element of length L_e, results in:

$$k_e^s = \begin{bmatrix}
\frac{kL_e}{3} & -\frac{kL_e}{3} & -\frac{kr}{2} & \frac{kL_e r}{12} & \frac{kL_e}{6} & -\frac{kL_e}{6} & \frac{kr}{2} & -\frac{kL_e r}{12} \\
-\frac{kL_e}{3} & \frac{kL_e}{3} & \frac{kr}{2} & -\frac{kL_e r}{12} & -\frac{kL_e}{6} & \frac{kL_e}{6} & -\frac{kr}{2} & \frac{kL_e r}{12} \\
-\frac{kr}{2} & \frac{kr}{2} & \frac{6kr^2}{5L_e} & \frac{kr^2}{10} & -\frac{kr}{2} & \frac{kr}{2} & -\frac{6kr^2}{5L_e} & \frac{kr^2}{10} \\
\frac{kL_e r}{12} & -\frac{kL_e r}{12} & \frac{kr^2}{10} & \frac{2kL_e r^2}{15} & -\frac{kL_e r}{12} & \frac{kL_e r}{12} & -\frac{kr^2}{10} & -\frac{kL_e r^2}{30} \\
\frac{kL_e}{6} & -\frac{kL_e}{6} & -\frac{kr}{2} & -\frac{kL_e r}{12} & \frac{kL_e}{3} & -\frac{kL_e}{3} & \frac{kr}{2} & \frac{kL_e r}{12} \\
-\frac{kL_e}{6} & \frac{kL_e}{6} & \frac{kr}{2} & \frac{kL_e r}{12} & -\frac{kL_e}{3} & \frac{kL_e}{3} & -\frac{kr}{2} & -\frac{kL_e r}{12} \\
\frac{kr}{2} & -\frac{kr}{2} & -\frac{6kr^2}{5L_e} & -\frac{kr^2}{10} & \frac{kr}{2} & -\frac{kr}{2} & \frac{6kr^2}{5L_e} & -\frac{kr^2}{10} \\
-\frac{kL_e r}{12} & \frac{kL_e r}{12} & \frac{kr^2}{10} & -\frac{kL_e r^2}{30} & \frac{kL_e r}{12} & -\frac{kL_e r}{12} & -\frac{kr^2}{10} & \frac{2kL_e r^2}{15}
\end{bmatrix}$$

Finally, the element stiffness matrix of a concrete-timber composite beam is given as $k = k^c + k^w + k^s$.

The load vector is obtained from the external virtual work, which in this study is given as:

$$TV_{ext} = \int_0^L q\,\delta v\, ds + \sum_{i=1}^N P_i\,\delta v(x_i) \tag{16}$$

where q is a distributed vertical force and P_i are vertical forces applied to nodes. It is to be noted that only vertical loads were considered in Equation 16, although its extension to other types of loads is trivial. The load vector for a q constant valued along the element is given by:

$$F = \left\{0\ ,0\ ,\frac{L_e q}{2},\frac{L_e^2 q}{12},0\ ,0\ ,\frac{L_e q}{2},-\frac{L_e^2 q}{12}\right\}^T \quad (17)$$

The nodal concentrated forces P_i are added to the algebraic problem by adding their values in their respective positions of the global load vector.

2.2 Computational solver

The solver is implemented on C++ language, using some classes from the finite element library PZ (DEVLOO [16]). In order to facilitate the use of the program, a graphical interface was implemented to input data and visualize results. Figure [7] shows the main screen of the program with the data to be input. The result graphics are the vertical displacement of the composite beam, bending moment and normal forces of each of the two beams and the connector shear force.

The implementation was verified comparing its results to the results presented in FORTI [11]. FORTI [11] presents some numerical results of the variational formulation and an analytical solution of the differential equation from STEVANOVIC [17]. The results are also compared to the experimental data of laboratory tests (SORIANO [4]), with good agreement of results.

3. Results and discussions

The developed program is applied to the problem of a concrete-timber beam presented in FORTI [11] for verifying the finite element solver implemented. The results are also compared to those obtained from the routines of the EUROCODE 5 [9].

Table 1 – Properties of the components of the composite beam

	Concrete	Timber
Cross section area (mm²)	12,000	7,500
Moment of inertia (mm⁴)	1,6 x 10⁶	14.063 x 10⁶
E* (N/mm²)	19,300	14,700

*Longitudinal Young's modulus obtained from a compressive test parallel to the fiber direction.
Connector slip modulus under service loading:
K1c (ser) = 15.464 N/mm;
Connector spacing (s) = 7.5 cm.

The input data is described in Table [1] and in Figures [8] and [9]. The connection between the two materials was made with 41 hex bolts of ½", with spacing of 7.5 cm. The slip modulus was obtained from shear laboratory tests. SORIANO [4] performed 5 tests and the average slip modulus under service load obtained was equal to $K_{ser} = 15464\ N/mm$. The ultimate modulus was $K_u = 10309\ N/mm$

In the experimental test of SORIANO [4], there were two loads to be considered (Figure [8]): one uniformly distributed load, correspondent to the self-weight of the beam q = 0.36 N/mm, and a concentrated force P_k applied vertically in the middle of the beam. The vertical displacement was measured from the moment the concentrated force was applied, i.e., the measured displacement does not include the vertical displacement caused by the self-weight of the

Figure 7 – Main screen of the program: input data and results

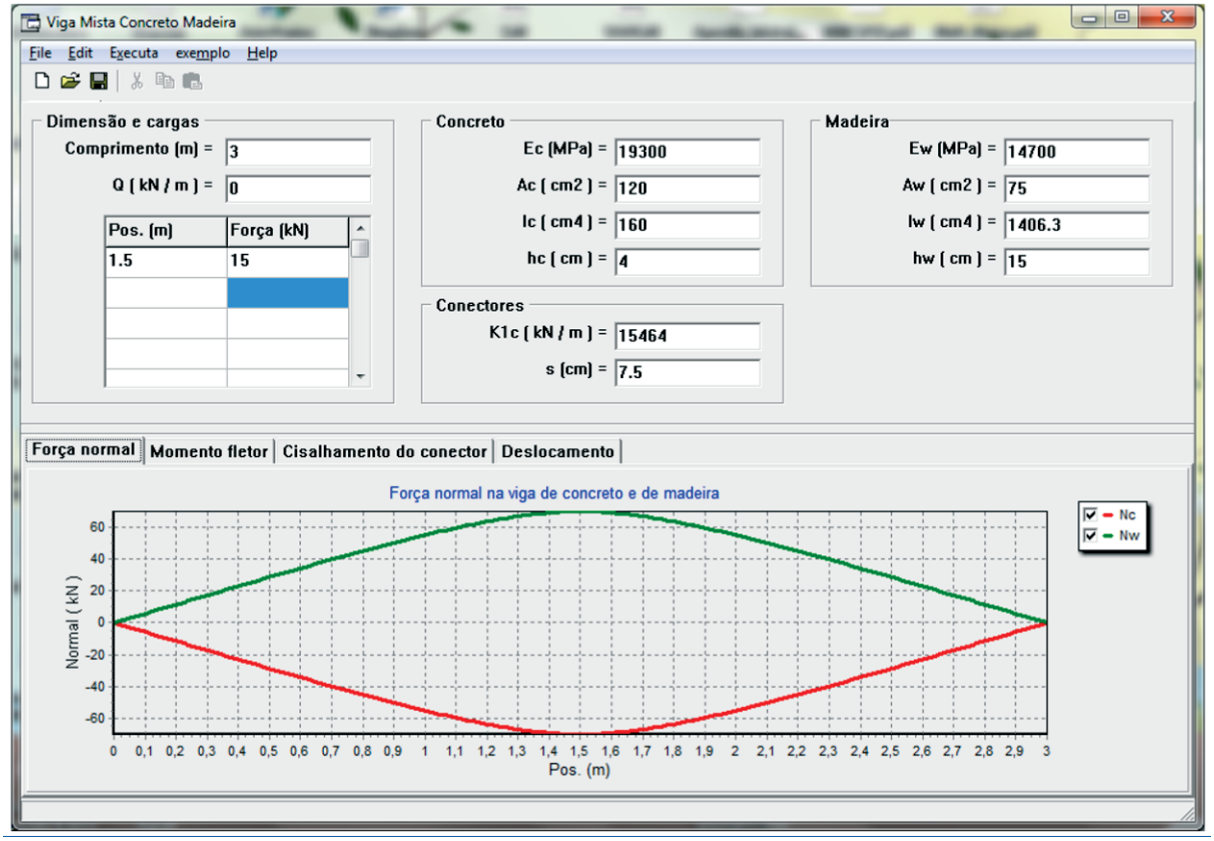

Figure 8 – Geometry of the tested composite beams (dimensions in cm). (SORIANO (4))

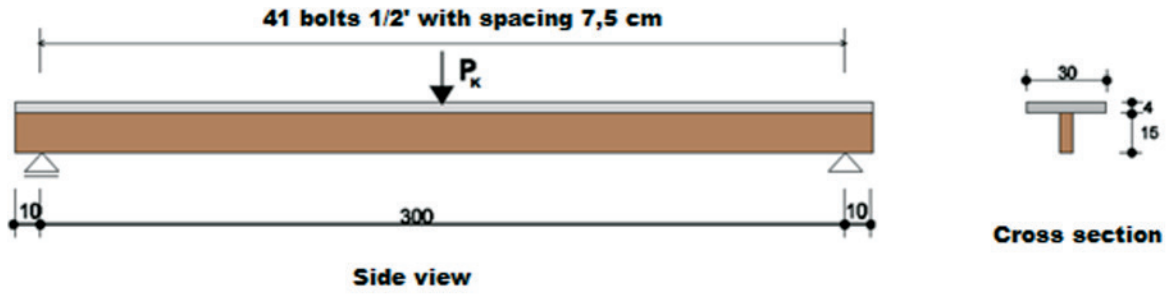

Figure 9 – Boundary conditions of the tested beams

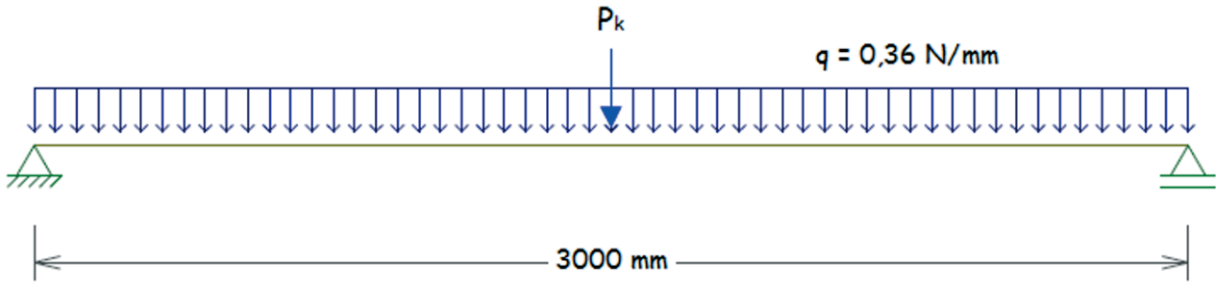

beam. Therefore, in the numerical analysis, only the concentrated force is simulated. This procedure is mathematically valid due to the linearity of the formulation adopted.

Table [2] complements the input data with the values of the force P_k, which varied from 0 to 30 kN, and brings the comparison of the results obtained in this work to those obtained from the literature. Table [2] brings the following results:

1. SORIANO [4]: the displacements from the two experimental tests (Exp. 1, Exp. 2, and the average values of the tests). It is worth noting that the structure collapsed in Exp. 1 and Exp. 2

Table 2 – Results of vertical displacements at L/2 of the composite beam

Load (kN)	Experimental (mm)			Numerical (mm)				Analytical (mm)	
Pk	Exp.1	Exp.2	Average	FORTI (11)	Difference[1]	FEM	Difference[2]	Eurocode 5	Difference[3]
0	0	0	0	0	0 %	0	0 %	0	0 %
5	4.13	4.43	4.28	3.96	7.5 %	3.96	7.5 %	3.91	8.6 %
10	8.34	8.72	8.53	7.92	7.2 %	7.92	7.2 %	7.81	8.4 %
15	12.26	13.01	12.64	11.88	6.0 %	11.88	6.0 %	11.72	7.2 %
20	16.76	17.76	1.26	15.84	8.2 %	15.85	8.2 %	15.62	9.5 %
25	22.94	23.68	23.31	19.80	15.1 %	19.80	15.1 %	19.53	16.2 %
30	30.61	29.08	29.85	23.76	20.4 %	23.76	20.4 %	23.44	21.5 %

$$\text{Difference}^1 = \frac{FORTI\,[11] - experimental\ average}{experimental average} \qquad \text{Difference}^2 = \frac{FEM - experimental\ average}{experimental average}$$

$$\text{Difference}^3 = \frac{Eurocode\,5 - experimental\ average}{experimental average}$$

Figure 10 – Graph of vertical displacement *versus* the applied force P_k

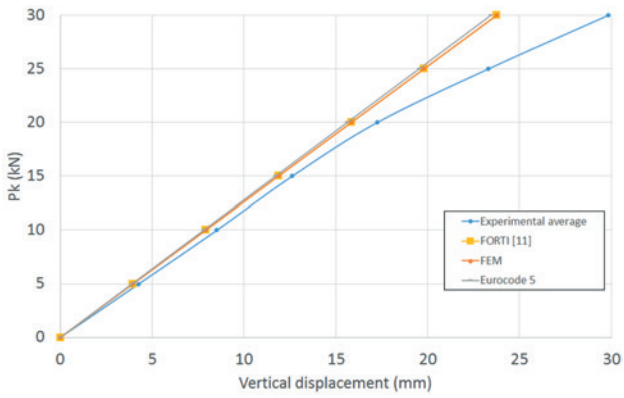

when P_k was equal to $37.811 kN$ and $36.694 kN$, respectively;

2. FORTI [11]: the results obtained from the variational formulation solved using the Rayleigh-Ritz method;
3. The results obtained in this work using the implemented finite element solver (FEM);
4. Calculating using the routines of the EUROCODE 5 [9], which defines an effective bending stiffness parameter (Equation 1). For this case the effective stiffness $(EI)_{ef} = 720.0542\, kN.m^2$ and the vertical displacement is calculated as $\frac{P_k L^3}{48(EI)_{ef}}$.

Table [2] also brings the comparison of the displacements calculated by the different methodologies and the experimental results. Figure [10] illustrates the comparison of results shown in Table [2]. It can be observed that the displacement curve from the experimental tests indicates a non-linear behavior beyond the point where the force is $P_k = 20 kN$.

Analyzing the data of Table [2], one can observe that:

- The finite element solution (FEM) of this work is equal to the solution of FORTI [11]. This conclusion was expected, since both works solve the same variational formulation. The agreement of results, in fact, verify the C++ code implemented, at least for this example.
- The numerical results are very similar to the experimental results, conclusion already observed in FORTI [11]. The values differ from less than 10% in the early stages of loading. With the increase of the load P_K, it can be observed the influence of the non-linear behavior of the materials and the consequent deviation of the results with a maximum difference of about 20% when $P_k = 30 kN$, near the point of collapse of the tested beams. This result evidences the quality of the variational formulation in representing the physical phenomenon while the structure is in the elastic domain.
- The results from the routines of the EUROCODE 5 [9] are in great agreement with the numerical solutions, with differences inferior to 1.5%. This is an evident quality of the analytical formulation, much simpler to be used.

The other results of the implemented program are presented in Figures [11], [12], [13], and [14] for the simulation with $P_k = 15 kN$. Figure [11] shows the vertical displacement of the composite beam. Figure [12] brings the curves of the bending moment for the concrete beam (M_c), the timber beam (M_w) and the total bending moment (M_{total}). Figure [13] shows the graphics of normal forces. In the absence of interaction between the two beams, the sum of the bending moment of the concrete beam to the moment of the timber beam would be equal to the total bending moment. Thus, it is interesting to observe that the interaction between the beams reduce the bending moment acting on each of the beams. However, there is the appearance of normal forces, which cancel each other. The normal force in the concrete beam is of compression and in the timber beam is of tension.

Figure [14] presents the shear force of the connectors.

Figure 11 – Graph of vertical displacement along the length of the beam for the applied force of P_k = 15 kN

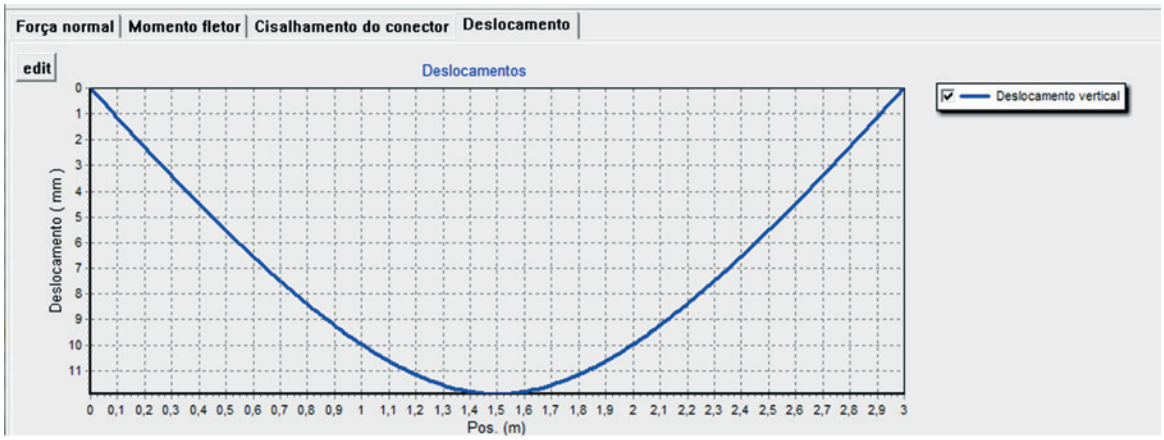

Figure 12 – Graph of bending moment of each of the beams (concrete and timber) and the total moment for the applied force of P_k = 15 kN

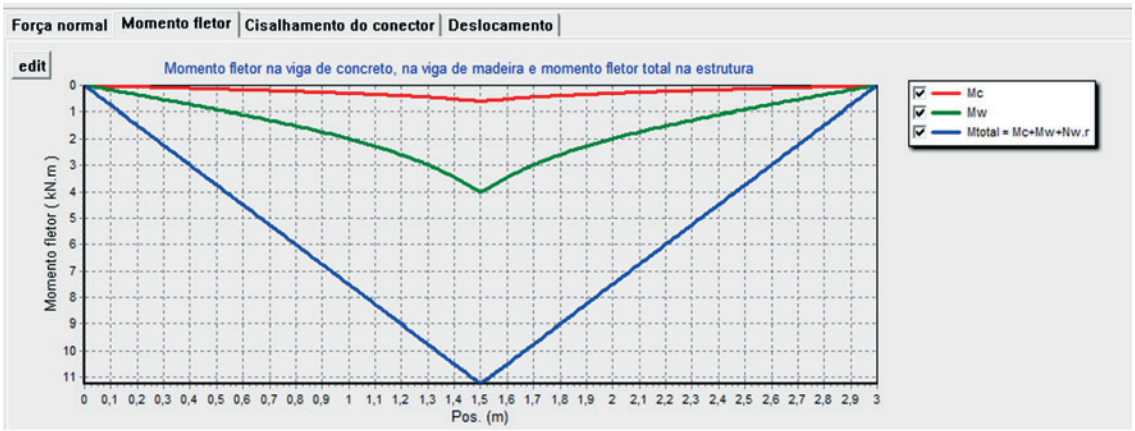

Figure 13 – Graph of normal forces on the concrete and timber beams for the applied force of P_k = 15 kN

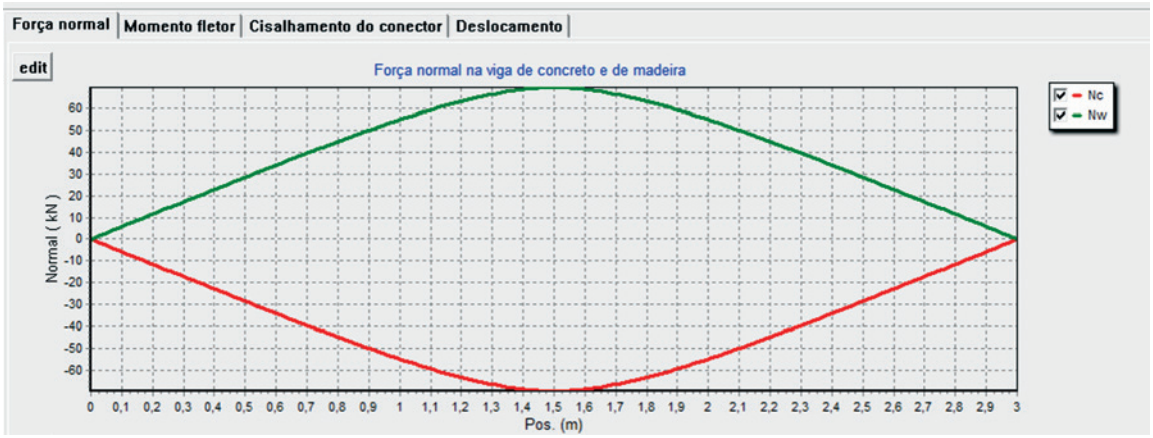

Figure 14 – Graph of the connection shear force along the length of the beam for P_k = 15 kN

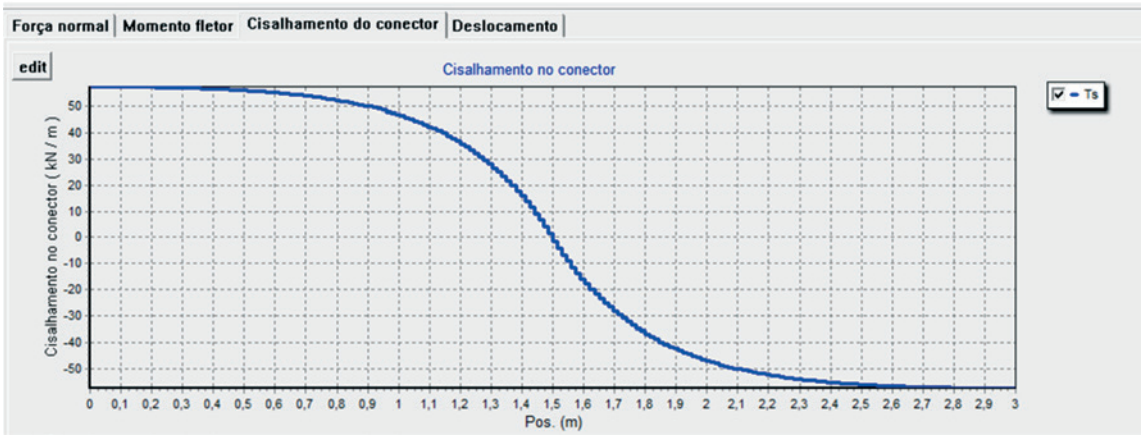

4. Conclusions

The technological development of the process of design and construction of timber structures has improved the knowledge of the behavior of this material and its subsequent use in composite structures. The employment of composite concrete-timber structures promotes the best use of the features of each material.

This work contributes with an analysis of concrete-timber composite beams. Two approaches for calculating the stress state of the beam are compared. One is based on a finite element formulation and the other is based on the analytical procedure of the standard EUROCODE 5.

The variational formulation, based on the principle of virtual work, accounts to the strain energy of the three main components of a composite beam: the reinforced concrete slab, the timber web and the connectors (or fasteners). The formulation is consistent and satisfies the equilibrium equations. It is coherent with laboratory test results.

The procedure of the EUROCODE 5 is based on an effective bending stiffness, which is function of the components of the composite beam, specially the slip modulus of connectors.

The implementation of a finite element formulation enables the use of the formulation in structural analysis programs. A software with user interface was developed and it is available to the community.

Some examples were performed to compare the simulation results to the results obtained from the procedure of the EUROCODE 5. It is observed great concordance of the results, which differ from less than 1.5%.

This development promotes, through the development of the computational program, a wider propagation of the procedures of design and the understanding of the mechanical behavior of composite beams, which may catalyze the use of this type of structure. The finite element formulation presented may be applied to other types of composite structures, for instance, a structure with a steel profile web associated to a concrete slab.

5. References

[1] CECCOTTI, A. Timber-concrete composite structures. In: Timber Engineering - STEP1. BLASS, H. J., AUNE, P., CHOO, B.S. et al., Almere: Centrum Hout, 1995, E13, p.1-12.

[2] TARANTINO, A. M., DEZI, L. Creep effects in composite beams with flexible shear connectors. Journal of Structural Engineering- ASCE, New York, n. 8, v.118, p.2063-2081. Aug. 1992.

[3] RACHER, P. Mechanical timber joints - general. In: Timber Engineering - STEP lecture C1. BLASS, H. J., AUNE, P., CHOO, B.S. et al., Almere: Centrum Hout, 1995, C1, p.1-10.

[4] SORIANO, J. Estruturas mistas de concreto e madeira: Análise de vigas e painéis e aplicações na construção civil. In Tese (Doutorado em Engenharia Civil) – Faculdade de Engenharia Civil, Universidade Estadual de Campinas, 2001.

[5] GIRHAMMAR, U. A., GOPU, V. K. A. Composite beam-columns with interlayer slip-exact analysis. Journal of Structural Engineering- ASCE, New York, n. 4, v.119, p.1265-1282. Apr. 1993.

[6] NICOLAS, E. A. Estudo de ligações em estruturas mistas de concreto-madeira. Universidade Estadual de Campinas – Faculdade de Engenharia Civil, Dissertação, 2001, p 103.

[7] BS 5400-5: Steel, concrete and composite bridges. Code of practice for design of composite bridges. (AMD 3998) (withdrawn), 1979

[8] NBR 8800: Projeto de Estruturas de aço e de estruturas mistas de aço e concreto de edifícios. Setembro, 2008.

[9] EUROCODE 5 (prEN 1995-1-1): Design of timber structures. Part 1-1: General – common rules and rules for buildings. Brussels, 2008.

[10] DIN 1052: Structural use of timber – part 1, 2 and 3. Berlin, 1988.

[11] FORTI, N. C. S. Análise numérica de vigas mistas em concreto e madeira. 2004. Tese (Mestrado) – Faculdade de Engenharia Civil, Universidade Estadual de Campinas, Campinas, 2004.

[12] MASCIA, NILSON T.; FORTI, NÁDIA C.S. ; SORIANO, JULIO ; NICOLAS, ELIAS A. ; FORTI, TIAGO L.D. . Study of concrete-timber composite beams using an analytical approach based on the principle of virtual work and experimental results. Engineering Structures, v. 46, p. 302-310, 2013.

[13] ODEN, J. T., CAREY G. F. e BECKER E. B. Finite Elements – An introduction. Vol 1. Prentice Hall Inc. USA. 1981.

[14] GERE, J. M. e WEAVER, W. Analysis of framed structures. 1965.

[15] SLHESSARENKO, F. L. - Análise tridimensional de edifícios por elementos finitos utilizando programação orientada a objetos. 1997. Tese (Mestrado) – Faculdade de Engenharia Civil, Universidade Estadual de Campinas, Campinas, 1997.

[16] DEVLOO, P. R. B. . PZ An Object Oriented Environment For Scientific Programming. COMPUTER METHODS IN APPLIED MECHANICS AND ENGINEERING, v. 150, n.1-4, p. 133-153, 1997.

[17] STEVANOVIC, B. Elastically coupled timber-concrete beams. In INTERNACIONAL WOOD ENGINEERING CONFERENCE, 1996, New Orleans. Proceedings... New Orleans, Oct. 1996. v.3. p.425-430.

Volume 8, Number 4 (August 2015) p. 507-528 • ISSN 1983-4195
http://dx.doi.org/10.1590/S1983-41952015000400006

REVISTA IBRACON DE ESTRUTURAS E MATERIAIS
IBRACON STRUCTURES AND MATERIALS JOURNAL

Finite element analysis of composite concrete-timber beams

Análise de vigas mistas de concreto e madeira pelo método dos elementos finitos

N. C. S. FORTI [a]
nadia.cazarim@puc-campinas.edu.br

T. L. D. FORTI [b]
forti@simworx.com.br

A. E. P. G. A. JACINTHO [a]
anajacintho@puc-campinas.edu.br

L. L. PIMENTEL [a]
lialp@puc-campinas.edu.br

Abstract

In the search for sustainable construction, timber construction is gaining in popularity around the world. Sustainably harvested wood stores carbon dioxide, while reforestation absorbs yet more CO2. One technique involves the combination of a concrete slab and a timber beam, where the two materials are assembled by the use of flexible connectors. Composite structures provide reduced costs, environmental benefits, a better acoustic performance, when compared to timber structures, and maintain structural safety. Composite structures combine materials with different mechanical properties. Their mechanical performance depends on the efficiency of the connection, which is designed to transmit shear longitudinal forces between the two materials and to prevent vertical detachment. This study contributes with the implementation of a finite element formulation for stress and displacement determination of composite concrete-timber beams. The deduced stiffness matrix and load vector are presented along to numerical examples. Numerical examples are compared to the analytical equations available in Eurocode 5 and to experimental data found in the literature.

Keywords: composite structures, finite element method and sustainable structures.

Resumo

A madeira tem se destacado na produção de edificações sustentáveis, principalmente pela possibilidade de emprego de madeiras provenientes de florestas plantadas. A combinação de vigas de madeira com um tabuleiro de concreto armado ligados entre si por conexões flexíveis é uma alternativa que traz aumento de rigidez à estrutura, ameniza problemas de durabilidade, quando exposta às intempéries, e melhora seu desempenho acústico, se comparada à uma estrutura em madeira. As estruturas mistas são constituídas pela associação de materiais com diferentes propriedades mecânicas e seu desempenho mecânico depende da eficiência da ligação entre eles. Os conectores flexíveis são responsáveis pela transmissão de forças de cisalhamento entre os dois materiais e por evitar o desprendimento vertical. Esta pesquisa desenvolveu e implementou uma formulação de elementos finitos para cálculo dos esforços internos da estrutura mista de concreto e madeira. A matriz de rigidez e o vetor de carga deduzidos são apresentados juntamente com exemplos numéricos e seus resultados são comparados com as equações analíticas do Eurocode 5 e resultados experimentais da literatura.

Palavras-chave: estruturas mistas, elementos finitos e estruturas sustentáveis.

[a] *School of Civil Engineering - PUC Campinas, Campinas, SP, Brasil;*
[b] *Simworx Engenharia, Pesquisa e Desenvolvimento, Campinas, SP, Brasil.*

Received: 03 Sep 2014 • Accepted: 22 May 2015 • Available Online: 7 Aug 2015

1. Introdução

As estruturas mistas constituídas por materiais de diferentes propriedades de elasticidade e de resistência podem ser associadas, como uma solução alternativa às estruturas de uso corrente na construção civil. Essa medida busca obter redução de custos de construção mantendo a segurança estrutural com um desempenho arquitetônico e ambiental vantajoso.

Com essa técnica pode-se alcançar, no caso de pontes, um aumento da rigidez da estrutura, diminuindo-se seus deslocamentos e aumentando-se sua frequência natural de vibração.

O sistema de tabuleiros mistos é constituído de uma placa de concreto conectada a elementos estruturais de madeira de tal modo que as partes funcionem em conjunto. O nível de transferência de esforços entre a placa de concreto e os elementos de madeira pode definir um comportamento monolítico, quando não há deslocamentos relativos entre esses materiais, ou comportamento "não monolítico" quando as transferências de tensões ocorrem com pequenos deslocamentos relativos.

Nos tabuleiros mistos, a placa de concreto protege a madeira contra intempéries, o desgaste superficial por abrasão, diminui as vibrações provocadas pelas cargas dinâmicas, aumenta o isolamento acústico, a proteção contra fogo e proporciona maior rigidez e resistência se comparado ao tabuleiro de madeira. A resistência ao carregamento aumenta na ordem do dobro e a rigidez de três a quatro vezes segundo CECCOTTI [1].

A leveza das estruturas mistas em concreto-madeira e o possível emprego de elementos de madeira laminada colada são fatores que contribuem para a sua produção pré-fabricada.

1.1 Sistemas de conexão em estruturas mistas de madeira e concreto

TARANTINO e DEZI [2] retratam em seus trabalhos a necessidade do estudo do sistema de ligação, responsável por transmitir a força de cisalhamento longitudinal na interface dos dois materiais combinados ao longo do comprimento da viga.

Na análise de ligações de peças de madeira, RACHER [3] ressalta a importância do sistema de ligação, visto que o seu comportamento afeta diretamente a distribuição de forças na peça e consequentemente deformações da estrutura.

Conforme SORIANO [4] o sistema de ligação, que caracteriza o comportamento de toda estrutura, pode ser denominado como rígido e semirrígido (flexível), Figura [1].

Um exemplo de conexão rígida é a utilização de adesivo estrutural epóxi, ao longo de toda superfície de contato entre os dois materiais, GIRHAMMAR e GOPU [5]. A ligação rígida consiste na integração total da seção, ou seja, a seção trabalha monoliticamente. Estudos desenvolvidos no Brasil, colando diretamente vigas de madeira a peças estruturais de concreto armado, foram apresentados por NICOLAS [6]. Também SORIANO [4] ensaiou vigas mistas de madeira e concreto com seção T, onde a alma de madeira foi colada à laje de concreto.

No sistema de conexão semirrígida, a ligação entre os materiais pode ser feita através de pinos de aço, pregos, parafusos, cavilhas e perfis metálicos. A ligação semi-rígida apresenta uma integração parcial da seção, havendo deslizamento relativo entre os dois materiais.

1.2 Modelo para análise de vigas mistas

Os principais modelos matemáticos para a representação do comportamento de estruturas mistas propostos na literatura são abordados com base no princípio de equações de equilíbrio e no princípio da energia. Diferentemente das estruturas mistas em aço-concreto, para as quais existem diversas publicações, incluindo normas internacionais, como por exemplo, a BS 5400 [7], e a nacional NBR 8800/02 [8], as estruturas concreto-madeira carecem de mais referências, não possuindo nenhuma normativa nacional. Uma norma internacional que trata de estruturas mistas com madeira é o EUROCODE 5 [9].

1.2.1 Modelo para análise de vigas mistas apresentado pelo Eurocode 5

Tanto a norma EUROCODE 5 [9], quanto o DIN 1052 [10] consideram a influência do deslizamento na interface do sistema pela adoção de um produto de rigidez efetivo, $(EI)_{ef}$, calculado conforme a Equação [1], onde as variáveis são: a forma da seção transversal, o módulo de elasticidade dos materiais constituintes, espaçamento entre os conectores e módulo de deslizamento da ligação.

$$(EI)_{ef} = E_c I_c + y_c E_c A_c a_c^2 + E_w I_w + y_w E_w A_w a_w^2 \quad (1)$$

Figura 1 – Deslocamentos verticais de uma viga mista

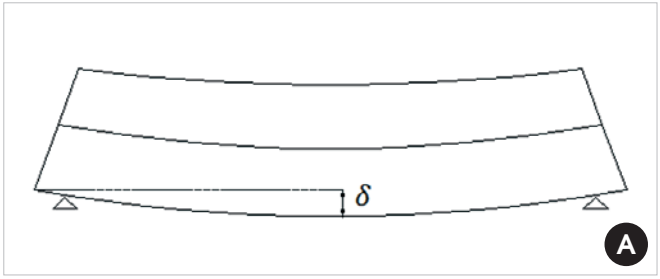

Composição rígida

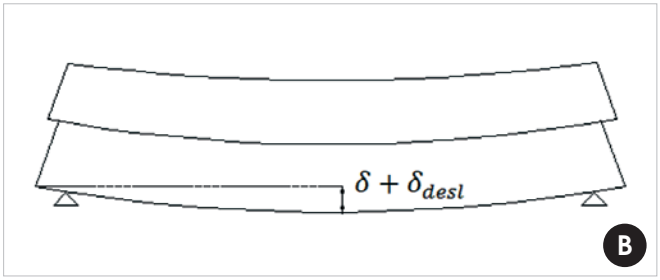

Composição semirrigida

Figura 2 – Representação de uma seção mista e das tensões normais. Fonte: adaptado do EUROCODE 5 (9)

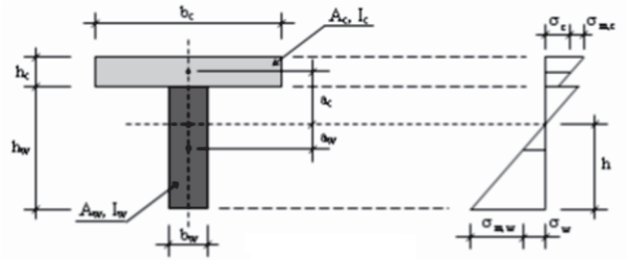

Na equação [1] E_c, E_w, I_c, I_w, A_c e A_w representam os valores médios dos módulos de elasticidade, os momentos de inércia e as áreas da seção transversal do concreto e da madeira, respectivamente; y_c é o fator parcial da mesa, calculado conforme Equação 2; $y_w = 1,0$ é o fator parcial da alma; a_c e a_w são as distâncias, calculadas conforme as Equações [3] e [4], respectivamente, Figura [2].

$$y_c = \left(1 + \frac{\pi^2 E_c A_c s}{K \cdot l^2}\right)^{-1} \quad (2)$$

$$a_c = \frac{(h_c + h_w)}{2} - a_w \quad (3)$$

$$a_w = \frac{y_c E_c A_c (h_c + h_w)}{2(y_c E_c A_c + y_w E_w A_w)} \quad (4)$$

1.2.2 Formulação variacional para vigas concreto-madeira

Neste trabalho foi utilizada a formulação de viga mista apresentada em FORTI [11] e MASCIA et al. [12]. Por ser uma formulação baseada no princípio dos trabalhos virtuais, ela pode facilmente ser empregada em um programa de computador tanto pelo método dos elementos finitos (ODEN et al. [13]) quanto pelo método dos deslocamentos matricial (GERE e WEAVER [14]).
Duas teorias para análise de vigas muito conhecidas são a teoria de viga de Euler-Bernoulli e a teoria de viga de Timoshenko (SLHESSARENKO [15]). Neste trabalho foi adotada a teoria de Euler-Bernoulli em duas dimensões.

1.2.2.1 Princípio dos trabalhos virtuais

A abordagem escolhida para a formulação de uma estrutura mista é a do princípio dos trabalhos virtuais. A viga mista é considerada como duas vigas independentes (uma de concreto e outra em madeira) conectadas. A energia de deformação da estrutura é dada como a soma das energias de deformação das duas vigas com a energia de deformação dos conectores e, por isso, o trabalho virtual das forças internas do conjunto será a soma dos três trabalhos virtuais internos individuais, ou seja, $TV_{int}^{C} + TV_{int}^{W} + TV_{int}^{S} = TV_{ext}$, onde os índices C, W e S se referem ao concreto, madeira e conectores, respectivamente.

Figura 3 -- Cinemática de uma viga mista

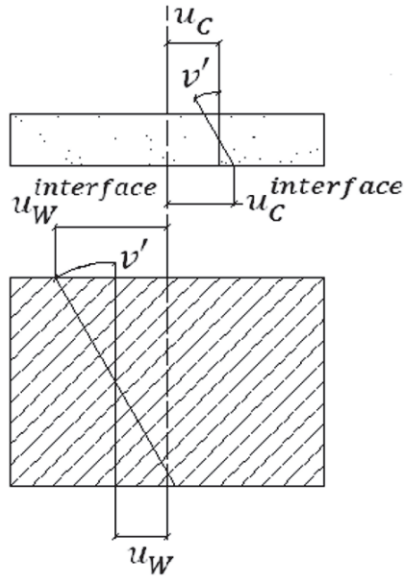

Como hipótese, assume-se que o deslocamento vertical das duas vigas é o mesmo, e por consequência suas derivadas também o são. Como a abordagem é a mesma de vigas de Euler-Bernoulli, a derivada do deslocamento vertical é igual ao giro da seção transversal, e as duas vigas têm o mesmo giro $\theta^C = \theta^W = v'(x)$. A força de cisalhamento (força por unidade de comprimento) dos conectores é dada por $Ts = K\Delta u$, em que K é o módulo de deslizamento dos conectores e Δu é o deslocamento relativo entre a fibra inferior da viga de concreto e a fibra superior da viga de madeira. A Figura [3] ilustra esse deslocamento relativo.
O deslocamento relativo (Δu) tem a expressão:

$$\Delta u = u_C^{interface} - u_W^{interface}$$

com

$$u_C^{interface} = u_C + \theta_C \frac{h_C}{2}$$

$$u_C^{interface} = u_C + \theta_C \frac{h_C}{2} \quad u_C^{interface} = u_C + \theta_C \frac{h_C}{2}$$

$$u_W^{interface} = u_W - \theta_W \frac{h_W}{2} \quad (5)$$

Visto que os giros das duas vigas são iguais, então:

$$\Delta u = u_C - u_W + v'\left(\frac{h_C + h_W}{2}\right) \quad (6)$$

Figura 4 – Conjunto de funções de base lineares por partes

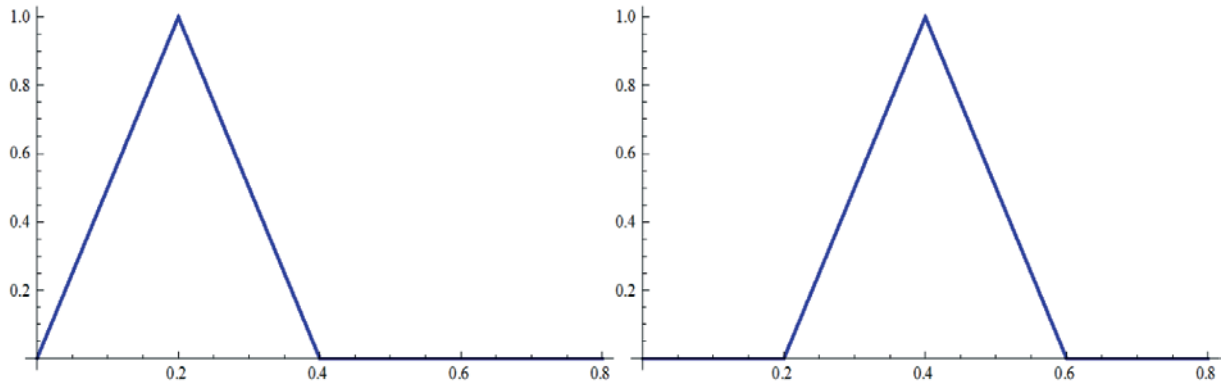

Denominando a distância entre os centros de gravidade das peças de r, tem-se

$$r = \left(\frac{h_C + h_W}{2} \right).$$

e $T_S = K\left(u_C - u_W + v'r\right)$ (7)

O trabalho virtual das forças internas do conector é dado por:

$$TV_{int}^{S} = \int_0^L T_S \, \delta\Delta u \, ds$$

$$TV_{int}^{S} = \int_0^L K\left(u_C - u_W + v'r\right)\left(\delta u_C - \delta u_W + \delta v'r\right) ds \quad (8)$$

Somando-se o trabalho virtual interno dos conectores ao do concreto e da madeira, temos a formulação de viga mista:

$$TV_{int}^{C} + TV_{int}^{W} + TV_{int}^{S} = TV_{ext}$$

em que

$$TV_{int}^{C} = \int_0^L \left(E_C A_C u_C' \delta u_C' + E_C I_C v'' \delta v'' \right) ds$$

$$TV_{int}^{W} = \int_0^L \left(E_W A_W u_W' \delta u_W' + E_W I_W v'' \delta v'' \right) ds$$

$$TV_{int}^{S} = \int_0^L K\left(u_C - u_W + v'r\right)\left(\delta u_C - \delta u_W + \delta v'r\right) ds$$

$$TV_{ext} = \int_0^L q\,\delta v\, ds + \sum_{i=1}^{N} P_i \, \delta v\left(x_i\right) \quad (9)$$

cujas incógnitas são os deslocamentos horizontais no centro de gravidade das peças $u_C(x)$ e $u_W(x)$ e o deslocamento vertical $v(x)$ e δu_C, δu_W e δv são seus respectivos deslocamentos virtuais.
Em FORTI [11], a formulação variacional é resolvida através do método de Rayleigh-Ritz. Entretanto, a solução através do método dos elementos finitos permite a aplicação de diferentes tipos de carregamentos e geometrias de vigas com mais generalidade e simplicidade de uso. Além disso, a abordagem é mais apropriada para inserção em programas de análise estrutural já existentes.

2. Método dos elementos finitos

O método dos elementos finitos consiste na utilização de funções que aproximam os deslocamentos u_c, u_w e v e também os deslocamentos virtuais δu_c, δu_w e δv. A adoção dessas funções de base aproximantes permite obter-se uma solução aproximada para o problema variacional. Neste trabalho são utilizadas duas famílias de funções, as funções lineares por partes e os polinômios cúbicos de Hermite.
As funções de base lineares por partes são definidas como sendo funções lineares que valem 1 em um dos nós da malha e zero nos demais nós. Também conhecidas como função chapéu, um exemplo de duas funções de base é apresentado na Figura [4].
Nota-se que a função tem valores diferentes de zero em uma região formada por 3 nós e vale zero no restante do domínio. Se

Figura 5 – Funções de forma lineares do elemento

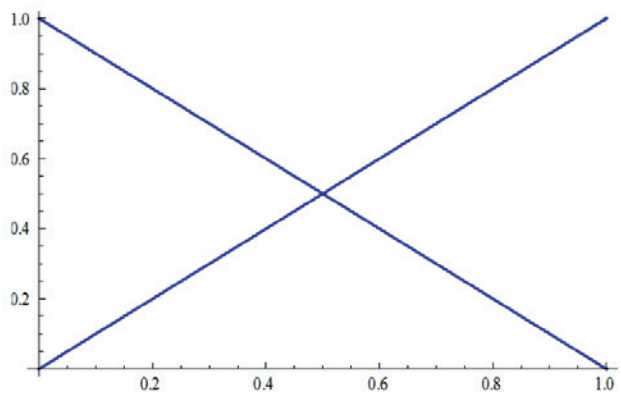

Figura 6 – Funções de forma cúbicas de Hermite de um elemento

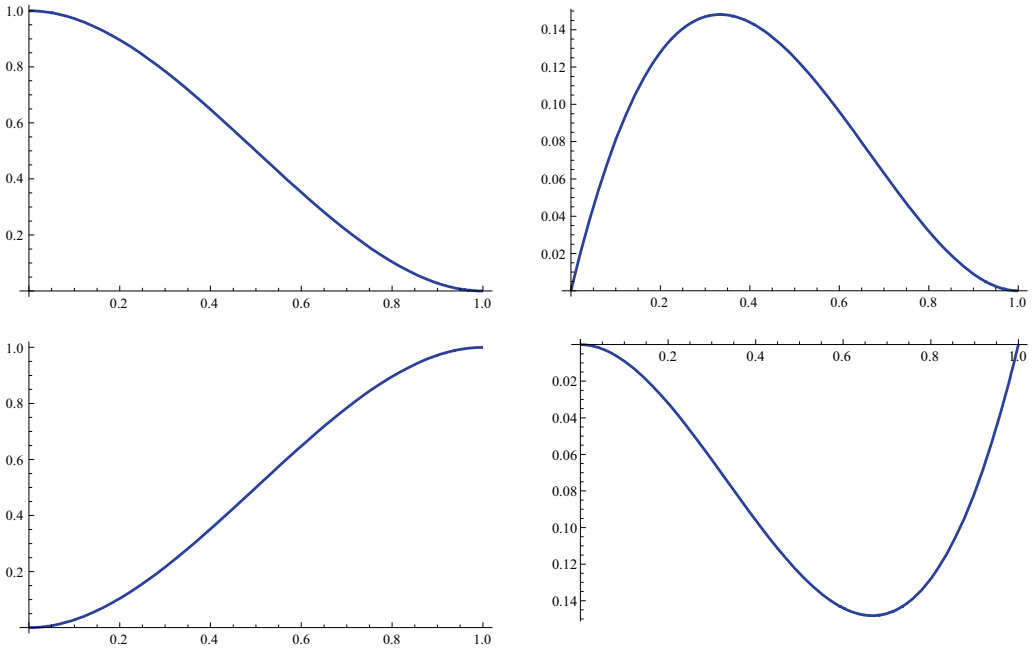

cada elemento é constituído por 2 nós, logo a função tem suporte local a 2 elementos e cada elemento contribui com as seguintes 2 funções, as quais são chamadas de funções de forma do elemento (Figura [5]). O suporte local das funções será utilizado na construção da matriz de rigidez local do elemento.

A combinação das funções de forma dos elementos constroi as funções de base aproximantes. As funções definidas têm como derivada funções constantes por partes. Logo, a derivada da função é descontínua entre elementos. Portanto, a derivada da função linear por partes adotada é integrável no domínio, mas sua segunda derivada não seria definida nos nós dos elementos.

As funções cúbicas de Hermite são também definidas por partes com suporte local ao elemento e seus vizinhos. As propriedades das funções cúbicas de Hermite envolvem o valor da função e suas derivadas. As funções de forma de um elemento são mostradas na Figura [6].

A primeira função tem a propriedade de valer 1 no nó inicial do elemento e zero no nó final. Adicionalmente, sua derivada vale zero tanto no nó inicial quanto no nó final. A segunda função vale zero nos nós e tem derivada unitária no nó inicial e zero no final. A terceira função tem valor unitário no nó final e a quarta função tem derivada unitária no nó final, tendo zero para os demais valores de função e derivadas. Essas funções são particularmente importantes porque compõem, em conjunto com os elementos vizinhos, funções cuja primeira derivada é contínua. Logo, essas funções são integráveis até a segunda derivada.

A formulação de elementos finitos é obtida substituindo-se as funções deslocamento pelas funções aproximantes, isto é, $u_w \cong \sum_{j=1}^{n} \alpha_j \varphi_j$, d $u_w \cong \sum_{j=1}^{n} \beta_j \varphi_j$ e $v \cong \sum_{j=1}^{m} \gamma_j \phi_j$. Da mesma forma, os deslocamentos virtuais são aproximados pelas mesmas funções. Logo, cada deslocamento virtual δu_c é adotado como igual a cada φ_i e assim por diante. Assim, temos:

$$TV_{ic}^{C} + TV_{iw}^{F} + TV_{iw}^{S} = TV_{ei}$$

em que

$$TV_{ic}^{C} = \int_0^L \left(E_C A_C \left(\sum_{j=1}^{n} \alpha_j \varphi_j' \right) \varphi_{i,c}' + E_C I_C \left(\sum_{j=1}^{m} \gamma_j \phi_j'' \right) \phi_i'' \right) ds$$

$$TV_{iw}^{F} = \int_0^L \left(E_W A_W \left(\sum_{j=1}^{n} \beta_j \varphi_j' \right) \varphi_{i,w}' + E_W I_W \left(\sum_{j=1}^{m} \gamma_j \phi_j'' \right) \phi_i'' \right) ds$$

$$TV_{iw}^{S} = \int_0^L K \left(\left(\sum_{j=1}^{n} \alpha_j \varphi_j \right) - \left(\sum_{j=1}^{n} \beta_j \varphi_j \right) + \left(\sum_{j=1}^{m} \gamma_j \phi_j' \right) r \right) \left(\varphi_{i,c} - \varphi_{i,w} + \phi_i' r \right) ds$$

$$TV_{ei} = \int_0^L q \phi_i \, ds + \sum_{i=1}^{N} P_i \phi_i(x_i)$$

(10)

A formulação variacional requer o cálculo de integrais que envolvem a primeira derivada dos deslocamentos horizontais u_c e u_w. Desse modo, podemos ver que as funções lineares por parte (chapéu) atendem aos requisitos necessários para aproximar os

deslocamentos horizontais, já que suas primeiras derivadas são integráveis em todo o domínio. Portanto, adotamos φ_j como sendo as funções lineares por partes, em que cada j diz respeito a um dos nós da malha. O deslocamento vertical, entretanto, requer que sua segunda derivada seja integrável, para se atender a formulação variacional de viga mista. Temos, portanto, que as funções cúbicas de Hermite são candidatas a ϕ_j já que elas têm segunda derivada integrável. Neste trabalho adotamos as funções de Hermite como função de forma para o deslocamento vertical v. É interessante observar que na formulação de viga de Euler-Bernoulli, o giro da seção é igual à primeira derivada da flecha, ou seja, $\theta = v'$. Assim, podemos entender que a primeira e terceira funções de Hermite apresentadas na Figura [6] se referem ao deslocamento vertical, enquanto a segunda e quarta são associadas ao giro, pois são funções com derivada unitária nos nós.

Como as funções aproximantes tem suporte local aos 2 elementos ligados ao nó, as integrais de 0 a L, de fato são feitas apenas sobre os elementos de suporte da função. Essa formulação pode ser escrita, em forma matricial como:

$$[K]\{u\} = \{F\} \tag{11}$$

em que a matriz K é composta pela soma das matrizes de cada elemento. O vetor u é dado por:

$$u = \left\{u_c^1, u_w^1, v^1, v'^1, u_c^2, u_w^2, \ldots, u_c^n, u_w^n, v^n, v'^n\right\}^T \tag{12}$$

que é a união dos deslocamentos horizontal, vertical e giro de cada nó da malha $\{u_c, u_w, v, v'\}$. A descrição das matrizes de cada elemento é apresentada a seguir.

2.1 Matriz de rigidez do elemento

A matriz de rigidez é apresentada em partes, relativas a cada um dos termos do trabalho virtual interno: concreto, madeira e conector. A matriz de rigidez associada ao concreto é dada pela expressão:

$$K_{ij}^c = \int_0^L \left(E_C A_C \varphi_j' \varphi_{i,c}' + E_C I_C \phi_j'' \phi_i''\right) ds \tag{13}$$

que para cada elemento da malha de tamanho L_e, dá:

$$k_{ij}^c = \int_0^{L_e} \left(E_C A_C \varphi_j' \varphi_{i,c}' + E_C I_C \phi_j'' \phi_i''\right) ds\,. \tag{14}$$

ou

$$k_e^c = \begin{bmatrix}
\frac{A_c E_c}{L_e} & 0 & 0 & 0 & -\frac{A_c E_c}{L_e} & 0 & 0 & 0 \\
0 & 0 & 0 & 0 & 0 & 0 & 0 & 0 \\
0 & 0 & \frac{12E_cI_c}{L_e^3} & \frac{6E_cI_c}{L_e^2} & 0 & 0 & -\frac{12E_cI_c}{L_e^3} & \frac{6E_cI_c}{L_e^2} \\
0 & 0 & \frac{6E_cI_c}{L_e^2} & \frac{4E_cI_c}{L_e} & 0 & 0 & -\frac{6E_cI_c}{L_e^2} & \frac{2E_cI_c}{L_e} \\
-\frac{A_c E_c}{L_e} & 0 & 0 & 0 & \frac{A_c E_c}{L_e} & 0 & 0 & 0 \\
0 & 0 & 0 & 0 & 0 & 0 & 0 & 0 \\
0 & 0 & -\frac{12E_cI_c}{L_e^3} & -\frac{6E_cI_c}{L_e^2} & 0 & 0 & \frac{12E_cI_c}{L_e^3} & -\frac{6E_cI_c}{L_e^2} \\
0 & 0 & \frac{6E_cI_c}{L_e^2} & \frac{2E_cI_c}{L_e} & 0 & 0 & -\frac{6E_cI_c}{L_e^2} & \frac{4E_cI_c}{L_e}
\end{bmatrix}$$

A matriz de rigidez associada à madeira, por sua vez, é dada por:

$$k_e^w = \begin{bmatrix}
0 & 0 & 0 & 0 & 0 & 0 & 0 & 0 \\
0 & \frac{A_w E_w}{L_e} & 0 & 0 & 0 & -\frac{A_w E_w}{L_e} & 0 & 0 \\
0 & 0 & \frac{12E_wI_w}{L_e^3} & \frac{6E_wI_w}{L_e^2} & 0 & 0 & -\frac{12E_wI_w}{L_e^3} & \frac{6E_wI_w}{L_e^2} \\
0 & 0 & \frac{6E_wI_w}{L_e^2} & \frac{4E_wI_w}{L_e} & 0 & 0 & -\frac{6E_wI_w}{L_e^2} & \frac{2E_wI_w}{L_e} \\
0 & 0 & 0 & 0 & 0 & 0 & 0 & 0 \\
0 & -\frac{A_w E_w}{L_e} & 0 & 0 & 0 & \frac{A_w E_w}{L_e} & 0 & 0 \\
0 & 0 & -\frac{12E_wI_w}{L_e^3} & -\frac{6E_wI_w}{L_e^2} & 0 & 0 & \frac{12E_wI_w}{L_e^3} & -\frac{6E_wI_w}{L_e^2} \\
0 & 0 & \frac{6E_wI_w}{L_e^2} & \frac{2E_wI_w}{L_e} & 0 & 0 & -\frac{6E_wI_w}{L_e^2} & \frac{4E_wI_w}{L_e}
\end{bmatrix}$$

Deve-se observar que as matrizes de rigidez do concreto e da madeira são, de fato, as mesmas utilizadas no método dos deslocamentos clássico em sua forma matricial. Somando-se as duas matrizes, teríamos a soma da rigidez à flexão das duas vigas (concreto e madeira) como se essas trabalhassem livres para deslizar. Não haveria nenhuma interação entre os deslocamentos horizontais da viga de concreto e a viga de madeira. A interação entre os materiais, com consequente aumento na rigidez à flexão da viga mista, é representada pela matriz de rigidez do conector. A matriz de rigidez do conector vem da equação do trabalho virtual do conector:

$$TV_{int}^S = \int_0^L K\left(u_C - u_W + v'r\right)\left(\delta u_C - \delta u_W + \delta v'r\right) ds \tag{15}$$

que, integrando-se sobre um elemento de tamanho L_e resulta em:

$$k_e^s = \begin{bmatrix}
\frac{kL_e}{3} & -\frac{kL_e}{3} & -\frac{kr}{2} & \frac{kL_er}{12} & \frac{kL_e}{6} & -\frac{kL_e}{6} & \frac{kr}{2} & -\frac{kL_er}{12} \\
-\frac{kL_e}{3} & \frac{kL_e}{3} & \frac{kr}{2} & -\frac{kL_er}{12} & -\frac{kL_e}{6} & \frac{kL_e}{6} & -\frac{kr}{2} & \frac{kL_er}{12} \\
-\frac{kr}{2} & \frac{kr}{2} & \frac{6kr^2}{5L_e} & \frac{kr^2}{10} & -\frac{kr}{2} & \frac{kr}{2} & -\frac{6kr^2}{5L_e} & \frac{kr^2}{10} \\
\frac{kL_er}{12} & -\frac{kL_er}{12} & \frac{kr^2}{10} & \frac{2kL_er^2}{15} & -\frac{kL_er}{12} & \frac{kL_er}{12} & -\frac{kr^2}{10} & -\frac{kL_er^2}{30} \\
\frac{kL_e}{6} & -\frac{kL_e}{6} & -\frac{kr}{2} & -\frac{kL_er}{12} & \frac{kL_e}{3} & -\frac{kL_e}{3} & \frac{kr}{2} & \frac{kL_er}{12} \\
-\frac{kL_e}{6} & \frac{kL_e}{6} & \frac{kr}{2} & \frac{kL_er}{12} & -\frac{kL_e}{3} & \frac{kL_e}{3} & -\frac{kr}{2} & -\frac{kL_er}{12} \\
\frac{kr}{2} & -\frac{kr}{2} & -\frac{6kr^2}{5L_e} & -\frac{kr^2}{10} & \frac{kr}{2} & -\frac{kr}{2} & \frac{6kr^2}{5L_e} & -\frac{kr^2}{10} \\
-\frac{kL_er}{12} & \frac{kL_er}{12} & \frac{kr^2}{10} & -\frac{kL_er^2}{30} & \frac{kL_er}{12} & -\frac{kL_er}{12} & -\frac{kr^2}{10} & \frac{2kL_er^2}{15}
\end{bmatrix}$$

Finalmente, a matriz de rigidez do elemento é obtida como $k = k^c + k^w + k^s$.

O vetor de carga é dado pelo trabalho virtual externo, que para este estudo é dado por:

$$TV_{ext} = \int_0^L q\,\delta v\,ds + \sum_{i=1}^{N} P_i\,\delta v(x_i) \qquad (16)$$

em que apenas cargas verticais foram consideradas, embora sua extensão para outros carregamentos seja trivial. O vetor de carga para q vertical constante no elemento é dado, portanto, por:

$$F = \left\{0\ ,0\ ,\frac{L_e q}{2},\frac{L_e^2 q}{12},0\ ,0\ ,\frac{L_e q}{2},-\frac{L_e^2 q}{12}\right\}^T \qquad (17)$$

As forças concentradas são adicionadas ao problema algébrico somando-se seu valor nas suas respectivas posições do vetor de carga.

2.2 Programa computacional

O código foi implementado em linguagem C++, utilizando-se algumas classes da biblioteca PZ (DEVLOO [16]). Para facilitar a utilização do programa, foi confeccionada uma interface gráfica para entrada de dados e visualização de resultados. A Figura [7] mostra a janela do programa com os dados de entrada a serem preenchidos. Os resultados apresentados pelo programa são o deslocamento vertical da viga mista, os esforços de momento fletor e força normal em cada viga e o cisalhamento no conector.

Tabela 1 – Propriedades dos componentes da viga mista

	Concreto	Madeira
Seção (mm²)	12.000	7500
Inércia (mm⁴)	1,6 x 10⁶	14,063 x 10⁶
E* (N/mm²)	19.300	14.700

*Módulos de elasticidade longitudinal obtido no ensaio de compressão na direção paralela às fibras
Módulo de deslizamento do conector no Estado Limite de Utilização:
K1c (ser) = 15.464 N/mm;
Espaçamento (s) = 7.5 cm.

O programa desenvolvido foi validado comparando seus resultados com os apresentados em FORTI [11]. Em FORTI [11] são apresentados resultados numéricos para a formulação variacional de viga mista e também solução analítica da equação diferencial (STEVANOVIC [17]). Os resultados são, ainda, comparados com resultados de ensaios de laboratório (SORIANO [4]), com boa concordância.

3. Resultados e discussões

O programa é aplicado em uma viga mista apresentada em FORTI [11] visando à validação do código de elementos finitos que foi implementado. Os resultados também são comparados aos obtidos com o EUROCODE 5 [9].
Os dados das análises estão descritos na Tabela [1] e nas Figuras [8] e [9]. As conexões entre os dois materiais foram feitas com 41

Figura 7 – Janela de entrada de dados

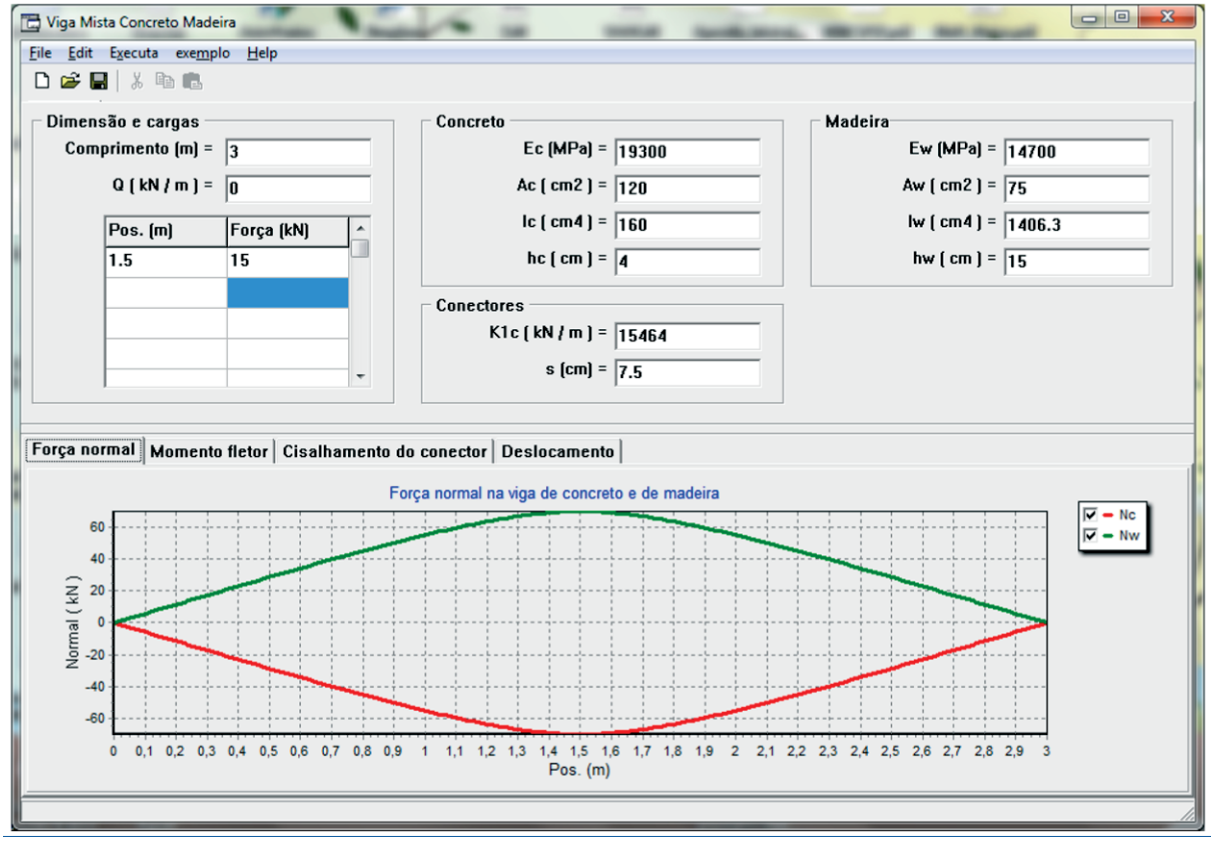

Figura 8 – Detalhe da viga mista (dimensões em cm). (SORIANO (4))

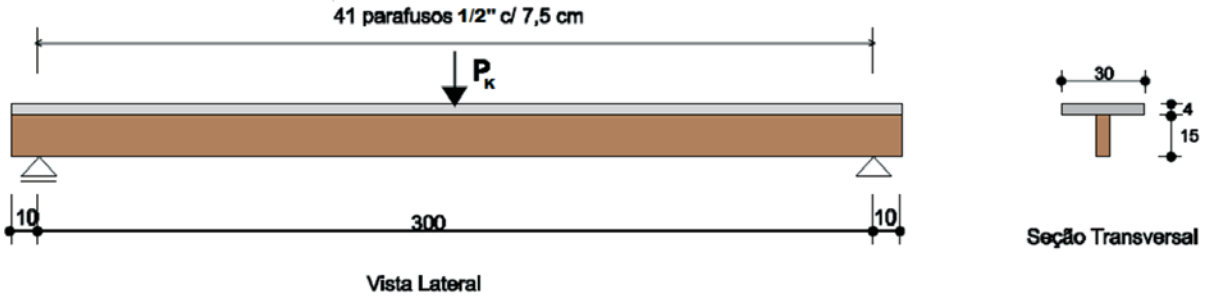

Figura 9 – Esquema estático da viga mista

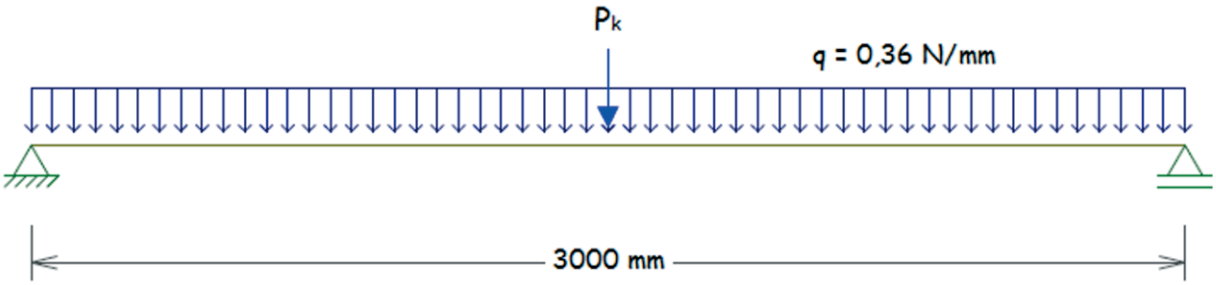

parafusos sextavados com rosca soberba 1/2", com espaçamento de 7,5 cm. A rigidez da ligações foi obtida através de ensaios de corpos-de-prova de cisalhamento. SORIANO [4] realizou ensaios com 5 corpos de prova e a média dos módulos de deslizamento de serviço foi igual a $K_{ser} = 15464\,N/mm$ e $K_u = 10309\,N/mm$ No ensaio experimental de SORIANO [4], havia duas cargas a serem consideradas (Figura [8]): uma carga uniformemente distribuída, correspondente ao peso próprio da viga q = 0,36 N/mm, e uma carga concentrada Pk, aplicada no meio do vão. O deslocamento vertical foi medido a partir da aplicação da força concentrada, ou seja, o deslocamento medido não inclui a parcela do peso próprio. Por isso, nas análises numéricas apenas a carga pontual

Tabela 2 – Resultados dos deslocamentos verticais a L / 2 da viga mista

Carga (kN)	Experimental (mm)			Numérico (mm)				Analítico (mm)	
Pk	Exp,1	Exp,2	Média	FORTI (11)	Diferença[1]	MEF	Diferença[2]	Eurocode 5	Diferença[3]
0	0	0	0	0	0 %	0	0 %	0	0 %
5	4,13	4,43	4,28	3,96	7,5 %	3,96	7,5 %	3,91	8,6 %
10	8,34	8,72	8,53	7,92	7,2 %	7,92	7,2 %	7,81	8,4 %
15	12,26	13,01	12,64	11,88	6,0 %	11,88	6,0 %	11,72	7,2 %
20	16,76	17,76	1,26	15,84	8,2 %	15,85	8,2 %	15,62	9,5 %
25	22,94	23,68	23,31	19,80	15,1 %	19,80	15,1 %	19,53	16,2 %
30	30,61	29,08	29,85	23,76	20,4 %	23,76	20,4 %	23,44	21,5 %

$$\text{Diferença}^1 = \frac{FORTI\,[11] - \text{Média experimental}}{\text{Média experimental}} \qquad \text{Diferença}^2 = \frac{MEF - \text{Média experimental}}{\text{Média experimental}}$$

$$\text{Diferença}^3 = \frac{Eurocode\,5 - \text{Média experimental}}{\text{Média experimental}}$$

Figura 10 – Gráfico do deslocamento vertical *versus* a força aplicada P_k

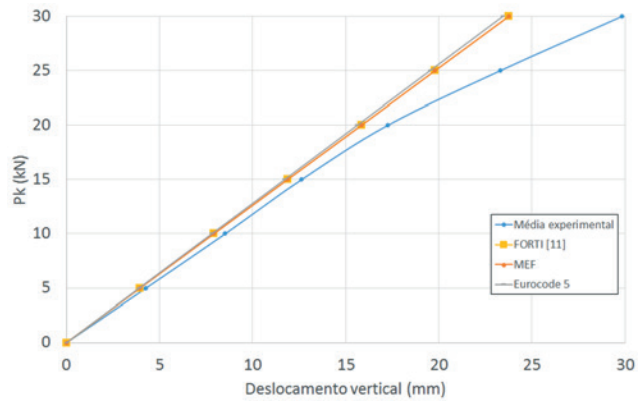

foi simulada. Esse procedimento é matematicamente válido devido à linearidade da formulação utilizada.

A Tabela [2] complementa os dados de entrada com o valor da carga pontual, a qual variou de 0 a 30 kN, e traz a comparação dos resultados obtidos neste trabalho com resultados da literatura:

1. SORIANO [4] com valores experimentais de deslocamentos da viga mista para os dois ensaios realizados (Exp.1 e Exp.2 e média dos dois experimentos). Vale observar que nos experimentos Exp. 1 e Exp. 2 o colapso da estrutura ocorreu com P_k igual a 37,811*kN* e 36,694*kN*, respectivamente;
2. FORTI [11] com valores encontrados através da formulação variacional (PTV) resolvida através do método de Rayleigh -Ritz;
3. Resultados obtidos através da implementação computacional apresentada neste trabalho (MEF);
4. Utilizando-se a formulação analítica apresentada pelo EUROCODE 5 [9], a qual define um valor de rigidez efetiva (equação 1). Para este caso a rigidez é igual a $(EI)_{ef} = 720,0542\,kN.m^2$ e o deslocamento vertical é calculado como $\frac{P_k L^3}{48(EI)_{ef}}$.

A Tabela [2] traz ainda a comparação entre os deslocamentos calculados pelas diferentes metodologias e os resultados experimentais. A Figura [10] ilustra os resultados da Tabela [2]. Observa-se que a curva dos deslocamentos dos experimentos apresenta um comportamento não-linear a partir do ponto de força P_k de $20\,kN$. Analisando a Tabela [2] pode-se observar que:

- A solução de elementos finitos (MEF) deste trabalho é igual à solução de FORTI [11]. Essa conclusão era esperada, uma vez que os dois trabalhos resolvem a mesma formulação variacional. A concordância de resultados verifica o código C++ implementado, ao menos para este exemplo.
- Os resultados numéricos são bastante próximos dos resultados experimentais, conclusão observada em FORTI [11]. Os valores diferem de menos de 10% nos estágios iniciais de carregamento. Com o aumento da carga P_k, observa-se a influência do comportamento não-linear dos materiais e o consequente distanciamento dos resultados, chegando-se a uma diferença de cerca de 20% para carga $P_k = 30\,kN$, próximo ao colapso das vigas ensaiadas. Esse resultado evidencia a qualidade da formulação variacional em representar o fenômeno físico enquanto a estrutura está em regime elástico.
- Os resultados do EUROCODE 5 [9] são muito próximos das soluções numéricas, diferentes em menos de 1.5%. Isso é uma qualidade evidente da formulação analítica, muito mais simples de ser utilizada que uma solução numérica.

Os demais resultados do programa são apresentados nas Figuras [11], [12], [13] e [14] para a simulação com a carga $P_k = 15\,kN$. A Figura [11] mostra o deslocamento vertical da viga mista.

A Figura [12] traz os gráficos de momento fletor da viga de concreto (M_c), da viga de madeira (M_w) e o momento fletor total (M_{total}) e a Figura [13] traz os gráficos de força normal. Na ausência de interação entre as vigas, a soma do momento fletor da viga de concreto com o momento da viga de madeira seria igual ao momento fletor

Figura 11 – Gráfico do deslocamento vertical apresentado pela viga mista para P_k = 15 kN

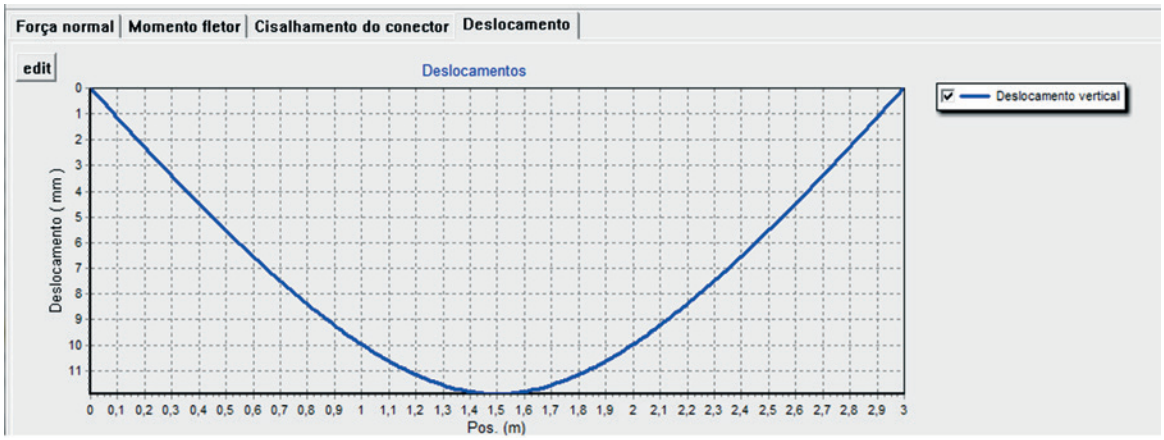

Figura 12 – Gráfico dos momentos fletores sofrido por cada camada da viga mista (concreto e madeira) e o momento fletor total da seção para P_k = 15 kN

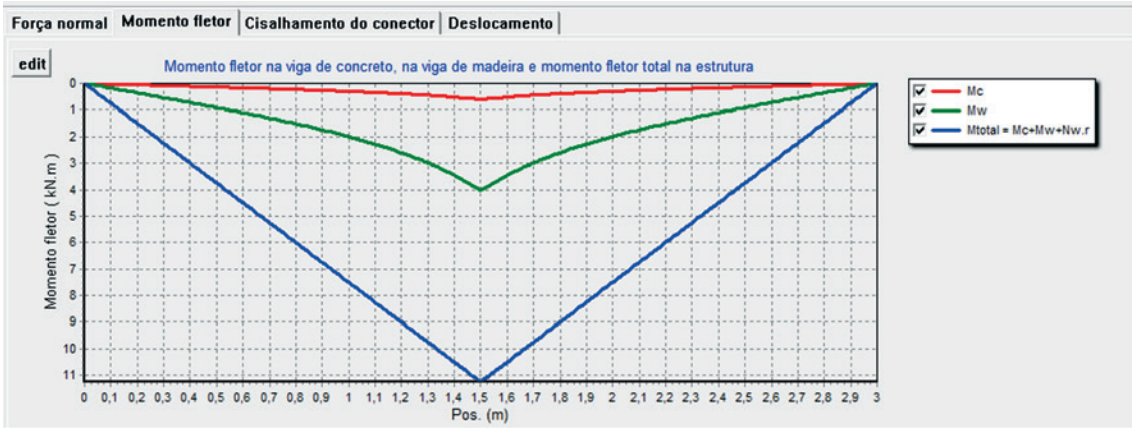

Figura 13 – Gráfico de força normal na viga de concreto e de madeira para P_k = 15 kN

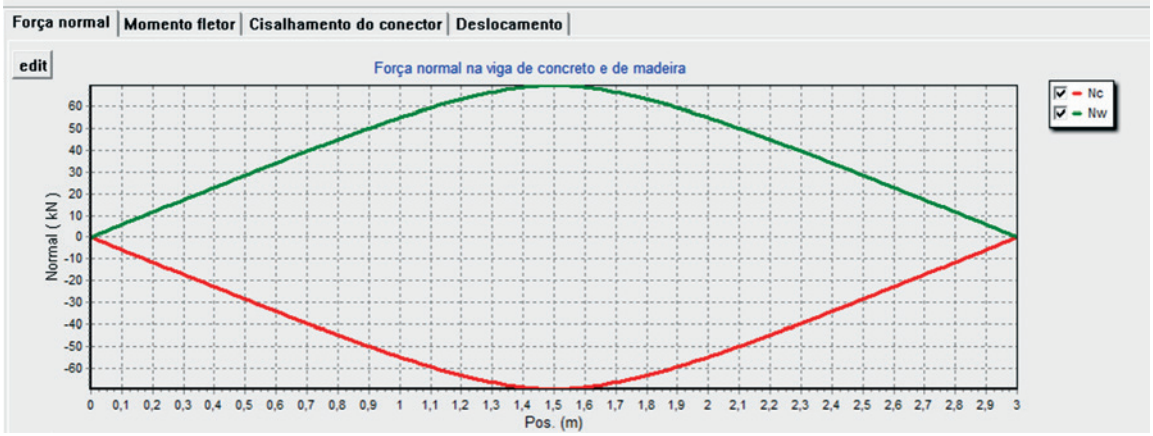

Figura 14 – Gráfico da força de cisalhamento dos conectores ao longo da viga para P_k = 15 kN

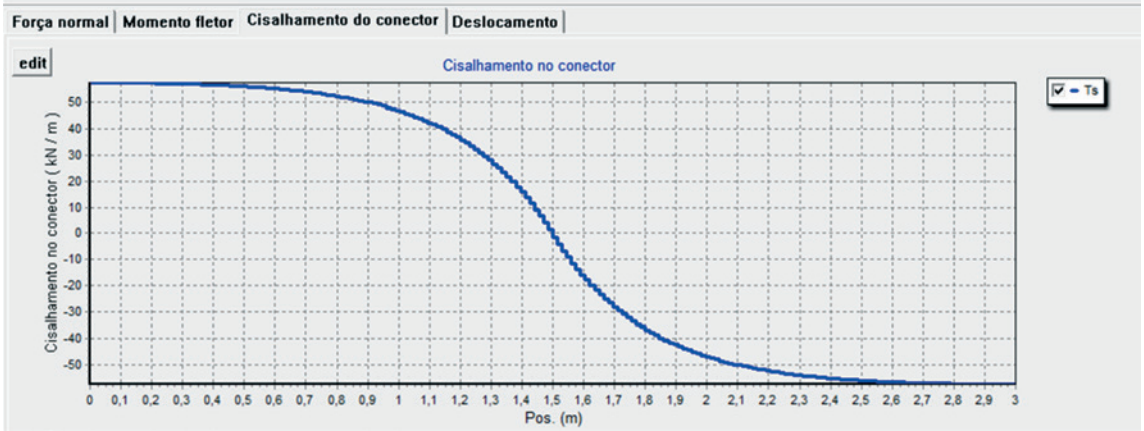

total. É interessante, portanto, observar que a interação entre as vigas reduz o momento fletor solicitante em cada uma das vigas. Em contrapartida, temos o surgimento de forças normais, que se anulam. A força normal na viga de concreto é de compressão e na viga de madeira de tração.
A Figura [14] apresenta o gráfico da força de cisalhamento dos conectores.

4. Conclusão

O desenvolvimento tecnológico do processo de concepção e construção de estruturas em madeira permitiu melhorar o conhecimento do comportamento desse material e seu consequente emprego em estruturas mistas. A aplicação de estruturas em concreto e madeira permite o uso racional das melhores características de cada material.
Este trabalho contribui com a análise de vigas mistas de concreto e madeira. Duas abordagens de cálculo do estado de tensão da viga são comparadas. Uma baseada em uma formulação de elementos finitos e outra com base em modelo analítico da norma Eurocode 5.
A formulação variacional, baseada no princípio dos trabalhos virtuais, contabiliza a energia de deformação dos três principais componentes da viga mista, o concreto armado, a madeira e os conectores. Ela é consistente e satisfaz as equações de equilíbrio. A formulação é coerente com os resultados de ensaios de laboratório.
O procedimento de cálculo do Eurocode 5 é baseado em uma rigidez equivalente da viga mista, a qual é função dos componentes da viga, em especial do módulo de deslizamento dos conectores.
A implementação em elementos finitos permite um maior emprego dessa formulação em programas de cálculo estrutural. Um programa com interface gráfica foi desenvolvido e está disponibilizado à comunidade.
Foram feitos exemplos numéricos comparando-se os resultados do programa de elementos finitos com os da metodologia de cálculo do Eurocode 5. Observa-se uma grande concordância dos resultados, os quais diferem em menos de 1.5%.
Esse desenvolvimento permite, através do desenvolvimento do programa computacional, uma maior divulgação dos procedimentos de cálculo e do comportamento de vigas mistas, o que pode ser um catalisador do emprego desse tipo de estrutura.
A formulação de elementos finitos apresentada pode ser aplicada para diferentes composições estruturais como, por exemplo, uma estrutura em que a alma da viga é metálica e sua mesa de concreto.

5. Referências bibliográficas

[1] CECCOTTI, A. Timber-concrete composite structures. In: Timber Engineering - STEP1. BLASS, H. J., AUNE, P., CHOO, B.S. et al., Almere: Centrum Hout, 1995, E13, p.1-12.

[2] TARANTINO, A. M., DEZI, L. Creep effects in composite beams with flexible shear connectors. Journal of Structural Engineering- ASCE, New York, n. 8, v.118, p.2063-2081. Aug. 1992.

[3] RACHER, P. Mechanical timber joints - general. In: Timber Engineering - STEP lecture C1. BLASS, H. J., AUNE, P., CHOO, B.S. et al., Almere: Centrum Hout, 1995, C1, p.1-10.

[4] SORIANO, J. Estruturas mistas de concreto e madeira: Análise de vigas e painéis e aplicações na construção civil. In Tese (Doutorado em Engenharia Civil) – Faculdade de Engenharia Civil, Universidade Estadual de Campinas, 2001.

[5] GIRHAMMAR, U. A., GOPU, V. K. A. Composite beam-columns with interlayer slip-exact analysis. Journal of Structural Engineering- ASCE, New York, n. 4, v.119, p.1265-1282. Apr. 1993.

[6] NICOLAS, E. A. Estudo de ligações em estruturas mistas de concreto-madeira. Universidade Estadual de Campinas – Faculdade de Engenharia Civil, Dissertação, 2001, p 103.

[7] BS 5400-5: Steel, concrete and composite bridges. Code of practice for design of composite bridges. (AMD 3998) (withdrawn), 1979

[8] NBR 8800: Projeto de Estruturas de aço e de estruturas mistas de aço e concreto de edifícios. Setembro, 2008.

[9] EUROCODE 5 (prEN 1995-1-1): Design of timber structures. Part 1-1: General – common rules and rules for buildings. Brussels, 2008.

[10] DIN 1052: Structural use of timber – part 1, 2 and 3. Berlin, 1988.

[11] FORTI, N. C. S. Análise numérica de vigas mistas em concreto e madeira. 2004. Tese (Mestrado) – Faculdade de Engenharia Civil, Universidade Estadual de Campinas, Campinas, 2004.

[12] MASCIA, NILSON T.; FORTI, NÁDIA C.S. ; SORIANO, JULIO ; NICOLAS, ELIAS A. ; FORTI, TIAGO L.D. . Study of concrete-timber composite beams using an analytical approach based on the principle of virtual work and experimental results. Engineering Structures, v. 46, p. 302-310, 2013.

[13] ODEN, J. T., CAREY G. F. e BECKER E. B. Finite Elements – An introduction. Vol 1. Prentice Hall Inc. USA. 1981.

[14] GERE, J. M. e WEAVER, W. Analysis of framed structures. 1965.

[15] SLHESSARENKO, F. L. - Análise tridimensional de edifícios por elementos finitos utilizando programação orientada a objetos. 1997. Tese (Mestrado) – Faculdade de Engenharia Civil, Universidade Estadual de Campinas, Campinas, 1997.

[16] DEVLOO, P. R. B. . PZ An Object Oriented Environment For Scientific Programming. COMPUTER METHODS IN APPLIED MECHANICS AND ENGINEERING, v. 150, n.1-4, p. 133-153, 1997.

[17] STEVANOVIC, B. Elastically coupled timber-concrete beams. In INTERNACIONAL WOOD ENGINEERING CONFERENCE, 1996, New Orleans. Proceedings... New Orleans, Oct. 1996. v.3. p.425-430.

Volume 8, Number 4 (August 2015) p. 529-546 • ISSN 1983-4195
http://dx.doi.org/10.1590/S1983-41952015000400007

REVISTA IBRACON DE ESTRUTURAS E MATERIAIS
IBRACON STRUCTURES AND MATERIALS JOURNAL

Use of Electrochemical Impedance Spectroscopy (EIS) to monitoring the corrosion of reinforced concrete

Uso da Espectroscopia de Impedância Eletroquímica (EIE) para monitoramento da corrosão em concreto armado



D.V. RIBEIRO [a]
verasribeiro@hotmail.com

C.A.C. SOUZA [b]
caldassouza@hotmail.com

J.C.C. ABRANTES [a]
jabrantes@estg.ipvc.pt

Abstract

Electrochemical techniques are among the most commonly techniques used for the evaluation and study of corrosion in reinforced concrete, including electrochemical impedance spectroscopy (EIS). Electrochemical impedance spectroscopy (EIS) is a powerful technique for characterizing a wide variety of electrochemical systems and for determining the contribution of electrode or electrolytic processes in these systems. The analysis of EIS results on samples of concrete is highly complex due to overlapping arcs from simultaneous phenomena and noise measurement, of course, associated with the heterogeneity of the samples and that complicate the analysis considerably. Thus, this paper proposes a new form of analysis based on the characteristic relaxation angular frequency, w, of each phenomenon and associating the typical capacitances and frequencies.

Keywords: corrosion, spectroscopy, concrete, durability, electrochemical techniques.

Resumo

Entre as técnicas mais utilizadas para a avaliação e estudo da corrosão em concreto armado estão as técnicas eletroquímicas, entre elas a espectroscopia de impedância eletroquímica (EIE). A EIE é uma técnica poderosa para a caracterização de uma grande variedade de sistemas eletroquímicos e para a determinação da contribuição de processos individuais de eletrodo ou eletrólito nestes sistemas. A análise dos resultados de EIE em amostras de concreto armado é de alta complexidade, devido à sobreposição de arcos provenientes de fenômenos simultâneos e a ruídos da medida, associados, evidentemente, à heterogeneidade das amostras e que dificultam de forma considerável esta análise. Assim, o presente trabalho propõe uma nova forma de análise, baseada na frequência angular de relaxação característica, w, de cada fenômeno e associando às capacitâncias e frequências típicas.

Palavras-chave: corrosão, espectroscopia, concreto, durabilidade, monitoramento.

[a] *Universidade Federal da Bahia, Departamento de Ciência e Tecnologia de Materiais, Escola Politécnica, Salvador, BA, Brasil;*
[b] *UIDM, EST G, Polytechnic Institute of Viana do Castelo, Viana do Castelo, Portugal.*

Received: 09 Sep 2014 • Accepted: 09 Jun 2015 • Available Online: 7 Aug 2015

1. Introduction

The term “corrosion of reinforced concrete” refers not only to the reinforcement corrosion problems, but also to conditions of greater or lesser rebar protection by concrete itself.

The protection of the steel by concrete is done in two ways: by a physical barrier, by the covering layer and due to chemical action that results from typical pH of concrete to allow the development of a passivation film on the rebar. Despite this dual protection, there are several factors or conditions that lead to the development of the corrosion process in the concrete, such as reduced coating thickness, low resistance of the concrete coating to penetration of CO_2, water and salts, poor compaction or vibration of concrete, presence of contaminants salts or gases such as SO_2 or CO_2, presence of sulfate-reducing bacteria, reduced amount of cement or elevated water/cement ratio.

The corrosion process in reinforced concrete is a “camouflaged” phenomenon, that is, the first signs of corrosion only appear long after the process began and spread, and therefore , their early identification is very difficult.

Several techniques can be employed for evaluation and study of corrosion in reinforced concrete, and among the most used are the electrochemical techniques. These techniques, besides analyze corrosion as a electrochemical phenomenon and therefore present greater reliability, have the advantage of being fast and not igniting serious damage to the structure at the time of application; in addition it can be used both in the laboratory and in the field.

Electrochemical impedance spectroscopy (EIS) is a powerful technique for characterizing a wide variety of electrochemical systems and for determining the contribution of electrode or electrolytic processes in these systems. It can be used to investigate the dynamics of linked or mobile charges on the volume of interface regions or any liquid or solid material, and assumes that a more or less elaborate circuit can represent the behavior of the steel within the concrete.

According to MONTENOR [1], the impedance of an electrical circuit is the measure of its opposition to an electrical signal (potential or current). It is a combination of passive elements of an electrical circuit: resistance, capacitance and inductance. The EIS technique works in the frequency domain and is based on the concept that an interface can be seen as a combination of passive electrical circuit elements, i.e., resistance, capacitance and inductance. When an alternating current is applied to these elements, the resulting current is obtained using Ohm’s law. However, due to the concrete heterogeneity, the analysis results of EIS become very difficult because there is a large overlap of arches from simultaneous phenomena and the measurement noise. This study aims to present an alternative of analysis to this powerful technique.

2. The Electrochemical Impedance Spectroscopy (EIS)

The principle of this technique is to apply an alternating signal of small amplitude (5 to 20 mV) to an electrode (rebar) inserted into an electrolyte (concrete), as observed in Figure 1.

The initial disturbance (applied) and the response of the electrode is compared by measuring the phase shift of the current and voltage components and by the measurements of their amplitudes. This can be done in the time domain or in the frequency domain, using a spectrum analyzer or frequency response analyzer, respectively. Importantly, the initial disturbance is a disturbance potential (ΔE) of sinusoidal type, which must be imposed at steady state of the system and the electrode response is a current (ΔI), also sinusoidal, but with a difference of phase (Φ) to the applied signal [2]. Therefore, the impedance which is represented by Z, measures the relationship between ΔE and ΔI.

The EIS technique works in the frequency domain and is based on the concept that an interface can be seen as a combination of passive electrical circuit elements, i.e., resistance, capacitance and inductance. When an alternating current is applied to these elements, the resulting current is obtained using Ohm’s law.

For the steel/concrete system, information on several parameters can be obtained, e.g., the presence of surface films, characteristics

Figure 1 – Apparatus for measuring the corrosion process by electrochemical impedance spectroscopy (EIS)

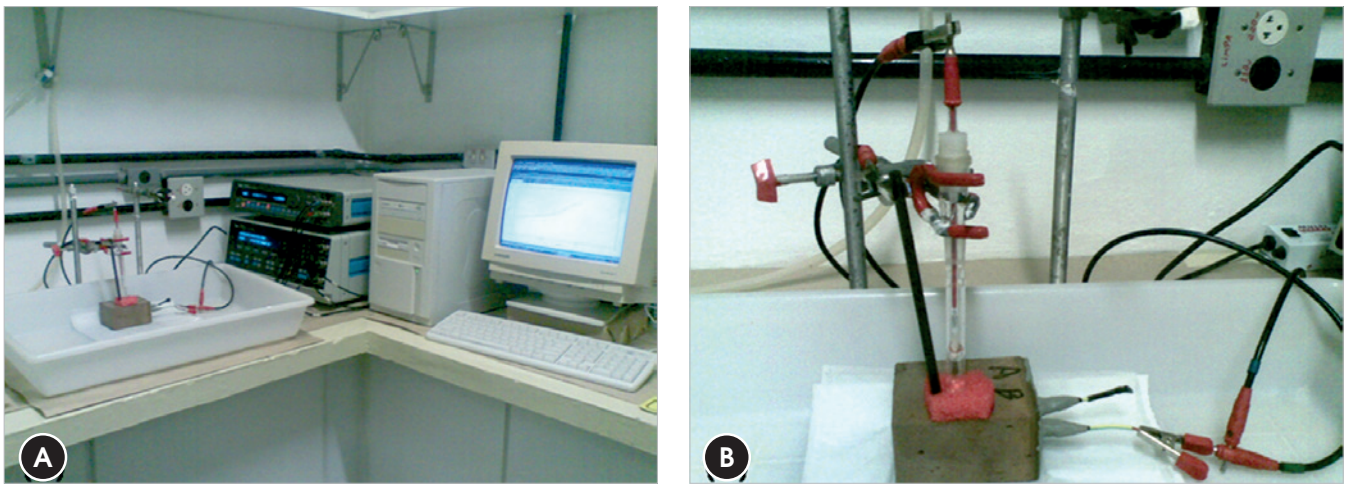

Figure 2 – Nyquist diagram and its equivalent circuit, showing the effect of diffusional impedance (SILVERMAN apud FREIRE (5))

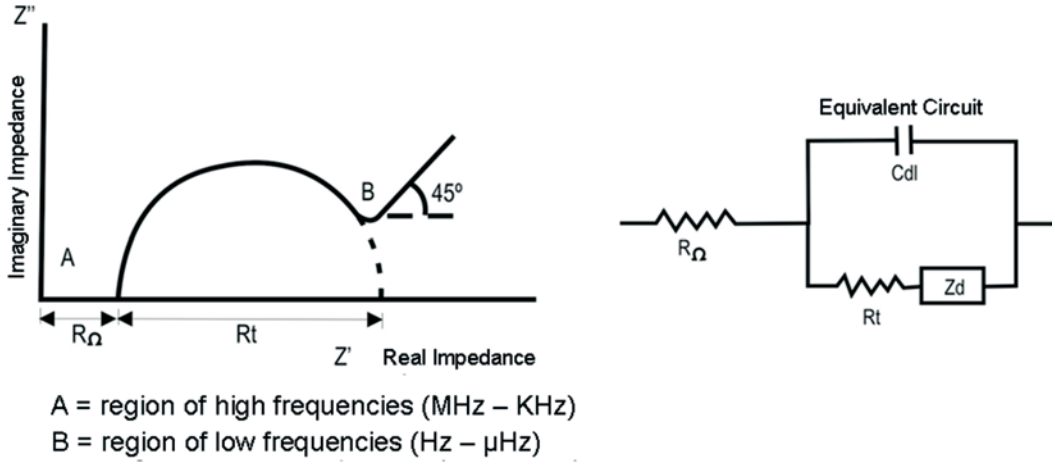

of the concrete, interfacial corrosion, and mass transfer phenomena. However, interpreting the results may be difficult and the use of an equivalent circuit, which can change according to the conditions of the steel, makes the technique more suitable for laboratory studies [1]. The main advantages of EIS are:

- It provides information about the corrosion kinetics.
- It is an accurate and reproducible technique suitable for highly resistive environments such as concrete.
- It provides data about the electrochemical control mechanism, indicating if corrosion occurs by activation, concentration or diffusion.
- It characterizes the state of the rebar and the morphology of the corrosion.
- It is a non-destructive and non-perturbative technique, since the signals applied are of small amplitude, so the corrosion potential is not changed; and
- It allows for monitoring of the evolution of the passive or active state over time.

2.1 *Interpretation of results*

The interpretation of the EIS measures is usually done by the correlation between the impedance data and the equivalent circuit representing the physical processes taking place in the system under investigation or through graphics.

The graph Z = Z' + jZ'' real part and imaginary part, respectively, measured at different frequencies is called "Nyquist diagram", impedance diagram or impedance spectrum. The other representation is called "Bode diagram" which shows the logarithm of the impedance modulus (log|Z|) and the phase displacement as function of the logarithm of frequency.

The Nyquist diagram (Figure 2), also known as Argand representation or Colo-Cole representation, consists of a series of points, each of which represent the magnitude and direction of the impedance vector of a particular frequency [3]. The diagram is a complex plane of Cartesian coordinates, where the abscissa is the real part (resistive terms) and the ordinate is the imaginary part (capacitive or inductive terms). Impedance data represented on the Cartesian plane under a wide range of frequencies (100 KHz to 10 mHz, usually 10 KHz to 0.1 mHz) generate typical configurations according to the predominant electrochemical mechanism. Figure 2 shows a typical Nyquist diagram, and its equivalent circuit.

After built the Nyquist diagram, the extrapolation of the right side of the semicircle is done to find the horizontal axis. The diameter of the semicircle extrapolated in the Nyquist diagram represents the charge transfer resistance R_t equivalent to the polarization resistance (R_p) [2]. Thus, the larger the diameter of the semicircle the higher the resistance, R_p, and hence, the lower the corrosion rate [4].

One of the difficulties of the impedance technique clearly evidenced in the Nyquist diagram is the characterization of an essentially passive rebar. In this state, the charge transfer along the rebar, which denotes a corrosion process, is very small. Thus, the capacitive semicircles or arcs of charge transfer in the electric double layer are poorly developed, compromising data interpretation [2].

The Bode diagram consists of a orthogonal axes plane, in which they have, on the ordinate axis, two quantities: the logarithm of the impedance (log|Z|) in ohms (Ω) and the phase angle (Φ) in degrees; and the abscissa axis there is the logarithm of the angular frequency (log ω) with ω in radians per second (rad/sec). It can also represent the abscissa the logarithm of the frequency (log f), with f in Hertz. With the configuration logω versus |Z| can be determined Rω and Rt, according to Figure 3; and by the phase angle versus logω it is possible to determine the capacitance of the electrical double layer Cdl, knowing that:

$$Rp = 2.|Z|.tgmax \quad (1)$$

Figure 3 – Bode diagram representing the impedance (modulus and phase angle) of an electrochemical corrosion system as a function of the angular frequency (3)

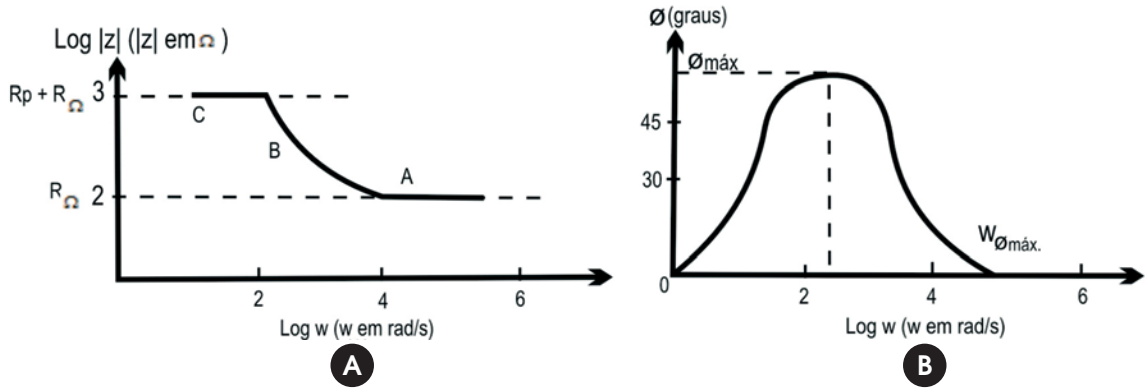

$$\omega_{\phi_{máx}} = \frac{1}{C_{dl}.R_P.(1+R_P/R_\Omega)^{1/2}} \quad (2)$$

, where: ϕ_{max} is the maximum phase angle of the system impedance, $\omega_{\phi max}$ is the angular frequency corresponding to the ϕ_{max} and |Z| is the impedance module matching to ϕ_{max}.

In the Bode diagram there are two clearly different regions: the high frequency region (Figure 3A, the region A) characterized by the presence of passivation films and other types of coating on the rebar; the medium frequency region (Figure 3A, region B) which reflects the change of electrical conductivity of the coating during exposure in a corrosive environment and, finally, the low-frequency region (Figure 3A, region C) where the corrosion reaction on the metal/coating interface can be studied [2].

2.2 Equivalent circuits

A major problem in using equivalent circuits is deciding which specific equivalent circuit, among many possibilities, should be used. A corrosion process involves several simultaneous physical processes and, therefore, the equivalent circuit is composed of various circuit elements. However, one process to another, the circuit elements may also vary the manner in which they are interconnected. In Table 1 is shown the correlation between physical processes and electrical circuit elements used in EIS.

The pioneers of the use of IES to monitor corrosion in reinforced concrete was JOHN et al.[6]. These authors proposed the circuit described in figure 4 and applied the IES on concrete samples immersed in seawater. The impedance at low frequency response was related to the charge transfer process, considering that the response at high frequencies was attributed to the presence of a surface film.

Another alternative for the interpretation of the steel/concrete system was proposed by MACDONALD et al. apud FREIRE [5]. The authors described a system response based on a model of transmission lines as shown in Figure 5, where R is the resistance bar/segment; Ri is the resistance concrete/segment; Zj interfacial impedance bar/concrete.

This model assumes that the electrical properties of steel and concrete are purely resistive, with the resistivity concrete being

Figure 4 – Equivalent circuit for concrete proposed by John et al. (6). Rc: concrete strength; Rf and Cf: resistance and capacitance of the film; Zd: diffusion impedance; Rct and Cdl: charge transfer resistance and double layer capacitance

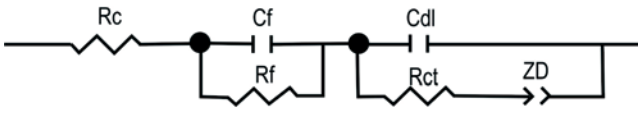

Table 1 – Properties of the components of the composite beam

Physical process	Electrical circuit element
Charge transfer	Resistors Re e Rp
Electrical double layer	Capacitor, Cdl
Dielectric surface layers (organic coatings and oxides)	14.700 Capacitor, C
Adsorption	Pseudocapacitor, Cw and resistor, R
Mass transport	Pseudocapacitor, Cw and pseudoresistor, Rw

Figure 5 – Transmission lines model described for reinforced concrete and proposed by MACDONALD et al. apud FREIRE (5)

dependent on the position due to the heterogeneity of matrix. Moreover, the model assumes that the interface is reactive due to the capacitor pseudocapacitor and diffusional components existence. The models show that the real part and the imaginary part of the impedance response and the phase angle to low frequencies allow to detect and locate the corrosion.

DHOUIBI-HACHANI et al. [7] proposed another approach shown in Figure 6, which includes the following items: (i) the products formed directly on the steel surface, (ii) products which are the result of reaction between corrosion products and the cement paste and (iii) the depth of the concrete cover.

The model shows a good agreement between the experimental data and the calculated Nyquist diagrams, where Rc is the concrete strength; R_1 represents the resistance of the corrosion products formed in the rebar; C_1 and R_4 are the capacitance and the dispersion resistance (frequency dependent); R_3 is the steel interface resistance; R_2 and C_2: capacitance and dispersion resistance due to homogeneity of the products on the metal surface.

Sometimes , despite the increasing development in the interpretation of the EIS spectra , they reveal behavior difficult to explain. These include the presence of low-frequency branches, semicircles displaced and high frequency effects. The first effect led to the introduction of a Warburg element (W) in series with the charge transfer resistance due to the replies of faradaic processes that occur at the interface . These effects explain why the steady state sometimes cannot be achieved with conventional direct current techniques (DC), even after a long waiting time. They also explain the long time constant observed in the impedance spectra at low frequencies and the need to extrapolate the polarization resistance values [1].

Figure 6 – Equivalent circuit for concrete proposed by DHOUIBI-HACHANI et al. (7)

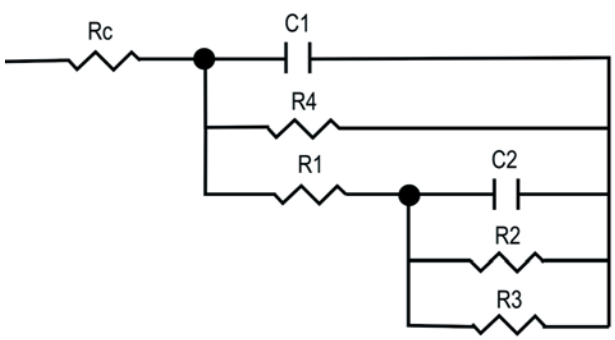

The presence of displaced semicircles suggests a non- ideal behavior of the capacitor , leading to the introduction of the constant phase element (CPE) to the equivalent circuits. SAGUES et al. [8] introduced this element in systems that show simple polarization processes. They concluded that some improvement is obtained if the CPE is used instead of an ideal capacitor. In another study, FELIU et al. [9] have proposed a more complex system and introduced a CPE and diffusion parameters in the equivalent circuit as shown in Figure 7. This has led to an increase in accuracy of determination of polarization resistance when this was possible.

The equivalent circuit proposed by Randles in Figure 8, has a wide application in many electrochemical systems. In this circuit, Re represents the solution and the corrosion product film resistances, which is also known, according SAGUES et al. [8] as the ohmic resistance of the electrolyte between the sensory point of reference electrode voltage and the electrode/electrolyte interface. R_t and C_{dl} represent the corrosion interface: Cdl is the double electric layer capacitance resulting from ions and water molecules adsorbed, due to the potential difference between the electrode suffering corrosion and the solution (or electrolyte), and Rt is the resistance to charges transfer, determining the corrosion rate of reaction and is a measure of electric charges transfer through the electrode surface. In a system controlled by activation, Rt is the portion measured by the polarization resistance technique, that is, Rt is equivalent to Rp.

In a recent study, MARTÍNEZ & ANDRADE [10] added two RC time constants, used when necessary, as can be seen in Figure 8B .

For the steel/concrete interface, the equivalent circuit is not as simple as the Randles circuit. The model proposed by CRENTSIL apud MACHADO [17] relates a semicircle at high frequencies to concrete properties. The second semi-circle, at intermediate frequencies, is attributed to the formation of corrosion products.

Figure 7 – Equivalent circuit with introduction of CPE, proposed by FELIU et al. (9). Re = electrolyte resistance; Rf = charge transfer resistance; CPE = constant phase element; ZD = Warburg diffusion

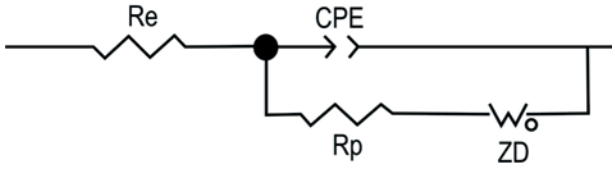

Figure 8 – (A) Simple equivalent circuit type Randles and; (B) Randles circuit modified with two time constants (10)

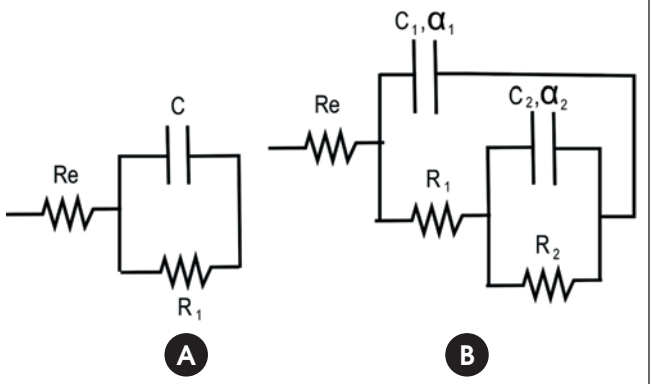

At low frequencies, the presence of a semicircle and a characteristic straight line with slope equal to one (1) involves the superposition of two effects.

concrete and the different constituents of the solid phase;

- Medium frequencies (KHz - Hz): the faradaic processes presents an answer. Typical capacitances are of the order of mF/cm^2. It may be found more than a time constant when there is a localized attack. The carbonated concrete produces a semicircle flattening in the Nyquist diagrams;
- Low frequencies (Hz - mHz): redox reactions Fe^{2+}« Fe^{3+} may occur, depending on the potential. The measured capacitances are in the order of mF/cm^2. Diffusion phenomena may appear through the passive layer.

Based on these mentioned frequencies, CHRISTENSEN et al. [11, 12] proposed a correlation between the corrosion phenomenon and the equivalent circuit and it is widely accepted in several researches. The equivalent circuit proposed by these authors is shown in Figure 10.

The equivalent diagram, presented in Figure 10, is associated to an "apparent offset" resistance (R_0) in series with the concrete (R_2Q_2) and connected also in series to the electrode (R_eQ_e). These elements are best viewed by Nyquist diagram shown in Figure 11. The variables shown in Figure 11 can be interpreted as:

- Electrode Resistance (R_e): The electrode resistance (in this case the rebar) is represented by the semicircle radius that

Figure 9 – Schematic representation of (A) steel/concrete interface; (B) equivalent circuit (m = matrix; f = film) and; (C) corresponding Nyquist diagram (4)

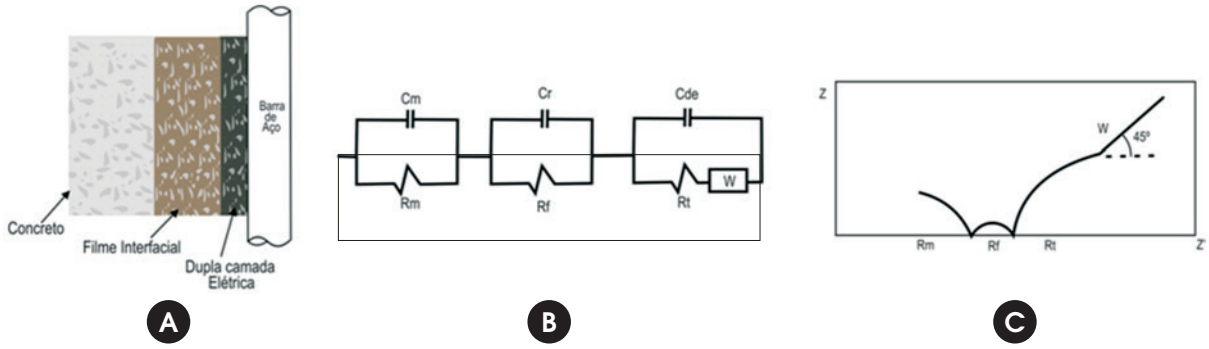

According to MACHADO [17], the semicircle reflects the corrosion kinetics effect and the straight is related to the diffusion of oxygen through the oxide layer, represented by an Warburg element, W. Figure 9 shows a schematic representation of steel/concrete interface, the equivalent electric circuit and the corresponding Nyquist diagram.

Then, it is possible to associate these three regions of the diagram to the mortar properties (matrix, m), to the interfacial film ($Ca(OH)_2$ layer) and to an interface region, with charges transfers and the double layer capacitance (interstitial solution/steel interface).

In simple terms, it´s possible to identify three frequency bands, in which different processes have an impedance response [4]:

- High frequencies (MHz - KHz): the electrolyte presents an answer. The capacitances are of the pF/cm^2 order. More than a time constant may appear due to the moisture content of the

appears in the low frequency regions. At first, the smaller this distance, the greater the corrosion;

Figure 10 – Equivalent circuit for concrete proposed by CHRISTENSEN et al. (11)

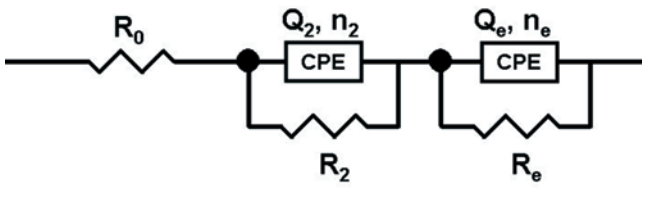

Figure 11 – (A) Nyquist diagram proposed for reinforced concrete and; (B) Expansion of the high frequency region of the previous diagram

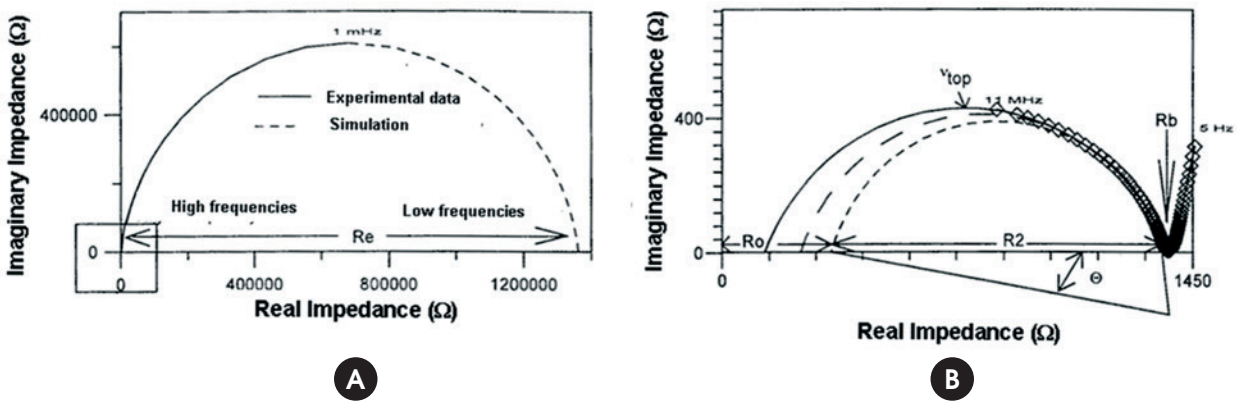

- Cement matrix of the Resistance (R_b): This value is easily detected in the impedance spectra corresponding to the intersection between the arcs regarding to electrode and the cement body itself;
- Offset Resistance (R_0): It's a "initial"resistance, without much interest for the process and no apparent physical meaning. In practical terms it can be neglected , considering $R_b = R_0 + R_2$.
- Depression angle (θ): Often expressed by the arc depression factor, n [$n = 1 - (2\theta/\pi)$], is related to the specimen imperfections, predominantly to the pore size distribution. The closer to zero (n close to 1), behaves as a perfect capacitor in the system.

As can be seen, there is a variety of equivalent circuits proposed that suit to different ways to evaluate the different materials used in the production of concrete and is an arduous task to determine an equivalent circuit that fully meets all the phenomena observed in the corrosion process.

3. Proposed method for the interpretation of EIS results

The analysis of the EIS results became increasingly complex, due to overlapping phenomena and to noise in the measurement resulting from the heterogeneity of the samples.

In view of these difficulties, we decided to change the way in which the analysis was performed. The basic theory states that these processes have a characteristic angular relaxation frequency, w (starting from which they no longer respond), which is given by $w = 1/RC$ and which can also be read graphically at the top of the arc of the impedance spectrum [13, 14]. Thus, we sought to associate the analyzable arcs with the typical capacitances and frequencies of each phenomenon.

The identified arcs were therefore isolated and related to each of the phenomena and a local analysis was performed, which improved the accuracy. A similar strategy was adopted by VERMOYAL *et al.* [13] in their studies. To this end, we used the simplified circuit shown in Figure 12.

When arcs are analyzed separately and fitted according to the simplified electrical circuit (Figure 12B), one obtains the following results: the arc resistance (R''), the values of the constant phase element (CPE), Q, and the "n" index. This index measures the perfection of this element, varying between 0 and 1, and comes closer to the unit value as the CPE approaches a perfect capacitor,

Figure 12 – Equivalent electrical circuits proposed for the steel-concrete interface, based on (A) a general analysis, and (B) analysis of individual arcs (simplified circuit) proposed by VERMOYAL et al. (13)

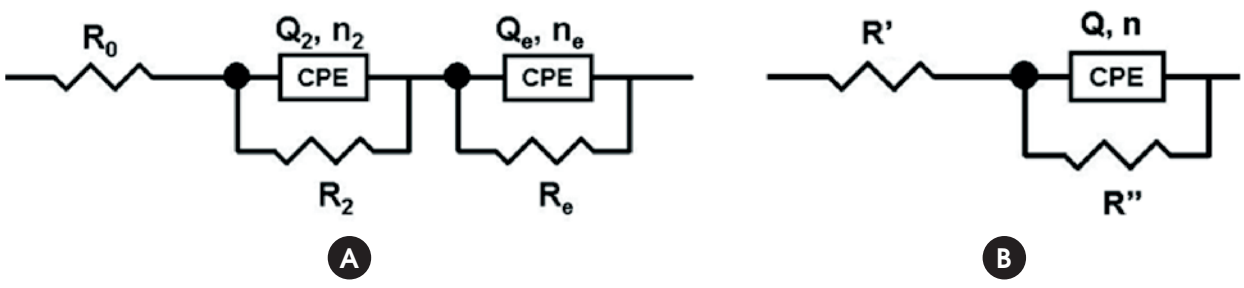

Figure 13 – Correlation between the capacitance and characteristic frequency of each phenomena observed by EIS

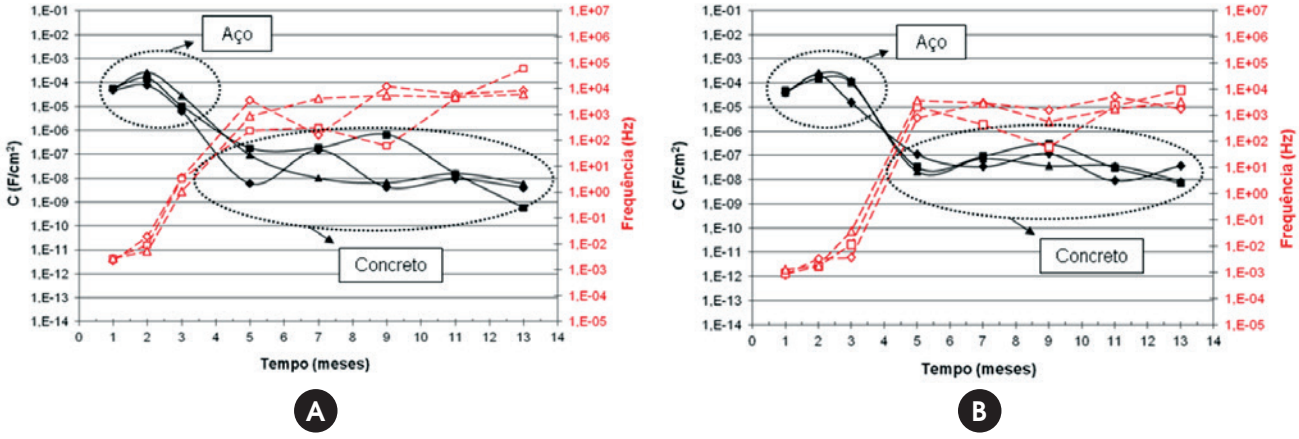

C [4, 11, 15]. Thus, the characteristic capacitance, C, can be calculated according to equation (3).

$$C = Q^{\frac{/}{n}} . R^{\frac{/-n}{n}} \quad (3)$$

The characteristic frequency (f) associated with this characteristic capacitance is calculated in Hertz, according to equations (4) and (5), where w = 1/RC [4, 14].

$$f(Hz) = \frac{w}{2\pi} \quad (4)$$

$$f(Hz) = \frac{1}{2\pi . R . C} \quad (5)$$

Observing the correlation between the characteristic capacitances and characteristic frequencies calculated for each phenomenon, it can be grouped as follows:

- Low frequencies in the range of 1 mHz to 10 Hz (10^{-3} – 10 Hz) correspond to the electrode resistance (R_e) and are thus related to the corrosion phenomenon. The characteristic capacitance of this frequency band ranges from 10^{-6} to 10^{-3} F/cm².
- Medium frequencies in the range of 100 Hz to MHz (10^{2} – 10^{6} Hz) correspond to the concrete resistance (R_2) and are related to the characteristics of the concrete surrounding and protecting the rebar. The characteristic capacitance of this frequency band lies between 10^{-9} and 10^{-6} F/cm².
- High frequencies above the MHz range (> 10^{6} Hz) are associated with the "offset resistance" (R_0), whose relevance is minor and whose values were neglected in this study.

This correlation between the characteristic capacitances and characteristic frequencies calculated for each phenomenon is shown in Figure 13. It is clearly observed that the characteristic frequencies are very well defined.

From, there, simply that the researcher associate each arch individually to the concrete resistivity (R_2) or the electrode, in the case, the rebar (Re) . This association will be based on the frequency at which the phenomenon occurs (f) or on capacitance (C). According to some studies [4, 16], the rebar is in the process of corrosion if the diameter of semicircle formed at low frequencies is decreased, as observed in the Nyquist diagram. Therefore, as lower are R_e values, more advanced is the corrosion process and the resistance of a typical electrode in a considerable corrosive process is in the order of KΩ.

4. Conclusions

This research led to the following conclusions:

- Electrochemical impedance spectroscopy (EIS) is a highly reproducible and powerful technique. However, its application is limited by the difficulties involved in interpreting EIS data and by the lack of internationally accepted criteria, indicating that this technique still lacks in-depth studies;
- The traditional analysis of the results of EIS, by direct analysis of the equivalent circuit can be very complicated due to the arcs overlapping as a function of the concrete heterogeneity, resulting in errors;
- The processes have an characteristic angular relaxation frequency, w (from which fail to respond), given by w = 1/RC , and which can also be graphically read at the top of the impedance spectrum arc;
- The relationship between the arcs observed in the spectroscopy results and the characteristic relaxation frequency proved to be an interesting alternative for the analysis of heterogeneous and complex systems such as reinforced concrete, increasing the accuracy of measurements.

- It's possible to associate each arch, individually, to the concrete resistivity (R_2) or rebar resistivity (Re), based on the frequency at which the phenomenon occurs (f) or according to its capacitance (C);
- The phenomena involved in reinforcement corrosion and the inherent characteristics of concrete are observed at low (1mHz a 10Hz) and médium (100Hz a MHz) requencies, respectively. The typical electrode resistance of an advanced corrosion process is the order of KΩ (10^3 Ω);
- The phenomena occurring at medium frequencies correspond to the concrete resistance (R_2), being associated to the matrix features that surrounds and protects the rebar and the phenomena that occur at high frequencies (higher than the MHz range), are associated with "offset" resistance (R_0), of without relevance and presenting negligible values.

5. References

[1] MONTEMOR, M. F.; SIMÕES, A.M.P.; FERREIRA, M.G.S. Chloride-induced corrosion on reinforcing steel: from the fundamentals to the monitoring techniques. Cement and Concrete Composites. v. 25, n. 4-5, p. 491-502, 2003.

[2] LANGFORD, P. BROOMFIELD, J. Monitoring the Corrosion of Reinforcing Steel. v.1, nº2. Construction Repair, p. 32-36, 1987

[3] WOLYNEC, S. Técnicas eletroquímicas em corrosão. São Paulo: EDUSP, 2003. 166 p.

[4] AGUILAR, A.; SAGÜÉS, A.; POWERS, R. Corrosion Rates of Steel in Concrete. ASTM-STP 1065, American Society for Testing and Materials, p. 66–85, 1990.

[5] FREIRE, K.R.R. Avaliação Do desempenho de inibidores de corrosão em armaduras de concreto. Curitiba, 2005. 192p. Dissertação (Mestrado), Universidade Federal do Paraná.

[6] JOHN, D.G.; SEARSON, P.C.; DAWSON, J.L. British Corrosion Journal. v. 16, p. 102, 1981.

[7] DHOUIBI-HACHANI, L.; et al. Comparing the steel-concrete interface state and its eletrochemical impedance. Cement and Concrete Research. v. 26, n. 2, p. 253-266, 1996.

[8] SAGUES, A.A.; KRANC, S.C.; MORENO, E.I. The time-domain response of a corrodyng system with constant phase angle interfacial component: application to steel in concrete. Corrosion Science. v. 37, n. 7, p.1097-1113, 1995.

[9] FELIU, V.; et al. Equivalent circuit for modelling the steel-concrete interface I: experimental evidence and theroretical predictions. Corrosion Science. v. 40, n. 6, p.975-993, 1998.

[10] MARTÍNEZ, I.; ANDRADE C. Application of EIS to cathodically protected steel: tests in sodium chloride solution and in chloride contaminated concrete. Corrosion Science. v. 50, n. 10, p. 2948–2958, 2008.

[11] CHRISTENSEN, B.J.; et al. Impedance spectroscopy of hydrating cement-based materials: measurement, interpretation, and application. Journal of the American Ceramic Society, n. 77, v. 11, p. 2789-2804, 1994.

[12] CHRISTENSEN, B.J.; MASON, T.O.; JENNINGS H.M.; Influence of silica fume on the early hydration of Portland cements using impedance spectroscopy. Journal of the American Ceramic Society, n. 75, v. 4, p. 939-945, 1992.

[13] VERMOYAL, J.J.; FRICHET, A.; DESSEMOND, L.; HAMMOU, A. AC impedance study of corrosion films formed on zirconium based alloys. Electrochimica Acta, v. 45, n. 7, p. 1039–1048, 1999.

[14] MAIA, L.F.; RODRIGUES, A.C.M. Electrical conductivity and relaxation frequency of lithium borosilicate glasses. Solid State Ionics, v. 168, n. 1-2, p. 87–92, 2004.

[15] COVERDALE, T.; et al. Interpretation of impedance spectroscopy of cement paste via computer modelling. Journal of Materials Science, v. 30, n. 20, p. 712-719, 1995.

[16] SILVA, F.G. Estudo de concretos de alto desempenho frente à ação de cloretos. 2006. 218p. Tese (Doutorado em Ciência e Engenharia de Materiais) – Área de Interunidades em Ciência e Engenharia de Materiais, Universidade de São Paulo, São Carlos, 2006.

[17] MACHADO, M.A.G.T.C. Inibidores de Corrosão em Concreto Armado contra o ataque de agentes da chuva ácida. São Carlos, 2004. 161p. Tese (Doutorado), Universidade Federal de São Carlos.

Volume 8, Number 4 (August 2015) p. 529-546 • ISSN 1983-4195
http://dx.doi.org/10.1590/S1983-41952015000400007

REVISTA IBRACON DE ESTRUTURAS E MATERIAIS
IBRACON STRUCTURES AND MATERIALS JOURNAL

Use of Electrochemical Impedance Spectroscopy (EIS) to monitoring the corrosion of reinforced concrete

Uso da Espectroscopia de Impedância Eletroquímica (EIE) para monitoramento da corrosão em concreto armado



D.V. RIBEIRO [a]
verasribeiro@hotmail.com

C.A.C. SOUZA [b]
caldassouza@hotmail.com

J.C.C. ABRANTES [a]
jabrantes@estg.ipvc.pt

Abstract

Electrochemical techniques are among the most commonly techniques used for the evaluation and study of corrosion in reinforced concrete, including electrochemical impedance spectroscopy (EIS). Electrochemical impedance spectroscopy (EIS) is a powerful technique for characterizing a wide variety of electrochemical systems and for determining the contribution of electrode or electrolytic processes in these systems. The analysis of EIS results on samples of concrete is highly complex due to overlapping arcs from simultaneous phenomena and noise measurement, of course, associated with the heterogeneity of the samples and that complicate the analysis considerably. Thus, this paper proposes a new form of analysis based on the characteristic relaxation angular frequency, w, of each phenomenon and associating the typical capacitances and frequencies.

Keywords: corrosion, spectroscopy, concrete, durability, electrochemical techniques.

Resumo

Entre as técnicas mais utilizadas para a avaliação e estudo da corrosão em concreto armado estão as técnicas eletroquímicas, entre elas a espectroscopia de impedância eletroquímica (EIE). A EIE é uma técnica poderosa para a caracterização de uma grande variedade de sistemas eletroquímicos e para a determinação da contribuição de processos individuais de eletrodo ou eletrólito nestes sistemas. A análise dos resultados de EIE em amostras de concreto armado é de alta complexidade, devido à sobreposição de arcos provenientes de fenômenos simultâneos e a ruídos da medida, associados, evidentemente, à heterogeneidade das amostras e que dificultam de forma considerável esta análise. Assim, o presente trabalho propõe uma nova forma de análise, baseada na frequência angular de relaxação característica, w, de cada fenômeno e associando às capacitâncias e frequências típicas.

Palavras-chave: corrosão, espectroscopia, concreto, durabilidade, monitoramento.

[a] *Universidade Federal da Bahia, Departamento de Ciência e Tecnologia de Materiais, Escola Politécnica, Salvador, BA, Brasil;*
[b] *UIDM, EST G, Polytechnic Institute of Viana do Castelo, Viana do Castelo, Portugal.*

Received: 09 Sep 2014 • Accepted: 09 Jun 2015 • Available Online: 7 Aug 2015

1. Introdução

A expressão “corrosão do concreto armado” refere-se não só aos problemas da corrosão da armadura, mas também às condições de maior ou menor proteção da armadura pelo próprio concreto.
A proteção do aço pelo concreto é feita de duas formas: por barreira física, pela camada de recobrimento e por ação química que resulta dos valores de pH característicos do concreto que permitem o desenvolvimento de um filme de passivação sobre a armadura.
Apesar dessa dupla proteção, vários são os fatores ou condições que conduzem ao desenvolvimento do processo corrosivo no concreto, como por exemplo, a reduzida espessura de recobrimento, baixa resistência do concreto de recobrimento à penetração de CO_2, sais e água, má compactação ou vibração do concreto, presença de sais contaminantes ou gases como o SO_2 ou CO_2, presença de bactérias redutoras de sulfato, reduzida quantidade de cimento ou elevada razão a/c.
O processo corrosivo no concreto armado é um fenômeno “camuflado”, ou seja, os primeiros sintomas de corrosão só aparecem muito depois do processo se ter iniciado e propagado e, por isso, a sua identificação precoce é muito difícil.
Diversas técnicas podem ser empregadas para avaliação e estudo da corrosão em concreto armado, e entre as mais utilizadas encontram-se as técnicas eletroquímicas. Essas técnicas, além de analisarem a corrosão como um fenômeno eletroquímico e, por isso, apresentarem maior confiabilidade, possuem a vantagem de serem rápidas e não acarretarem sérios danos à estrutura no momento da sua aplicação; além de poderem ser utilizadas tanto em laboratório quanto em campo.
A espectroscopia de impedância eletroquímica (EIE) é uma técnica poderosa para a caracterização de uma grande variedade de sistemas eletroquímicos e para a determinação da contribuição de processos individuais de eletrodo ou eletrólito nestes sistemas. Pode ser usada para investigar a dinâmica de cargas ligadas ou móveis nas regiões de volume ou de interface de qualquer tipo de material líquido ou sólido.
A técnica de impedância parte do pressuposto que um determinado circuito elétrico mais ou menos elaborado pode representar o comportamento do aço dentro do concreto.
Segundo MONTENOR [1], a impedância de um circuito elétrico representa o nível de dificuldade pelo qual um sinal elétrico (potencial ou corrente) enviado a esse circuito encontra ao percorrê-lo. É uma combinação de elementos passivos de um circuito elétrico: resistência, capacitância e indutância. No entanto, em função da heterogeidade do concreto, a análise dos resultados de EIE se torna muito árdua pois há uma grande sobreposição de arcos provenientes de fenômenos simultâneos e a ruídos da medida. O presente trabalho busca apresentar uma alternativa de análise para este poderosa técnica.

2. A Espectroscopia de Impedância Eletroquímica (EIE)

Pode-se dizer que o princípio desta técnica consiste em aplicar um sinal alternado de pequena amplitude (5 a 20 mV) a um eletrodo (armadura) inserido num eletrólito (concreto), conforme observamos na Figura 1.
Compara-se, então, a perturbação inicial (aplicada) com a resposta do eletrodo, pela medida da mudança de fase dos componentes de corrente e voltagem e pela medida de suas amplitudes. Isso pode ser feito nos domínios de tempo ou nos domínios de frequência, utilizando-se um analisador de espectro ou um analisador de resposta de frequência, respectivamente. É importante salientar que a perturbação inicial é uma perturbação de potencial (ΔE), do tipo senoidal, que deve ser imposta no estado estacionário do sistema, e a resposta do eletrodo é uma corrente (ΔI), também senoidal, porém com uma diferença de fase Φ em relação ao sinal aplicado [2]. Portanto, a impedância, que se representa por Z, mede a relação entre ΔE e ΔI.
A espectroscopia de impedância eletroquímica (EIE) é uma técnica que trabalha no domínio de frequência. O conceito básico envolvido em EIE é que uma interface pode ser vista como uma

Figura 1 – Realização do ensaio de Espectroscopia de Impedância Eletroquímica (EIE)

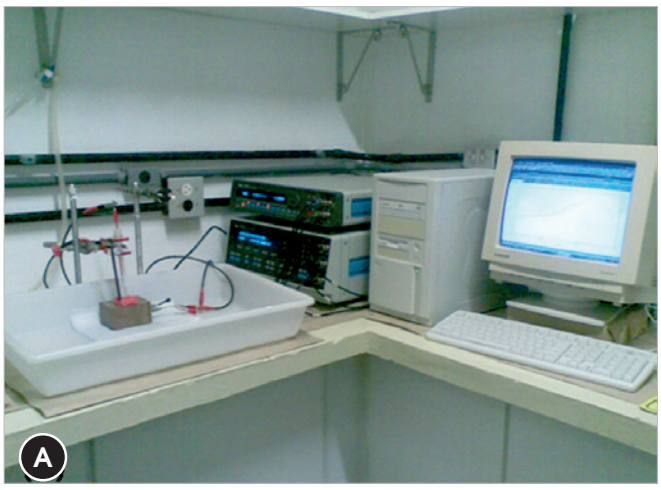

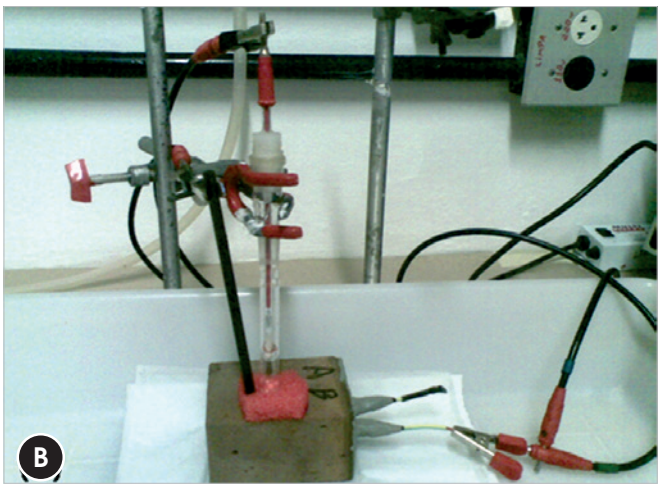

Figura 2 – Diagrama de Nyquist, com seu circuito equivalente, mostrando o efeito da impedância difusional (SILVERMAN apud FREIRE (5))

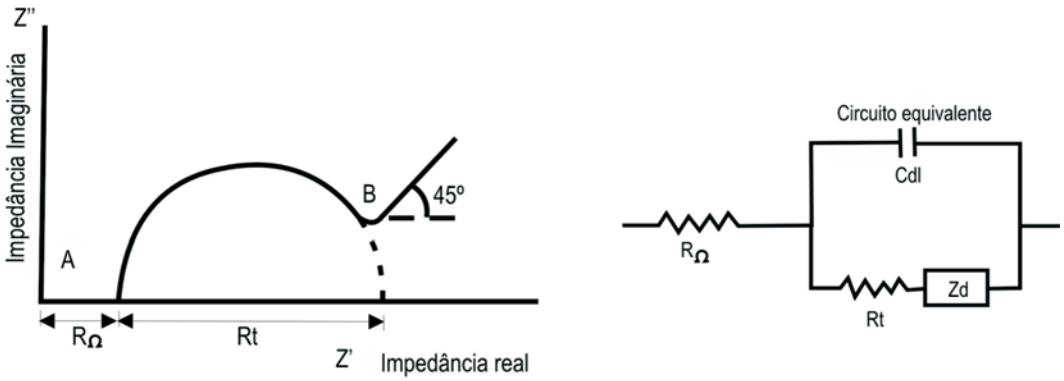

A = Região de altas frequências (100 a 70 kHz)
B = Região de baixas frequências (10^{-3} a 10^{-4} Hz)

combinação de elementos de circuito elétricos passivos, isto é, resistência, capacitância e indutância. Quando uma corrente alternada é aplicada a esses elementos, a corrente resultante é obtida usando a lei de Ohm.

Para o sistema de aço/concreto é possível obter informações sobre vários parâmetros, como a presença de filmes de superfície, características do concreto, corrosão interfacial e fenômenos de transferência de massa. Porém, a interpretação dos resultados pode ser uma tarefa difícil, e a necessidade de um circuito equivalente, que pode mudar conforme as condições do aço, torna a técnica mais satisfatória para estudos de laboratório [1]. As principais vantagens desta técnica são:

- Fornece informações sobre a cinética do processo, pela velocidade de corrosão;
- Técnica precisa e reprodutiva, apropriada para ambientes de alta resistividade como é o caso do concreto;
- Fornece dados a respeito do mecanismo de controle eletroquímico, indicando se o processo corrosivo se dá por ativação, concentração ou difusão;
- Caracteriza o estado da armadura e a morfologia da corrosão;
- Técnica não destrutiva e não perturbativa, uma vez que sinais aplicados são de pequena amplitude, de forma que o potencial de corrosão não é alterado;
- Permite o acompanhamento da evolução do estado passivo ou ativo ao longo do tempo.

2.1 Interpretação dos resultados

A interpretação das medidas de EIE geralmente é feita pela correlação dos dados de impedância com um circuito elétrico equivalente que representa os processos físicos que estão ocorrendo no sistema em investigação ou por meio de gráficos.

O gráfico Z = Z' + jZ'', parte real e parte imaginária, respectivamente, medido a diferentes frequências é chamado de diagrama de "Nyquist", diagrama de impedância ou espectro de impedância. A outra representação é chamada de "Bode", que apresenta o logaritmo do módulo da impedância (log|Z|) e o deslocamento de fase como função do logaritmo da frequência.

O diagrama de Nyquist (Figura 2), também conhecido como representação de Argand ou Colo-Cole, consiste em uma série de pontos, cada um representando a grandeza e a direção do vetor de impedância para uma frequência em particular [3]. O diagrama é um plano complexo (real imaginário) de coordenadas cartesianas, em que se tem na abscissa a parte real (termos resistivos) e na ordenada a parte imaginária (termos capacitivos ou indutivos). Os dados de impedância representados no plano cartesiano sob uma larga variação de frequência (100 KHz a 10 mHz; em geral 10 KHz a 10^{-4} Hz) gera configurações típicas, de acordo com o mecanismo eletroquímico predominante. A Figura 2 mostra um diagrama de Nyquist típico, acompanhado se seu circuito equivalente.

Uma vez construído o diagrama de Nyquist, faz-se a extrapolação da parte direita do semicírculo até encontrar o eixo horizontal. O diâmetro do semicírculo é a resistência à transferência de carga R_t, equivalente à resistência de polarização (R_p) [2]. Assim, quanto maior o diâmetro deste semicírculo, maior a resistência R_p e, consequentemente, menor a taxa de corrosão [4].

Uma das dificuldades da impedância nitidamente evidenciada no diagrama de Nyquist diz respeito à caracterização de uma armadura essencialmente passiva. Nesse estado, a transferência de carga ao longo da armadura, que denota um processo de corrosão, é muito pequena. Sendo assim, os semicírculos ou arcos capacitivos de transferência de carga na dupla camada elétrica são pobremente desenvolvidos, prejudicando a interpretação de dados [2].

O diagrama de Bode consiste em um plano de eixos ortogonais, nos quais se têm, no eixo das ordenadas, duas grandezas: o logaritmo da impedância (log|Z|) em ohms (Ω) e o ângulo de fase (Φ) em graus; e no eixo das abscissas, tem-se o logaritmo da frequência angular (logω), com ω em radianos por segundo (rad/s). Pode-se também representar as abscissas pelo logaritmo da frequência (logf), com f em Hertz. Com a configuração logω versus |Z| pode-se determinar Rω e Rt, de acordo com a Figura 3; e por

Figura 3 – Diagrama de Bode representando a impedância (módulo e ângulo de fase) de um sistema eletroquímico de corrosão em função da frequência angular (3)

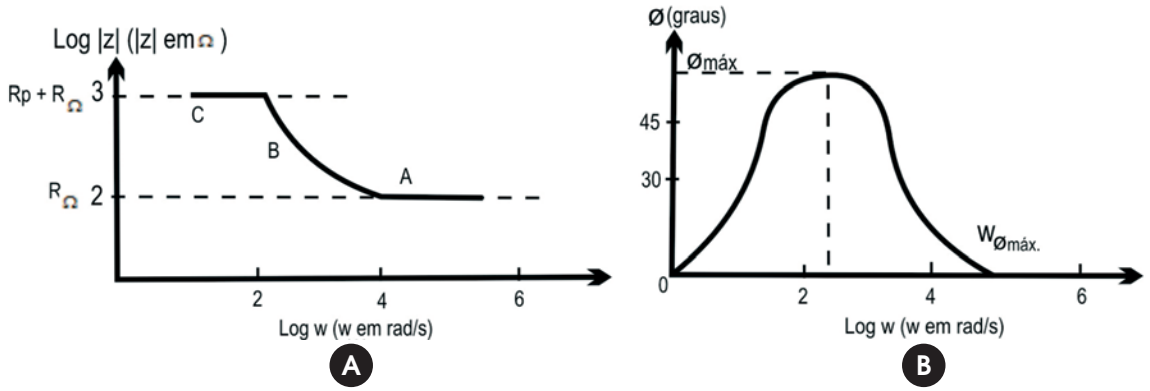

meio de ângulo da fase versus logω, é possível a determinação da capacitância da dupla camada elétrica Cdl, sabendo-se que:

$$Rp = 2.|Z|.tgmax \quad (1)$$

$$\omega_{\phi_{máx}} = \frac{1}{C_{dl}.R_P.(1+R_P/R_\Omega)^{1/2}} \quad (2)$$

onde: ϕ_{max} é o ângulo de fase máximo da impedância do sistema, $\omega_{\phi max}$ é a frequência angular correspondente ao ϕ_{max} e |Z| é o módulo de impedância correspondente ao ϕ_{max}.

No diagrama de Bode distingue-se claramente a região de alta frequência (Figura 3a, região A), caracterizada pela presença de películas de passivação e outros tipos de revestimento sobre a armadura, a região de frequência média (Figura 3A, região B), que reflete a mudança de condutividade elétrica do revestimento durante exposição em meio corrosivo e, finalmente, a região de baixa frequência (Figura 3A, região C), onde a reação de corrosão na interface metal/revestimento pode ser estudada [2].

Figura 4 – Circuito equivalente para concreto proposto por JOHN et al. (6). Rc: resistência do concreto; Rf e Cf: resistência e capacitância do filme; Zd: impedância difusional; Rct e Cdl: resistência de transferência de carga e capacitância de dupla camada

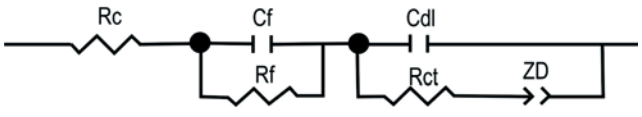

2.2 Circuitos equivalentes

Um dos maiores problemas em se utilizar circuitos equivalentes é decidir qual circuito equivalente específico, entre tantas possibilidades, deverá ser utilizado.

Um processo corrosivo envolve simultaneamente diversos processos físicos e, portanto, o seu circuito equivalente será composto por diferentes elementos de circuito. Contudo, de um processo para outro, os elementos de circuito podem variar também a forma com que os mesmos são interconectados. Na Tabela 1 é mostrada a correlação entre processos físicos e elementos de circuito elétrico usados na EIE.

Um dos precursores do uso da EIE para monitorar corrosão em concreto armado foi JOHN et al. [6]. Esses autores propuseram o circuito descrito na Figura 4 e aplicaram EIE em amostras de concreto imersas em água do mar. A resposta de impedância na baixa frequência foi relacionada com o processo de transferência de carga, considerando que a resposta em altas frequências foi atribuída à presença de um filme de superfície.

Tabela 1 – Correlação entre os processos físicos e os elementos de circuito elétrico (3)

Processo físico	Elemento de circuito
Transferência de carga	Resistores Re e Rp
Dupla camada elétrica	Capacitor, Cdl
Camadas superficiais dielétricas (revestimentos orgânicos e óxidos)	Capacitor, C
Adsorção	Pseudocapacitor, Cw e resistor, R
Transporte de massa	Pseudocapacitor, Cw e pseudoresistor, Rw

Figura 5 – Modelo de linhas de transmissão descrito para concreto armado proposto por MACDONALD et al. apud FREIRE (5)

Outra alternativa para a interpretação do sistema aço/concreto foi proposta por MACDONALD et al. apud FREIRE [5]. Os autores descreveram a resposta de sistema baseados em um modelo de linhas de transmissão como mostrado na Figura 5, onde R é a resistência barra/segmento; Ri a resistência concreto/segmento e; Zj a impedância interfacial segmento barra/concreto.

Esse modelo assume que as propriedades elétricas de aço e concreto são puramente resistivas, com a resistividade do concreto sendo dependente na posição devido à não homogeneidade de matriz. Por outro lado, o modelo assume que a interface é reativa devido à existência de capacitor, pseudocapacitor e componentes difusionais. Os modelos mostram que a parte real e a parte imaginária da resposta de impedância e o ângulo de fase a baixas frequências permitem detectar e localizar a corrosão.

DHOUIBI-HACHANI et al. [7] propuseram outra aproximação mostrada na Figura 6, que inclui os itens seguintes: (i) produtos formados diretamente na superfície do aço, (ii) produtos que são o resultado de reação entre produtos de corrosão e a pasta de cimento e (iii) o tamanho da cobertura de concreto.

O modelo mostra um bom acordo entre os dados experimentais e os diagramas de Nyquist calculados, onde R_c: resistência do concreto; R_1: resistência dos produtos formados na armadura; C_1 e R_4: capacitância e resistência de dispersão (dependente da frequência); R_3: resistência da interface aço; C_2 e R_2: capacitância e resistência de dispersão devido à homogeneidade dos produtos na superfície do metal.

Às vezes, apesar do desenvolvimento crescente na interpretação dos espectros de EIE, eles revelam a presença de características difíceis de explicar. Estas incluem: presença de ramos de baixa frequência, semicírculos deslocados e efeitos de altas frequências.

Figura 6 – Circuito equivalente para o concreto proposto por DHOUIBI-HACHANI et al. (7)

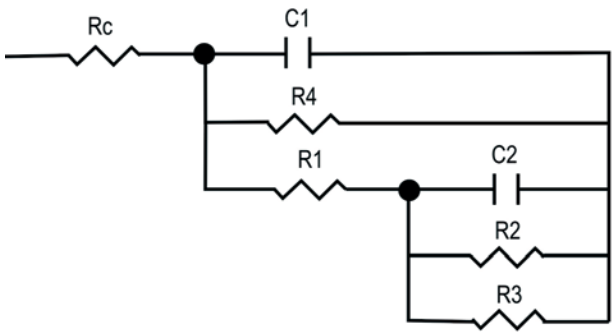

O primeiro efeito conduziu à introdução de um elemento de Warburg (W) em série com a resistência de transferência de carga por causa das respostas dos processos faradaicos que acontecem na interface. Esses efeitos explicam por que o estado estacionário às vezes não pode ser alcançado com técnicas de corrente direta (DC) convencionais, até mesmo depois de muito tempo de espera. Eles também explicam as longas constantes de tempo observadas nos espectros de impedância a baixas frequências e a necessidade para extrapolar os valores da resistência de polarização [1].

A presença de semicírculos deslocados sugere um comportamento não ideal do capacitor, conduzindo à introdução do elemento de fase constante (CPE) nos circuitos equivalentes. SAGUES et al. [8] introduziram esse elemento em sistemas que exibem processos de polarização simples. Eles concluíram que alguma melhoria é obtida se o CPE é usado em vez de um capacitor ideal. Em outro trabalho, FELIU et al. [9] propuseram um sistema mais complexo e introduziram um CPE e parâmetros difusionais no circuito equivalente, como mostrado na Figura 7. Isso conduziu a um aumento na precisão da determinação da resistência de polarização quando isso era possível.

O circuito equivalente proposto por Randles, na Figura 8, tem uma larga aplicação em muitos sistemas eletroquímicos. Nele, Re representa a resistência da solução e do filme do produto de corrosão, que também é conhecido, segundo SAGUES et al. [8], como a resistência ôhmica do eletrólito entre o ponto sensitivo de voltagem do eletrodo de referência e a interface eletrodo/eletrólito. Rt e Cdl representam a interface de corrosão: Cdl é a capacitância da dupla camada elétrica resultante de íons e moléculas de água adsorvidos, devido à diferença de potencial entre eletrodo em corrosão e a solução (ou eletrólito) e Rt é a resistência à transferência de carga, que determina a taxa da reação de corrosão e é uma medida da transferência de cargas elétricas através da superfície

Figura 7 – Circuito equivalente com introdução de CPE, proposto por FELIU et al. (9). Re = resistência do eletrólito; Rp = resistência de transferência de carga; CPE = elemento constante de fases; ZD = difusão Warburg

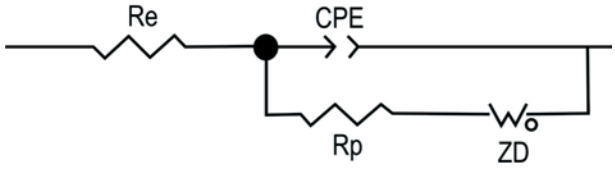

Figura 8 – (A) Circuito equivalente simples do tipo Randles e; (B) Circuito Randles modificado com duas constantes de tempo (10)

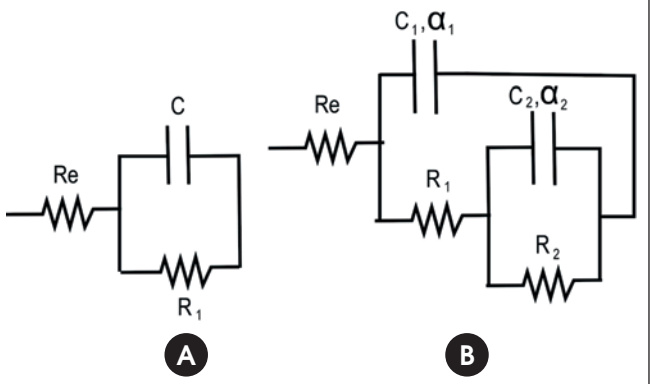

do eletrodo. Em um sistema controlado por ativação, Rt é a parcela medida pela técnica de resistência de polarização, isto é, Rt equivale a Rp.

interface aço/concreto, o circuito elétrico equivalente e o correspondente diagrama de Nyquist.

Assim, podem-se associar essas três regiões do diagrama às propriedades relativas à argamassa (matriz, m), ao filme interfacial (camada de $Ca(OH)_2$) e a uma região de interface, com transferência de cargas e capacitância da dupla camada (interface solução intersticial/aço).

De forma simplificada, podem-se identificar três faixas de frequências, em que diferentes processos apresentam uma resposta de impedância [4]:

- Altas frequências (MHz–KHz): o eletrólito apresenta uma resposta. As capacitâncias são da ordem de pF/cm^2. Mais de uma constante de tempo pode aparecer devido ao grau de umidade do concreto e aos diferentes constituintes das fases sólidas.
- Médias frequências (KHz–Hz): os processos faradaicos apresentam uma resposta. As capacitâncias típicas são da ordem de mF/cm^2. Pode-se encontrar mais de uma constante de tempo quando existe ataque localizado. O concreto carbonatado produz um achatamento do semicírculo nos diagramas de Nyquist.
- Baixas frequências (Hz–mHz): as reações redox $Fe^{2+} \leftrightarrow Fe^{3+}$ podem ocorrer, dependendo do potencial. As capacitâncias medidas são da ordem de mF/cm^2. Fenômenos de difusão podem aparecer através da camada passiva.

Figura 9 – Representação esquemática de (A) interface aço/concreto; (B) circuito elétrico equivalente (m = matriz e f = filme) e; (C) diagrama de Nyquist correspondente (4)

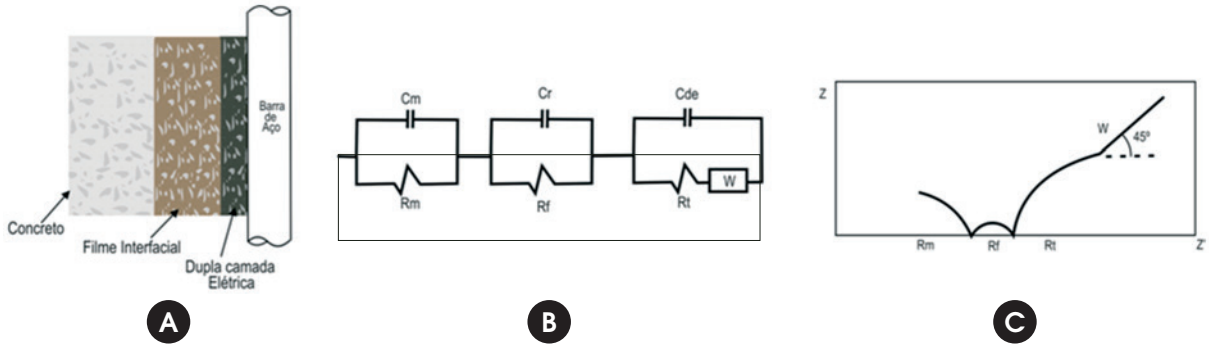

Em estudo recente, MARTÍNEZ & ANDRADE [10] adicionaram duas constantes de tempo RC, utilizadas quando necessário, como pode ser verificado na Figura 8B.

Para a interface aço/concreto, o circuito equivalente não é tão simples como o circuito de Randles. O modelo proposto por CRENTSIL apud MACHADO [17] relaciona um semicírculo em altas frequências às propriedades do concreto. O segundo semicírculo, em frequências intermediárias, é atribuído à formação de produtos de corrosão. Em baixas frequências, a presença de um semicírculo e uma reta com inclinação característica igual a 1 (um) envolve a sobreposição dos dois efeitos.

Ainda segundo MACHADO [17], o semicírculo reflete o efeito da cinética de corrosão e a reta relaciona a difusão de oxigênio através da camada de óxido, representada por um elemento de Warburg, W. A Figura 9 mostra a representação esquemática dessa

Com base nestas frequências citadas, CHRISTENSEN et al. [11, 12] propuseram uma correlação entre o fenômeno de corrosão e

Figura 10 – Circuito equivalente típico proposto por CHRISTENSEN et al. (11)

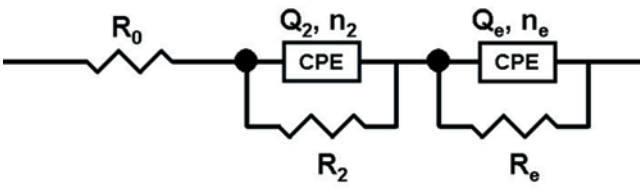

Figura 11 – (A) Diagrama de Nyquist proposto para o concreto armado e; (B) Ampliação da região de alta frequência do diagrama anterior

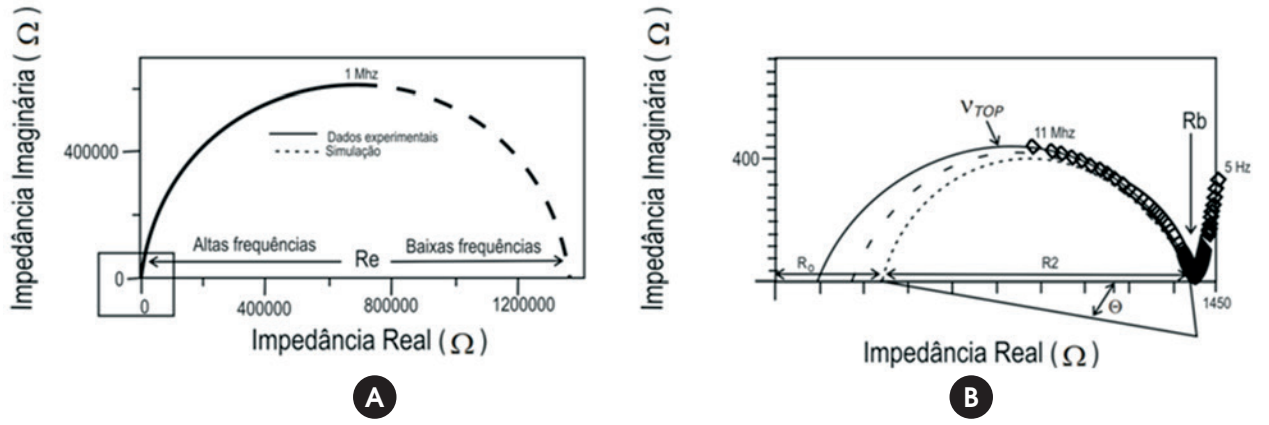

o circuito equivalente e que é bastante aceita em diversas pesquisas. O circuito equivalente proposto por estes autores é apresentado na Figura 10.

O diagrama equivalente, apresentado na Figura 10, está associado a uma resistência "offset aparente" (R_0) em série com a rede de concreto (R_2Q_2) e conectada, também em série, ao eletrodo (R_eQ_e). Esses elementos são mais bem visualizados pelo diagrama de Nyquist apresentados na Figura 11.

As variáveis mostradas na Figura 11 podem ser interpretadas como:

- Resistência do Eletrodo (R_e): A resistência do eletrodo (no caso, a armadura) é representada pelo raio do semicírculo que se apresenta nas regiões de baixa frequência. A princípio, quanto menor esse raio, maior a corrosão.
- Resistência da matriz de cimento (R_b): Este valor é facilmente detectado dos espectros de impedância, correspondendo à intersecção entre os arcos referentes ao eletrodo e ao corpo de cimento propriamente dito.
- Resistência Offset (R_0): É uma resistência "de partida", sem muito interesse para o processo e sem significado físico aparente. Em termos práticos, pode ser desprezado, considerando-se $R_b = R_0 + R_2$.
- Ângulo de Depressão (θ): Muitas vezes expresso pelo fator de depressão do arco, n (n = 1 - (2θ/ π), está relacionado às imperfeições do corpo de prova, predominantemente, com a distribuição de tamanho de poros. Quanto mais próximo de zero (n próximo de 1), se comporta como um capacitor perfeito no sistema.

Como se pode observar, existe uma infinidade de circuitos equivalentes propostos e que se adéquam às diferentes formas de avaliar os diferentes materiais utilizados na produção do concreto e é uma árdua tarefa determinar um circuito equivalente que atenda completamente a todos os fenômenos observados no processo corrosivo.

3. Método proposto para a interpretação dos resultados de EIE

A análise dos resultados de EIE em amostras de concreto armado é de alta complexidade, devido à sobreposição de arcos provenientes de fenômenos simultâneos e a ruídos da medida, associados, evidentemente, à heterogeneidade das amostras e que dificultam de forma considerável sua análise.

Figura 12 – Circuitos elétricos equivalentes para a interface aço-concreto, segundo (A) análise geral e (B) análise por arcos individualizados (circuito simplificado), propostos por VERMOYAL et al. (13)

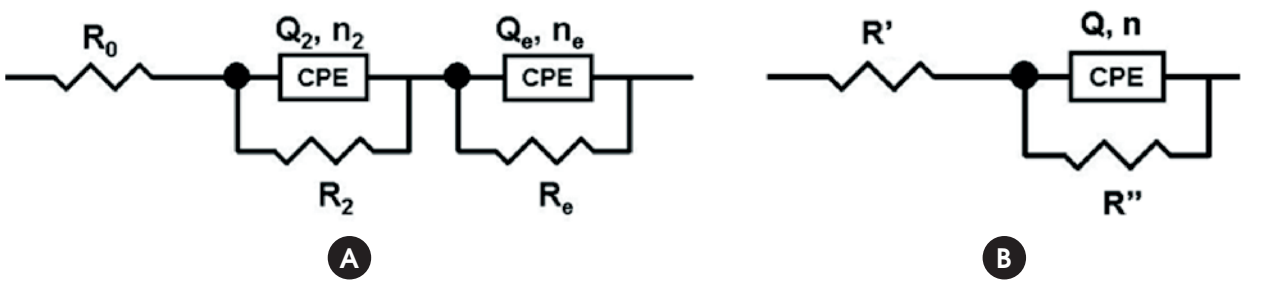

Figura 13 – Correlação entre as capacitâncias e as frequências características para cada fenômeno do processo de degradação do concreto armado

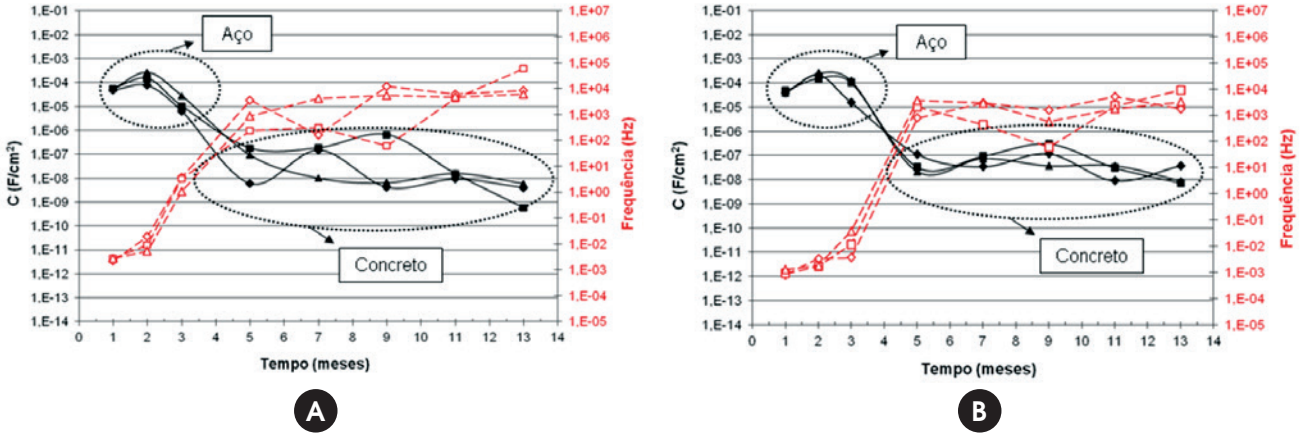

Devido a essas dificuldades, propõe-se uma nova forma de análise. A teoria de base diz que os processos têm uma frequência angular de relaxação característica, w (a partir da qual deixam de responder) e que é dada por w = 1/RC e que também pode ser lida graficamente no topo do arco do espectro de impedâncias [13, 14]. Assim, é possível associar os arcos a serem analisados com as capacitâncias e frequências típicas de cada um dos fenômenos.

Dessa forma, isolam-se os arcos identificados e relacionados a cada um dos fenômenos e faz-se uma análise local, melhorando, assim, a precisão. Estratégia semelhante havia sido adotada em seus estudos por VERMOYAL et al. [13]. Para tal, utilizou-se o circuito simplificado apresentado na Figura 12.

Quando os arcos são analisados isoladamente e fitados segundo o circuito elétrico simplificado (Figura 12B), têm-se como resultados, além da resistência do arco em questão (R''), os valores do elemento de fase constante (CPE), Q, e do índice "n" que mede a perfeição desse elemento, variando entre 0 e 1 e sendo mais próximo do valor unitário à medida que o CPE se aproxima de um capacitor perfeito, C [4, 11, 15]. Assim pode-se calcular a capacitância característica, C, de acordo com a Equação 3.

$$C = Q^{\frac{1}{n}} . R^{\frac{1-n}{n}} \quad (3)$$

Já a frequência característica (f) associada a essa capacitância característica é calculada, em Hertz, de acordo com as Equações 4 e 5, onde w = 1/RC [4, 14].

$$f(Hz) = \frac{w}{2\pi} \quad (4)$$

$$f(Hz) = \frac{1}{2\pi . R.C} \quad (5)$$

Observando-se a correlação entre as capacitâncias e frequências características, calculadas para cada um dos fenômenos, é possível agrupá-las como:

- Baixas frequências: Na faixa de 1mHz a 10Hz (10^{-3}–10 Hz), correspondem à resistência do eletrodo (R_e), logo, estão associadas ao fenômeno de corrosão. A capacitância característica desta faixa está compreendida entre 10^{-6} e 10^{-3} F/cm².
- Médias frequências: Na faixa de 100Hz a MHz (10^{2}–10^{6} Hz), correspondem à resistência do concreto (R_2), estando associadas às características da matriz que envolve e protege a armadura. A capacitância característica desta faixa está compreendida entre 10^{-9} e 10^{-6} F/cm².
- Altas frequências: Superiores à faixa dos MHz (> 10^{6} Hz) estão associadas à resistência "offset" (R_0), de pequena relevância e valores desprezíveis no presente estudo.

Esta correlação entre as capacitâncias e freqüências características calculadas para cada um dos fenômenos pode ser visualizada na figura 13, cujos resultados foram obtidos experimentalmente pelos autores. Observa-se claramente que as frequências características são muito bem definidas.

A partir, daí, basta que o pesquisador associe cada arco, individualmente, à resistividade do concreto (R_2) ou do eletrodo, no caso, a armadura (R_e). Esta associação será baseada na freqüência na qual o fenômeno ocorre (f) ou na capacitância (C). Segundo alguns estudos realizados [4, 16], a armadura está em processo de corrosão à medida que há o fechamento do semicírculo formado a baixas frequências, observado no diagrama de Nyquist. Assim, quanto menores os valores de R_e, mais acentuado é o processo corrosivo e a resistência do eletrodo típica de um processo corrosivo considerável é da ordem de KΩ.

4. Conclusões

De acordo com os estudos realizados, é possível concluir que:

- A EIE é uma precisa e poderosa técnica de anpalise do processo corrosivo que precisa ser melhor explorada pela construção civil;
- A análise tradicional dos resultados de EIE, por meio da análise direta dos circuitos equivalentes, pode ser muito dificultada devido à sobreposição dos arcos, que ocorre em função da heterogeidade do concreto, implicando em erros;
- Os processos têm uma frequência angular de relaxação característica, w (a partir da qual deixam de responder) e que é dada por w = 1/RC e que também pode ser lida graficamente no topo do arco do espectro de impedâncias;
- É possível associar cada arco, individualmente, à resistividade do concreto (R_2) ou daa armadura (R_e), com base na freqüência na qual o fenômeno ocorre (f) ou na sua capacitância (C);
- Fenômenos que ocorrem em baixas frequências (1mHz a 10Hz) correspondem à resistência do eletrodo (R_e), logo, estão associadas ao fenômeno de corrosão. Os fenômenos que ocorrem em médias frequências (100Hz a MHz) correspondem à resistência do concreto (R_2), estando associadas às características da matriz que envolve e protege a armadura e fenômenos que ocorrem em altas frequências (superiores à faixa dos MHz), estão associados à resistência "offset" (R_0), de pequena relevância e valores desprezíveis.

5. Referências

[1] MONTEMOR, M. F.; SIMÕES, A.M.P.; FERREIRA, M.G.S. Chloride-induced corrosion on reinforcing steel: from the fundamentals to the monitoring techniques. Cement and Concrete Composites. v. 25, n. 4-5, p. 491-502, 2003.

[2] LANGFORD, P. BROOMFIELD, J. Monitoring the Corrosion of Reinforcing Steel. v.1, nº2. Construction Repair, p. 32-36, 1987

[3] WOLYNEC, S. Técnicas eletroquímicas em corrosão. São Paulo: EDUSP, 2003. 166 p.

[4] AGUILAR, A.; SAGÜÉS, A.; POWERS, R. Corrosion Rates of Steel in Concrete. ASTM-STP 1065, American Society for Testing and Materials, p. 66–85, 1990.

[5] FREIRE, K.R.R. Avaliação Do desempenho de inibidores de corrosão em armaduras de concreto. Curitiba, 2005. 192p. Dissertação (Mestrado), Universidade Federal do Paraná.

[6] JOHN, D.G.; SEARSON, P.C.; DAWSON, J.L. British Corrosion Journal. v. 16, p. 102, 1981.

[7] DHOUIBI-HACHANI, L.; et al. Comparing the steel-concrete interface state and its eletrochemical impedance. Cement and Concrete Research. v. 26, n. 2, p. 253-266, 1996.

[8] SAGUES, A.A.; KRANC, S.C.; MORENO, E.I. The time-domain response of a corrodyng system with constant phase angle interfacial component: application to steel in concrete. Corrosion Science. v. 37, n. 7, p.1097-1113, 1995.

[9] FELIU, V.; et al. Equivalent circuit for modelling the steel-concrete interface I: experimental evidence and theroretical predictions. Corrosion Science. v. 40, n. 6, p.975-993, 1998.

[10] MARTÍNEZ, I.; ANDRADE C. Application of EIS to cathodically protected steel: tests in sodium chloride solution and in chloride contaminated concrete. Corrosion Science. v. 50, n. 10, p. 2948–2958, 2008.

[11] CHRISTENSEN, B.J.; et al. Impedance spectroscopy of hydrating cement-based materials: measurement, interpretation, and application. Journal of the American Ceramic Society, n. 77, v. 11, p. 2789-2804, 1994.

[12] CHRISTENSEN, B.J.; MASON, T.O.; JENNINGS H.M.; Influence of silica fume on the early hydration of Portland cements using impedance spectroscopy. Journal of the American Ceramic Society, n. 75, v. 4, p. 939-945, 1992.

[13] VERMOYAL, J.J.; FRICHET, A.; DESSEMOND, L.; HAMMOU, A. AC impedance study of corrosion films formed on zirconium based alloys. Electrochimica Acta, v. 45, n. 7, p. 1039–1048, 1999.

[14] MAIA, L.F.; RODRIGUES, A.C.M. Electrical conductivity and relaxation frequency of lithium borosilicate glasses. Solid State Ionics, v. 168, n. 1-2, p. 87–92, 2004.

[15] COVERDALE, T.; et al. Interpretation of impedance spectroscopy of cement paste via computer modelling. Journal of Materials Science, v. 30, n. 20, p. 712-719, 1995.

[16] SILVA, F.G. Estudo de concretos de alto desempenho frente à ação de cloretos. 2006. 218p. Tese (Doutorado em Ciência e Engenharia de Materiais) – Área de Interunidades em Ciência e Engenharia de Materiais, Universidade de São Paulo, São Carlos, 2006.

[17] MACHADO, M.A.G.T.C. Inibidores de Corrosão em Concreto Armado contra o ataque de agentes da chuva ácida. São Carlos, 2004. 161p. Tese (Doutorado), Universidade Federal de São Carlos.

Volume 8, Number 4 (August 2015) p. 547-566 • ISSN 1983-4195
http://dx.doi.org/10.1590/S1983-41952015000400008

REVISTA IBRACON DE ESTRUTURAS E MATERIAIS
IBRACON STRUCTURES AND MATERIALS JOURNAL

Impacts in the structural design of the 2014 revision of the brazilian standard ABNT NBR 6118

Impactos no projeto estrutural da versão 2014 da norma brasileira ABNT NBR 6118

R. M. CERUTTI [a]
raphaelmbx@poli.ufrj.br

S. H. C. SANTOS [b]
sergiohampshire@gmail.com

Abstract

With the issuing of the 2014 version of the Brazilian Standard ABNT NBR 6118 – Design of Concrete Structures, several procedures followed in the design offices shall be altered. The purpose of this paper is to furnish data to the designers, in order to facilitate the transition to the new version of the Standard. A summary of some of the main modifications with direct impact in the design is presented, being shown, among others, the topics: characteristics of the concretes of class up to C90, including the new stress-strain diagrams and respective simplification criteria for these diagrams, the new deformation domains, the values of design tensile stresses in concrete and the new criteria for limiting the depth of the neutral axis; new design criteria for designing and detailing of special elements, including the application of strut-and-tie models; new design criteria, minimum dimensions and detailing criteria for columns, walls and slabs; new criteria for considering global imperfections; new criteria for considering creep and shrinkage; new values for minimum reinforcement in pure bending; new expressions for evaluating the elasticity modulus of concrete. A new table for the design of concrete sections under pure bending is furnished, and new diagrams for designing rectangular sections under bending with compression forces are presented.

Keywords: brazilian standard, structural concrete, design, detailing.

Resumo

Com a promulgação da versão 2014 da Norma Brasileira ABNT NBR 6118 – Projeto de Estruturas de Concreto, diversos procedimentos adotados nas empresas de projeto deverão ser alterados. O objetivo deste trabalho é fornecer subsídios aos projetistas, de forma a facilitar a transição para a nova versão da Norma. É apresentado um resumo de algumas das principais alterações que tem impacto direto no projeto, sendo abordados, entre outros, os temas: características dos concretos de classe até C90, incluindo os novos diagramas tensão-deformação e respectivos critérios de simplificação destes diagramas, os novos domínios de deformação, os valores de tensão de tração de cálculo no concreto e os novos critérios de limitação da profundidade da linha neutra; novos critérios de dimensionamento e detalhamento de elementos especiais, inclusive com a aplicação de Modelos Biela-Tirante; novos critérios de projeto, dimensões mínimas e detalhamento de pilares, pilares-parede e lajes; novos critérios para a consideração de imperfeições globais; novos critérios para a consideração de retração e fluência; novos valores para a armadura mínima de peças em flexão simples; novas expressões para a avaliação do módulo de elasticidade do concreto. É também fornecida uma nova tabela de dimensionamento na flexão simples e apresentados novos ábacos para o dimensionamento de seções retangulares na flexão composta reta.

Palavras-chave: norma brasileira, concreto estrutural, dimensionamento, detalhamento.

[a] *Universidade Federal do Rio de Janeiro, Escola Politécnica, Programa de Projeto de Estruturas, Rio de Janeiro, RJ, Brasil;*
[b] *Universidade Federal do Rio de Janeiro, Escola Politécnica, Departamento de Estruturas, Rio de Janeiro, RJ, Brasil.*

Received: 22 Dec 2014 • Accepted: 25 May 2015 • Available Online: 7 Aug 2015

1. Introduction

After several months of intense work of the Committee of Study charged of its revision, the 2014 revision of the Brazilian Standard ABNT NBR 6118 – Design of Concrete Structures [1] was finally issued. This revision puts the ABNT NBR 6118 in the same level of actualization of the more respected international Standards, reflecting the disposition of the Brazilian Association of Technical Standards (ABNT) and also of the Brazilian technical community of achieving an elevated quality level in the design and construction of concrete structures. Among several other important modifications, the range of application of the ABNT NBR 6118 criteria is now extended from the Concrete Class C50 up to the Class C90. A brief summary of some of these new criteria is presented herein. Some of these new criteria were already presented by SANTOS [2].

2. Characteristics of the concrete

2.1 Modulus of Elasticity

The advance towards better understanding of the properties of the concrete, achieved in the last years, allowed to a more precise definition of the concrete modulus of elasticity, in the absence of specific tests for its determination.
An estimative of the tangent modulus of elasticity, to be used, for instance, in the evaluation of prestressing losses, is given by:
- for f_{ck} from 20 MPa to 50 MPa;

$$E_{ci} = \alpha_E \cdot 5600 \sqrt{f_{ck}} \quad (1)$$

- for f_{ck} from 55 MPa to 90 MPa:

$$E_{ci} = 21.5 \cdot 10^3 \cdot \alpha_E \cdot \left(\frac{f_{ck}}{10} + 1.25\right)^{1/3} \quad (2)$$

Figure 1 – Tangent and secant modulus of elasticity of concrete

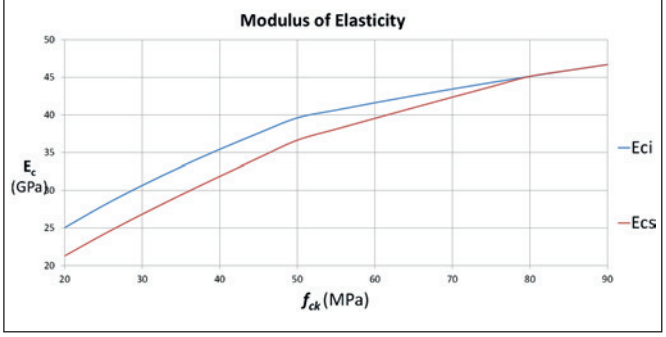

Figure 2 – Design stress-strain curves of concrete

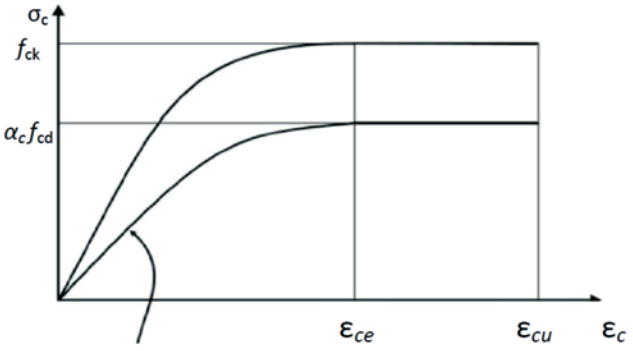

$$\sigma_c = \alpha_c f_{cd} \left[1 - \left(1 - \frac{\varepsilon_c}{\varepsilon_{ce}}\right)^n\right]$$

For $f_{ck} \leq 50$ MPa: n=2
For $f_{ck} \geq 50$ MPa:
$n = 1.4 + 23.4\,[(90 - f_{ck})/100]^4$

The parameter α_E depends on the base rock of the used gravel:
$\alpha_E = 1.2$ for basalt and diabase;
$\alpha_E = 1.0$ for granite and gneiss;
$\alpha_E = 0.9$ for calcarium;
$\alpha_E = 0.7$ for arenite.
An estimative for the secant modulus of elasticity, to be used in the evaluation of the general behavior of a structural member or of a specific transversal section is given by:

$$E_{cs} = \alpha_i \cdot E_{ci} \quad (3)$$

$$\alpha_i = 0.8 + 0.2 \frac{f_{ck}}{80} \leq 1.0 \quad (4)$$

The two moduli converge for the same value with the increase of the concrete strength, as long as the initial part of the stress-strain diagrams becomes closer to a straight line.
A graphical visualization of the variation of these two parameters (for $\alpha_E = 1.0$) is presented in Figure 1.

2.2 Stress-strain curves

The characteristic and design stress-strain curves for the high-strength concretes reflect their greater fragility, as long as their strength increases. The Figure 2 reproduced from the ABNT NBR 6118, defines the new characteristics of these stress-strain curves. The values to be adopted for the parameters ε_{c2} (concrete strain in the beginning of the plastic region) and ε_{cu} (concrete strain in the rupture) are:
- for concretes of classes up to C50:

Figure 3 – Variation of parameters n, ε_{c2} e ε_{cu}

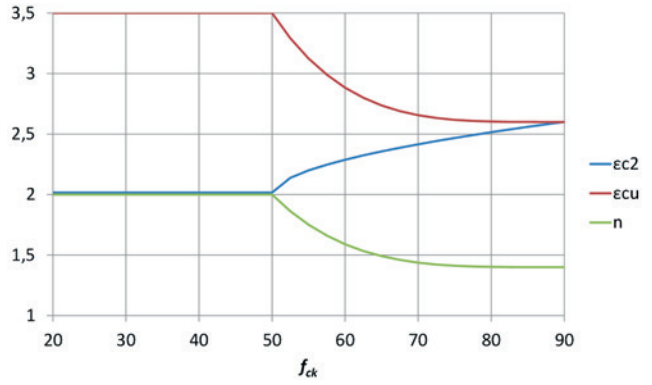

$$\varepsilon_{c2} = 2.0^{0}/_{00} \quad (5)$$

$$\varepsilon_{cu} = 3.5^{0}/_{00} \quad (6)$$

- for concretes of classes from C50 to C90:

$$\varepsilon_{c2} = 2.0^{0}/_{00} + 0.085^{0}/_{00}.(f_{ck} - 50)^{0,53} \quad (7)$$

$$\varepsilon_{cu} = 2.6^{0}/_{00} + 35^{0}/_{00}.[(90 - f_{ck})/100]^{4} \quad (8)$$

The parameters n, ε_{c2} e ε_{cu} are graphically shown in Figure 3.

2.3 Tensile strength

In the absence of specific tests, the values of average tensile strengths shall be evaluated with the expressions:
- for concretes with $f_{ck} \leq 50$ MPa:

$$f_{ct,m} = 0.3\ f_{ck}^{\ 2/3} \quad (9)$$

- for concretes with f_{ck} 50 MPa up to 90 MPa:

Figure 4 – Average concrete tensile strength

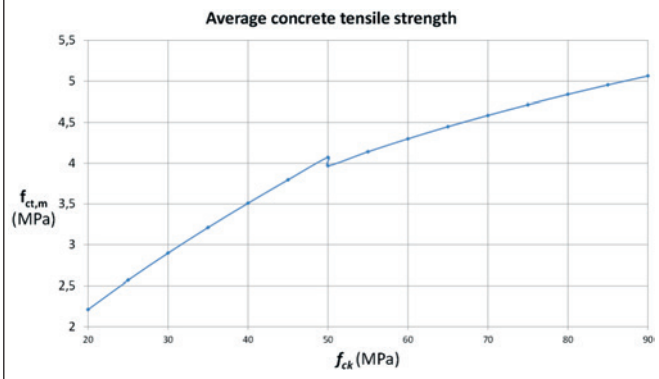

$$f_{ct,m} = 2.12 \ln (1 + 0.11\ f_{ck}) \quad (10)$$

It shall be noticed that the concrete tensile strengths increases more slowly with respect to the increase of the concrete compression strengths. A graphical representation of these variations is given in Figure 4.

3. Design for bending and axial forces

3.1 New deformation criteria in the ultimate limit state for the design

The Figure 17.1 of the Standard has been revised, being now defined as reproduced in Figure 5.

3.2 Simplification of the stress-strain concrete curves

Considering the typical fragility of the concretes of class superior

Figura 5 – Deformation regions in the ultimate limit state

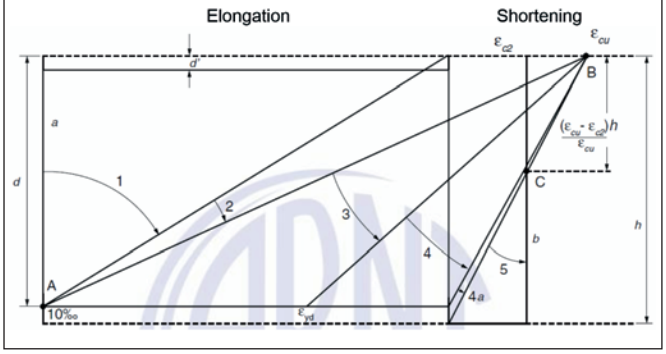

Figure 6 – Curves of strains and design concrete stresses

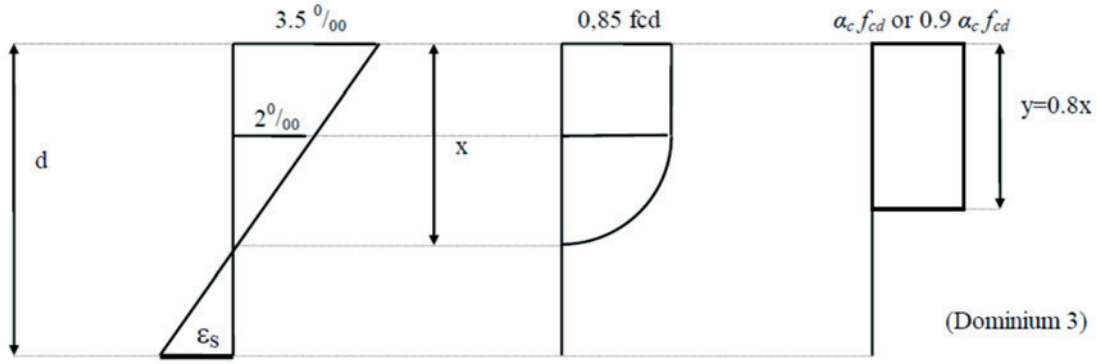

to C50, the criteria for the simplification of the stress-strain curves have been revised, in order that the simplified curves furnish the value of the compression resulting force as well as its position in the sections, both compatible with the ones obtained with the real curves.

For understanding the simplification now defined, typical curves of strains and real and simplified curves of stresses along of the height of a section under bending are shown in Figure 6.

The real curve can be substituted by a rectangle with depth (y) equal λx, where the value of the parameter λ is defined as:

- for concretes with $f_{ck} \leq 50$ MPa:

$$\lambda = 0.8 \quad (11)$$

- for concretes with f_{ck} 50 MPa up to 90 MPa:

$$\lambda = 0.8 - \frac{(f_{ck} - 50)}{400} \quad (12)$$

The constant stress acting up to the depth y can be taken as $\alpha_c \cdot f_{cd}$, in the cases in which the section width do not reduces from the neutral axis to the more compressed face and equal to $0{,}9\ \alpha_c\ f_{cd}$, in the contrary case.

The parameter α_c is defined as:

- for concretes with $f_{ck} \leq 50$ MPa:

$$\alpha_c = 0.85 \quad (13)$$

- for concretes with f_{ck} 50 MPa up to 90 MPa:

$$\alpha_c = 0.85 \cdot \left(1 - \frac{(f_{ck} - 50)}{200}\right) \quad (14)$$

The following limits for the depth of the neutral axis (x/d) shall be considered:

- for concretes with $f_{ck} \leq 50$ MPa:

$$\frac{x}{d} \leq 0.45 \quad (15)$$

- for concretes with f_{ck} 50 MPa up to 90 MPa:

$$\frac{x}{d} \leq 0.35 \quad (16)$$

The variation of the parameters λ e α_c is graphically shown in Figure 7.

3.3 New table for the bending design

Considering the new definitions of the Standard, a new table for the bending design of rectangular reinforced concrete sections, without compression reinforcement, is herein presented (Table 1). In this table, the variables defined below are used. The black horizontal lines in the columns indicate the limits between deformation regions 2 and 3.

Figure 7 – Parameters γ e α_c

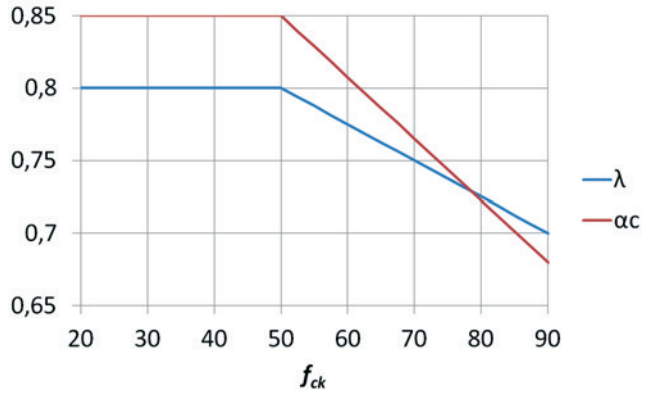

Table 1 – Bending design

f_{ck}	≤ 50MPa		60 MPa		70 MPa		80 MPa		90 MPa	
ε_{cu} and k_{lim23}	3.500	0.259	2.884	0.224	2.656	0.210	2.604	0.207	2.600	0.206
λ e α_c	0.800	0.850	0.775	0.808	0.750	0.765	0.725	0.723	0.700	0.680
k_x	k_z	K_{md}	k_z	K_{md}	k_z	K_{md}	k_z	K_{md}	k_z	K_{md}
0.02	0.992	0.013	0.992	0.012	0.993	0.011	0.993	0.010	0.993	0.009
0.04	0.984	0.027	0.985	0.025	0.985	0.023	0.986	0.021	0.986	0.019
0.06	0.976	0.040	0.977	0.037	0.978	0.034	0.978	0.031	0.979	0.028
0.08	0.968	0.053	0.969	0.049	0.970	0.045	0.971	0.041	0.972	0.037
0.10	0.960	0.065	0.961	0.060	0.963	0.055	0.964	0.050	0.965	0.046
0.12	0.952	0.078	0.954	0.072	0.955	0.066	0.957	0.060	0.958	0.055
0.14	0.944	0.090	0.946	0.083	0.948	0.076	0.949	0.070	0.951	0.063
0.16	0.936	0.102	0.938	0.094	0.940	0.086	0.942	0.079	0.944	0.072
0.18	0.928	0.114	0.930	0.105	0.933	0.096	0.935	0.088	0.937	0.080
0.20	0.920	0.125	0.923	0.115	0.925	0.106	0.928	0.097	0.930	0.089
0.22	0.912	0.136	0.915	0.126	0.918	0.116	0.920	0.106	0.923	0.097
0.24	0.904	0.148	0.907	0.136	0.910	0.125	0.913	0.115	0.916	0.105
0.26	0.896	0.158	0.899	0.146	0.903	0.135	0.906	0.123	0.909	0.112
0.28	0.888	0.169	0.892	0.156	0.895	0.144	0.899	0.132	0.902	0.120
0.30	0.880	0.180	0.884	0.166	0.888	0.153	0.891	0.140	0.895	0.128
0.32	0.872	0.190	0.876	0.175	0.880	0.162	0.884	0.148	0.888	0.135
0.34	0.864	0.200	0.868	0.185	0.873	0.170	0.877	0.156	0.881	0.143
0.35	0.860	0.205	0.864	0.189	0.869	0.174	0.873	0.160	0.878	0.146
0.37	0.852	0.214	–	–	–	–	–	–	–	–
0.39	0.844	0.224	–	–	–	–	–	–	–	–
0.41	0.836	0.233	–	–	–	–	–	–	–	–
0.43	0.828	0.242	–	–	–	–	–	–	–	–
0.45	0.820	0.251	–	–	–	–	–	–	–	–

$$k_x = \frac{x}{d}; k_z = \frac{z}{d}; K_{md} = \frac{M_d}{b.d^2.f_{cd}}; A_s = \frac{M_d}{d.k_z.f_{yd}} \quad (17)$$

Where:
x – neutral axis depth;
d – effective section height;
b – section width;
z – level arm in bending;
M_d – design value of the bending moment;
f_{cd} – design value of concrete strength;
f_{yd} – design value of yielding stress of the reinforcing steel.
It shall be noticed that this table can be also applied for the design of sections with compression reinforcement. In this case, the table can be used for the evaluation of the part of the tensile reinforcement in equilibrium with the compression resisted by the concrete. The remaining part of the tensile reinforcement, equilibrated by the compression reinforcement, can be evaluated in the usual way.

3.4 New table for minimum reinforcement in bending

The Table 17.3 of ABNT NBR 6118 has been completely reformulated and it is partially reproduced in Table 2.

3.5 New design charts for eccentric compression

New design charts for eccentric compression have been developed for the concretes of class superior to C50. Due to the new definitions of ABNT NBR 6118, the design charts for these high-strength concretes present numerical values very different from the ones obtained with the charts developed for concretes of class up to C50.

Table 2 – Values of de ρ_{min} ($A_{s,min}$/Ac) (%) as a function of f_{ck}

f_{ck}	20	30	40	50	60	70	80	90
ρ_{min}	0.150	0.150	0.179	0.208	0.219	0.233	0.245	0.256

Figure 8 – Dimensionless design chart – Type 2 – d'/h = 0,10 – C50

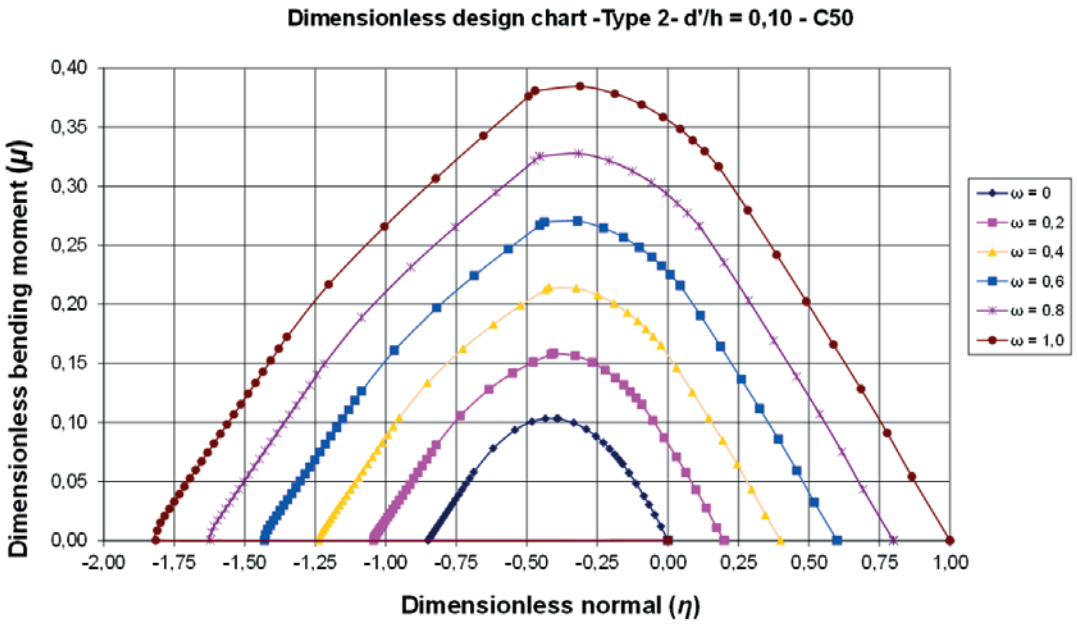

These new charts can be obtained as presented by CERUTTI [3]. In this work, it has been shown that, for the concretes of class superior to C50, the use of the rectangular block of stresses is not applicable to the cases of small eccentricities, since in these cases the results are excessively conservative. This leads to the obligatory consideration of the real strain-stress curves of the concrete. In the Figures 8 and 9, a comparison is presented between design charts drawn for concretes of class up to C50 and for concrete class C90, respectively (both for the rectangular section called Type 2, with reinforcement uniformly distributed in its perimeter). The design charts use the parameters η, μ e ω (respectively dimensionless normal forces and bending moments and mechanical reinforcement ratio), as defined below:

$$\eta = \frac{N_d}{b.h.f_{cd}} \; ; \; \mu = \frac{M_d}{b.h^2.f_{cd}} \; ; \; \omega = \frac{A_s.f_{yd}}{b.h.f_{cd}} \qquad (18)$$

Figure 9 – Dimensionless design chart – Type 2 – d'/h = 0,10 – C90

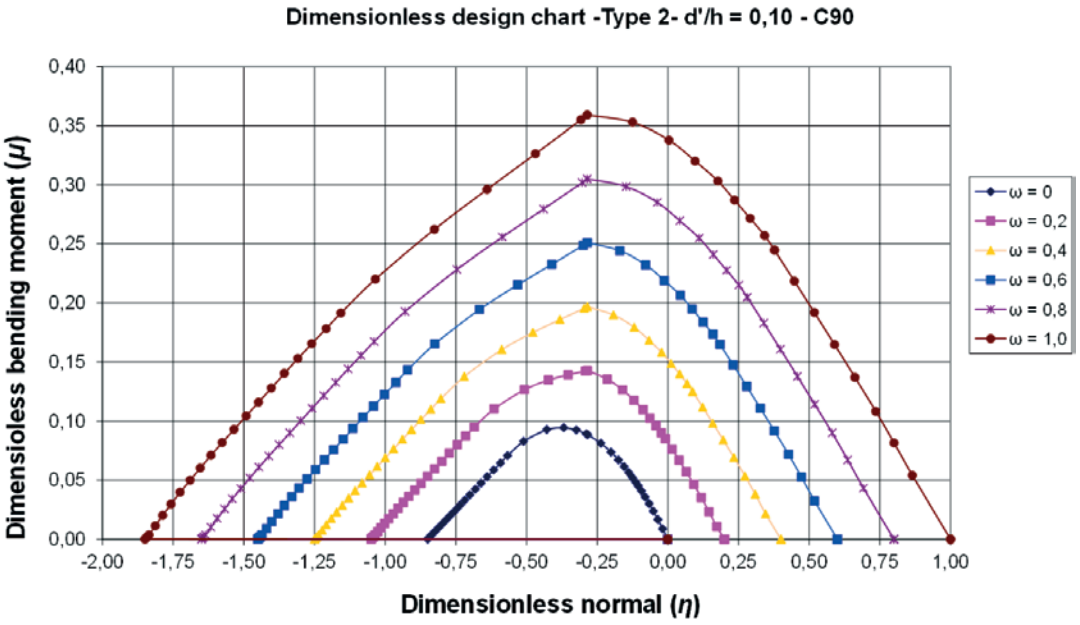

In the hyperlink mentioned as a reference in CERUTTI [3], this work can be directly accessed, where several design charts can be found, developed for several distributions of reinforcement. Several examples of application of the charts can be also found therein.

4. Design with strut-and-tie models

The Figure 22.1 of ABNT NBR 6118, reproduced in Figure 10, shows several typical situations of D regions, of geometrical discontinuity of stresses or of application of concentrated loads, which can be analyzed using strut-and-tie models. The 2014 revision of the Standard defines new criteria for the verification of concrete stresses in these special regions.

The stress limits f_{cd1}, f_{cd2} e f_{cd3}. are defined as follows.

$$f_{cd1} = 0.85\ \alpha_{v2}\ f_{cd} \quad (19)$$

$$f_{cd2} = 0.60\ \alpha_{v2}\ f_{cd} \quad (20)$$

$$f_{cd3} = 0.72\ \alpha_{v2}\ f_{cd} \quad (21)$$

Where:

$\alpha_{V2} = 1 - f_{ck}/250$

The limit f_{cd1} is applicable to the verification of regions with transversal compression stresses or without transversal tensile stresses and in nodes where only compression struts converge. The limit f_{cd2} is applicable to the verification of regions with tensile transversal stresses and in nodes where two or more tensioned ties converge. The limit f_{cd3} is applicable to nodes where only one tensioned tie converges.

The Figure 11 presents the application of these three compression stress limits in the case of the analysis of a simply supported beam.

Design and detailing of columns and structural walls

5.1 Minimum dimensions

The minimum value for the thickness of columns and structural walls is from now on 14 cm. When this thickness is inferior to 19 cm, a correction coefficient γ_n for adjusting the loads is applicable, to be multiplied by the safety factors for loads γ_f, as defined below (*b* is the thickness of the column in cm):

$$\gamma_n = 1{,}95 - 0{,}05b \quad (22)$$

Some important changes have been included in section 11.3.3.4.1 of the Standard, regarding the evaluation of global geometric imperfections in buildings. The Figure 12 shows a scheme illustrating the effects of these global imperfections.

The range of variation of the coefficient q_1 is now, for framed

Figure 10 – Typical situations of Regions D

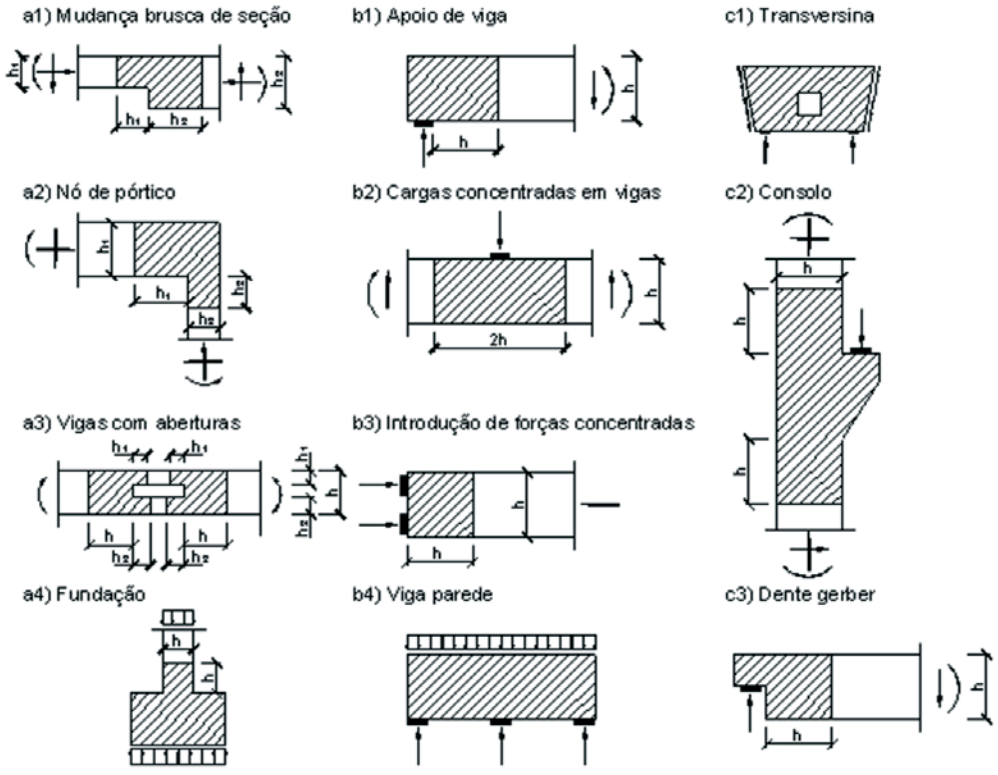

Figure 11 – Regions for the application of the concrete compression stresses

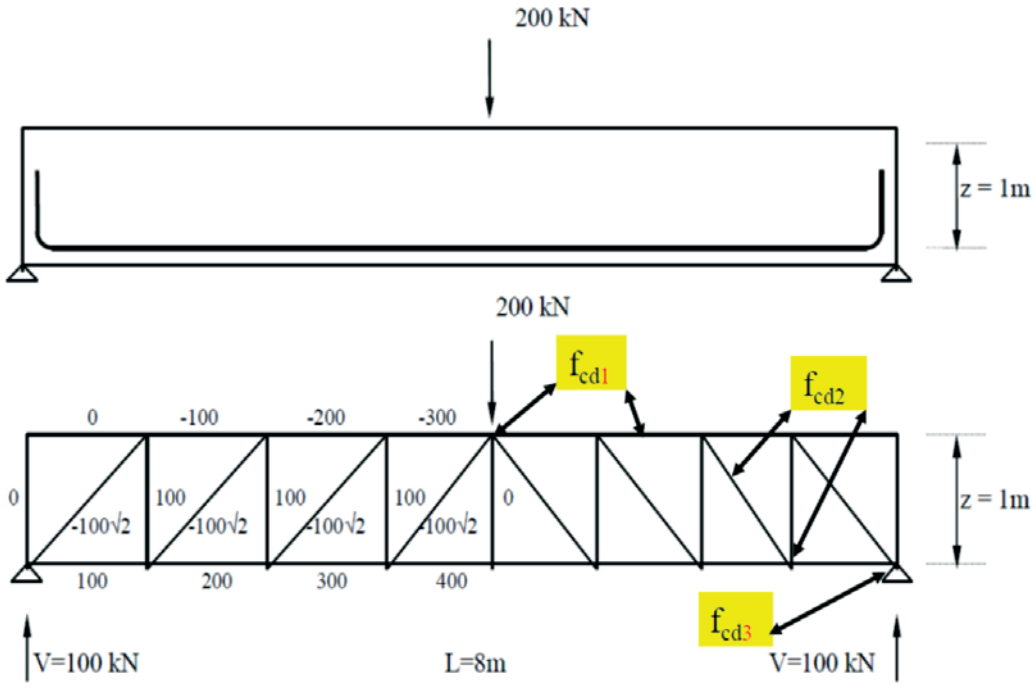

structures and for the evaluation of local imperfections, from q_{1min} = 1/300 to q_{1max} = 1/200.

It is now necessary an investigation of the necessity of superposition of effects of global imperfections and wind. This superposition will be necessary whether the smaller of the two effects, measured according the global resulting moments at the base of the structure, is superior to 30% of the greater effect. In this comparison, the building inclination may be evaluated considering the angle q_1, and not the angle q_{1min}.

When the superposition is necessary, and wind effects are the predominant ones, these wind effects shall be combined with global imperfections corresponding to θ_1, not being considered the angle θ_{1min}. If the effects of global imperfections are predominant, the angle θ_{1min} shall be taken into account.

6. Design of slabs

6.1 Minimum thickness of slabs

Important changes were introduced in the definition of the minimum thickness of slabs, in the section 13.2.4.1 of the Standard, as follows:

- 7 cm for roof slabs not cantilevered;
- 8 cm for floor slabs not cantilevered;
- 10 cm for cantilevers.

In order to assure a greater reliability for the cantilevered slabs with thickness smaller than 19 cm, a correction coefficient γ_n for adjusting the loads is applicable, to be multiplied by the safety factors for loads γ_f, which have the same numerical expression defined in Equation (22) for slender columns, with the substitution in the equation of *b* by *h*, slab thickness.

6.2 Detailing of Slabs

According to section 19.3.3.2 of ABNT NBR 6118, it is now necessary a minimum negative (superior) reinforcement, even in the sup-

Figure 12 – Scheme of global imperfections

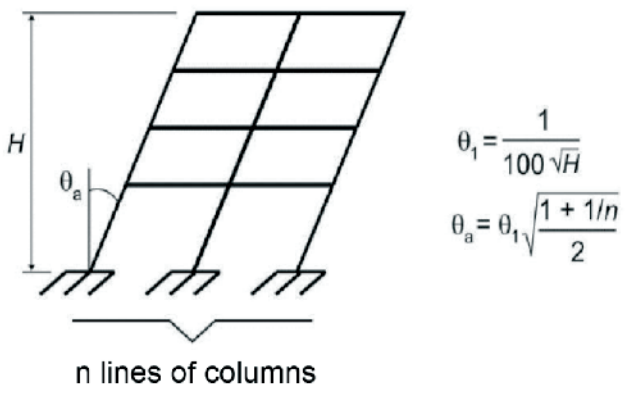

Table 3 – Characteristic superior values of shrinkage $\varepsilon_{cs}(t\infty,t0)$ and creep $\varphi(t\infty,t0)$

Average realive humidity %		40		55		75		90	
Equivalent thickness $2A_c/u$ cm		20	60	20	60	20	60	20	60
$\varphi(t\infty,t0)$ Concrete of class C20 to C45	5	4.6	3.8	3.9	3.3	2.8	2.4	2.0	1.9
	30	3.4	3.0	2.9	2.6	2.2	2.0	1.6	1.5
	60	2.9	2.7	2.5	2.3	1.9	1.8	1.4	1.4
$\varphi(t\infty,t0)$ Concrete 0f class C50 to C90	5	2.7	2.4	2.4	2.1	1.9	1.8	1.6	1.5
	30	2.0	1.8	1.7	1.6	1.4	1.3	1.1	1.1
	60	1.7	1.6	1.5	1.4	1.2	1.2	1.0	1.0
$\varepsilon_{cs}(t\infty,t0)$ 0/00	5	- 0.53	- 0.47	- 0.48	- 0.43	- 0.36	- 0.32	- 0.18	- 0.15
	30	- 0.44	- 0.45	- 0.41	- 0.41	- 0.33	- 0.31	- 0.17	- 0.15
	60	- 0.39	- 0.43	- 0.36	- 0.40	- 0.30	- 0.31	- 0.17	- 0.15

t_0 days

ports of slabs (usually beams) which does not present continuity with adjacent slabs, but with elastic connection with the support elements.

This negative reinforcement shall comply with the minimum reinforcement ratio $\rho_s \geq 0.67\ \rho_{min}$, according to the Table 19.1 of the Standard. This reinforcement shall cover at least 0.15 of the smaller span of the analyzed slab, from the face of the support.

It is now necessary, in slabs reinforced in one or two directions and for which transversal reinforcement is not necessary, that all the positive reinforcement should placed up to the supports, with 4 cm beyond the theoretical axis of the supports. This requirement may be dispensed if an explicit evaluation on the increases of the reinforcement due to the torsional moments in the slabs would be done.

7. Detailing of deep beams

The section 22.4.4.1 of the Standard defines new criteria for the detailing of deep beams. The positive (inferior) reinforcement shall be placed in a strip of height up to 0.15 *h* (*h* – effective height of the deep beam).

The negative reinforcement A_s shall be distributed considering three strips in the effective height *h*, which shall be smaller than the theoretical beam span ℓ ($3 \geq \ell/h \geq 1$):

$$\text{Superior 20\% of } h: \quad A_{S1} = (\ell/2h - 0.50)\,.\,A_S \qquad (23a)$$

$$\text{Central 60\% of } h: \quad A_{S2} = (1.50 - \ell/2h)\,.\,A_S \qquad (23b)$$

$$\text{Inferior 20\% of } h: \quad A_{S3} = 0 \qquad (23c)$$

The minimum vertical and horizontal reinforcement is of 0,075% *b* (thickness), per face, per meter.

8. Creep and shrinkage

Important changes have been introduced in the criteria for the evaluation of effects of creep and shrinkage, reflecting the evolution of the knowledge on these subjects in the last years. The coefficients defined in the Table 8.2 of the Standard, and reproduced next in Table 3, considers now different values for the creep coefficients for concretes with $f_{ck} \geq 50$ MPa.

In the revision 2014 of the Standard, regarding the revision of 2007, the values of creep are reduced, mainly for concretes with $f_{ck} \geq 50$ MPa, but there is an important increase in the shrinkage coefficients. It should be noticed that the more detailed criteria defined in the Appendix A of the Standard were also modified.

9. Conclusion

Some of the main changes introduced in the 2014 revision of ABNT NBR 6118, which will have direct impact in the safety verifications of reinforced concrete structures have been shortly summarized herein. It shall be noticed that, differently from the previous revisions, this one has immediate compulsory application after its issuing. New work processes, as the obligatory verification of the design by an independent design office, of all the structural projects, shall be also implemented. In this way, an immediate adaptation of the criteria currently applied in the

design practice of the engineering firms shall be adopted, considering the new requirements of the revision 2014 of the Brazilian Standard.

10. Bibliographic references

[1] ASSOCIAÇÃO BRASILEIRA DE NORMAS TÉCNICAS (ABNT). NBR 6118. Projeto de estruturas de concreto – Procedimento. Rio de Janeiro. 2014 (in Portuguese).

[2] SANTOS, S.H.C.- Os Concretos de Alta Resistência na NBR 6118:2014, Revista Concreto & Construções nº 73, pg. 52-57, January/Março 2014 (in Portuguese).

[3] CERUTTI, R. M. B. – Análise do Comportamento do Concreto de Alta Resistência na Flexão Composta com Base na NBR 6118:2014, Graduation Monography, Polytechnic School, UFRJ, 2014. Available in:http://monografias.poli.ufrj.br/monografias/monopoli10010812.pdf (in Portuguese).

Volume 8, Number 4 (August 2015) p. 547-566 • ISSN 1983-4195
http://dx.doi.org/10.1590/S1983-41952015000400008

REVISTA IBRACON DE ESTRUTURAS E MATERIAIS
IBRACON STRUCTURES AND MATERIALS JOURNAL

Impacts in the structural design of the 2014 revision of the brazilian standard ABNT NBR 6118

Impactos no projeto estrutural da versão 2014 da norma brasileira ABNT NBR 6118

R. M. CERUTTI [a]
raphaelmbx@poli.ufrj.br

S. H. C. SANTOS [b]
sergiohampshire@gmail.com

Abstract

With the issuing of the 2014 version of the Brazilian Standard ABNT NBR 6118 – Design of Concrete Structures, several procedures followed in the design offices shall be altered. The purpose of this paper is to furnish data to the designers, in order to facilitate the transition to the new version of the Standard. A summary of some of the main modifications with direct impact in the design is presented, being shown, among others, the topics: characteristics of the concretes of class up to C90, including the new stress-strain diagrams and respective simplification criteria for these diagrams, the new deformation domains, the values of design tensile stresses in concrete and the new criteria for limiting the depth of the neutral axis; new design criteria for designing and detailing of special elements, including the application of strut-and-tie models; new design criteria, minimum dimensions and detailing criteria for columns, walls and slabs; new criteria for considering global imperfections; new criteria for considering creep and shrinkage; new values for minimum reinforcement in pure bending; new expressions for evaluating the elasticity modulus of concrete. A new table for the design of concrete sections under pure bending is furnished, and new diagrams for designing rectangular sections under bending with compression forces are presented.

Keywords: brazilian standard, structural concrete, design, detailing.

Resumo

Com a promulgação da versão 2014 da Norma Brasileira ABNT NBR 6118 – Projeto de Estruturas de Concreto, diversos procedimentos adotados nas empresas de projeto deverão ser alterados. O objetivo deste trabalho é fornecer subsídios aos projetistas, de forma a facilitar a transição para a nova versão da Norma. É apresentado um resumo de algumas das principais alterações que tem impacto direto no projeto, sendo abordados, entre outros, os temas: características dos concretos de classe até C90, incluindo os novos diagramas tensão-deformação e respectivos critérios de simplificação destes diagramas, os novos domínios de deformação, os valores de tensão de tração de cálculo no concreto e os novos critérios de limitação da profundidade da linha neutra; novos critérios de dimensionamento e detalhamento de elementos especiais, inclusive com a aplicação de Modelos Biela-Tirante; novos critérios de projeto, dimensões mínimas e detalhamento de pilares, pilares-parede e lajes; novos critérios para a consideração de imperfeições globais; novos critérios para a consideração de retração e fluência; novos valores para a armadura mínima de peças em flexão simples; novas expressões para a avaliação do módulo de elasticidade do concreto. É também fornecida uma nova tabela de dimensionamento na flexão simples e apresentados novos ábacos para o dimensionamento de seções retangulares na flexão composta reta.

Palavras-chave: norma brasileira, concreto estrutural, dimensionamento, detalhamento.

[a] *Universidade Federal do Rio de Janeiro, Escola Politécnica, Programa de Projeto de Estruturas, Rio de Janeiro, RJ, Brasil;*
[b] *Universidade Federal do Rio de Janeiro, Escola Politécnica, Departamento de Estruturas, Rio de Janeiro, RJ, Brasil.*

Received: 22 Dec 2014 • Accepted: 25 May 2015 • Available Online: 7 Aug 2015

1. Introdução

Após muitos meses de intenso trabalho da Comissão de Estudo encarregada de sua revisão, foi finalmente emitida a versão 2014 da Norma Brasileira ABNT NBR 6118 – Projeto de Estruturas de Concreto [1]. Esta versão coloca a ABNT NBR 6118 no mesmo nível de atualização das normas internacionais mais conceituadas, refletindo todo um esforço da Associação Brasileira de Normas Técnicas e de toda a comunidade técnica brasileira de atingir um elevado patamar de qualidade no projeto e construção das estruturas de concreto. Dentre outras importantes alterações, a faixa de aplicação dos critérios da ABNT NBR 6118 é estendida da Classe C50 até a Classe C90. Apresenta-se aqui um breve resumo de alguns dos novos critérios desta revisão da Norma. Alguns desses novos aspectos foram já apresentados por SANTOS [2].

2. Características do Concreto

2.1 Módulo de Elasticidade

O avanço no maior conhecimento das propriedades do concreto obtido nos últimos anos permitiu uma definição mais precisa do módulo de elasticidade do concreto, na ausência de ensaios específicos para sua determinação.
A estimativa para o módulo de elasticidade inicial, a ser utilizado, por exemplo, na avaliação de perdas de protensão, passa a ser:
- para f_{ck} de 20 MPa a 50 MPa;

$$E_{ci} = \alpha_E \cdot 5600 \sqrt{f_{ck}} \quad (1)$$

- para f_{ck} de 55 MPa a 90 MPa:

$$E_{ci} = 21.5 \cdot 10^3 \cdot \alpha_E \cdot \left(\frac{f_{ck}}{10} + 1.25 \right)^{1/3} \quad (2)$$

O parâmetro α_E depende da rocha matriz da brita empregada:

Figura 1 – Módulos de elasticidade tangente e secante do concreto

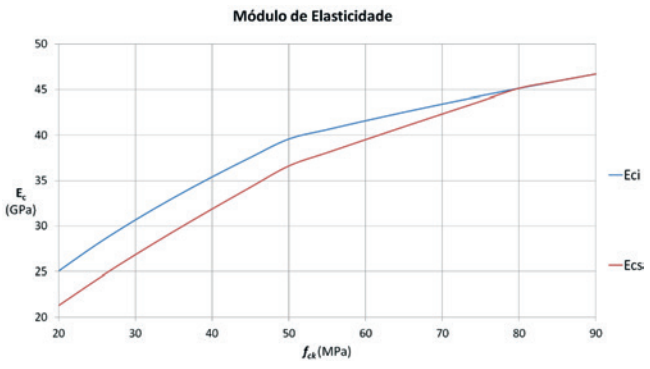

Figura 2 – Diagrama tensão-deformação de cálculo do concreto

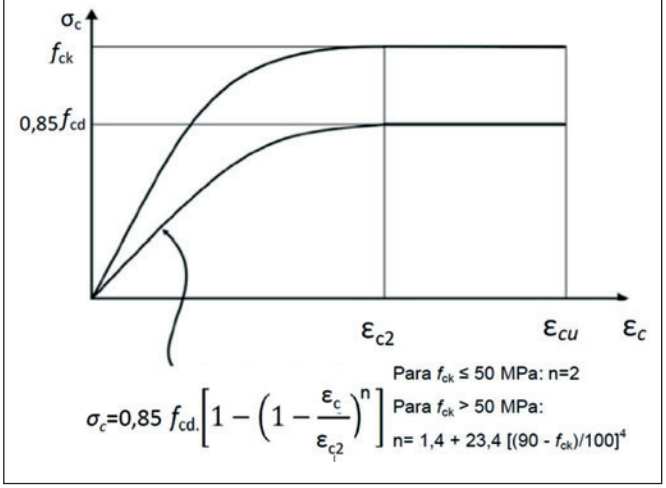

α_E = 1,2 para basalto e diabásio;
α_E = 1,0 para granito e gnaisse;
α_E = 0,9 para calcário;
α_E = 0,7 para arenito.
A estimativa para o módulo de elasticidade secante, a ser utilizado na avaliação do comportamento de um elemento estrutural em geral ou de uma seção transversal, passa a ser:

$$E_{cs} = \alpha_i \cdot E_{ci} \quad (3)$$

$$\alpha_i = 0.8 + 0.2 \frac{f_{ck}}{80} \leq 1.0 \quad (4)$$

Os dois módulos confluem para o mesmo valor com o aumento da resistência do concreto, na medida em que o trecho inicial do diagrama tensão-deformação vai se tornando mais próximo do linear. A visualização gráfica da variação destes dois parâmetros (para α_E = 1,0) é apresentada na Figura 1.

2.2 Diagramas tensão-deformação

Os diagramas tensão-deformação característicos e de cálculo dos concretos de alta resistência irão refletir sua maior fragilidade, na medida em que ele vai crescendo em resistência. A Figura 2, reproduzida da ABNT NBR 6118:2014, define as novas características destes diagramas tensão-deformação.
Os valores a serem adotados para os parâmetros ε_{c2} (deformação específica de encurtamento do concreto no início do patamar plástico) e ε_{cu} (deformação específica de encurtamento do concreto na ruptura) são:

Figura 3 – Variação dos parâmetros n, ε_{c2} e ε_{cu}

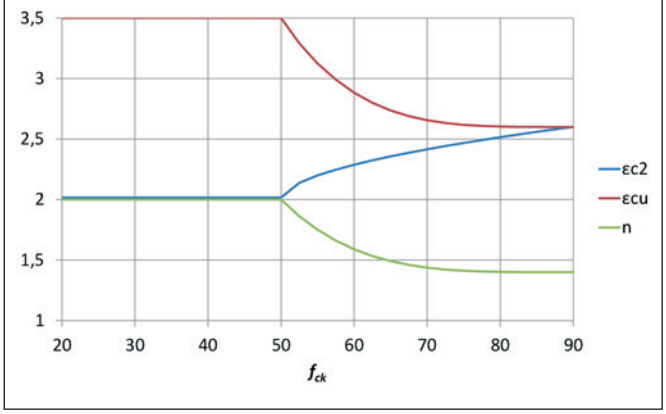

$$\varepsilon_{c2} = 2.0^{0}/_{00} \quad (5)$$

$$\varepsilon_{cu} = 3.5^{0}/_{00} \quad (6)$$

- para concretos de classes de C50 até C90:

$$\varepsilon_{c2} = 2.0^{0}/_{00} + 0.085^{0}/_{00}.(f_{ck} - 50)^{0,53} \quad (7)$$

$$\varepsilon_{cu} = 2.6^{0}/_{00} + 35^{0}/_{00}.[(90 - f_{ck})/100]^{4} \quad (8)$$

Os parâmetros n, ε_{c2} e ε_{cu} são mostrados graficamente na Figura 3.

2.3 Resistência à tração

Na ausência de ensaios específicos, os valores de resistência média à tração do concreto devem ser estimados pelas expressões:
- para concretos com $f_{ck} \leq 50$ MPa esta estimativa não é alterada:

$$f_{ct,m} = 0.3\ f_{ck}^{\ 2/3} \quad (9)$$

- para concretos com f_{ck} 50 MPa até 90 MPa:

Figura 4 – Resistência à tração média do concreto

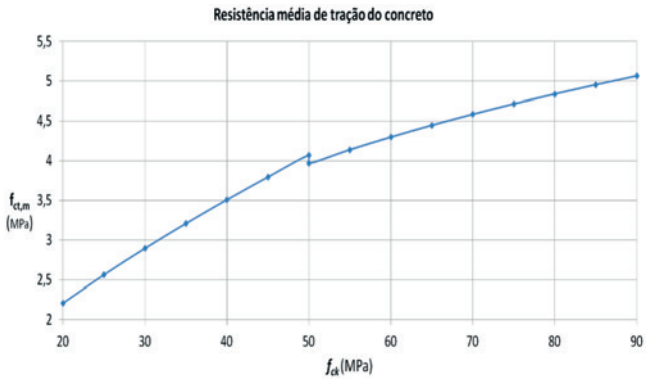

$$f_{ct,m} = 2.12 \ln (1 + 0.11\ f_{ck}) \quad (10)$$

Observe-se que a resistência à tração do concreto cresce mais lentamente em relação ao aumento da resistência à compressão. A expressão gráfica desta variação é dada na Figura 4.

3. Dimensionamento à flexão simples e composta

3.1 Novos domínios de deformação no estado limite último

A Figura 17.1 da Norma passa a ter a definição reproduzida na Figura 5.

3.2 Simplificação do diagrama tensão-deformação do concreto

Tendo em vista as características de fragilidade dos concretos de

Figura 5 – Domínios de deformação no estado limite último

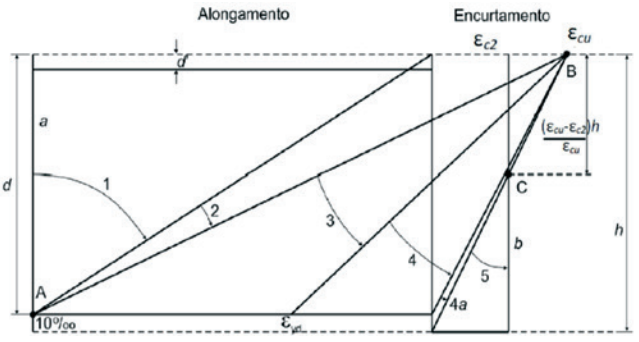

Figura 6 – Esquemas de deformação específica e diagramas de tensões

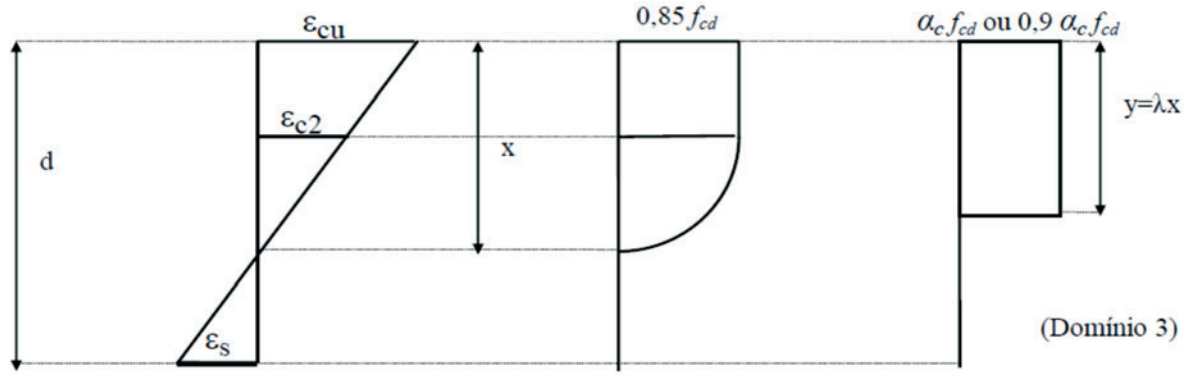

classe acima de C50, os critérios de simplificação dos diagramas tensão-deformação foram revistos, de forma que os diagramas simplificados forneçam um valor de resultante e de seu posicionamento nas seções, ambos compatíveis com os obtidos com o diagrama real.

Para o entendimento da simplificação agora proposta, apresentam-se na Figura 6 esquemas típicos de deformação específica e diagramas real e simplificado de tensões ao longo da altura de uma seção em flexão simples no Domínio 3.

O diagrama real pode ser substituído por um retângulo de profundidade (y) igual a λx, onde o valor do parâmetro λ é definido como:

- para concretos com $f_{ck} \leq 50$ MPa:

$$\lambda = 0.8 \qquad (11)$$

- para concretos com f_{ck} 50 MPa até 90 MPa:

$$\lambda = 0.8 - \frac{(f_{ck} - 50)}{400} \qquad (12)$$

A tensão constante atuante até a profundidade y pode ser tomada igual a $\alpha_c \cdot f_{cd}$, no caso da largura da seção não diminuir a partir da linha neutra para a borda comprimida, e igual a $0{,}9\ \alpha_c\ f_{cd}$, no caso contrário.

O parâmetro α_c é definido como:

- para f_{ck} de 20 MPa a 50 MPa é mantido o valor de:

$$\alpha_c = 0.85 \qquad (13)$$

- para concretos com f_{ck} maior que 50 MPa (até 90 MPa):

$$\alpha_c = 0.85 \cdot \left(1 - \frac{(f_{ck} - 50)}{200}\right) \qquad (14)$$

Devem ser considerados na flexão simples os limites de *x/d*:

- para f_{ck} de 20 MPa a 50 MPa:

$$x/d \leq 0.45 \qquad (15)$$

- para concretos com f_{ck} maior que 50 MPa (até 90 MPa):

$$x/d \leq 0.35 \qquad (16)$$

A variação dos parâmetros λ e α_c é apresentada graficamente na Figura 7.

3.3 Nova tabela para o dimensionamento à flexão simples

Considerando as novas definições normativas, é aqui apresentada uma nova tabela para o dimensionamento à flexão simples de seções retangulares de concreto armado, sem armadura de compressão (Tabela 1). Nesta tabela empregam-se as variáveis adimensionais abaixo definidas. A linha horizontal em negrito nas colunas indica a fronteira dos domínios de deformação 2 e 3.

Figura 7 – Parâmetros γ e α_c

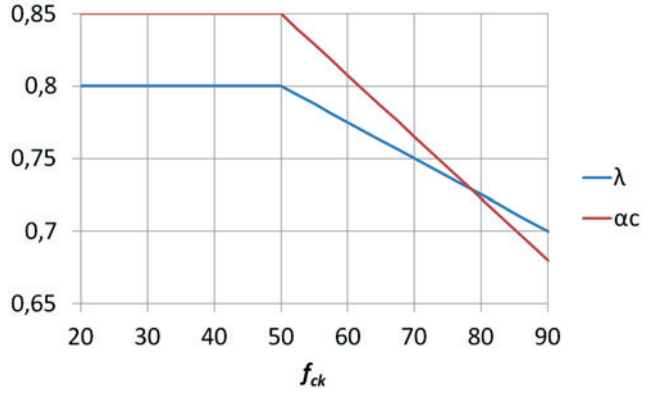

Tabela 1 – Dimensionamento à flexão simples

f_{ck}	≤ 50MPa		60 MPa		70 MPa		80 MPa		90 MPa	
ε_{cu} e k_{lim23}	3.500	0.259	2.884	0.224	2.656	0.210	2.604	0.207	2.600	0.206
λ e α_c	0.800	0.850	0.775	0.808	0.750	0.765	0.725	0.723	0.700	0.680
k_x	k_z	K_{md}	k_z	K_{md}	k_z	K_{md}	k_z	K_{md}	k_z	K_{md}
0,02	0,992	0,013	0,992	0,012	0,993	0,011	0,993	0,010	0,993	0,009
0,04	0,984	0,027	0,985	0,025	0,985	0,023	0,986	0,021	0,986	0,019
0,06	0,976	0,040	0,977	0,037	0,978	0,034	0,978	0,031	0,979	0,028
0,08	0,968	0,053	0,969	0,049	0,970	0,045	0,971	0,041	0,972	0,037
0,10	0,960	0,065	0,961	0,060	0,963	0,055	0,964	0,050	0,965	0,046
0,12	0,952	0,078	0,954	0,072	0,955	0,066	0,957	0,060	0,958	0,055
0,14	0,944	0,090	0,946	0,083	0,948	0,076	0,949	0,070	0,951	0,063
0,16	0,936	0,102	0,938	0,094	0,940	0,086	0,942	0,079	0,944	0,072
0,18	0,928	0,114	0,930	0,105	0,933	0,096	0,935	0,088	0,937	0,080
0,20	0,920	0,125	0,923	0,115	0,925	0,106	0,928	0,097	0,930	0,089
0,22	0,912	0,136	0,915	0,126	0,918	0,116	0,920	0,106	0,923	0,097
0,24	0,904	0,148	0,907	0,136	0,910	0,125	0,913	0,115	0,916	0,105
0,26	0,896	0,158	0,899	0,146	0,903	0,135	0,906	0,123	0,909	0,112
0,28	0,888	0,169	0,892	0,156	0,895	0,144	0,899	0,132	0,902	0,120
0,30	0,880	0,180	0,884	0,166	0,888	0,153	0,891	0,140	0,895	0,128
0,32	0,872	0,190	0,876	0,175	0,880	0,162	0,884	0,148	0,888	0,135
0,34	0,864	0,200	0,868	0,185	0,873	0,170	0,877	0,156	0,881	0,143
0,35	0,860	0,205	0,864	0,189	0,869	0,174	0,873	0,160	0,878	0,146
0,37	0,852	0,214	–	–	–	–	–	–	–	–
0,39	0,844	0,224	–	–	–	–	–	–	–	–
0,41	0,836	0,233	–	–	–	–	–	–	–	–
0,43	0,828	0,242	–	–	–	–	–	–	–	–
0,45	0,820	0,251	–	–	–	–	–	–	–	–

$$k_x = \frac{x}{d}; k_z = \frac{z}{d}; K_{md} = \frac{M_d}{b.d^2.f_{cd}}; A_s = \frac{M_d}{d.k_z.f_{yd}} \quad (17)$$

Onde:
x – profundidade da linha neutra;
d – altura útil da seção;
b – largura da seção;
z – braço de alavanca na flexão simples;
M_d - momento fletor de cálculo;
f_{cd} – resistência à compressão de cálculo de concreto;
f_{yd} – tensão de escoamento de cálculo do aço.

Observar que esta tabela pode ser também aplicada ao dimensionamento de seções com armadura de compressão, sendo no caso aplicada para a avaliação da armadura correspondente à parcela do momento fletor de cálculo equilibrada com a compressão resistida pelo concreto, e sendo a parcela do momento equilibrada utilizando armadura de compressão avaliada na forma usual.

3.4 Nova tabela para as armaduras mínimas na flexão simples

A Tabela 17.3 da ABNT NBR 6118 foi totalmente reformulada e é parcialmente reproduzida na Tabela 2.

3.5 Novos ábacos para o dimensionamento à flexão composta reta

Novos ábacos para o dimensionamento à flexão composta reta devem ser desenvolvidos para os concretos das classes superiores a C50. Devido às novas definições da ABNT NBR 6118, os ábacos para estes concretos de alta resistência apresentam valores muito distintos dos

Tabela 2 – Valores de ρ_{min} ($A_{s,min}$/Ac) (%) em função do f_{ck}

f_{ck}	20	30	40	50	60	70	80	90
ρ_{min}	0,150	0,150	0,179	0,208	0,219	0,233	0,245	0,256

Figura 8 – Ábaco adimensional de interação – Tipo 2 – d'/h = 0,10 – C50

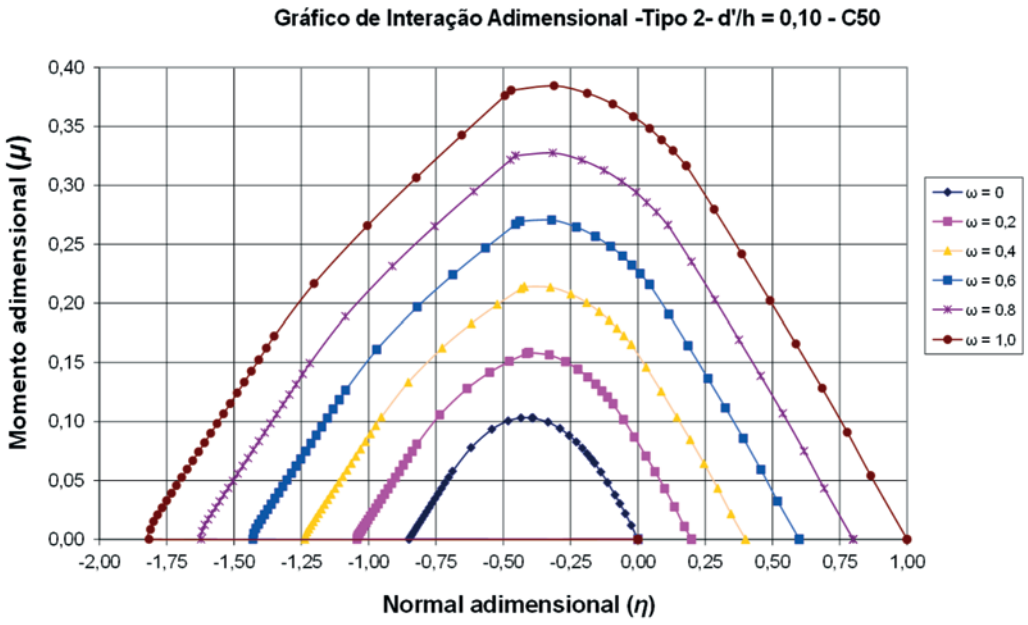

traçados para os concretos de classe até C50. Estes novos ábacos podem ser desenvolvidos como apresentado por CERUTTI [3].
Neste trabalho constatou-se que, para os concretos de categoria superior a C50, o uso do diagrama retangular não se aplica ao domínio 5, por levar a resultados excessivamente conservadores. Isto obriga à utilização dos diagramas tensão-deformação reais do concreto. As Figuras 8 e 9 comparam ábacos de dimensionamento adimensionais traçados para concreto até C50 e para concreto C90, respectivamente (para a seção retangular chamada de Tipo 2, com armadura uniformemente distribuída em sua periferia). Os ábacos utilizam os parâmetros adimensionais η, μ e ω (respectivamente força normal adimensional, momento fletor adimensional e taxa mecânica de armadura) abaixo definidos:

$$\eta = \frac{N_d}{b.h.f_{cd}} \; ; \; \mu = \frac{M_d}{b.h^2.f_{cd}} \; ; \; \omega = \frac{A_s.f_{yd}}{b.h.f_{cd}} \qquad (18)$$

Figura 9 – Ábaco adimensional de interação – Tipo 2 – d'/h = 0,10 – C90

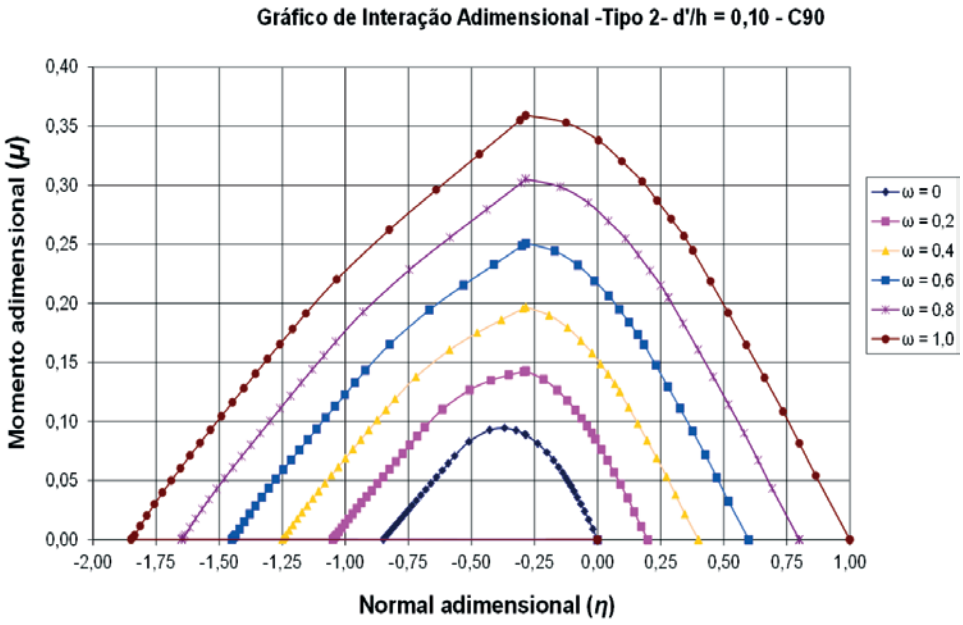

No “hiperlink” citado na referência de CERUTTI [3], este trabalho pode ser diretamente acessado, onde podem ser encontrados os diversos ábacos de dimensionamento desenvolvidos para várias distribuições de armadura na periferia de seções retangulares, assim como diversos exemplos de aplicação destes ábacos.

4. Dimensionamento com modelos biela-tirante

A Figura 22.1 da ABNT NBR 6118:2014, reproduzida na Figura 10, exemplifica diversas situações típicas de Regiões D, de descontinuidade geométrica, de descontinuidade de tensões ou de aplicação de cargas concentradas, que podem ser analisadas com modelos de biela-tirante. Esta versão da Norma passa a definir critérios de verificação de tensões no concreto para estas regiões especiais.

São definidos a seguir estes limites de tensão f_{cd1}, f_{cd2} e f_{cd3}.

$$f_{cd1} = 0.85\ \alpha_{v2}\ f_{cd} \qquad (19)$$

$$f_{cd2} = 0.60\ \alpha_{v2}\ f_{cd} \qquad (20)$$

$$f_{cd3} = 0.72\ \alpha_{v2}\ f_{cd} \qquad (21)$$

Onde:

$\alpha_{V2}=1 - f_{ck}/250$

O limite f_{cd1} aplica-se à verificação de regiões com tensões de compressão transversal ou sem tensões de tração transversal e em nós onde confluem somente bielas de compressão. O limite f_{cd2} aplica-se à verificação de regiões com tensões de tração transversal e em nós onde confluem dois ou mais tirantes tracionados. O limite f_{cd3} aplica-se à verificação de em nós onde conflui somente um tirante tracionado.

A Figura 11 ilustra a aplicação destes três limites de compressão no concreto no caso da análise de uma viga simples biapoiada.

5. Projeto e detalhamento de pilares e pilares-parede

5.1 Dimensões mínimas

Passa a ser exigida a dimensão mínima de 14 cm no lado menor de pilares e pilares-parede. Quando este lado menor for inferior a 19 cm, continua sendo aplicável o coeficiente γ_n de ajuste de cargas, multiplicativo aos coeficientes de majoração de cargas γ_f, conforme definido a seguir (*b* é a menor dimensão do pilar em cm):

Figura 10 – Situações típicas de Regiões D

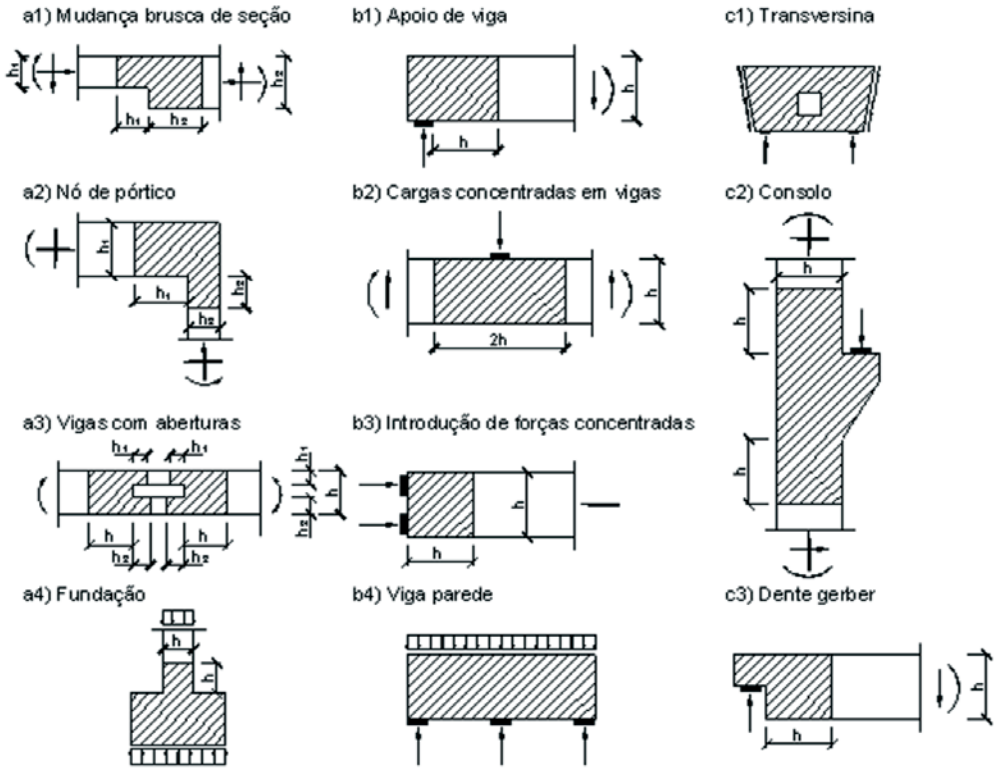

Figura 11 – Regiões de aplicação dos limites de compressão no concreto

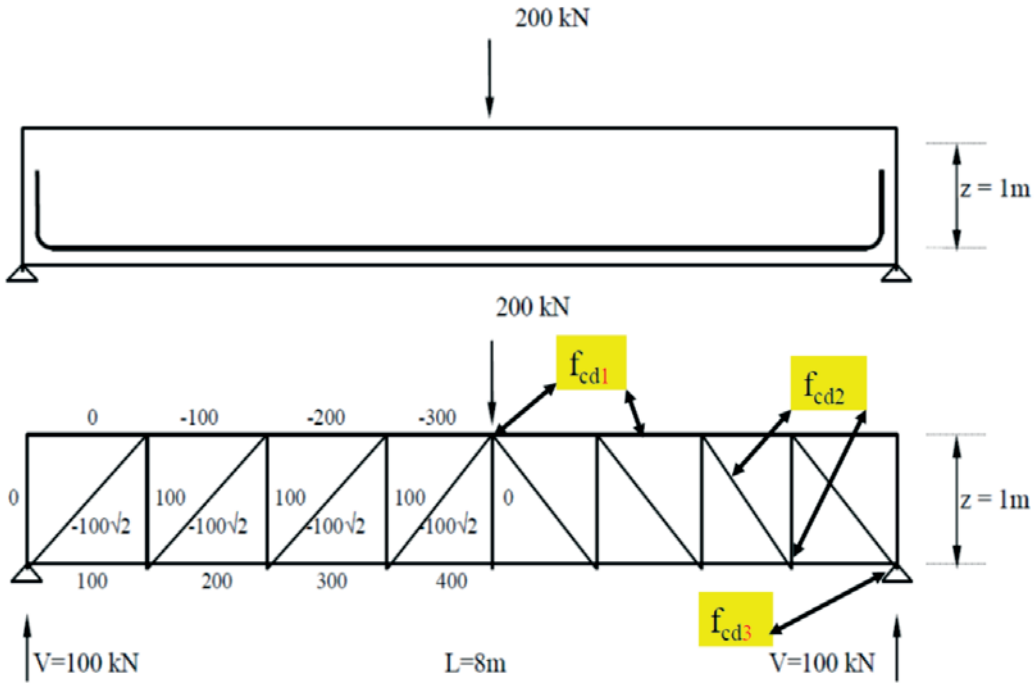

$$\gamma_n = 1{,}95 - 0{,}05b \qquad (22)$$

Algumas importantes alterações são incluídas no item 11.3.3.4.1 relativamente à avaliação dos efeitos das imperfeições globais nos edifícios. A Figura 12 esquematiza estes efeitos de imperfeições globais. A faixa de aplicação do coeficiente q_1 passa a ser, em estruturas reticuladas e para a avaliação de imperfeições locais, de q_{1min} = 1/300 a q_{1max} = 1/200.

Passa a ser agora necessária a investigação da possibilidade de superposição dos efeitos das imperfeições globais e do vento. A sobreposição será necessária se o menor dos dois efeitos, mensurado em termos do momento global resultante na base da estrutura, for superior a 30% do maior efeito.

Nesta comparação, deve-se considerar o desaprumo correspondente a q_1, não se considerando o q_{1min}.

Quando a superposição for necessária, e o vento predominar, deve-se combinar com o vento o desaprumo correspondente a θ_1, não se considerando θ_{1min}. Se o efeito de desaprumo for predominante, o valor de θ_1 deve atender ao θ_{1min}.

6. Projeto de lajes

6.1 Dimensões mínimas das lajes

Importantes alterações foram introduzidas na definição de espessuras mínimas de lajes, no item 13.2.4.1 da Norma, a saber:

- 7 cm para coberturas não em balanço;
- 8 cm para lajes de piso não em balanço;
- 10 cm para lajes em balanço.

De forma a assegurar uma maior confiabilidade às lajes em balanço, quando apresentarem espessura inferior a 19 cm, elas passam a ser afetadas por um coeficiente γ_n de ajuste de cargas, multiplicativo aos coeficientes de majoração de cargas γ_f. Este coeficiente tem a mesma expressão numérica definida na Equação (22)

Figura 12 – Esquema das imperfeições globais

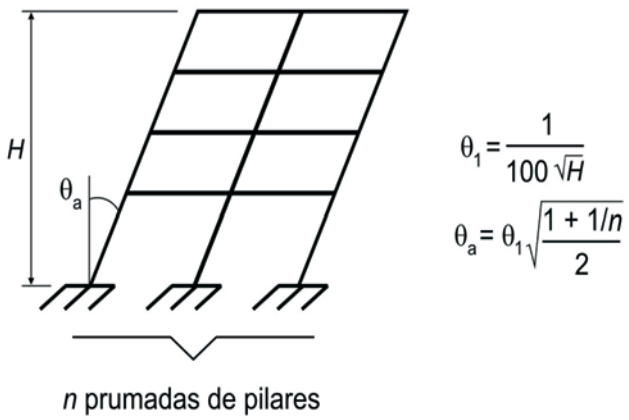

Tabela 3 – Valores característicos superiores da retração $\varepsilon_{cs}(t\infty,t0)$ e da fluência $\varphi(t\infty,t0)$

Umidade média ambiente %		40		55		75		90	
Espessura fictícia $2A_c/u$ cm		20	60	20	60	20	60	20	60
$\varphi(t\infty,t0)$ Concreto das classes C20 a C45	t_0 days 5	4,6	3,8	3,9	3,3	2,8	2,4	2,0	1,9
	30	3,4	3,0	2,9	2,6	2,2	2,0	1,6	1,5
	60	2,9	2,7	2,5	2,3	1,9	1,8	1,4	1,4
$\varphi(t\infty,t0)$ Concreto das classes C50 a C90	5	2,7	2,4	2,4	2,1	1,9	1,8	1,6	1,5
	30	2,0	1,8	1,7	1,6	1,4	1,3	1,1	1,1
	60	1,7	1,6	1,5	1,4	1,2	1,2	1,0	1,0
$\varepsilon_{cs}(t\infty,t0)$ 0/00	5	- 0,53	- 0,47	- 0,48	- 0,43	- 0,36	- 0,32	- 0,18	- 0,15
	30	- 0,44	- 0,45	- 0,41	- 0,41	- 0,33	- 0,31	- 0,17	- 0,15
	60	- 0,39	- 0,43	- 0,36	- 0,40	- 0,30	- 0,31	- 0,17	- 0,15

para os pilares esbeltos, mas substituindo-se na equação *b* por *h*, espessura da laje.

6.2 Detalhamento de lajes

De acordo com o item 19.3.3.2 da ABNT NBR 6118, passa a ser obrigatória a disposição de uma armadura negativa mínima, mesmo no apoio de lajes que não apresentem continuidade com lajes adjacentes, mas que tenham ligação com os elementos de apoio. Esta armadura deverá atender à percentagem mínima $\rho_s \geq 0{,}67\ \rho_{min}$, conforme a Tabela 19.1 da Norma. Essa armadura deve se estender até pelo menos 0,15 do vão menor da laje em questão, a partir da face do apoio.

Passa a ser obrigatório, nas lajes maciças armadas em uma ou em duas direções, e em que seja dispensada armadura transversal, que toda a armadura positiva seja levada até os apoios e prolongada no mínimo 4 cm além do eixo teórico do apoio, não se permitindo escalonamento desta armadura. Este requisito poderá ser dispensado se houver avaliação explícita dos acréscimos das armaduras decorrentes da presença dos momentos volventes nas lajes.

7. Detalhamento de vigas parede

O item 22.4.4.1 da Norma explicita novos critérios de detalhamento de vigas-parede.

As armaduras positivas devem ser distribuídas em uma altura de até cerca de 0,15 *h* (*h* – altura efetiva da viga-parede).

As armaduras negativas A_s devem ser distribuídas considerando-se três faixas na altura *h*, não se considerando para *h* valores superiores ao vão teórico ℓ ($3 \geq \ell/h \geq 1$):

$$\text{20\% superiores de h: } A_{s1} = (\ell/2h - 0{,}50)\ .\ A_s \qquad \text{(23a)}$$

$$\text{60\% centrais de h: } A_{s2} = (1{,}50 - \ell/2h)\ .\ A_s \qquad \text{(23b)}$$

$$\text{20\% inferiores de h: } A_{s3} = 0 \qquad \text{(23c)}$$

As armaduras horizontais e verticais mínimas são de 0,075% *b* por face, por metro.

8. Fluência e retração

Importantes alterações são introduzidas nos critérios de avaliação dos efeitos de fluência e retração, refletindo a evolução do conhecimento sobre estes temas nos últimos anos. Os coeficientes definidos na Tabela 8.2 da Norma e reproduzidos a seguir na Tabela 3, consideram agora um valor diferenciado de fluência para os concretos com $f_{ck} \geq 50$ MPa.

Na versão 2014 da Norma, com relação à versão de 2007, os valores de fluência são reduzidos, especialmente para os concretos com $f_{ck} \geq 50$ MPa, mas há um acréscimo expressivo nos coeficiente de retração. Observe-se que os critérios mais detalhados, definidos no Anexo A da Norma, foram também modificados.

9. Conclusão

Algumas das principais alterações introduzidas na versão 2014 da ABNT NBR 6118, que terão impacto direto nas verificações de segurança das estruturas de concreto armado, foram brevemente resumidas. Observar que, de forma diferente das revisões

anteriores, esta revisão da ABNT NBR 6118 entrou em vigor e tem aplicação obrigatória imediatamente após sua publicação. Novos processos de trabalho, como o da verificação obrigatória, por empresa independente, de todos os projetos estruturais, também deverão ser implementados. Desta forma, deve haver uma imediata adaptação dos critérios atualmente adotados na prática das empresas de projeto considerando estes novos requisitos normativos.

10. Referências bibliográficas

[1] ASSOCIAÇÃO BRASILEIRA DE NORMAS TÉCNICAS (ABNT). NBR 6118. Projeto de estruturas de concreto – Procedimento. Rio de Janeiro. 2014.

[2] SANTOS, S.H.C.- Os Concretos de Alta Resistência na NBR 6118:2014, Revista Concreto & Construções nº 73, pg. 52-57, Janeiro/Março 2014.

[3] CERUTTI, R. M. B. – Análise do Comportamento do Concreto de Alta Resistência na Flexão Composta com Base na NBR 6118:2014 – Projeto de Graduação, Escola Politécnica, UFRJ, 2014. Disponível: http://monografias.poli.ufrj.br/monografias/monopoli10010812.pdf

Volume 8, Number 4 (August 2015) p. 567-576 • ISSN 1983-4195
http://dx.doi.org/10.1590/S1983-41952015000400009

REVISTA IBRACON DE ESTRUTURAS E MATERIAIS
IBRACON STRUCTURES AND MATERIALS JOURNAL

Behavior of granular rubber waste tire reinforced soil for application in geosynthetic reinforced soil wall

Comportamento de solo reforçado com resíduo granular de borracha de pneu para aplicação em parede de solo reforçada com geossintético

G. G. D. RAMIREZ [a]
gduran@pucp.pe

M. D. T. CASAGRANDE [a]
michele_casagrande@puc-rio.br

D. FOLLE [b]
daiane.folle@imed.edu.br

A. PEREIRA [b]
alvaro.pereira@imed.edu.br

V. A. PAULON [b]
vpaulon@hotmail.com

Abstract

Large quantities of waste tires are released to the environment in an undesirable way. The potential use of this waste material in geotechnical applications can contribute to reducing the tire disposal problem and to improve strength and deformation characteristics of soils. This paper presents a laboratory study on the effect of granular rubber waste tire on the physical properties of a clayey soil. Compaction tests using standard effort and consolidated-drained triaxial tests were run on soil and mixtures. The results conveyed an improvement in the cohesion and the angle of internal friction the clayey soil-granular rubber mixture, depending on the level of confining stress. These mixtures can be used like backfill material in soil retaining walls replacing the clayey soil due to its better strength and shear behavior and low unit weight. A numerical simulation was conducted for geosynthetic reinforced soil wall using the clayey soil and mixture like backfill material to analyzing the influence in this structure.

Keywords: triaxial tests, granular rubber, waste, reinforced soil.

Resumo

Uma grande quantidade de resíduo de pneu é descartada no meio ambiente de forma indesejada. O potencial de uso deste resíduo em aplicações geotécnicas podem contribuir para a redução do problema de descarte e melhorar as características de resistência e deformação dos solos. Este artigo apresenta um estudo laboratorial dos efeitos da aplicação dos resíduos granulares de pneus nas propriedades físicas de solos argilosos. Foram desenvolvidos testes de compactação usando esforços padrão e ensaios triaxiais consolidados drenados em amostras de solo e suas misturas. Os resultados apresentam uma melhoria na coesão e no ângulo de atrito do solo argiloso e a mistura com borracha granular, dependendo do confinamento das tensões. Estas misturas podem ser utilizadas como material de aterro em paredes de contenção em substituição de solos argilosos devido a um melhor desempenho na resistência ao cisalhamento e baixo peso unitário. Uma simulação numérica foi realizada para parede de solo reforçada com geossintético utilizando solo argiloso e misturas para materiais de aterro com a finalidade de analisar a influência nesta estrutura.

Palavras-chave: ensaios triaxiais, borracha granular, resíduo, reforço de solo.

[a] *Department of Civil Engineering, Pontifical Catholic University of Rio de Janeiro; Rio de Janeiro, RJ, Brazil;*
[b] *Civil Engineering School, Faculty IMED, Passo Fundo; Passo Fundo, RS, Brazil.*

Received: 20 Oct 2014 • Accepted: 23 Jun 2015 • Available Online: 7 Aug 2015

1. Introduction

Scrap tires are increasing every year and their disposal is a major environmental problem. Particles of rubber tires are been using in landfill engineering as subgrade reinforcement for construction roads over soft soil and others researches suggest their application in civil engineering because of their low density, high durability, high thermal insulation and low cost compared with other fill materials (Cetin, [1]; SZELIGA, [2], RAMIREZ, [3]). In Brazil is being using a specific granular rubber of scrap tires mixed with asphalt for the cap asphaltic road.

This research aimed to understand the viability of this granular rubber as reinforcement material in geotechnical works (layers of landfills, embankments on soft soils and temporary landfills), obtaining a first knowledge of the behavior of reinforced clayey soil with this granular rubber from scrap tires. Finally, use of this alternative material would decrease the demand of natural resources, reducing the environmental impact and adding value to this waste.

2. Materials

2.1 Clayey soil

The clayey soil used in this study is a residual tropical soil (Figure 1) with a limit liquid of 53%, a limit plastic of 39% and specific gravity 2.72. It was collected in the Experimental Field II located in the PUC-Rio Campus. The grain size distribution curve is shown in Figure 3. This clayey soil is classified as MH according to SUCS. This soil has a micro-granular texture, constituted by quartz, altered garnet, clay minerals (mainly kaolinite) and iron and aluminum oxides.

Figure 1 – Clayey soil

Figure 2 – Granular rubber

2.2 Granular rubber

The granular rubber used for reinforced the clayey soil (Figure 2) is by-products of the tire retread process. The specific gravity of this material is 1,12. Its middle diameter is 1,0 mm, varying between 0,2 mm and 2,0 mm. The particle size distribution is shown in Figure 3. This material is composed of 50% by weight of particular cars tire and 50% by weight of trucks tire. In Brazil this granular rubber is mainly used in road construction area. A mixture of asphalt and granular rubber is being used as an efficient technology to achieve Brazilian road requirements.

Figure 3 – Particle size distribution curve of granular rubber and clayey soil

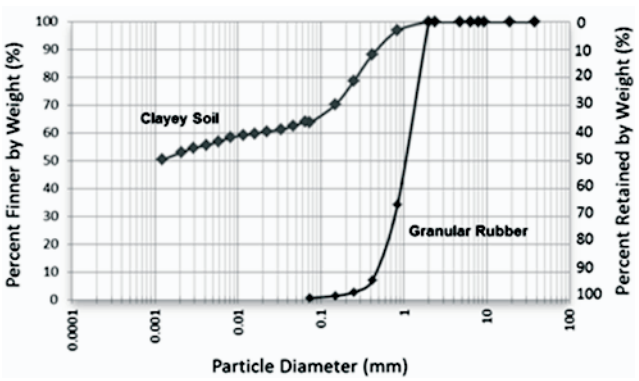

Table 1 – Symbols used to denote the soil and mixtures

Material / Mixture	Soil (%)	Granular rubber (%)	Symbol
Clayey soil	100	0	S100
Mixture 1	95	5	S95/B5
Mixture 2	90	10	S90/B10
Mixture 3	80	20	S80/B20

2.3 Mixtures

Clayey soil was mixed with 5%, 10% and 20% of granular rubber by dry weight of soil. Water was added according to the optimum moisture and the maximum dry density obtained from Standard Proctor Test (standard compactive effort) performed on each material (S100, S95/B5, S90/B10 and S80/B20). The abbreviations used to denote the soil and mixtures are shown in Table 1.

3. Experimental procedure

In order to obtain the optimum rubber content was performed triaxial tests on samples with 5%, 10% and 20% of granular rubber by dry weight of clayey soil (S100). Physical characterization and standard proctor tests were run on clayey soil and mixtures.

Figure 4 – Standard proctor test curves

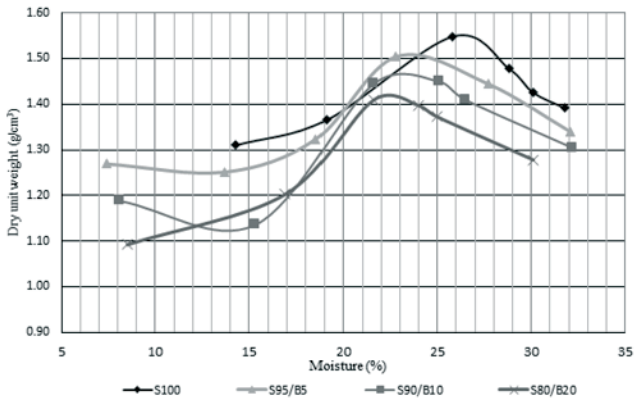

solids, particle size analysis, liquid limit and plastic limit tests were performed using the material finer than size #40 (0,425 mm). An important step to obtain the specific gravity of soil solids is removing the entrapped air in the soil with a vacuum pump. Then was added water to the pycnometers until complete its capacity. Four pycnometers were used to calculate an average value of Gs. The particle size analysis for coarse soil was done according to the standards by sieving, while the distribution of particle size for fine soil was determined by sedimentation process using a hydrometer.

Table 2 – Clayey soil physical characterization

Gs	Sand (%)	Clay (%)	LL (%)	LP (%)	IP (%)	SUCS
2.72	36.4	10.8	53	39	14	MH

3.1 Physical characterization tests

Characterization tests were performed to determine the index properties of clayey soil samples, from the Experimental Field II. The soil was prepared according to the Brazilian technical standard (Brazilian Association of Technical Standards – ABNT). The performed tests followed next standards:

- NBR 6457/1986 – Samples of Soil – Preparations for using in Proctor Test and Characterization.
- NBR 7181/1984 – Soil – Particle Size Analysis.
- NBR 6508/1984 – Soil – Specific Gravity of Soil Solids.
- NBR 6459/1984 – Soil – Liquid Limit.
- NBR 7180/1984 – Soil – Plastic Limit.

The specific gravity of soil

3.2 Standard proctor tests

Standard proctor tests were conducted on the clayey soil (S100) and mixtures (S95/B5, S90/B10 and S80/B20) to determinate the optimum moisture (wopt) and the maximum dry density (γdmax) of all materials. These tests were made according to NBR 7182, using the standard compactive effort.

The compaction was made in a small cylindrical mold (internal diameter 10 cm and height 12,7 cm). It applied 26 blows in each layer (three layer in total) with a manual rammer, of 2,5 kg of weight, falling 30,5 cm of height. Carefully was trimmer the top of the compacted specimen until to form a plane surface with the top of the mold. Then was determined the mass of the specimen inside the mold using a balance and subtracting the mold weight.

Table 3 – Optimum moisture and maximum dry unit weight

Material / Mixture	Wopm (%)	γ_{dmax} (%)
S100	26.3	1.56
S95/B5	23.5	1.51
S90/B10	23.1	1.47
S80/B20	22.5	1.42

The material was removed from the mold to obtain a specimen for moisture. Then, with each moisture and dry density was plotted the points of the compaction curve. At least were used two molding water content points in each side of the curve (wet and dry side).

3.3 Triaxial tests

Standard triaxial testing procedures were followed. The specimens were saturated using backpressure and percolation of

Figure 5 – Results of drained triaxial tests for clayey soil (S100) and mixture (S95/B5)

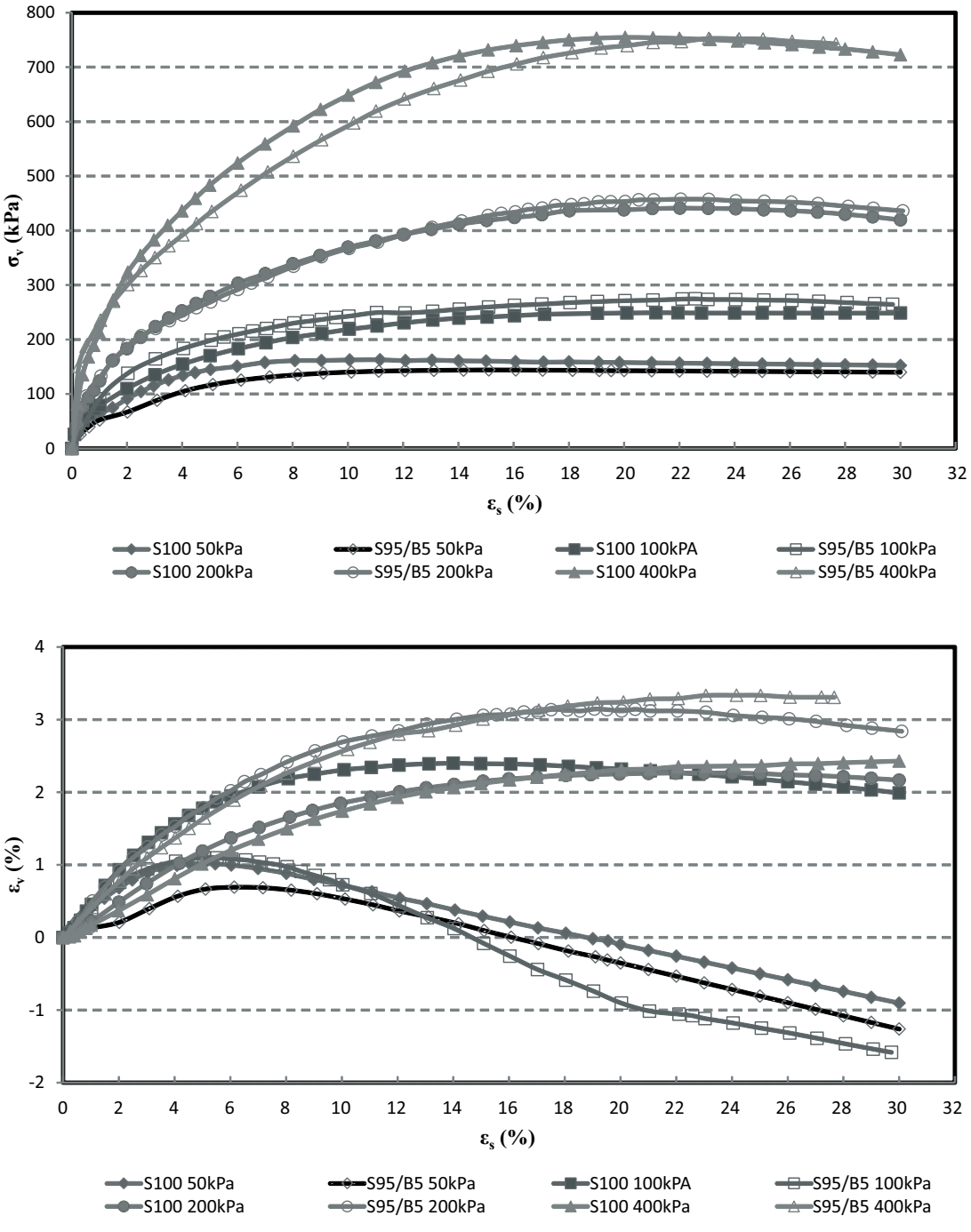

water through the samples. The final saturation was estimated with Skempton parameter (B = 0,97). Consolidated-drained (CD) tests were conducted on clayey soil and mixtures. According to HEAD [5], the maximum rate of deformation was determined using the minimum time of failure 8,5t100. The rate of deformation used in the shear phase was 0,022 mm/min for all samples. After compact the clayey soil and the mixtures with their optimum moistures and maximum dry densities were

Figure 6 – Results of drained triaxial tests for clayey soil (S100) and mixture (S90/B10)

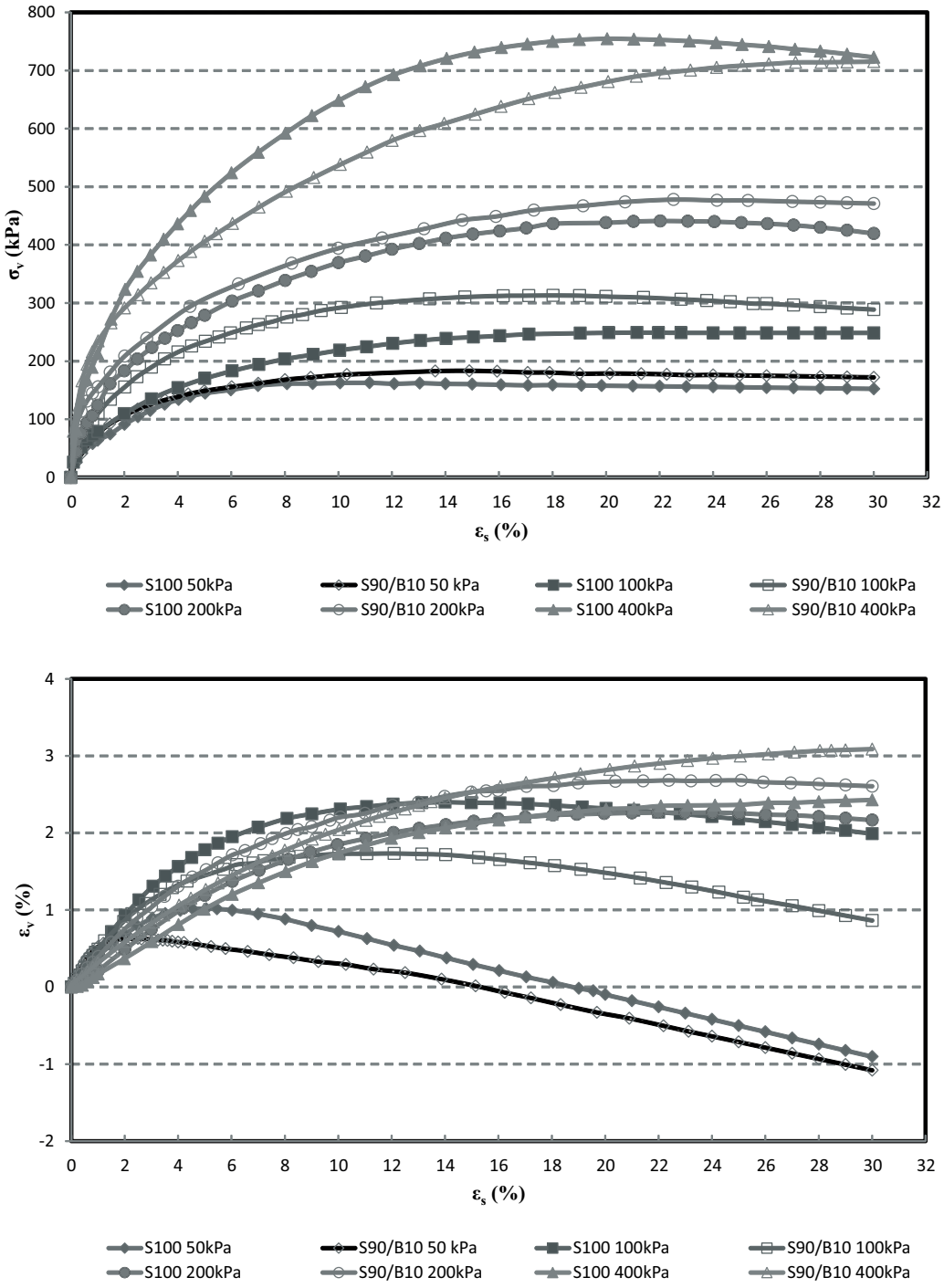

molded samples with 3,8 cm of diameter and 7,2 cm of height.

4. Results and analysis

The results of specific gravity (Gs), liquid limit (LL), plastic limit (LP) and a resume of particle size are shown in Table 2. According with SUCS this soil is classified as a silt high plasticity (MH), but in this research it is named clayey soil due to it has more than 50% of clay. The soil particle size distribution curve is shown in Figure 3. The compaction results showed the maximum dry unit weights and the optimum moistures of mixtures are lower than those for clayey soil (S100). This decrease is mainly due to lower specific gravity

Figure 7 – Results of drained triaxial tests for clayey soil (S100) and mixture (S80/B20)

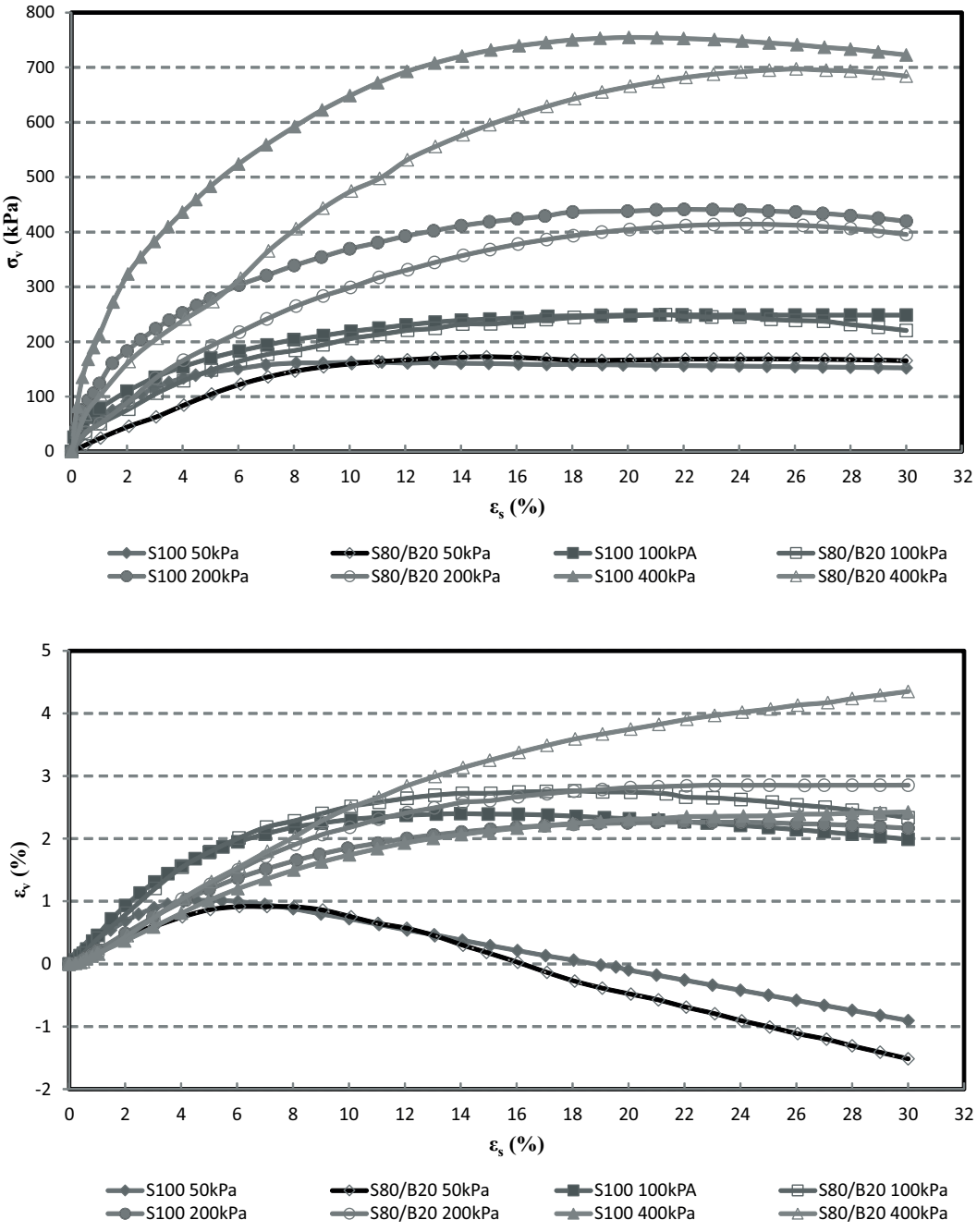

Figure 8 – Sheared mixture speciemens. Confining stress: (a) 100 kPa, (b) 200 kPa and (c) 400 kPa

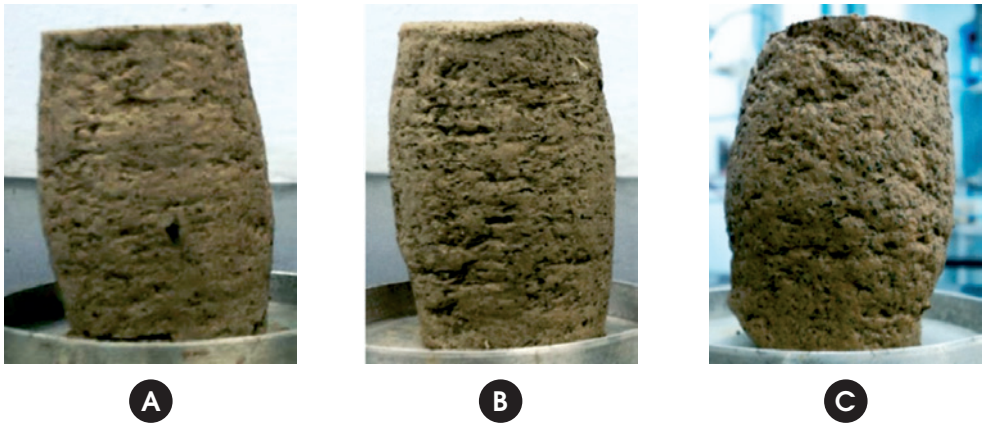

of the rubber. The Figure 4 and Table 3 show the results of the standard compaction tests performed on clayey soil and mixtures. The triaxial tests showed that exist a positive influence of granular rubber reinforcement on the shear strength behavior of the clayey soil. The mixture with 10% of rubber has the better behaviour compared with the others mixtures (See Figures 5, 6 and 7).

The shear strength of the mixture (S90/B10) increase in relation to clayey soil (S100), this occur until 200 kPa of effective confine stress, beyond of this confine stress the presence of granular rubber degrade the shear strength of the clayey soil. The shear strength of clayey soil reached 162, 250, 440 kPa at 50, 100 and 200 kPa of confinement stress, respectively. On the other hand, the shear strength of S90/B10 mixture attained 184, 312, 478 kPa at same confining stresses. The increases of strength were 52%, 124% and 10% for 50, 100 and 200 kPa of confinement stress, showing clearly the influence of confining stress on shear strength. In large strain, the shear strength of the mixture maintains larger that strength of the clayey soil. Only for 400 kPa of effective confinement stress, the

Figure 9 – Strength envelopes of clayey soil (S100) and mixture (S90/B10)

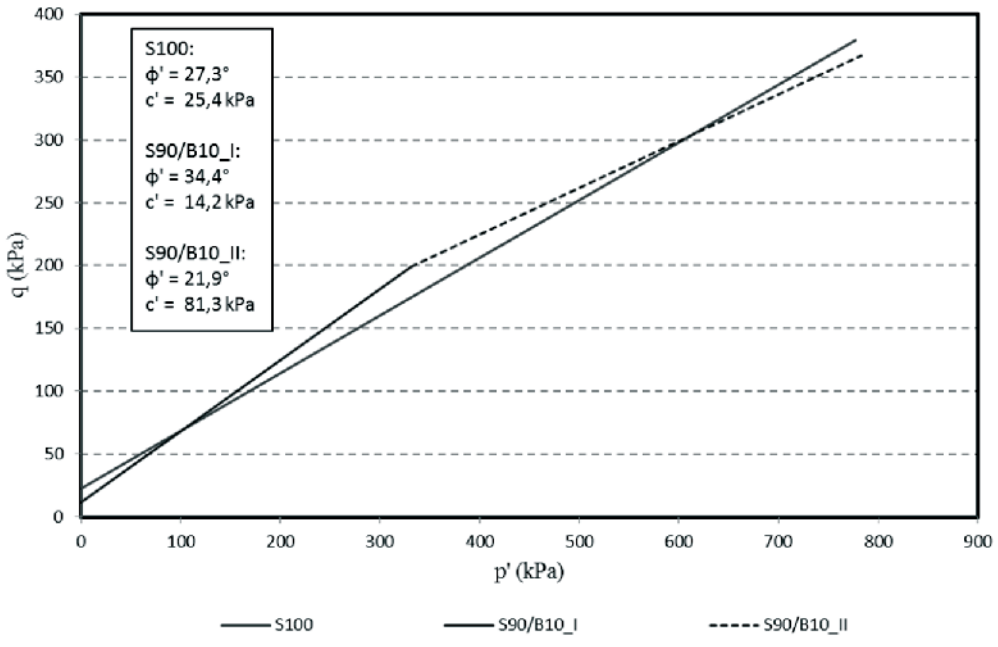

Figure 10 – Geosyntetic reinforced soil wall model

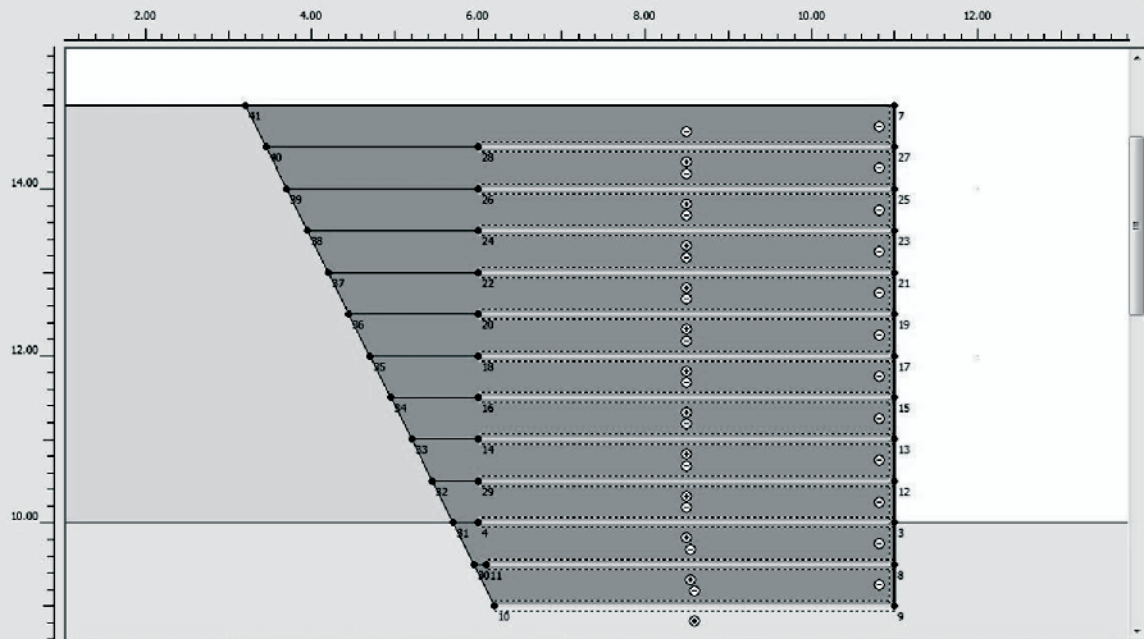

Figure 11 – Deformation generated after the last construction phase

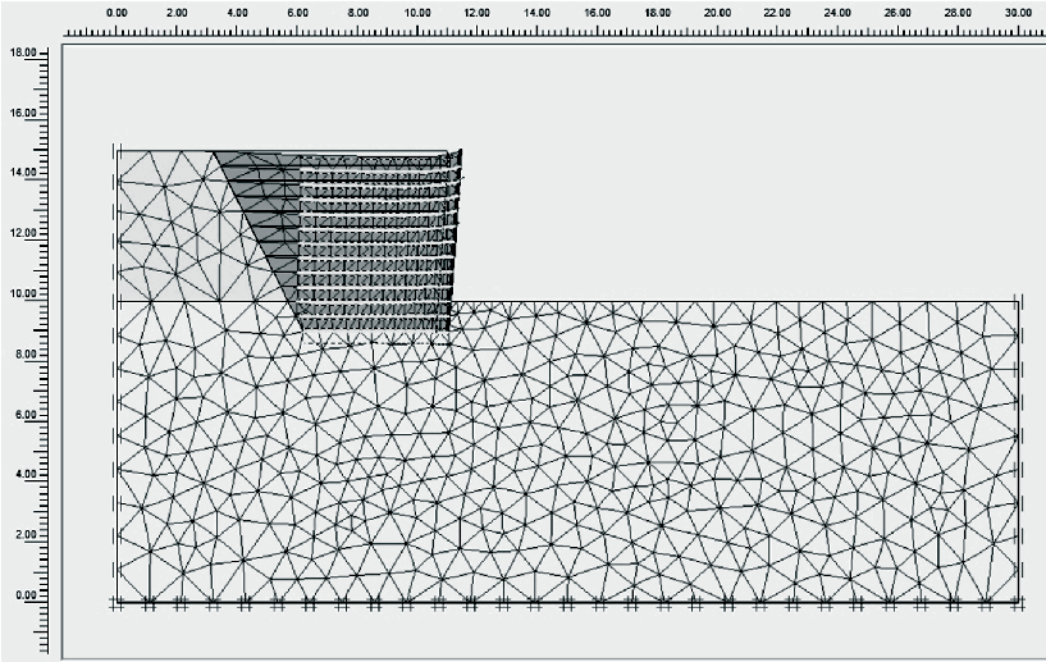

Figure 12 – Horizontal Displacements on precast concrete wall

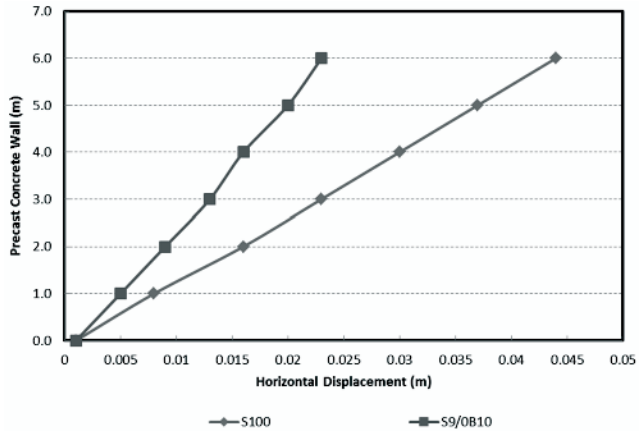

shear strength of the mixture was shorter than strength of clayey soil, however from 30% of strain can it appreciate that the shear strength of clayey soil has a tendency to be shorter than mixture and the shear strength of the mixture tend to arise. Volume changes caused by shearing differ for clayey soil and mixtures. S90/B10 mixture shows less contraction comparing with S100 for 50, and 100 kPa confining stress. Furthermore, these both specimens show higher rate of dilatation than other mixtures and higher shear strength than the clayey soil. Dilatation could mobilize the tensile stress on rubber, adding strength during shear stage. The tested S90/B10 mixture specimens are shown in Figure 8.

In the Figure 9 are shown the strength envelopes of the clayey soil and the mixture 2 (S90/B10). This envelope were plotted in p':q space. The strength envelope of the mixture shows bilinearity due to confining stress influence. For high levels of confinement the strength decrease and can be less than strength of clayey soil. The first part of the mixture strength envelope has a friction angle of 34,4° and the second parte decreases to 21,9°. In the other hand, the cohesion of the first part of the envelope is 14,2 kPa, arising in the second part to 81,3 kPa.

5. Numerical simulation of a geosynthetic reinforced soil wall

It was performed a numerical simulation of a geosynthetic reinforced soil wall. This structure was formed with layer of compacted soil (backfill) reinforced with geogrids. A precast concrete face completed the structure. It was considered 6,0 m of height and 12 layer of 0,5 m of thickness (See Figure 10).

It was using the finite element program PLAXIS to run this example. The purpose of this simulation was to compare the behaviour of the geosynthetic reinforced soil wall when the backfill is constituted for clayey soil (S100) or mixture 2 (S90/B10). There were defined points in the precast concrete face to know the horizontal displacements generated for the backfill. The Hardening soil model was used for the backfill materials and the Mohr Coulomb model was assigned to foundation soil. Horizontal displacement on top

Figure 13 – Effective relative stresses (S100 backfill)

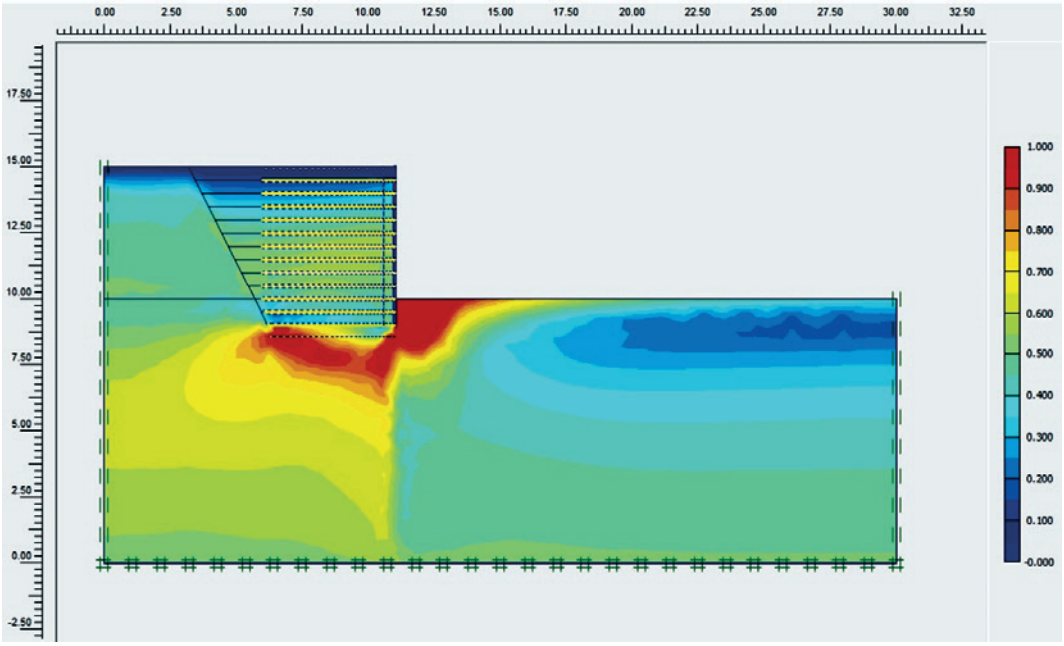

Figure 14 – Effective relative stresses (S90/10 backfill)

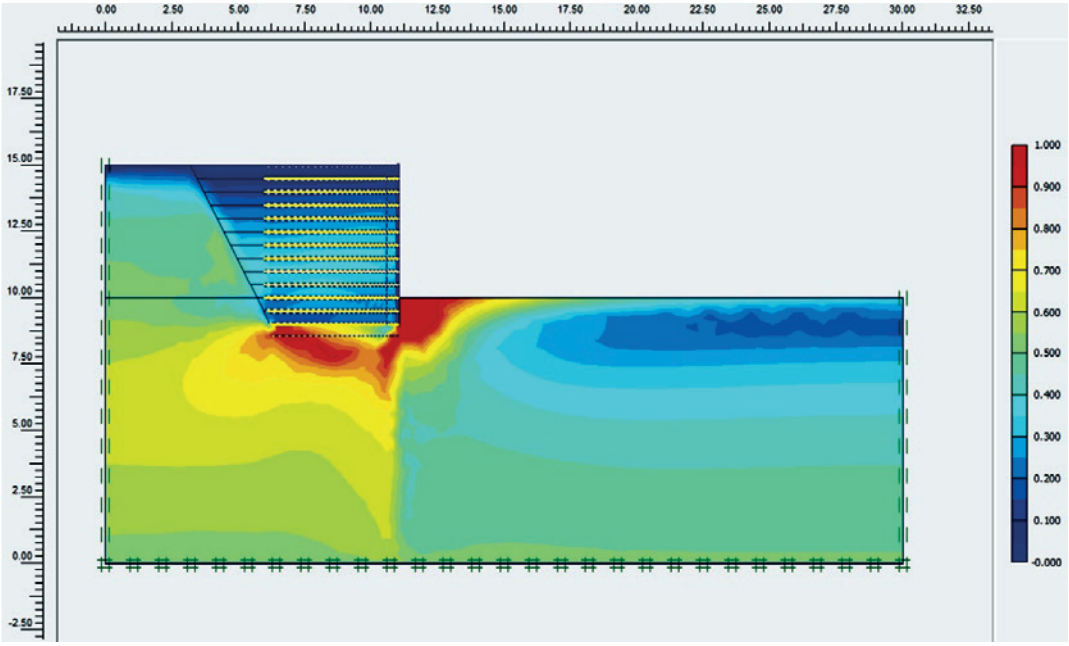

wall was 4.4 cm for clayey soil backfill. Moreover, S90/B10 backfill induced 2.3 cm of horizontal displacement on top wall. The horizontal displacement along the wall was less when S90/B10 material was used as backfill. The Figure 11 show the deformations generated after the last construction phase.

In addition, when it was used S90/B10 backfill the effective relative stresses were less than the effective relative stresses registered when S100 backfill was used. See Figures 13 and 14.

6. Conclusions

- Addition of granular rubber enhances the clayey soil behavior improving its shear strength.
- For large deformation, the shear strength of mixture is higher than clayey soil and the development of strength has a better behavior than clayey soil.
- The influence of the confinement in the mixture behavior is important. Exist a limiting confining pressure beyond which the presence of the granular rubber degrades the strength of the clayey soil. This could be explained because of the excessive confinement that restricts dilatation, in consequence the granular rubbers cannot mobilize tensile stress. Thus, this mixture will have a better performance than clayey soil under low confinement levels (Özkul and Baykal,[6]).
- Results of the numerical simulation showed minors horizontal displacements in the precast concrete wall when the mixture S90/B10 was used as backfill.
- Low effective stresses were generated when S90/B10 backfill was used in the retaining wall.
- This mixture is an adequate material to be used in some geotechnical application as layers of landfills, backfill in retaining walls, small embankments on soft soils, temporary landfills, subgrade reinforcement for construction roads over soft soil. In these projects the presence of low confinement stresses enable the use of this material.
- An important contribution to the environmental, low cost of the projects and major quality of this geotechnical structures would be possible with more researches in non-conventional material particularly with waste (Ramirez and Casagrande, [4]).

7. References

[1] CETIN, H.; FENER, M.; GUNAYDIN, O. Geotechnical properties of tire-cohesive clayey soil mixtures as a fill material. Engineering Geology, n.88, 2006. p. 110-120.

[2] SZELIGA, L. Avaliação do comportamento de solos reforçados com borracha moída de pneus inservíveis para aplicação em obras. PUC-Rio, Rio de Janeiro, 2011

[3] RAMIREZ, G. G. D. Estudo Experimental de Solos Reforçados com Borracha de Pneus Inservíveis. PUC-Rio, Rio de Janeiro, 2012.

[4] RAMIREZ, G. G. D. and CASAGRANDE, M. D. T. Experimental Study of Granular Rubber Waste Tire Reinforced Soil for Geotechnical Applications. Non-Conventional and Technologies for Sustainable Engineering, Key Engineering Materials, vol. 600, p 585-596, 2014.

[5] HEAD, K. H. Manual of Soil Laboratory Testing: Effective Stress Test. Wiley, 2da ed., vol. 3, West Sussex, Inglaterra, p. 227, 1986.

[6] ÖZKUL, Z. H. and BAYKAL, G. Shear Behavior of Compacted Rubber Fiber-Clay Composite in Drained and Undrained Loading. Journal of Geotechnical and Geoenvironmental Engineering, vol. 133, n.7, p. 767-781, 2007.

IBRACON

REVISTA IBRACON DE ESTRUTURAS E MATERIAIS

IBRACON STRUCTURES AND MATERIALS JOURNAL

Volume 8, Number 4
August 2015
ISSN: 1983-4195

Contents